CHEMIA

STUDIA
UNIVERSITATIS BABEŞ-BOLYAI

CHEMIA

EDITORIAL BOARD OF
STUDIA UNIVERSITATIS BABEŞ-BOLYAI CHEMIA

S T U D I A
UNIVERSITATIS BABEŞ–BOLYAI
CHEMIA

2
Tom II

CUPRINS – CONTENT – SOMMAIRE – INHALT

Studia Universitatis Babes-Bolyai Chemia has been selected for coverage in Thomson Reuters products and custom information services. Beginning with V. 53 (1) 2008, this publication is indexed and abstracted in the following:

- Science Citation Index Expanded (also known as SciSearch®)
- Chemistry Citation Index®
- Journal Citation Reports/Science Edition

RESIN TYPE INFLUENCE ON MOULDED PARTS FINAL DIMENSIONS

SEVER-ADRIAN RADU[a], VASILE DANUȚ LEORDEAN[a], NICOLAE BÂLC[a], OVIDIU NEMEȘ[b,*]

ABSTRACT. Silicone rubber moulding is a perfect solution to fill the gap between rapid prototyping and prototyping injection moulding. Silicone moulds reproduce the tiniest of details, so the quality of the pattern is critical; they are also a fast and affordable solution for functional prototypes and low volume production. A experimental method using vacuum casting of resin parts in flexible moulds is presented in this paper. During the experimental investigations technological features of casted material, volume of air traps, optimal working parameters and dimensional accuracy of the manufactured parts were studied. Based on these results, the corrective coefficients applicable to CAD dimensions in order to fabricate the master models by SLS were determined.

Keywords: Rapid Prototyping, Resin injection, Viscosity, Silicone rubber moulds

INTRODUCTION

The Rapid Tooling (RT) technology has evolved a lot in the last decades. Today it is possible to fabricate a complex pattern and other tooling for casting in a few hours while a casting may take up to several days. In the last decades, many companies have made great investments to improve manufacturing technologies in order to develop new products [1]. These technologies include CAD (Computer Aided Design) software and they are used to design complex geometries and also for solving some problems with high degrees of difficulty, including the medical field [2, 3]. In the last decade, many researches about RP (Rapid Prototyping) and RT (Rapid Tooling) technologies have been released, while the casting of the wax parts in a silicone rubber moulds was less studied [4÷6]. The resin patterns can be obtained at room temperature or in special conditions with good accuracy using vulcanizing silicone rubber moulds. Others author like Yang and Hannula, [7] studied the influence of injection parameters

[a] *Technical University of Cluj-Napoca, Faculty of Machine Building, 103-105 Muncii Blvd., RO-400641, Cluj-Napoca, Romania.*
[b] *Technical University of Cluj-Napoca, Faculty of Materials and Environmental Engineering, 103-105 Muncii Blvd., RO-400641, Cluj-Napoca, Romania.*
[*] *Corresponding author: ovidiu.nemes@sim.utcluj.ro*

on the dimensional stability of resin patterns produced by injection moulding process. In our case, we found the relation between various process parameters and their dependency on other parameters [8]. From all the parameters studied, it was found that the injection temperature is relevant for the dimensional accuracy of the parts. Nowadays, RT technology is the perfect options to solve the problems on resin moulded request by the market. It is estimated that total profits on new products are often reduced by as much as 60% because of the company's inability to get the product market quickly enough [9].

In the last few years, RT technology has evolved toward building moulds that provide up to 40% faster cycles than are possible with conventional technology [10]. That emphasis on productivity accompanies a shift in applications from prototype to full production tooling.

The advantages of flexible moulds are: efficiency, by reducing waste and energy consumption; agility for enable customization and flexibility for the modification and implementation of design concepts [11÷14].

In this paper, a new concept for obtaining flexible moulds together with the CAD model used for optimal dimensioning of rubber moulds is presented.

RESULTS AND DISCUSSION

In order to determine the influence of the resin type used in the manufacture of flexible moulds, measurements of resins moulded parts were achieved using Zeiss Navigator Prismo equipment, according to the sketch shown in Figure 1.
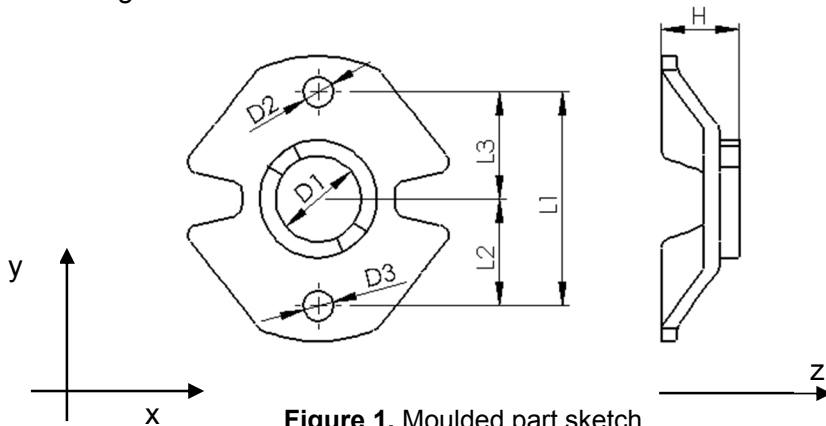
Figure 1. Moulded part sketch.

Additionally, the circularity deviations of diameters D1 = ∅24, D2, D3 = ∅8.4 has been analysed (denoted in the following by D1 = Dim. 1.1, D2 = Dim. 2.1, and D3 = Dim. 3.1) as well as the flatness deviation relative to dimension 7 in measurement sketch (denoted in the following by Dim. 7.1). Dimensions

measured were compared with CAD model and master model dimensions. Dimensions 1, 2, 3 are measured on the Y axis, 4, 5, 6 are the dimensions measured in the X axis and 7 is the only dimension measured on Z. It can be seen that on the axis X the average deviation is below the 1.5%, on the Y axis it has a value less than 0.65%, while the Z axis deviations occur up to 4%.

Then the percentage contractions of each dimension have been measured by comparing the required dimensions of resins parts and the CAD model, but also in relation to the dimensions of SLS master model. Deviations recorded (mean of 5 values measured) are shown in figure 2 and figure 3.
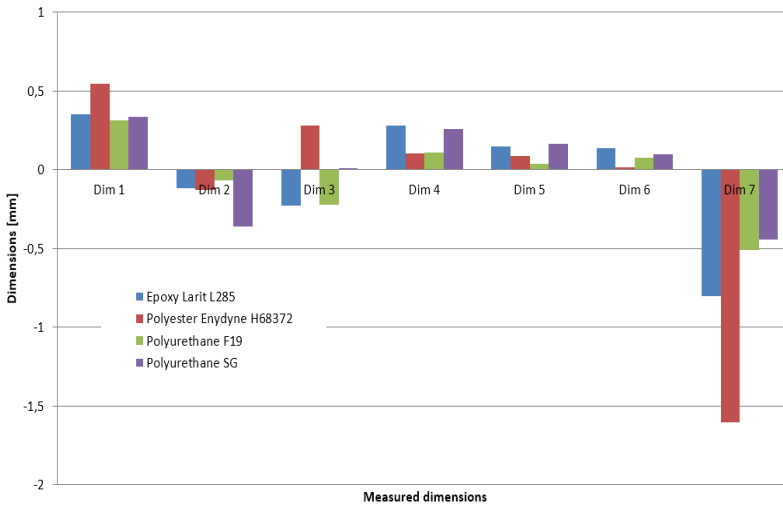
Figure 2. Deviations of resins parts dimensions related to CAD model and SLS master model
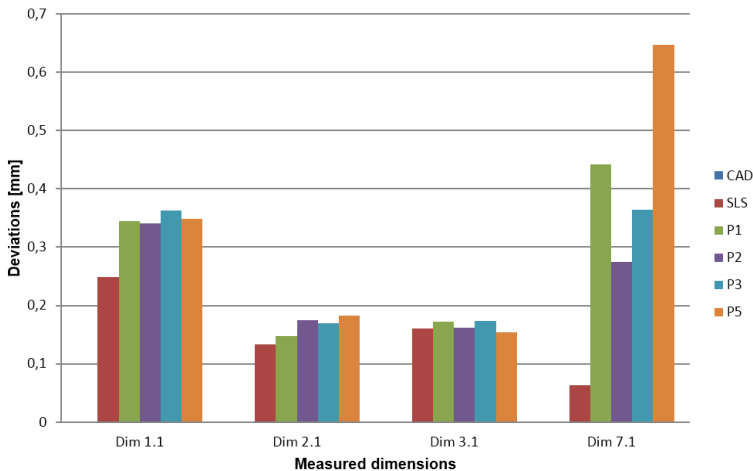
Figure 3. Flatness and circularity deviations

One of the main experimental parameters, important in achieving the flexible moulds, is the viscosity of the resin.

Figure 4 shows the variation in viscosity of the polyurethane resin based on mixing time of the two components of the resin while keeping constant the temperature at which the mould is heated. We observe that, if the times mixing increase, the resin viscosity increase also, due to the polymerization reaction.

Figure 5 presents the variation of viscosity according to the temperature of the mixture, keeping this time constant during the mixing of the components. It is noted that the viscosity increases also with the temperature if the mould is heated.
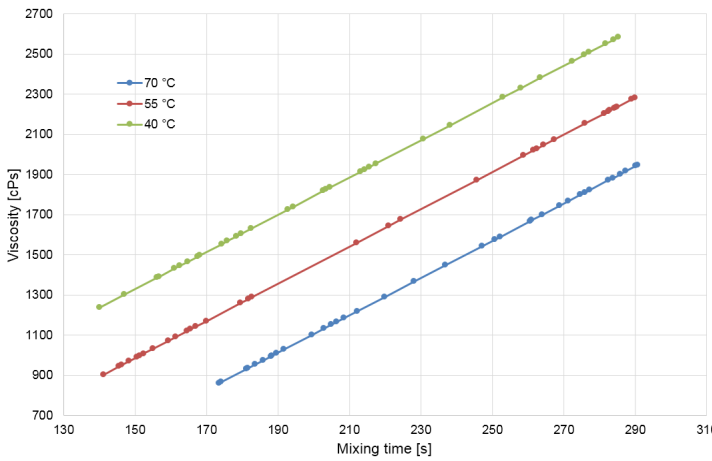
Figure 4. The variation of the viscosity depending on the time of mixing.
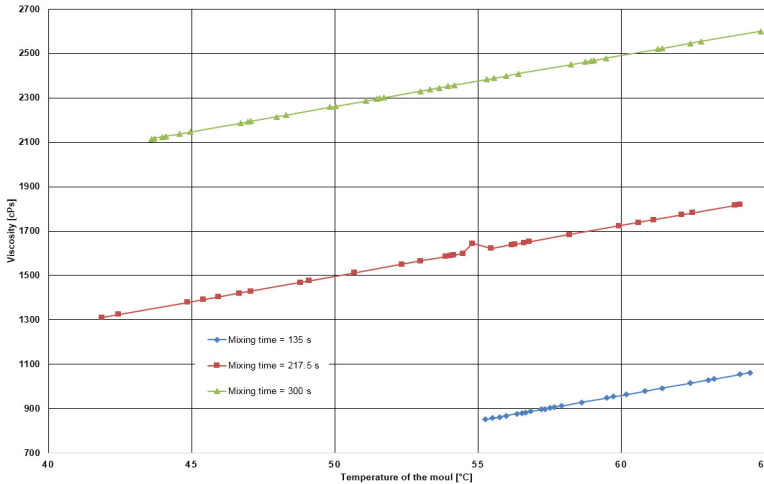
Figure 5. The variation of the viscosity depending on the temperature of the mould.

Experimental determination of resin density after polymerization is also very important in making the final product with the desired characteristics.

Because the resins used in casts are made up of two components (the density is known to each one) it is very difficult to determine the density of the mixture by theoretical methods. For this reason they have been made geometric forms with defined volume, for which the density is easily calculated [16].

After the curing of the resins and weighing each rectangular piece (figure 6) the calculating the volume density was easily determined.

Figure 6. Rectangular pieces well defined volume

In order to determine resin density (ρ) after polymerization, the volume for each parallelepiped was calculated according to the relationship:

$$V = L \cdot l \cdot h \tag{1}$$

where: V – part volume [cm^3]; L – length of the part [cm]; l – width of the part [cm]; h – height of the part [cm].

The experimental values of density after polymerization, $\rho = m/L\, l\, h,$ were showed in table 1 together with the main geometrical parameters of the rectangular obtained pieces.

Table 1. Determination of resins density after polymerization

	Polyurethane F19 resin	Epoxy resin	Polyester resin
Parts dimensions [cm]	L = 3.8360 l = 1.3840 H = 1.2550	L = 2.7980 l = 2.2400 H = 0.4850	L = 2.8200 l = 2.4500 H = 0.7500
The volume [cm^3]	6.6628	3.0397	5.1818
Weight rectangular pieces [g]	7.0995	3.5056	6.0512
Density [g/cm^3]	1.0655	1.1533	1.1678

Experimental determination of density resin after polymerization led to the determination of the weightings of the CAD model [17]. The resin parts dimensions, based on the relationship 3, are presented in table 2.

Table 2. Resin parts dimensions

Sample	D1 [mm]	D2 [mm]	D3 [mm]	L1 [mm]	L2 [mm]	L3 [mm]	H [mm]
CAD model	24.0000	8.4000	8.4000	60.0000	30.0000	30.0000	17.2500
SLS part	23.7158	8.1326	7.5519	59.6925	29.9099	29.7820	17.2502
P. 1.1	24.3669	8.5692	7.8162	60.3033	30.1146	30.1885	16.7955
P. 1.2	24.3929	8.5398	7.8669	60.6776	30.3894	30.2871	16.3860
P. 1.3	24.0076	7.7905	8.2621	59.7460	29.7431	30.0022	16.8426
P. 1.4	24.5381	7.9463	8.8660	60.7144	30.3630	30.3505	15.7217
P. 1.5	24.4680	8.5664	8.0395	59.9678	30.1239	29.8433	16.4893
P. 2.1	24.4064	8.5830	8.2510	59.7979	30.2808	29.5160	15.4736
P. 2.2	24.5332	8.1908	8.7364	60.1256	29.9437	30.1803	15.8147
P. 2.3	24.6897	8.2416	8.8475	60.2111	30.1658	30.0431	15.4242
P. 2.4	24.6918	8.2649	8.8297	60.4084	30.1153	30.2913	15.8715
P. 2.5	24.4099	8.0754	8.7258	59.9858	29.9291	30.0553	15.6499
P. 3.1	24.1477	7.8780	8.3704	59.8086	29.7456	30.0606	17.0035
P. 3.2	24.3205	8.4434	8.0568	60.2403	30.3325	29.9072	16.1595
P. 3.3	24.3405	8.5333	7.9884	60.1635	30.1717	29.9907	16.5231
P. 3.4	24.4162	8.7627	7.9184	60.2740	30.0003	30.2723	17.1941
P. 3.5	24.3462	8.0380	8.5589	60.0662	29.9231	30.1398	16.8124
P. 5.1	24.4812	8.0184	8.5206	60.6067	30.1122	30.4931	16.4912
P. 5.2	24.3312	7.8027	8.4163	60.4418	30.0365	30.4053	16.8814
P. 5.3	24.4570	8.4673	8.1602	60.4080	30.4476	29.9589	16.0380
P. 5.4	24.1264	7.9940	8.4313	59.7262	30.2254	29.5007	17.5102
P. 5.5	24.2779	7.9265	8.5231	60.1156	29.9969	30.1183	17.1020

$$M = \frac{1}{n} \cdot \sum_{i=1}^{n} x_i$$

(3)

where: n – the number of items summed; x_i – measured dimensions which will be summed;

In order to calculate the contraction, the relation 4 was applied.

$$C = \frac{d_{CAD} - d_{masurat}}{d_{CAD}} \cdot 100$$

(4)

where: d_{CAD} – projected dimensions [mm]; $d_{masurat}$ – measured dimensions [mm];

From Table 3 it is noted that the dimensional deviations relative to the CAD model for $\varnothing$24 mm rate does not exceed the value of 0.55 mm in absolute value (for polyester resin), which is the relative error of less than 2.27%.The Z axis is the biggest errors found in polyester resin which reached 9.29% relative error. On the Y axis we share dimensional deviations from 60 mm up to 0.28 mm for epoxy resin which means maximum relative errors of 0.46%. It was determined experimentally by mixing polyurethane resin viscosity 40 g component A and 60 g component B using rotational viscometer using a disc Rheotest S6 $\varnothing$18 mm diameter at a speed of 50 rev/min.

The initial temperature of the two components was increased to 22°C and 30°C temperature in just 45 seconds. Following research it was noted that the Z axis all types of vacuum casting resin used to have high levels of dimensional variation, to around 3 ÷ 9.3% with a maximum deviation of about 8% for the polyester resin. These high values and deviations occurred because of problems closing the moulds, because, if the both halves of the mould are not tightening, the risk that the mould is not filled with resin appears.

Table 3. The relative dimensional error of the resin parts compared to the CAD model

Dimensions	Value [mm]	Resin	Measured average dimensions [mm]	Error	
				[mm]	[%]
D1	24	Epoxy resin	24.3547	+0.3547	1.47
		Polyester resin	24.5462	+0.5462	2.27
		Polyurethane F19	24.3142	+0.3142	1.3
		Polyurethane SG95	24.3347	+0.3347	1.39
D2	8.4	Epoxy resin	8.2824	-0.1176	1.39
		Polyester resin	8.2711	-0.1289	1.53
		Polyurethane F19	8.3310	-0.0690	0.82
		Polyurethane SG95	8.0417	-0.3583	4.26
D3	8.4	Epoxy resin	8.1701	-0.2299	2.73
		Polyester resin	8.6780	+0.2780	3.31
		Polyurethane F19	8.1785	-0.2215	2.63
		Polyurethane SG95	8.4103	+0.0103	0.12
L1	60	Epoxy resin	60.2818	+0.2818	0.46
		Polyester resin	60.1057	+0.1057	0.17
		Polyurethane F19	60.1105	+0.1105	0.18
		Polyurethane SG95	60.2596	+0.2596	0.43
L2	30	Epoxy resin	30.1468	+0.1468	0.48
		Polyester resin	30.0869	+0.0869	0.28
		Polyurethane F19	30.0346	+0.0346	0.11
		Polyurethane SG95	30.1637	+0.1637	0.54
L3	30	Epoxy resin	30.1343	+0.1343	0.44
		Polyester resin	30.0172	+0.0172	0.05
		Polyurethane F19	30.0741	+0.0741	0.24
		Polyurethane SG95	30.0952	+0.0952	0.31
H	17.25	Epoxy resin	16.4470	-0.8030	4.65
		Polyester resin	15.6467	-1.6033	9.29
		Polyurethane F19	16.7385	-0.5115	2.96
		Polyurethane SG95	16.8045	-0.4455	2.58

To avoid this inconvenient it is recommended that future the CAD model to be compensated with some correction factors.

CONCLUSIONS

Thermosetting resins generally are practical in nature at temperatures between 40°C and 70°C responsive to 2 and 5 minutes.

Viscosity of polyurethane resin should be up to a maximum of 1400 cPs, after this value there is a risk that the rapid polymerization of the silicone rubber moulds not to be filled. The amount of 1400 cPs viscosity is reached by mixing the two components of the resin for up to 3 minutes, to a mould temperature of 40°C.

The resin parts are casted in vacuum moulding the silicone rubber on the Y axis deviation does not exceed 1%.

Vacuum castings polyester resin has high dimensional deviations on the 3 axis, Z axis is the most affected with the relative error of 9.29%.

X -axis scaling coefficient is 1, the scaling factor Y-axis has the value 0.99, while the Z-axis scaling coefficient has the value of 1.04 for the epoxy resin Larit L285, 1.1 to H68372 polyester resin, 1.03 for F19 polyurethane resin and polyurethane resin 1.02 for SG95.

EXPERIMENTAL SECTION

For experimental determination of the density, function of body weight, the piece it weighed in air and in a liquid. The relationship used for calculating the density of moulded parts [15], of the resin is:

$$\rho_p = \frac{m_{p\_air}}{m_{p\_air} - m_{p\_water}} \cdot \rho_{water} \tag{2}$$

where:

ρ_p – density of analysed part [g/cm^3]; m_{p_air} – piece mass, weighed in air [g]; m_{p_water} – piece mass, weighed in water [g]; ρ_{water} – water density [g/cm^3].

The viscosity of the used resins was determined using rotational viscometer Rheotest S6. The unit contains 19 sets of wheels and gears (from 0.3 - 100 rpm), thus allowing optimal choice of scales for measuring structural viscosity and it is used not only for determining the dynamic viscosity of Newtonian liquids but also to conduct thorough examinations on rheological non-Newtonian fluids.

The volumes of bubbles in casting in silicone rubber moulds were made using Shimadzu electronic balance, model AX 120.

Water density was measured using thermo-digital dens meter. The value of measured density is 0.9976 g/cm^3 at 22 °C.

The density of the water was measured using a thermo-digital dens meter, Anton Paar DMA 33N and the balance used to weighing the parts resin is VWR SE 1202 model.

In terms of measuring the vacuum castings a machine Zeiss Navigator Prismo was used.

ACKNOWLEDGMENTS

REFERENCES

1. M. Horacek, S. Lubos, *9th World Conference on Investment Casting*, San Francisco, pp.1-20, **1996**.
2. P. Bere, M.V. Dudescu, N. Balc, P. Bere, A.M. Iurian, O. Nemes, *Materiale Plastice*, **2014**, *51*, 2, 145-149.
3. A. Popescu, L. Hancu, P. Bere, *Applied Mechanics and Materials*, **2013**, *371*, 394-398.
4. H. Iancau, P. Bere, M. Borzan, L. Hancu, A. Crai, *Materiale Plastice*, **2008**, *45*, 3, 251-256.
5. P. Yarlagadda, T.S. Hock, *Journal of Materials Technology*, **2003**, *138*, 75-81.
6. I.P. Ilyas, C.M. Taylor and K.W. Dalgarno, *Proceedings of the 6th National Conference of Rapid Design, Prototyping and Manufacturing, High Wycombe*, June, 10, **2005**, 109-116.
7. Y. Yang, S.P. Hannula, *Materials Science and Engineering*, **2008**, *1-2* (*477*), 63-68.
8. R. Sever-Adrian "Cercetari teoretice si experimentale privind turnarea sub vid a pieselor complexe nemetalice" – teza de doctorat, Cluj-Napoca, **2011**.
9. B. O'Donnchadha, A. Tansey, *Journal of Materials Processing Technology*, **2004**, *1* (*153-154*), 28-34.
10. S.A. Radu, D. Fratila, *Proceedings of the Romanian Academy – series A*, ISSN 1454-9069, **2012**, *4*(*13*), 343-350.
11. I. Gibson, L.K. Cheung, S.P. Chow, W. L. Sheung, S.L. Beh, W. Savalani, S.H. Lee, *Rapid Prototyping Journal*, **2006**, *1*(*12*), 53-58.
12. I.P. Ilyas, C.M. Taylor and K.W. Dalgarno, *Proceedings of the 6th National Conference of Rapid Design, Prototyping and Manufacturing, High Wycombe*, June, 10, **2005**, 109-116.
13. J.E. Folkestad, R.L. Johnston, *Journal of Industrial Technology*, **2001**, *4*(*17*), 1-7.

14. D.R. Bareta, A.S. Pouzada, C.A. Costa, *PMI International Conference on Polymer and Moulds Innovations*, Gent/Belgium, **2007**.
15. Shimadzu Corporation Kyoto, *Instruction Manual for Simple Specific Gravity Measurement* Kit AW/AX/AY Series, Japan, **2010**.
16. R. Sever-Adrian "Cercetari teoretice si experimentale privind turnarea sub vid a pieselor complexe nemetalice" – teza de doctorat, Cluj-Napoca, **2011**.
17. P. Berce, N. Bâlc, N. Caizar, R. Pacurar, S.A. Bratian, I. Fodorean, *Tehnologii de fabricație prin adăugare de material și aplicațiile lor*, ISBN 978-973-27-2396-8, Editura Academiei Romane, Bucuresti, **2014**.

COMPUTING THE ANTI-KEKULÉ NUMBER OF CERTAIN NANOTUBES AND NANOCONES

MEHAR ALI MALIK[a,*], MUHAMMAD IMRAN[a]

ABSTRACT. Let $G(V,E)$ be a connected graph. A set M subset of E is called a *matching* if no two edges in M have a common end-vertex. A matching M in G is *perfect* if every vertex of G is incident with an edge in M. The perfect matchings correspond to Kekulé structures which play an important role in the analysis of resonance energy and stability of hydrocarbons. The anti-Kekulé number of a graph G, denoted as $ak(G)$, is the smallest number of edges which must be removed from a connected graph G with a perfect matching, such that the remaining graph stay connected and contains no perfect matching.

In this paper, we calculate the anti-Kekulé number of $TUC_4C_8(S)[p,q]$ nanotube, $TUC_4C_8(S)[p,q]$ nanotori for all positive integers p, q and $CNC_{2k-1}[n]$ nanocones for all positive integers k and n.

Keywords: Perfect matching, Anti-Kekulé number, Nanotubes, Nanocones

INTRODUCTION

Mathematical chemistry is a branch of theoretical chemistry in which we discuss and predict the chemical structure by using mathematical tools and does not necessarily refer to the quantum mechanics. *Chemical graph theory* is a branch of mathematical chemistry in which we apply tools of graph theory to model the chemical phenomenon mathematically. This theory plays a prominent role in the fields of chemical sciences. A *moleculer / chemical graph* is a simple finite graph in which vertices denote the atoms and edges denote the chemical bonds between these atoms in the underlying chemical structure. It is important to mention that the hydrogen atoms are often omitted in a molecular graph.

A *nanostructure* is an object of intermediate size between microscopic and molecular structures. It is a product derived through engineering at molecular scale. This is something that has a physical dimension smaller than 100 nanometers, ranging from clusters of atoms to dimensional layers. *Carbon nanotubes* (CNTs)

---

[a] *Department of Mathematics, School of Natural Sciences, National University of Sciences and Technology, Sector H-12, Islamabad, Pakistan*
* *Corresponding author: alies.camp@gmail.com*

are types of nanostructure which are allotropes of carbon and have a cylindrical shape. Carbon nanotubes, a type of fullerene, have potential in fields such as nanotechnology, electronics, optics, materials science, and architecture. Carbon nanotubes provide a certain potential for metal-free catalysis of inorganic and organic reactions. Nanotube-based field emitters have applications as nanoprobes in metrology and biological and chemical investigations and as templates for the creation of other nanostructures. *Carbon nanocones* are conical structures which are allotropes of carbon having at least one dimension of the order one micrometer or smaller.

An edge set M of a graph G is called a matching if no two edges in M have a common end vertex. A matching M of G is perfect if every vertex of G is incident with an edge in M. In organic moleculer graphs, perfect matchings correspond to Kekulé structures, playing an important role in analysis of the resonance energy and stability of hydrocarbon compounds [1]. For example, it is well known that carbon compounds without Kekule structures are unstable. The study of Kekule structures of chemical compounds is very important, because they have many "hidden treasures" that may explain their physical and chemical properties [2]. The notations used in this paper are mostly taken from [3].

The *anti-Kekulé number* of a connected graph G is the smallest number of edges that must be removed from the graph G such that the remaining graph is still connected but has no Kekulé structures. For benzenoids, Vukičević and Trinajstić proved in [4] that the anti-Kekulé number of parallelograms with at least three rows and at least three columns is equal to 2, they also showed in [5] that cata-condensed benzenoids have anti-Kekulé number either 2 or 3 and both classes are characterized. Later on, Veljan and Vukičević showed that the anti-Kekulé numbers of the infinite triangular, rectangular and hexagonal grids are 9, 6 and 4, respectively [6]. For fullerene graphs, Vukičević showed that the anti-Kekulé number of the icosahedron C_{60} (buckminister fullerene) is 4. In general, Kutnar et al. proved in [7] that the anti-Kekulé number of all leapfrog fullerene graphs is either 3 or 4 and afterwards Yang et al proved that the anti-Kekulé number of all fullerene graphs is 4 [8]. For further study on anti-Kekulé number of different graphs please consult [9, 10, 11].

Let $G(V, E)$ be a connected graph with vertex set V and edge set E and let G has at least one perfect matching (i.e., Kekulé structure). For $S \subseteq E(G)$, let $G - S$ denote the graph obtained from G by deleting all the edges in S. We call S an anti-Kekulé set if $G - S$ is connected but has no perfect matching. The anti-Kekulé set of minimum cardinality in G is called the anti-Kekulé number, and denoted by $ak(G)$.

MAIN RESULTS

In this paper, we calculate the anti-Kekulé number of $TUC_4C_8(S)[p,q]$ nanotube and $TUC_4C_8(S)[p,q]$ nanotori. The anti-Kekulé number of $CNC_{2k}[n]$ nanocones $\forall\, k \in \mathbb{N}$, was discussed by the present authors in [12]. Now we discuss the anti-Kekulé number of $CNC_{2k-1}[n]$ nanocones $\forall\, k \in \mathbb{N}$.

RESULTS FOR NANOTUBES

In this section, we compute the anti-Kekulé number for $TUC_4C_8(S)[p,q]$ nanotube. This nanotube is a net of C_4 and C_8, and it can be constructed by alternating C_4 and C_8 following a trivalent decoration as shown in Fig. 2. This type of tiling can cover a cylinder and a torus nanotube. In a 2-dimensional lattice of the $TUC_4C_8(S)[p,q]$ nanotube, p is the number of octagons in one row and q is the number of periods in the whole lattice. A period consist of two rows of edges as shown in Fig. 1. Further detail on the construction of $TUC_4C_8(S)[p,q]$ nanotubes can be found in [13].

Carbon nanotubes are molecular-scale tubes of graphitic carbon with outstanding properties. They are among the stiffest and strongest fibres known, and have remarkable electronic properties and many other unique characteristics. For these reasons they have attracted huge academic and industrial interest, with thousands of papers on nanotubes being published every year. Commercial applications have been rather slow to develop, however, primarily because of the high production costs of the best quality nanotubes.

For our purpose, we call the vertices of degree 2 as the *boundary* vertices of a nanotube. One can observe that the boundary vertices lie on the first and the last layer of the nanotube.

Theorem 2.1 *Let* $G = TUC_4C_8(S)[p,q]$ *nanotube, then* $ak(G) = 3$.

Proof. Consider the set $S = \{e_1, e_2, e_3\} \subseteq E(G)$, then the graph $G - S$ contains a vertex v such that v is adjacent to two vertices of degree 1, say u and w (see Fig. 1). Since the vertices u and w cannot be matched simultaneously, the graph $G - S$ is connected but contains no perfect matching. This implies that $ak(G) \leq 3$.

Conversely, let $U = \{e, e'\} \subseteq E(G)$. We will show that the graph $G - U$ is connected and it contains a perfect matching. Clearly, the graph $G - U$ will be connected if and only if e and e' are not adjacent to the same boundary vertex.
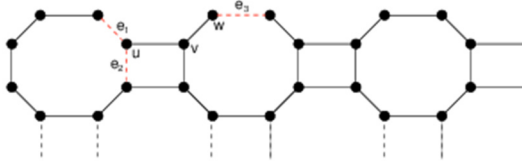
Figure 1. One period of the graph of $TUC_4C_8(S)[p,q]$ with Anti-Kekulé set $S = \{e_1, e_2, e_3\}$ shown by the red edges.

The graph G is tiled with the cycles of lengths 4 and 8, such that each period contain p octagons and there are q such periods. Then the order of G is $|V(G)| = 8pq$ and the number of cycles of length 4 (and length 8 as well) in G is $p(2q - 1)$. Let us label all the cycles of length 4 and 8 in G by $C_{k,l}^4$ and $C_{k,l}^8$ (respectively), where $1 \le k \le q$ and $1 \le l \le p$ (see Fig. 2). Let $E(C_{k,l}^4)$ (and $E(C_{k,l}^8)$) denote the edge set of the cycle $C_{k,l}^4$ (resp. $C_{k,l}^8$) and let $E(C_{k,l}^4) = E^1(C_{k,l}^4) \cup E^2(C_{k,l}^4)$, where $E^1(C_{k,l}^4)$ and $E^2(C_{k,l}^4)$ be the sets containing alternatively the edges of the cycle $C_{k,l}^4$, for each k and l.
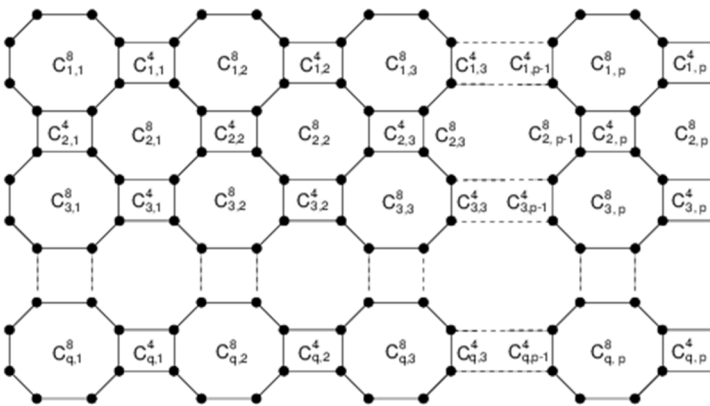
Figure 2. The cycles of length 4 and 8 in $TUC_4C_8(S)[p, \dfrac{q+1}{2}]$ nanotube

Similarly, let $E(C_{k,l}^8) = E^1(C_{k,l}^8) \cup E^2(C_{k,l}^8)$, where $E^1(C_{k,l}^8)$ and $E^2(C_{k,l}^8)$ be the sets containing alternatively the edges of the cycle $C_{k,l}^8$, for each k and l.

It can be observed that $|E^1(C_{k,l}^4)| = |E^2(C_{k,l}^4)| = 2$. Clearly, either $E^1(C_{k,l}^8)$ or $E^2(C_{k,l}^8)$ contains some edges of the cycles of length 4. Without loss of generality, we assume that

$$\begin{cases} E^2(C_{k,l}^8) \cap \{E(C_{k+i,l}^4) \cup E(C_{k,l-j}^4)\} = \varnothing, & for \quad k = odd; \\ E^2(C_{k,l}^8) \cap \{E(C_{k+i,l}^4) \cup E(C_{k,l+j}^4)\} = \varnothing, & for \quad k = even, \end{cases} \tag{1}$$

where $i \in \{-1,1\}, j \in \{0,1\}$. We can define two disjoint perfect matchings in G as follows.

$$M_1 = \bigcup_{k,l} E^1(C_{k,l}^8) \quad and \quad M_2 = \bigcup_{k,l} E^2(C_{k,l}^8). \tag{2}$$

Clearly, $M_1 = \bigcup_{k,l} E(C_{k,l}^4)$ and $M_2 = E(G) - M_1$. We consider the following three cases.

Case 1. Let e and e' do not lie on a cycle of length 8. Then we have a perfect matching M_1 (or M_2) in the connected graph $G - U$.

Case 2. Let one of e and e' lie on a cycle of length 8. Suppose on contrary that e lies on $C_{k,l}^8$, then without loss of generality we can assume that $e \in E^1(C_{k,l}^8)$. Then we have a perfect matching M_2 in the connected graph $G - U$.

Case 3. Suppose that both e and e' lie on the cycles $C_{k,l}^8$ and $C_{s,t}^8$ (respectively), for $1 \le k, s \le q$ and $1 \le l, t \le p$.

When $(k,l) \ne (s,t)$ then if $e \in E^1(C_{k,l}^8)$ and $e' \in E^1(C_{s,t}^8)$, then M_2 is a perfect matching in the connected graph $G - U$. Similarly, when $e \in E^1(C_{k,l}^8)$ and $e' \in E^2(C_{s,t}^8)$, then $M' = M_1 - E^1(C_{k,l}^8) + E^2(C_{k,l}^8)$ is the required perfect matching in the connected graph $G - U$.

When $(k,l) = (s,t)$, both edges e and e' lie on the same cycle of length 8, say $C_{k,l}^8$. Then we have the following two subcases.

(1) Let e and e' lie in the same class, say $E^1(C_{k,l}^8)$. Then M_2 will be a perfect matching in the connected graph $G - U$.

(2) Let e and e' lie in different classes, say $e \in E^1(C_{k,l}^8)$ and $e' \in E^2(C_{k,l}^8)$. When e and e' are adjacent, it is clear that the edges e and e' cannot be adjacent to the same boundary vertex, as the graph will be disconnected. Then consider a matching N' in $G - U$ defined in four cases corresponding to the possibilities of the edges e and e', as follows.

$$N' = M_1 - \bigcup_{i,j} E^1(C_{k+i,l+j}^8) \cap \{e\}, \ where \ (i,j) = \begin{cases} (0,0) \ and \ (0,1); \\ (0,0) \ and \ (2,0); \\ (0,0) \ and \ (0,-1); \\ (0,0) \ and \ (-2,0). \end{cases} \quad (3)$$

It can be seen that each pair of octagons in the matching defined in Equ. 3 are joined by the cycle $C_{k+i,l+j}^4$, where

$$(i,j) = \begin{cases} (0,0) \ for \ k = odd \ and \ (0,1) \ for \ k = even; \\ (1,0); \\ (0,-1) \ for \ k = odd \ and \ (0,0) \ for \ k = even; \\ (-1,0). \end{cases} \quad (4)$$

Since $e \in E^1(C_{k,l}^8)$ therefore $e \in M_1$ and thus lies on a cycle of length 4, whereas e' does not. Let $E(C_{k+i,l+j}^4) = \{c_1, c_2, c_3, c_4\}$, for (i,j) as mentioned in Equ. 4. Clearly, $e \in \{c_1, c_2, c_3, c_4\}$. Then label these edges with $e = c_1$ in the clockwise direction starting from e.

Now, using the matching defined in Equ. 3, we can construct a matching N in the graph $G - U$ as follows.

$$N = N' - \{c_3\} + \{c_2, c_4\}. \quad (5)$$

Then N is a perfect matching in the connected graph $G - U$, which implies that $ak(G) \geq 3$, and completes the proof.
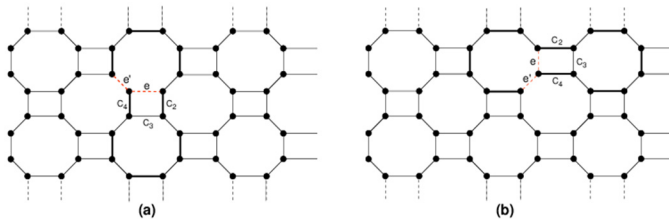
Figure 3. The matching for the pair of octagons corresponding to the first two cases in Equ. (3). The rest of the periods are matched by the matching M_1.

RESULTS FOR $TUC_4C_8(S)[p,q]$ NANOTORI

The $TUC_4C_8(S)[p,q]$ nanotorus (or nanotori) is obtained from the $TUC_4C_8(S)[p,q]$ nanotube by joining the ends of the tube, so giving it the shape of a torus. The spoke type edges in the last layer will be joined to the corresponding vertices in the first layer (see Fig. 4).
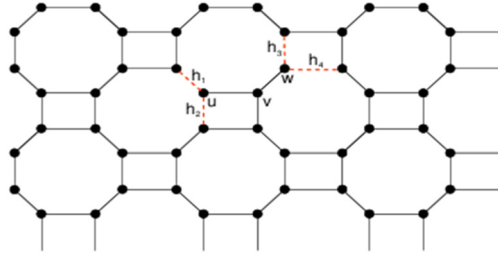
Figure 4. The embedded graph of the $TUC_4C_8(S)[3,2]$ nanotori

Theorem 2.2 Let $G = TUC_4C_8(S)[p,q]$ nanotori, then $ak(G) = 4$.

Proof. Consider a period of the 3-regular graph of $TUC_4C_8(S)[p,q]$ nanotori, as shown in Fig. 5. Let E_1, E_2 and E_3 be the edge partitions of $E(G)$ containing all the edges labelled e_1, e_2 and e_3, respectively. It is easy to see that E_1, E_2 and E_3 form three (disjoint) perfect matchings in G.

Let $S = \{h_1, h_2, h_3, h_4\} \subseteq E(G)$, as shown in Fig. 4. Then the graph $G - S$ contains a vertex v such that v has two pendent vertices adjacent to it, which cannot be matched simultaneously. Since no more than two vertices from S are adjacent to a single vertex, the graph G remains connected. Thus, $ak(G) \leq 4$.

Conversely, let $U = \{b_1, b_2, b_3\} \subseteq E(G)$, where all edges of U are not adjacent to a single vertex in G. We have the following three cases to be discussed.

Case 1. When all elements of U belong to same edge class, say E_1. Then we have M_2 (or M_3) as a perfect matching in the graph $G - U$.

Case 2. When two elements of U belong to the same edge class, say E_1. Then the third element of U can be in one of the remaining two edge classes, say E_2. Thus E_3 will be a perfect matching in the connected graph $G - U$.
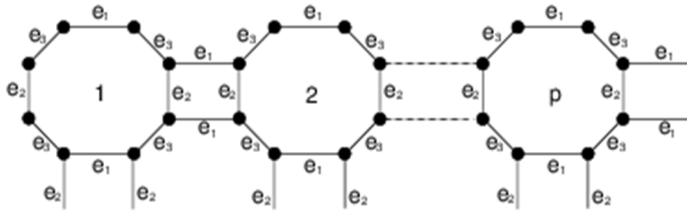
Figure 5. A period of $TUC_4C_8(S)[p,q]$ nanotori

Case 3. When all elements of U belong to different edge classes, say $b_1 \in E_1$, $b_2 \in E_2$ and $b_3 \in E_3$. Consider the labeling of all the cycles of length 4 and 8 in G, as done in Theorem 2.1, respectively by $C_{k,l}^4$ and $C_{k,l}^8$. With one extra row of edges joining the vertices in the last row to corresponding vertices in the first row, and thus $1 \le k \le q+1$ and $1 \le l \le p$. Since $b_1 \in E_1$, which is the class of all horizontal edges, we can assume that $b_1 \in E(C_{k,l}^4)$, for some k and l. Label the edges of $C_{k,l}^4$ with $\{c_1, c_2, c_3, c_4\}$ and let $b_1 = c_1$. Consider a matching M in $G - U$ defined as follows.

$$M = E_1 - \{c_1, c_3\} + \{c_2, c_4\}. \tag{6}$$

Clearly, M is a perfect matching in the connected graph $G - U$. Thus $ak(G) \ge 4$, which completes the proof.

RESULTS FOR $CNC_k[n]$ NANOCONES

Now we determine the anti-Kekulé number of $CNC_k[n]$ nanocones, where $k = 2q - 1, q \ge 2, n \ge 1$. This family of nanocones is parameterized in such a manner that k denotes the length of the cycle placed at the core of the nanocone and n is the number of hexagonal layers placed at the conical surface of the nanocone. Now we calculate the anti-Kekulé number of this class of nanocones.

Theorem 2.3 *Let G be the graph of $CNC_k[n]$ nanocone, where $k = 2q - 1, q \ge 2, n \ge 1$, then $ak(G) = 2$.*

Proof. First we show that $ak(G) \le 2$. For this purpose, consider a set $S = \{s_1, s_2\} \subseteq E(G)$ and a $\{uvw\}$ – path in G as shown in Fig. 6. Then,
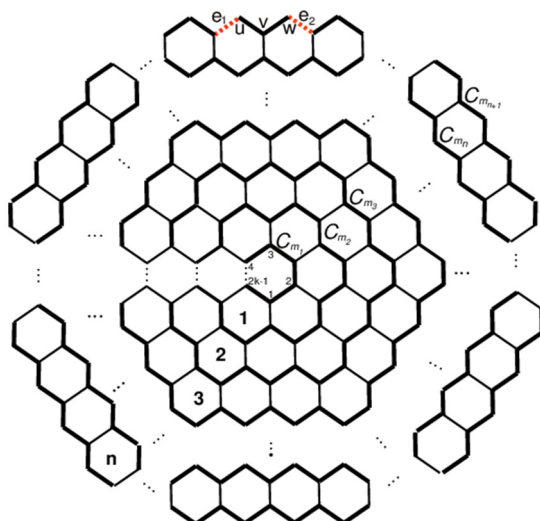
Figure 6. A representation of $CNC_k[n]$ nanocone, with k being an odd integer, with C_{n+1} cycles and a $uvw - $ path.

there does not exist any perfect matching in the graph $G - S$. Thus $ak(G) \le 2$.
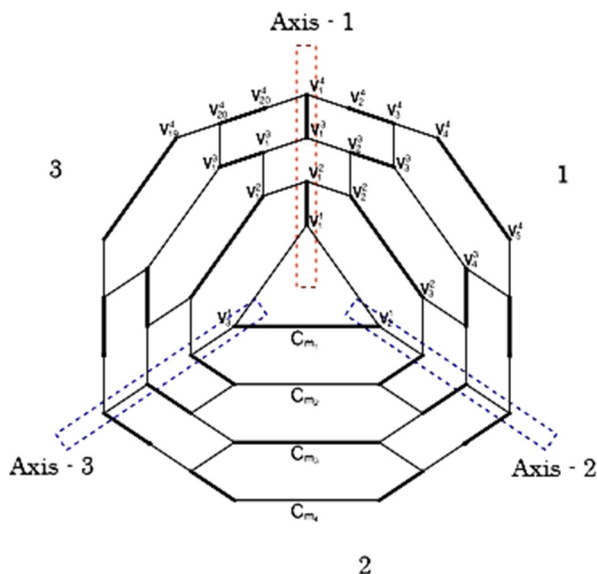
Figure 7. The perfect matching M_1 in $CNC_3[3]$ nanocone obtained by matching the edges on Axis-1. M_2 and M_3 can be obtained by matching other Axis.

Conversely, let $C_{m_i} = \{v_1^i, v_2^i, \ldots, v_{m_i}^i\}$, for $1 \le i \le n+1$, be the cycles as shown in Fig. 7. Then the length of the cycle C_{m_i} is $m_i = k(2i-1)$. Clearly, m_i (for $1 \le i \le n+1$) is always odd.

There are k different perfect matchings of the graph G (as constructed in Fig. 7, for $k = 3$), which can be obtained by relabeling the vertices of the graph or just by rotating the graph G. Let $M_1, M_2, \ldots, M_k$ be the perfect matchings in the graph G obtained by selecting the edges of the graph G lying on different axis. The k axis of the $CNC_k[n]$ nanocone (k odd) are shown in Fig. 8.
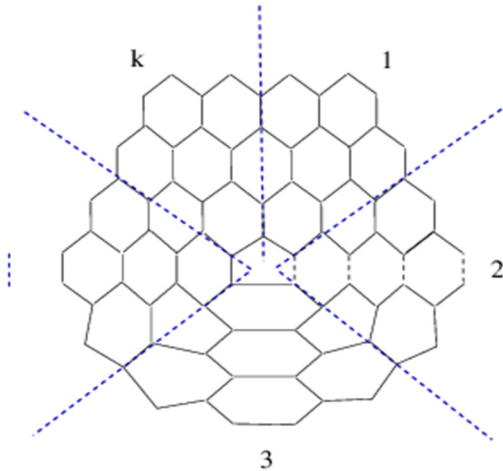
Figure 8. The k axis for the $CNC_k[n]$ nanocone for odd k

The k perfect matchings M_l, for $1 \le l \le k$, are defined as follows.

$$M_l = \{v_{l+2(l-1)(i-1)}^i v_{l+2(l-1)i}^{i+1}, \ v_{l+2(l-1)(i-1)+s}^i v_{l+2(l-1)(i-1)+s+1}^i, \ v_{l+2(l-1)i+s}^{i+1} v_{l+2(l-1)i+s+1}^{i+1} \mid$$

$$1 \le i \le n+1, \quad s+z \equiv z \pmod{m_i}, \quad where\ i, s\ are\ odd\}.$$

It can be seen that the (l)−phase of the matchings M_l and M_{l+1}, for $1 \le l \le k-1$, are same (see Fig. 7, for instance), and the rest of the phases are all different. The edges lying on the axis lines are not included in any phase.

Let $e \in E(G)$, then we have the following two cases.

Case 1. When e lies on an axis line. Since each matching M_l, $1 \leq l \leq k$, contains a single axis line. There will be $k-1$ perfect matchings in the graph $G - \{e\}$.

Case 2. When e does not lie on an axis line. Then e lies in one of the k phases of the nanocone, say phase $-(l)$. Then if e belongs to the edges of the graph G matched under M_l then we have $k-2$ perfect matchings M_t, $1 \leq t \leq k$ where $t \neq l$ and $t \neq l+1$, in the connected graph $G - \{e\}$. Thus $ak(G) \geq 2$, which completes the proof.

CONCLUDING REMARKS

The perfect matchings in a graph correspond to Kekulé structures which play an important role in the analysis of resonance energy and stability of hydrocarbons. Nanotubes and nanocones are allotropes of carbon having enormous applications in the field of nanotechnology, electronics, optics, materials science, and architecture. In this study, we proved that the anti-Kekulé number of the finite families of $TUC_4C_8(S)[p,q]$ nanotubes, $TUC_4C_8(S)[p,q]$ nanotubes $\forall p,q \in \mathbb{N}$ and for $CNC_{2k}[n]$ nanocones $\forall k,n \in \mathbb{N}$, is respectively 3, 4 and 2. Calculations showed that the anti-Kekulé number of almost all nanotubes is 2 or 3 in finite case and 4 or 5 if we consider their infinite 2 D lattices. Furthermore, our result of the anti-Kekulé number of a nanotorus agree with the anti-Kekulé number of fulerenes [8].

REFERENCES

1. I. Gutman, O. Polansky, Mathematical Concepts in Organic Chemistry, *Springer-Verlag, Berlin*, **1986**.
2. M. Randic, *Chem. Rev*, **2003**, *103*, 34.
3. N. Trinajstic, Chemical Graph Theory, CRC Press, Boca Raton, FL, **1992**.
4. D. Vukičević, N. Trinajstić, *J. Math. Chem.*, **2007**, *42*, 575.
5. D. Vukičević, N. Trinajstić, *J. Math. Chem.*, **2008**, *43*, 719.
6. D. Veljan, D. Vukičević, *J. Math. Chem.*, **2008**, *43*, 243.
7. K. Kutnar, J. Sedlar, D. Vukičević, *J. Math. Chem.*, **2009**, *45*, 431.
8. Q. Yang, D. Ye, H. Zhang, *MATCH Commun. Math. Comput. Chem.*, **2012**, *67*, 281.
9. S. Tang, H. Deng, *Dig. J. Nanomater. Bios.,* **2011**, *6*, 439.
10. A. Xavier, A. S. Shanthi, M. J. Raja, *Intel. J. Pure App. Math.*, **2013**, *86*, 1019.
11. D. Ye, *Discr. Appl. Math.*, **2013**, *161*, 2196.
12. M.A. Malik, S. Hayat, M. Imran, *J. Comput. Theor. Nanos.*, accepted, in press.
13. M. Stefu, M. V. Diudea, *MATCH Commun. Math. Comput. Chem.*, **2004**, *50*, 133.

ON SOME TOPOLOGICAL INDICES OF THE GENERALIZED HIERARCHICAL PRODUCT OF GRAPHS

FREYDOON RAHBARNIA[a,*], MOSTAFA TAVAKOLI[a]
ALI REZA ASHRAFI[b]

ABSTRACT. The generalized hierarchical product of graphs was introduced very recently by L. Barriére et al. In this paper, revised Szeged and new version of Zagreb indices of generalized hierarchical product of two connected graphs are obtained. Using the results obtained here, some known results are deduced as corollaries. Finally, we obtain the Sz^*, M^*_1 and M^*_2 indices of the zig-zag polyhex nanotube $TUHC_6[2n, 2]$, linear phenylene F_n, hexagonal chain L_n and truncated cube as a consequence of our results.

Keywords: Generalized hierarchical product, Cartesian product, Revised Szeged index, Zagreb indices.

INTRODUCTION

Throughout this paper all graphs considered are finite, simple and connected. The **distance** $d(u,v)$ between the vertices u and v of a graph G is equal to the length of a shortest path that connects u and v. Suppose G is a graph with vertex and edge sets $V = V(G)$ and $E = E(G)$, respectively. Suppose $e = uv \in E(G)$. The set of vertices of G whose distance to the vertex u is smaller than the distance to the vertex v is denoted by $N_u^G(e)$. In addition, let $N_0^G(e)$ denote the set of vertices with equal distances to u and v. The **Szeged** and **revised Szeged indices** of the graph G are defined as:

$$Sz(G) = \sum_{e=uv \in E(G)} |N_u^G(e)||N_v^G(e)| \text{ [1, 2, 3]},$$

$$Sz^*(G) = \sum_{e=uv \in E(G)} \left(|N_u^G(e)| + \frac{|N_0^G(e)|}{2} \right)\left(|N_v^G(e)| + \frac{|N_0^G(e)|}{2} \right) \text{ [4, 5, 6]}.$$

[a] *Department of Mathematics, Ferdowsi University of Mashhad, P. O. Box 1159, Mashhad 91775, Iran.*
[b] *Department of Pure Mathematics, Faculty of Mathematical Sciences, University of Kashan, Kashan 87317-51167, I.R. Iran.*
* *Corresponding author: Rahbarnia@ferdowsi.um.ac.ir*

F. RAHBARNIA, M. TAVAKOLI, A. R. ASHRAFI

The **Zagreb indices** have been introduced by Gutman and Trinajstic as $M_1(G) = \sum_{u \in V(G)} (deg_G(u))^2$ and $M_2(G) = \sum_{uv \in E(G)} deg_G(u)deg_G(v)$, where $deg_G(u)$ denotes the degree of vertex u [7, 8]. In [9], a new version of Zagreb indices were defined as $M_1^*(G) = \sum_{uv \in E(G)} [\varepsilon_G(u) + \varepsilon_G(v)]$, $M_1^{**}(G) = \sum_{u \in V(G)} (\varepsilon_G(u))^2$ and $M_2^*(G) = \sum_{uv \in E(G)} \varepsilon_G(u)\varepsilon_G(v)$, where $\varepsilon_G(u)$ is the largest distance between u and any other vertex v of G. The total connectivity index $\zeta(G)$ of a graph G is defined as $\zeta(G) = \sum_{u \in V(G)} \varepsilon_G(u)$, see [10].

A graph G with a specified vertex subset $U \subseteq V(G)$ is denoted by $G(U)$. Suppose G and H are graphs and $U \subseteq V(G)$. The **generalized hierarchical product**, denoted by $G(U) \Pi H$, is the graph with vertex set $V(G) \times V(H)$ and two vertices (g, h) and (g', h') are adjacent if and only if $g = g' \in U$ and $hh' \in E(H)$ or, $gg' \in E(G)$ and $h = h'$, see Figure 1. This graph operation introduced recently by Barriere et al. [11, 12] and found some applications in computer science. The **Cartesian product**, $G \times H$, of graphs G and H has the vertex set $V(G \times H) = V(G) \times V(H)$ and $(u, x)(v, y)$ is an edge of $G \times H$ if $u = v$ and $xy \in E(H)$ or, $uv \in E(G)$ and $x = y$ [13, 14].

We denote by P_n and C_n the path and cycle with n vertices, respectively. A bipartite graph is a graph whose vertices can be partitioned into two disjoint subsets U_1 and U_2 such that every edge connects a vertex in U_1 to one in U_2; that is, U_1 and U_2 are independent sets. Our other notations are standard and taken mainly from the standard books of graph theory.

RESULTS AND DISCUSSION

We first introduce some notations. Let $G = (V, E)$ be a graph and $U \subseteq V$. In $G(U)$, an u–v path through U is an u–v path in G containing some vertex $w \in U$ (vertex w could be the vertex u or v). Let $d_{G(U)}(u,v)$ denote the length of a shortest u–v path through U in G. Notice that, if one of the vertices u and v belong to U, then $d_{G(U)}(u,v) = d_G(u,v)$. Furthermore, let $\varepsilon_{G(U)}(u) = max\{ d_{G(U)}(v, u) \mid v \in V(G(U))\}$, then $\zeta(G(U))$, $M_1^*(G(U))$, $M_2^*(G(U))$ and $M_1^{**}(G(U))$ can be defined as follows:

$$\zeta(G(U)) = \sum_{u \in V(G(U))} \varepsilon_{G(U)}(u), \quad M_1^*(G(U)) = \sum_{uv \in E(G(U))} [\varepsilon_{G(U)}(u) + \varepsilon_{G(U)}(v)],$$

$$M_1^{**}(G(U)) = \sum_{u \in V(G(U))} (\varepsilon_{G(U)}(u))^2 \text{ and}$$

$$M_2^*(G(U)) = \sum_{uv \in E(G(U))} \varepsilon_{G(U)}(u)\varepsilon_{G(U)}(v).$$

For an edge $e = ab$ of $G(U)$, $N_a^{G\ (U)}(e)$ denotes the set of vertices closer to a than b through U in G and $N_0^{G\ (U)}(e)$ denotes the set of equidistant vertices of e through U in $G(U)$, i.e.

$$N_a^{G(U)}(e) = \{u \in V(G(U)) \mid d_{G(U)}(u,a) < d_{G(U)}(u,b)\},$$
$$N_0^{G(U)}(e) = \{u \in V(G(U)) \mid d_{G(U)}(u,a) = d_{G(U)}(u,b)\}.$$

Then $Sz^*(G(U))$, $Sz^{**}(G(U))$ and $Sz^{***}(G(U))$ can be defined as follows:

$$Sz^*(G(U)) = \sum_{e=uv \in E\ (G)} (|N_u^{G\ (U)}(e)| + \frac{|N_0^{G\ (U)}(e)|}{2})\ (|N_v^{G\ (U)}(e)| + \frac{|N_0^{G\ (U)}(e)|}{2}),$$

$$Sz^{**}(G(U)) = \frac{1}{2} \sum_{e=uv \in E\ (G\ (U)\ )} (|N_u^{G\ (U)}(e)|\,|N_v^{G}(e)| + |N_v^{G\ (U)}(e)|\,|N_u^{G}(e)|),$$

$$Sz^{**}(G(U)) = \frac{1}{2} \sum_{e=uv \in E\ (G\ (U)\ )} (|N_u^{G\ (U)}(e)|\,|N_u^{G}(e)| + |N_v^{G\ (U)}(e)|\,|N_v^{G}(e)|).$$

Therefore, it is clear that if $U = V(G)$, then $Sz^{**}(G) = Sz(G)$.
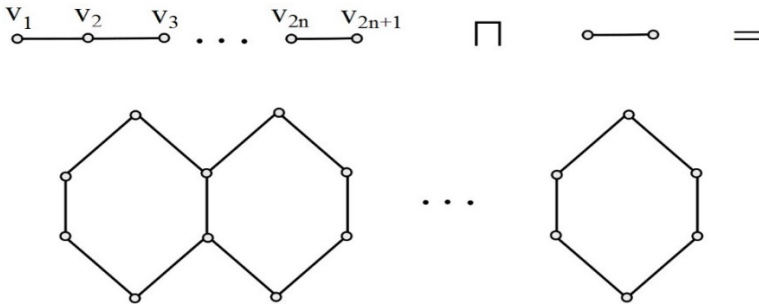
Figure 1. Hexagonal chain $L_n = P_{2n+1}(U)\ \Pi P_2$, where $U = \{v_1, v_3, v_5, \ldots, v_{2n+1}\}$.

Lemma 1. (See [12]). Let G and H be graphs with $U \subseteq V(G)$. Then we have

(a) If $U = V(G)$, then the generalized hierarchical product $G(U)\ \Pi H$ is the Cartesian product of G and H,

(b) $|V(G(U)\ \Pi H)| = |V(G)||V(H)|$, $|E(G(U)\ \Pi H)| = |E(G)||V(H)| + |E(H)||U|$,

(c) $G(U)\ \Pi H$ is connected if and only if G and H are connected,

(d) $\quad d_{G\ (U)\Pi H}\ ((g,h),\ (g',h'\ )) = \begin{cases} d_{G(U)}(g,g')+d_H(h,h') & \text{if } h \neq h', \\ d_G(g,g') & \text{if } h = h'. \end{cases}$

Theorem 2. Let G and H be two connected graphs and let U be a nonempty subset of $V(G)$. Then

$$Sz^*(G(U)\Pi H) = |V(H)|(|V(H)|-1)^2 Sz^*(G(U)) + |V(H)|Sz^*(G)$$
$$+ |V(H)|(|V(H)|-1)\big(Sz^{**}(G(U)) - Sz^{***}(G(U))\big)$$
$$+\frac{1}{2}|E(G)||V(G)|^2|V(H)|(|V(H)|-1) + |U||V(G)|^2\,Sz^*(H).$$

Proof. Let G and H be two connected graphs and let U be a nonempty subset of $V(G)$. For our convenience, we partition the edge set of $G(U)\ \Pi H$ into two sets,

$$E_1 = \{(g,h)(g',h') \mid gg' \in E(G) \text{ and } h = h' \in V(H)\},$$
$$E_2 = \{(g,h)(g',h') \mid hh' \in E(H) \text{ and } g = g' \in U\}.$$

Let $e = (g,h)(g',h) \in E_1$. Suppose $(x,y) \in V(G(U)\Pi H)$, thus by Lemma 1, $(x,y) \in N_{(g,h)}^{G\ (U)\Pi H}(e)$, if $y = h$ and $x \in N_g^G(gg')$ or, $y \neq h$ and $x \in N_g^{G(U)}(gg')$. Therefore, we have

$$|N_{(g,h)}^{G\ (U)\Pi H}(e)| = (|V(H)|-1)\,|N_g^{G\ (U)}(gg')| + |N_g^G(gg')|\,,$$
$$|N_{(g',h)}^{G\ (U)\Pi H}(e)| = (|V(H)|-1)\,|N_{g'}^{G\ (U)}(gg')| + |N_{g'}^G(gg')|\,,$$
$$|N_0^{G\ (U)\Pi H}(e)| = (|V(H)|-1)\,|N_0^{G\ (U)}(gg')| + |N_0^G(gg')|\,.$$

Thus, the summation of $[|N_{(g,h)}^{G\ (U)\Pi H}(e)| + \frac{1}{2}|N_0^{G(U)\Pi H}(e)|] \times [|N_{(g',h)}^{G(U)\Pi H}(e)| + \frac{1}{2}|N_0^{G(U)\Pi H}(e)|]$ over all edges of E_1, is equal to:

$$Sz_1 = |V(H)|(|V(H)|-1)^2 Sz^*(G(U)) + |V(H)|Sz^*(G)$$
$$+|V(H)|(|V(H)|-1)\big(Sz^{**}(G(U)) - Sz^{***}(G(U))\big)$$
$$+\frac{1}{2}|E(G)||V(G)|^2|V(H)|(|V(H)|-1).$$

On the other hand, assume that $e = (g,h)(g,h') \in E_2$ and let $(x,y) \in V(G(U)\Pi H)$, thus by Lemma 1, $(x,y) \in N_{(g,h)}^{G\ (U)\Pi H}(e)$ if $y \in N_h^H(hh')$. Then

$$|N_{(g,h)}^{G\ (U)\Pi H}(e)| = |V(G)||\,N_h^H(hh')|,\quad |N_{(g,h')}^{G\ (U)\Pi H}(e)| = |V(G)||\,N_h^H(hh')|,$$

$$|N_0^{H\ (U)\Pi H}(e)| = |V(G)||\ N_0^H(hh')|.$$

Therefore, the summation of

$$[|N_{(g,h)}^{G(U)\Pi H}(e)| + \tfrac{1}{2}\ |N_0^{G(U)\Pi H}(e)|]\ [|N_{(g',h')}^{G(U)\Pi H}(e)| + \tfrac{1}{2}\ |N_0^{G(U)\Pi H}(e)|]$$

over all edges of E_2, is equal to:

$$Sz_2 = |U||V(G)|^2 Sz^*(H).$$

By summation of Sz_1 and Sz_2, the result can be proved.   □

By definition of Sz^*, Sz^{**} and Sz^{***}, we have

$$2Sz^*(G) - Sz^{**}(G) + Sz^{***}(G) = \frac{1}{2}\ |E(G)||V(G)|^2.$$

In the above theorem, if we set $U = V(G)$, then by the above equality, we obtain the following corollary.

Corollary 3. Let G and H be two connected graphs. Then

$$Sz^*(G \times H) = |V(H)|^3 Sz^*(G) + |V(G)|^3 Sz^*(H).$$ □

Theorem 4. Let G and H be two connected graphs and let U be a nonempty subset of $V(G)$. Then

$$M_1^*(G(U)\ \Pi H) = |V(H)|M_1^*(G(U)) + |U|M_1^*(H) + 2|E(G)|\zeta(H)$$
$$+2|E(H)|\sum_{u \in U}\varepsilon_{G\ (U)}(u).$$

Proof. Let G and H be two connected graphs and let U be a nonempty subset of $V(G)$. For our convenience, we partition the edge set of $G(U)\ \Pi H$ into two sets,

$$E_1 = \{(g,h)(g',h') \mid gg' \in E(G) \text{ and } h = h' \in V(H)\},$$

$$E_2 = \{(g,h)(g',h') \mid hh' \in E(H) \text{ and } g = g' \in U\}.$$

Suppose $(x,y) \in V(G(U)\ \Pi H)$, then by Lemma 1,

$$\varepsilon_{G\ (U\Pi H}((x,y)) = \varepsilon_{G\ (U)}(x) + \varepsilon_H(y).$$

Therefore,

$$M_1^*(G(U)\Pi H) = \sum_{(g,h)(g',h') \in E(G(U)\Pi H)}[\varepsilon_{G\ (U)\Pi H}((g,h)) + \varepsilon_{G(U)\Pi H}((g',h'))]$$

$$= \sum_{(g,h)(g',h)\in E_1}[\varepsilon_{G(U)\Pi H}((g,h))+\varepsilon_{G(U)\Pi H}((g',h))]$$

$$+ \sum_{(g,h)(g,h')\in E_2}[\varepsilon_{G(U)\Pi H}((g,h))+\varepsilon_{G(U)\Pi H}((g,h'))]$$

$$= \sum_{h\in V(H)}\sum_{gg'\in E(G)}\left(\varepsilon_{G(U)}(g)+2\varepsilon_H(h)+\varepsilon_{G(U)}(g')\right)$$

$$+ \sum_{g\in U}\sum_{hh'\in E(H)}\left(2\varepsilon_{G(U)}(g)+\varepsilon_H(h)+\varepsilon_H(h')\right)=|V(H)|M_1^*(G(U))$$

$$+ |U|M_1^*(H) + 2|E(G)|\zeta(H) + 2|E(H)|\sum_{u\in U}\varepsilon_{G(U)}(u). \qquad \square$$
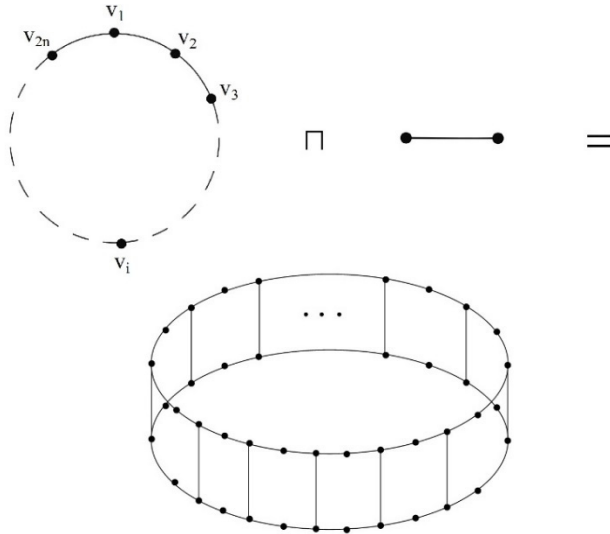
Figure 2. The zig-zag polyhex nanotube $TUHC_6[2n,2] = C_{2n}(U)\,\Pi P_2$, where $U = \{v_2, v_4, \ldots, v_{2n}\}$.

By a similar argument as in the proof of the previous theorem, we have:

Theorem 5. Let G and H be two connected graphs and let U be a nonempty subset of $V(G)$. Then

i). $M_2^*(G(U)\,\Pi H) = |V(H)|M_2^*(G(U)) + |U|M_2^*(H) + \zeta(H)M_1^*(G(U)) + |E(G)|M_1^{**}(H) + |E(H)|\sum_{u\in U}(\varepsilon_{G(U)}(u))^2 + M_1^*(H)\sum_{u\in U}\varepsilon_{G(U)}(u)$.

ii). $M_1^{**}(G(U)\,\Pi H) = |V(H)|M_1^{**}(G(U)) + |V(G)|M_1^{**}(H) + 2\zeta(G(U))\zeta(H). \qquad \square$

The exact formulas for M_2^* of the Cartesian product of graphs were obtained in [9]. We claim that this result is incorrect. The aim of the next corollary is to improve this result. In the part (i) of the above theorem, if we set $U = V(G)$, we obtain the following corollary.

Corollary 6. Let G and H be two connected graphs. Then

$$M_2^* (G \times H) = |V(H)|M_2^* (G) + |E(G)|M_1^{**} (H) + \zeta(H)M_1^* (G)$$
$$+ |V(G)|M_2^* (H) + |E(H)|M_1^{**} (G) + \zeta(G)M_1^* (H). \qquad \square$$

For the graphs in Figs.1 and 2, namely, zig-zag polyhex nanotube $TUHC_6[2n,2]$ and hexagonal chain L_n , some graph invariants were studied in [15, 16, 17, 18]. Here we obtain Sz^*, M_1^* , M_2^* and M_1^{**} of zig-zag polyhex nanotube and the hexagonal chain L_n.

Example 7. Consider the zig-zag polyhex nanotube $TUHC_6[2n,2]$ (see Fig. 2). Diudea, who was the first chemist which considered the problem of computing topological indices of nanostructures, introduced the notation $TUHC_6$. The zig-zag polyhex nanotube is the graph $C_{2n}(U) \Pi P_2$, where $U = \{v_2, v_4, …, v_{2n}\}$, see Fig. 2. On the other hand, one can easily see that $Sz^{**}(C_{2n}(U)) = Sz^{***}(C_{2n}(U)) = Sz^*(C_{2n}) = 2n^3$ and $Sz^*(C_{2n}(U)) = 2n(n^2 – 1)$ and so, by Theorem 2, we have

$$Sz^*(TUHC_6[2n,2]) = 20n^3 – 4n.$$

Example 8. Consider the hexagonal chain L_n (see Fig. 1). The hexagonal chain L_n is the graph $P_{2n+1}(U) \Pi P_2$, where $U = \{v_1, v_3, …, v_{2n+1}\}$, see Fig. 1. On the other hand, it is not difficult to check that $Sz^*(P_{2n+1}) = Sz^*(P_{2n+1}(U)) = \frac{4}{3} n^3 + 2n^2 + \frac{2}{3} n$, $Sz^{**}(P_{2n+1}(U)) = \frac{4}{3} n^3 + 2n^2 + \frac{5}{3} n$ and $Sz^{***}(P_{2n+1}(U)) = \frac{8}{3} n^3 + 2n^2 – \frac{2}{3} n$ and so, by Theorem 2, we obtain

$$Sz^*(L_n) = \frac{44}{3} n^3 + 24n^2 + \frac{43}{3} n + 1.$$
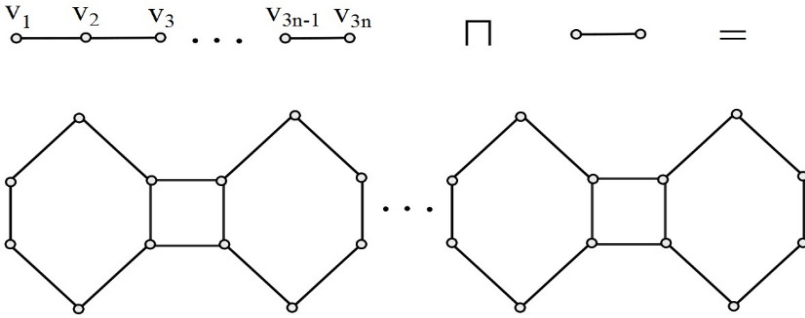
Figure 3. The linear phenylene $F_n = P_{3n}(U) \Pi P_2$, where
$U = \{v_{3k+1} \mid 0 \le k \le n - 1\} \cup \{v_{3k} \mid 1 \le k \le n\}$.

Example 9. Consider the linear phenylene F_n including n benzene ring (see Fig. 3). The linear phenylene F_n is the graph $P_{3n}(U) \Pi P_2$, where $U = \{v_{3k+1} \mid 0 \le k \le n - 1\} \cup \{v_{3k} \mid 1 \le k \le n\}$, see Fig. 3. On the other hand, it is not difficult to check that $Sz^*(P_{3n}) = Sz^*(P_{3n}(U)) = \frac{9}{2} n^3 - \frac{1}{2} n$, $Sz^{**}(P_{3n}(U)) = \frac{9}{2} n^3 + \frac{1}{2} n$ and $Sz^{***}(P_{3n}(U)) = 9n^3 - \frac{9}{2} n^2 - \frac{1}{2} n$ and so, by Theorem 2, we obtain $Sz^*(F_n) = Sz^*(P_{3n}(U) \Pi P_2) = 54n^3$.

In [19, Example 3.2], the authors claim that $Sz(F_n) = 54n^3 - 4n$. We claim that this result is incorrect. By [19, Example 3.2], $Sz(F_1) = 50$ and $Sz(F_2) = 424$ that, are incorrect. The correct values are $Sz(F_1) = 54$ and $Sz(F_2) = 432$. Note that F_n is bipartite and so $Sz^*(F_n) = Sz(F_n)$. On the other hand, by the above example, $Sz^*(F_n) = 54n^3$ and so, $Sz(F_n) = 54n^3$.
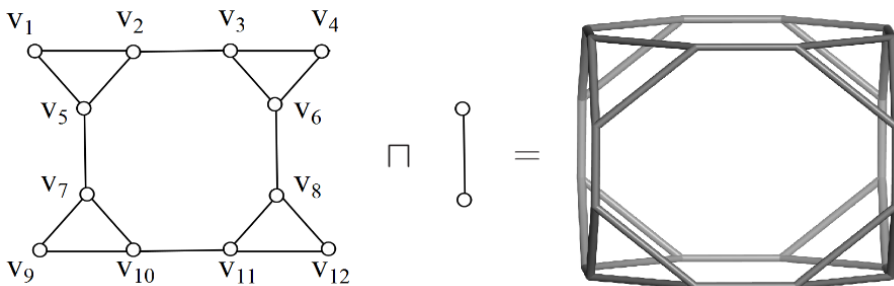
Figure 4. The molecular graph of truncated cube $H = G(U) \Pi P_2$,
where $U = \{v_1, v_4, v_9, v_{12}\}$.

Example 10. Let H be the graph of truncated cube. Then $H = G(U) \Pi P_2$, where $U = \{v_1, v_4, v_9, v_{12}\}$, as shown in Figure 4. It is not difficult to check that $Sz^*(G) = Sz^*(G(U)) = 526$, $Sz^{**}(G(U)) = 380$, $Sz^{***}(G(U)) = 280$ and so, by Theorem 2, we have $Sz^*(H) = Sz^*(G(U) \Pi P_2) = 3264$.

Example 11. Consider the hexagonal chain L_n and the zig-zag polyhex nanotube $TUHC_6[2n,2]$ and truncated cube H depicted in Figs. 1, 2 and 4, respectively, such that n > 1. One can easily see that $M_1^*(P_{2n+1}(U)) = 6n^2$, $M_2^*(P_{2n+1}(U)) = \frac{14}{3}n^3 - \frac{2}{3}n$, $M_1^*(C_{2n}(U)) = 4n^2$, $M_2^*(C_{2n}(U)) = M_1^{**}(C_{2n}(U)) = M_1^{**}(C_{2n}) = 2n^3$, $M_1^*(G(U)) = 160$, $M_2^*(G(U)) = 400$, $\sum_{g \in U} \varepsilon_{C_{2n}(U)}(g) = n^2$,

$$\sum_{g \in U}(\varepsilon_{C_{2n}(U)}(g))^2 = n^3, \quad \sum_{g \in U}\varepsilon_{P_{2n+1}(U)}(g) = \begin{cases} \frac{3}{2}n^2 + 2n + \frac{1}{2} & 2 \mid n \\ \frac{3}{2}n^2 + 2n & 2 \nmid n \end{cases},$$

$$\sum_{g \in U}(\varepsilon_{P_{2n+1}(U)}(g))^2 = \begin{cases} \frac{7}{3}n^3 + 4n^2 + \frac{5}{3}n & 2 \mid n \\ \frac{7}{3}n^3 + 4n^2 + \frac{2}{3}n & 2 \nmid n \end{cases}, \quad \sum_{g \in U}\varepsilon_{G(U)}(g) = 20,$$

$\sum_{g \in U}(\varepsilon_{G(U)}(g))^2 = 10$ and so, by Theorems 4 and 5, for n > 1, we have:

1. $M_1^*(L_n) = M_1^*(P_{2n+1}(U) \Pi P_2) = \begin{cases} 15n^2 + 14n + 3 & 2 \mid n \\ 15n^2 + 14n + 2 & 2 \nmid n \end{cases}.$

2. $M_1^*(TUHC_6[2n,2]) = M_1^*(C_{2n}(U) \Pi P_2) = 10n(n+1).$

3. $M_2^*(L_n) = M_2^*(P_{2n+1}(U) \Pi P_2) = \begin{cases} \frac{35}{3}n^3 + 19n^2 + \frac{28}{3}n + 2 & 2 \mid n \\ \frac{35}{3}n^3 + 19n^2 + \frac{25}{3}n + 1 & 2 \nmid n \end{cases}.$

4. $M_2^*(TUHC_6[2n,2]) = M_2^*(C_{2n}(U) \Pi P_2) = 5n^3 + 10n^2 + 5n.$

5. $M_1^*(H) = M_1^*(G(U) \Pi P2) = 432.$

6. $M_2^*(H) = M_2^*(G(U) \Pi P_2) = 1296.$

ACKNOWLEDGMENTS

REFERENCES

1. S. Klavžar, A. Rajapakse, I. Gutman, The Szeged and the Wiener index of graphs, *Appl. Math. Lett.,* **1996**, *9*, 45.
2. M. Tavakoli, F. Rahbarnia, A.R. Ashrafi, Further results on hierarchical product of graphs, *Discrete Appl. Math*., **2013**, *161*, 1162.
3. M.H. Khalifeh, H. Yousefi-Azari, A.R. Ashrafi and S.G. Wagner, Some new results on distance-based graph invariants, *European J. Combin*., **2009**, *30*, 1149.
4. T. Pisanski, M. Randić, Use of the Szeged index and the revised Szeged index for measuring network bipartivity, *Discrete Appl. Math.,* **2010**, *158*, 1936.
5. M. Randić, On generalization of Wiener index for cyclic structures, *Acta Chim. Slovenica,* **2002**, *49*, 483.
6. R. Xing, B. Zhou, On the revised Szeged index, *Discrete Appl. Math*., **2011**, *159*, 69.
7. I. Gutman, N. Trinajstic, Graph theory and molecular orbitals. Total *л*-electron energy of alternant hydrocarbons, *Chem. Phys. Lett.,* **1972**, *17*, 535.
8. I. Gutman, B. Ruscic, N. Trinajstic, C.F. Wilcox, Graph theory and molecular orbitals. XII. Acyclic polyenes, *J. Chem. Phys.,* **1975**, *62*, 3399.
9. M. Ghorbani and M.A. Hosseinzadeh, A New Version of Zagreb Indices, *Filomat*, **2012**, *1*, 93.
10. A.R. Ashrafi, M. Saheli, M. Ghorbani, The eccentric connectivity index of nanotubes and anotori, *J. Comput. Appl. Math.,* **2011**, *235*, 4561.
11. L. Barriére, F. Comellas, C. Dafló, M.A. Fiol, The hierarchical product of graphs, *Discrete Appl. Math.,* **2009**, *157*, 36.
12. L. Barriére, F. Comellas, C. Dafló, M.A. Fiol and M. Mitjana The generalized hierarchical product of graphs, *Discrete Math.,* **2009**, *309*, 3871.
13. R. Hammack, W. Imrich and S. Klavžar, Handbook of Product Graphs, Second edition, Taylor Francis Group, **2011**, chapter 5.
14. M. Tavakoli, H. Yousefi-Azari, A.R. Ashrafi, Note on edge distance-balanced graphs, *Trans. Combin.,* **2012**, *1*, 1.
15. M. Eliasi, A. Iranmanesh, The hyper-Wiener index of the generalized hierarchical product of graphs, *Discrete Appl. Math.,* **2011**, *159*, 866.
16. M.V. Diudea, Polyhex tori originating in square tori. In: M.V. Diudea, Ed., Nanostructures-Novel Architecture, NOVA, New York, **2005**, 111.
17. M.V. Diudea, M. Stefu, B. Parv, and P.E. John, Wiener index of armchair polyhex nanotubes. *Croat. Chem. Acta*, **2004**, *77*, 111.
18. P.E. John and M.V. Diudea, Wiener index of zig-zag polyhex nanotubes, *Croat. Chem. Acta*, **2004**, *77*, 127.
19. M. Arezoomand, B. Taeri, Applications of generalized hierarchical product of graphs in computing the Szeged index of chemical graphs, *MATCH Commun. Math. Comput. Chem.,* **2010**, *64*, 591.

SOME CONNECTIVITY INDICES OF CAPRA-DESIGNED PLANAR BENZENOID SERIES $Ca_n(C_6)$

MOHAMMAD REZA FARAHANI[a], MIRANDA PETRONELLA VLAD[b]

ABSTRACT. A molecular graph can be transformed using map operations, one of these, named Capra, being defined by *Diudea*. In this paper, we focus on the structure of *Capra-designed planar benzenoid series $Ca_n(C_6)$* (*k≥0*) and compute some connectivity indices of this family. A connectivity index is a real number related to a molecular graph and is invariant under graph automorphism.

Keywords: Benzenoid, Capra map operation, Connectivity index.

INTRODUCTION

Let $G=(V,E)$ be a molecular graph with the vertex set $V(G)$ and the edge set $E(G)$. $|V(G)|=n$, $|E(G)|=e$ are the number of vertices and edges. In chemical graph theory, the vertices and edges correspond to the atoms and bonds, respectively; the number of incident edges in the vertex v is its degree, denoted by d_v. The vertices u and v are adjacent if there exist an edge $e=uv$ between them. A molecular graph is a connected graph, i.e. there exist a path between any pair of vertices.

A variety of topological indices have been defined; a topological index is a real number related to the structure of graph, which is invariant under graph automorphism.

In 1975 Randić proposed a structural descriptor called the branching index [1-4] that later named the Randić molecular connectivity index (or simply Randić index). It is defined as:

$$\chi(G) = \sum_{e=uv \in E(G)} \frac{1}{\sqrt{d_u d_v}}$$

[a] *Department of Mathematics of Iran University of Science and Technology, (IUST) Narmak, Tehran 16844, Iran, Mr_Farahani@Mathdep.iust.ac.ir*
[b] *Dimitrie Cantemir University, Bucharest, Faculty of Economic Sciences, No 56 Teodor Mihali Street, 400591, Cluj Napoca, Romania, mirandapv@yahoo.com*

Recently, a version, called the Sum-connectivity index, was introduced by *Zhou* and *Trinajstić* [5,6]:

$$X(G) = \sum_{v_u v_v} \frac{1}{\sqrt{d_u + d_v}}$$

where d_u and d_v are the degrees of the vertices u and v, respectively.

More recently, *Vukicevic* and *Furtula* [7] proposed two topological indices, named *geometric-arithmetic index* and *atom-bond connectivity index* (denoted by *GA(G)* and *ABC(G),* respectively), see [7-9]. They are defined as follows:

$$GA(G) = \sum_{e=uv \in E(G)} \frac{2 \times \sqrt{d(u)d(v)}}{d(u) + d(v)}$$

$$ABC(G) = \sum_{e=uv \in E(G)} \sqrt{\frac{d(u) + d(v) - 2}{d(u)d(v)}}$$

Definition 1. Let *G* be a molecular graph and d_v being the degree of vertex $v \in V(G)$. We divide the vertex set *V(G)* and edge set *E(G)* of *G* into several partitions, as follow:

$$\forall i, \delta < i < \Delta, V_i = \{v \in V(G) \mid d_v = i\},$$
$$\forall j, 2\delta \leq j \leq 2\Delta, E_j = \{e = uv \in E(G) \mid d_v + d_u = j\}$$
$$\forall k, \delta^2 \leq k \leq \Delta^2, E_k^* = \{e = uv \in E(G) \mid d_v \times d_u = k\}.$$

Note that $\delta = Min\{d_v \mid v \in V(G)\}$ and $\Delta = Max\{d_v \mid v \in V(G)\}$.

MAIN RESULTS AND DISCUSSION

In this section, we compute Randić connectivity index, sum- connectivity index, geometric-arithmetic index and atom-bond connectivity index of Capra-designed planar benzenoid series *Ca_k(C_6)*.

A mapping is a new drawing of an arbitrary planar graph *G* on the plane. Capra map operation was introduced by *Diudea* [10,11]. This method enables one to build a new structure, according to Figure 1 and Definition 2:
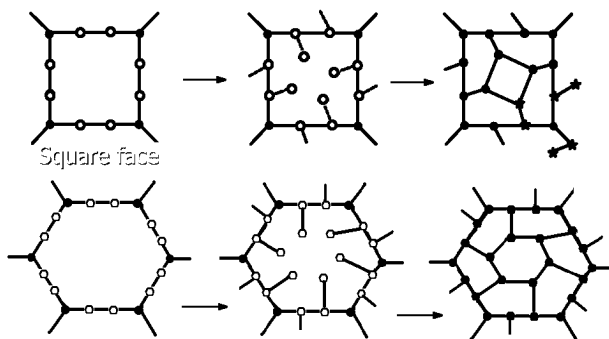
Figure 1. Capra map operation on the square and hexagonal face, respectively

Definition 2. Let *G* be a cyclic planar graph. Capra map operation is achieved as follows:
  (i)   insert two vertices on every edge of G;
  (ii) add pendant vertices to the above inserted ones and
  (iii) **c**onnect the pendant vertices in order (-1,+3) around the boundary of a face of G. By running these steps for every face/cycle of *G,* one obtains the Capra-transform of *G Ca(G)*, see Figure 1.
     By iterating the Capra-operation on the hexagon (i.e. benzene graph C_6) and its Ca-transforms, a benzenoid series, as shown in Figures 2 and 3, can be designed. We will use the Capra-designed benzene series to calculate some connectivity indices (see below).

$Ca(C_6)$
(Capra of planar benzenoid)

C_6
(benzene)

$Ca_2(C_6)$
(Capra of Capra of planar benzenoid)

● The vertices with degree two
━ The common edge between two adjacent flowers
━ The edge of center flower
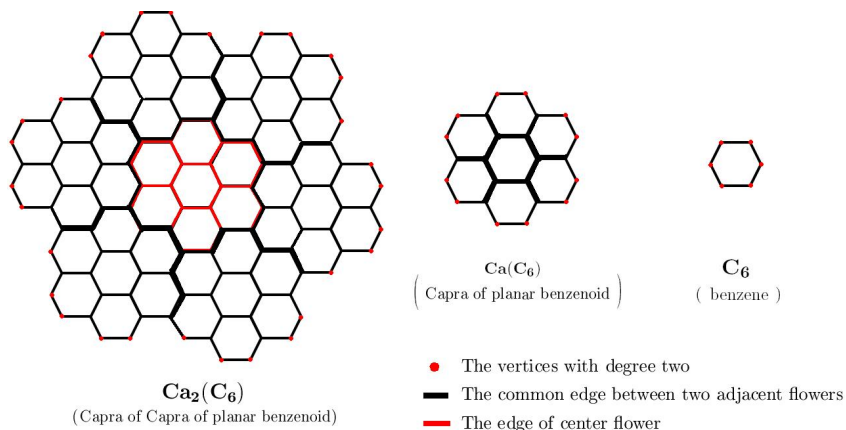
Figure 2. The first two graphs: *Ca(C₆)* and *Ca₂(C₆)* of the benzenoid family *Caₖ(C₆)*.
Coloring is according to Definition 1.
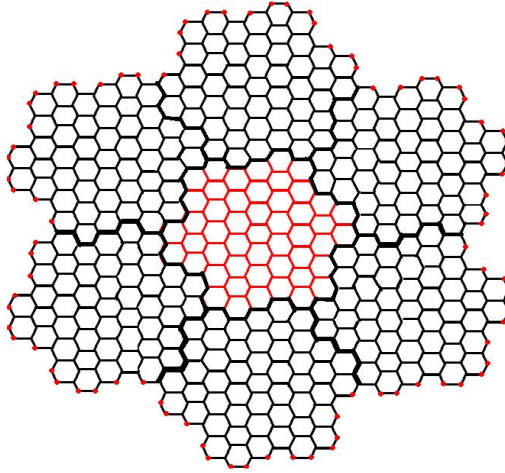
Figure 3. Graph $Ca_3(C_6)$ is the third member of Capra-designed planar benzenoid series.

Theorem 1. Let $G=Ca_k(C_6)$ $k \in N$ be the Capra-designed planar benzenoid series. Randić connectivity index is as follows:

$$\chi(Ca_k(C_6)) = \frac{2(7^k) + (4\sqrt{6}-1)3^{k-1} + 1}{2}$$

Proof. Let $G=Ca_k(C_6)$ $(k \geq 0)$ be the Capra-designed planar benzenoid series. The structure $Ca_k(C_6)$ collects seven times of structure $Ca_{k-1}(C_6)$ (we call "flower" the substructure $Ca_{k-1}(C_6)$ in the graph $Ca_k(C_6)$). Therefore, by a simple induction on k, the vertex set of $Ca_k(C_6)$ will have $7 \times |V(Ca_k(C_6))|-6(2 \times 3^{k-1}+1)$ members. Because, there are $3^{k-1}+1$ and 3^{k-1} common vertices between seven flowers $Ca_{k-1}(C_6)$ in $Ca_k(C_6)$, marked by full black color in the above figures. Also, by a similar inference, the edge set $E(Ca_k(C_6))$ has $7 \times |E(Ca_k(C_6))|-6(2 \times 3^{k-1}+1)$ members. Thus, there are 3^{k-1} and 3^{k-1} common edges, see Figures 2 and 3. Now by solving the recursive sequences, $n_k=|V(Ca_k(C_6))|$ and $e_k=|E(Ca_k(C_6))|$. Thus the size of vertex set and edge set of Capra-designed planar benzenoid series $Ca_k(C_6)$ $(k \geq 0)$ are equal to:

$$|V(Ca_k(C_6))|=2 \times 7^k+3^{k+1}+1, \quad |E(Ca_k(C_6))|=3(7^k+3^k).$$

Now, we can divide $V(Ca_k(C_6))$ and $E(Ca_k(C_6))$ to two and three partitions, respectively (See Definition 1). According to Figures 2 and 3, we see that the number of vertices with degree two of graph $Ca_k(C_6)$ (denoted

by $v_2^{(k)}$) is equal to $6(3\left(\dfrac{v_2^{(k-1)}}{6}\right))-6$. Therefore, we have $v_2^{(k)}=3v_2^{(k-1)}-6$

$=3(3v_2^{(k-2)}-6)-6 \;=\ldots=3^k v_2^{(0)}-6\sum_{i=0}^{k-1}3^i=3^{k+1}+3$ and $e_4^{(k)}=|E_4|=|E_4^*|$

$=v_2^{(k-1)}=3^k+3$.

Alternatively, the number of vertices of degree three is $|V_3|=|\{v\in V\,(Ca_k\,(C_6))\,|\,d_v=3\}|=2(7^k-1)$, (denoted by $v_3^{(k)}$).

On the other hand, according to the structure of Capra-designed planar benzenoid series, $G=Ca_k(C_6)$, $e_5^{(k)}=|E_5|=|E_6^*|=2v_2^{(k)}-2e_4^{(k)}$. Thus, $e_5^{(k)}=2v_2^{(k)}-2v_2^{(k-1)}=4(3^k)$. The size of edge set E_5 and E_6^* is: $e_5^{(k)}=2(3^{k+1}+3-3^k-3)=4(3^k)$. Thus, it is obvious that:

$$e_6^{(k)}=|E_6|=|E_9^*|=3\left(7^k+3^k\right)-e_5^{(k)}-e_4^{(k)}$$
$$=3\times 7^k+3^{k+1}-4\times 3^k-3^k-3$$
$$=3\times 7^k-2\times 3^k-3$$
$$=3(7^k-2(3^{k-1})-1).$$

Then, by using of size $V_2, V_3, E_4, E_4^*, E_5, E_6^*, E_6$ and E_9^*, we can compute Randić connectivity index of Capra-designed planar benzenoid series $G=Ca_k(C_6)$ as follows:

$$\chi(Ca_k\,(C_6))=\sum_{uv\in E\,(Ca_k\,(C_6))}\frac{1}{\sqrt{d\,(u)d\,(v)}}$$

$$=\sum_{uv\in E_9^*}\frac{1}{\sqrt{d\,(u)d\,(v)}}+\sum_{uv\in E_6^*}\frac{1}{\sqrt{d\,(u)d\,(v)}}+\sum_{uv\in E_4^*}\frac{1}{\sqrt{d\,(u)d\,(v)}}$$

$$=\frac{|E_9^*|}{\sqrt{9}}+\frac{|E_6^*|}{\sqrt{6}}+\frac{|E_4^*|}{\sqrt{4}}$$

$$=\frac{3(7^k-2(3^{k-1})-1)}{\sqrt{9}}+\frac{4(3^k)}{\sqrt{6}}+\frac{3^k+3}{\sqrt{4}}.$$

Finally, the Randić index of $Ca_k(C_6)$ is

$$\chi(Ca_k(C_6))=\frac{2(7^k)+(4\sqrt{6}-1)3^{k-1}+1}{2}.$$

thus completing the proof of Theorem 1.

Theorem 2. Sum-connectivity index of Capra-designed planar benzenoid series $Ca_k(C_6)$ for integer k is equal to:

$$X(\mathbf{Ca_k}(\mathbf{C_6})) = \frac{3(3^{k-1}+1)+\sqrt{6}(7^k-1)}{2} + 3^{k-1}\left(\frac{12\sqrt{5}-5\sqrt{6}}{5}\right).$$

Proof: By using the results from the above proof, it is immediate that

$$X(Ca_k(C_6)) = \sum_{e=uv\in E(G)} \frac{1}{\sqrt{d_u+d_v}}$$

$$= \sum_{e=uv\in E_4} \frac{1}{\sqrt{d_u+d_v}} + \sum_{e=uv\in E_5} \frac{1}{\sqrt{d_u+d_v}} + \sum_{e=uv\in E_6} \frac{1}{\sqrt{d_u+d_v}}$$

$$= \frac{|E_4|}{\sqrt{4}} + \frac{|E_5|}{\sqrt{5}} + \frac{|E_6|}{\sqrt{6}}$$

$$= \frac{3^k+3}{\sqrt{4}} + \frac{4(3^k)}{\sqrt{5}} + \frac{3(7^k-2(3^{k-1})-1)}{\sqrt{6}}.$$

Thus $X(\mathbf{Ca_k}(\mathbf{C_6})) = \frac{3(3^{k-1}+1)+\sqrt{6}(7^k-1)}{2} + 3^{k-1}\left(\frac{12\sqrt{5}-5\sqrt{6}}{5}\right).$

Theorem 3. Geometric-Arithmetic index and Atom-Bond connectivity index of Capra-designed planar benzenoid series are equal to (for all $k \in N$)

$$GA(Ca_k(C_6)) = 3(7^k) + \left(\frac{8\sqrt{6}}{5}-1\right)3^k$$

$$ABC(Ca_k(C_6)) = 2(7^k) + (\frac{15\sqrt{2}-8}{2})3^{k-1} + (\frac{3\sqrt{2}-4}{2})$$

Proof. Let $G=Ca_k(C_6)$ $(k≥1)$ be Capra-designed planar benzenoid series. According to the proof of Theorem 1, we have $|E_6|=|E_9^*|=3(7^k-2(3^{k-1})-1)$, $|E_5|=|E_6^*|=4(3^k)$ and $|E_4|=|E_4^*|=3^k+3$. Thus, we can compute two connectivity topological indices geometric-arithmetic index and atom-bond connectivity index of $G=Ca_k(C_6)$ for any $k≥1$ as follows:

$$GA\,(Ca_k\,(C_6)) = \sum_{uv \in E\,(Ca_k\,(C_6))} \frac{2\sqrt{d\,(u)d\,(v)}}{d\,(u) + d\,(v)}$$

$$= \sum_{e = uv \in E_4} \frac{2\sqrt{4}}{4} + \sum_{e = uv \in E_5} \frac{2\sqrt{6}}{5} + \sum_{e = uv \in E_6} \frac{2\sqrt{9}}{6}$$

$$= e_6^{(k)} \frac{6}{6} + e_5^{(k)} \frac{2\sqrt{6}}{5} + e_4^{(k)} \frac{4}{4}$$

$$= 3(7^k) + \left(\frac{8\sqrt{6}}{5} - 1 \right) 3^k$$

The geometric-arithmetic index of $Ca_k(C_6)$ is

$$GA\,(Ca_k\,(C_6)) = 3(7^k) + \left(\frac{8\sqrt{6}}{5} - 1 \right) 3^k.$$

Finally,

$$ABC\,(Ca_k\,(C_6)) = \sum_{uv \in E\,(Ca_k\,(C_6))} \sqrt{\frac{d\,(u) + d\,(v) - 2}{d\,(u)d\,(v)}}$$

$$= \sum_{uv \in E_9^*} \frac{1}{\sqrt{d\,(u)d\,(v)}} + \sum_{uv \in E_6^*} \frac{1}{\sqrt{d\,(u)d\,(v)}} + \sum_{uv \in E_4^*} \frac{1}{\sqrt{d\,(u)d\,(v)}}$$

$$= e_6^{(k)} \sqrt{\frac{6-2}{9}} + e_5^{(k)} \sqrt{\frac{5-2}{6}} + e_4^{(k)} \sqrt{\frac{4-2}{4}}$$

$$= 3(7^k - 2(3^{k-1}) - 1) \frac{2}{3} + 4(3^k) \frac{\sqrt{2}}{2} + (3^k + 3) \frac{\sqrt{2}}{2}.$$

Therefore, atom-bond connectivity index of $Ca_k(C_6)$ will be

$$ABC(Ca_k(C_6)) = 2(7^k) + (\frac{15\sqrt{2} - 8}{2})3^{k-1} + (\frac{3\sqrt{2} - 4}{2}).$$

Here, the proof of Theorem 3 is completed.

REFERENCES

1. M. Randić, On characterization of molecular branching, *J. Amer. Chem. Soc*., **1975**, *97,* 6609.
2. M. Ghorbani and M. Ghazi, *Digest. J. Nanomater. Bios*., **2010**, *5(4),* 1107.
3. M. Ghorbani and M. Ghazi, *Digest. J. Nanomater. Bios*., **2010**, *5(4),* 837.
4. J. Rada, O. Araujo, and I. Gutman, *Croat. Chem. Acta*, **2001**, *74,* 225.
5. B. Zhou and N. Trinajstić, On a novel connectivity index, *J. Math. Chem.,* **2009**, *46*, 1252.
6. B. Zhou and N. Trinajstić, On general sum-connectivity index, *J. Math. Chem.,* **2010**, *47*, 210.
7. D. Vukicevic and B. Furtula, *J. Math. Chem*., **2009**, *46,* 1369.
8. L. Xiao, S. Chen, Z. Guo and Q. Chen, *Int. J. Contemp. Math. Sci.,* **2010**, *5(45),* 2225.
9. Y. Yuan, B. Zhou and N. *Trinajstić, J. Math. Chem.,* **2010**, *47,* 833.
10. M.V. Diudea, Capra-a leapfrog related operation on maps, *Studia UBB Chemia*, **2003**, *48* (2), 3.
11. M.V. Diudea, Nanoporous carbon allotropes by septupling map operations. *J. Chem. Inf. Model*, **2005**, *45,* 1002.

FAT CONTENT IN YOGHURTS VERSUS NON-FAT FORTIFYING–A RHEOLOGICAL AND SENSORIAL APPROACH

INA VASILEAN[a], IULIANA APRODU[a], LIVIA PATRASCU[a*]

ABSTRACT. This study investigated the effect of fat content (3.5; 1.5 and 0.1 % w/w), together with total solids content on selected rheological and sensorial characteristics of yoghurt samples fermented with exopolysaccharides producing lactic acid bacteria (*Streptococcus termophilus* and *Lactobacillus delbrueckii* ssp. *Bulgaricus*). Rheological flow and oscillatory tests showed that all tested yoghurt samples behave like thixotropic fluids. Pronounced hysteresis areas were obtained for skimmed yoghurts with added solids (skim milk powder and lactose, 2 and 3% w/v). Higher levels of fat favored the flow properties of the yogurt samples, enabling the formation of more stable viscoelastic gel networks. Sensorial characteristics were highly appreciated for samples with higher fat content.

Keywords: *yoghurt, exopolysaccharides, fat content, fortification, flow, viscoelastic gel*

INTRODUCTION

Fermented milk products are very popular all over the world[1], mainly because of their sensorial characteristics but also due to their potential in maintaining and even improving consumers` health [2]. The most widely used lactic acid bacteria for yogurt fermentation are *Streptococcus thermophilus* and *Lactobacillus delbrueckii* ssp. *Bulgaricus*, which are responsible for the development of specific taste and consistency.

The structure, microstructure and rheological characteristics of the yogurts highly influence the perception of the product during consumption [3]. It is well known that many technological parameters and starter culture can modulate textural properties of the yoghurts [4]. The knowledge of the yoghurt rheological properties can offer essential information about products texture

[a] *Universitatea Dunarea de Jos, Facultatea de Stiinta si Ingineria Alimentelor, Str. Domneasca, Nr. 111, RO-800201 Galati, Romania.*
[*] *Corresponding author: livia.mantoc@ugal.ro*

and gel stability. Skriver et al. [5] investigated both rheological and sensorial characteristics of stirred yogurts showing that gel firmness can be correlated with viscoelastic properties (G', G'') while palatability was closely related to the shear stress. It is well known that textural and rheological characteristics of fermented lactic products with low fat and high protein content differ from those with no added solids, milk supplementation strongly influencing the texture of fermented products [6]. In order to improve rheological properties of skimmed dairy products different methods for increasing total solids content are approached. These compositional modifications are required in order to overcome problems associated with weak texture gels and whey separation [7].

Yoghurt bacteria can form a polysaccharide covering lair named glycocalyx. These macromolecular compounds can be partially released during fermentation process being generically named exopolysaccharides (EPS). The EPS producing starter bacteria ensure a stable yoghurt structure, a more consistent texture and higher viscosity by preventing gel rupture and whey releasing [8, 9, 10, 11,12]. The presence of EPS in lactic fermented milk products was found to improve rheological properties due to their thickening capacity, texture and products taste [13]. The EPS also have excellent water binding properties [14]. It was shown that yoghurt viscosity depends on EPS concentration and their specific volume [11]. However, Amatayakul et al. [15] concluded that using EPS-producing lactic acid bacteria could not compensate the reduction of total solids of yoghurt and these starter cultures are not efficient in improving the firmness of the low solid content products.

The aim of the present study was first to obtain yoghurt samples with different fat contents through fermentation with a pure culture of EPS producing lactic acid bacteria, and to characterize the obtained products in terms of rheological and sensory properties. Moreover, the influence of skim milk powder and lactose addition on the properties of skimmed yogurt was tested.

RESULTS AND DISCUSSION

Quality of the set yogurt obtained by fermenting milk with different fat contents (3.5, 1.5 and 0.1%) with EPS producing lactic acid bacteria was estimated by testing rheological behavior and sensory properties of the samples.

Rheological analyses. Two different types of tests were performed for rheological characterization of the samples: controlled shear-rate measurements by progressively increasing and decreasing the shear rate to check the viscosity dependence by the shear rate and small deformation oscillatory rheological test to gain insight into the structural particularities of the samples.

The flow parameters and hysteresis loop area obtained when performing shear thinning tests on the yoghurts with different fat contents are presented in Table 1.

Table 1. Rheological flow parameters for yoghurt samples with different fat and total solids content

Sample	Yield stress, Pa	Hysteresis area, Pa/s	Rate index		Viscosity, Pa*s	
			up curve	down curve	up curve	down curve
FY	1.907±0.01	18.1±0.35	0.350±0.01	0.409±0.01	1.017±0.03	0.778±0.02
NY	0.348±0.01	4.5±0.01	0.644±0.01	0.679±0.00	0.107±0.01	0.091±0.01
SY	1.632±0.01	30.4±0.21	0.324±0.02	0.445±0.01	0.907±0.01	0.516±0.01
SY_1	3.210±0.3	70.0±0.74	0.263±0.01	0.384±0.1	2.007±0.2	1.107±0.1
SY_2	3.344±0.3	71.2±0.77	0.260±0.00	0.374±0.01	2.098±0.12	1.198±0.03

Values represent means of three replicates ± SD. FY - Yoghurt with high fat content (3.5% fat w/w); NY – Partially skimmed yoghurt (1.5% fat w/w); SY – Skimmed yoghurt (0.1% fat w/w); SY_1 – Skimmed yoghurt enriched with 2% skim milk powder and 2% lactose (w/v); SY_2 - Skimmed yoghurt enriched with 3% skim milk powder and 3% lactose (w/v).

The flow behavior of the yogurt samples is represented in Figures 1 and 2. In order to improve appearance and quality of low fat yoghurts we proceeded to the fortification with skim milk powder (2 and 3% w/v) and lactose (2 and 3% w/v). Rheological characteristics of skimmed yoghurt were compared with those of the fortified products (Figure 2). Flow test revealed the thixotropic behavior for tested yoghurt samples as indicated by rate index values (Table 1). The shear thinning characteristic can be also seen in viscosity curves (decreasing viscosity when increasing shear rate) (Figures 1 and 2).

Regarding hysteresis phenomenon one can see that yoghurt with normalized fat content to 1.5% (w/w) recorded the lowest value, indicating that when speaking of yoghurts, high fat content does not necessary ensure flow stability. Moreover, samples with high fat contents (3.5% w/w) requested a rather high yield stress value (calculated with Bingham equation) in order to flow, compared to the samples with 1.5% and 0.1% fat contents and no added foreign solids. Adding solids to the skimmed yoghurt samples resulted in higher values for the yield stress, with no significant differences (p>0.05) between SY_1 and SY_2 sample (Table 1). The yoghurt samples supplemented with 2% of lactose and skim milk powder (SY_1) presented higher values of the hysteresis area compared to the un-fortified skimmed yogurt. Further increase of the solid content (SY_2 sample) did not led to significant differences (p>0.05) in terms of hysteresis area.

□ FY up curve   △ NY up curve   ○ SY up curve
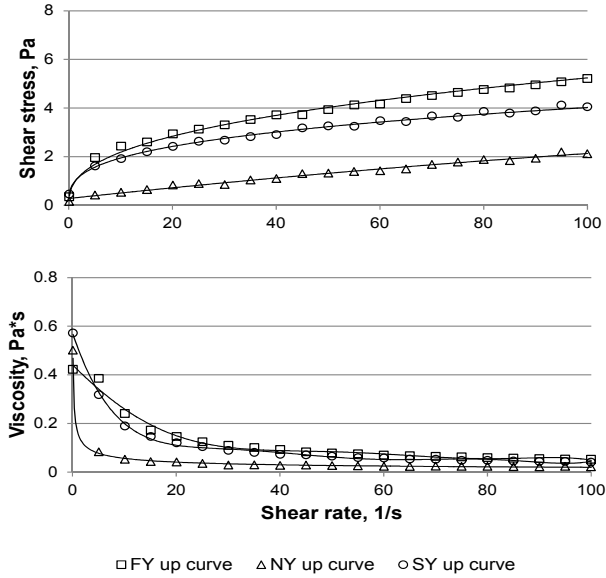
Figure 1. Flow behaviour of yoghurt samples with different fat contents. FY - Yoghurt with high fat content (3.5% fat w/w); NY – Partially skimmed yoghurt (1.5% fat w/w); SY – Skimmed yoghurt sample (0.1% fat w/w);

△ SY1 up curve   ▲ SY1 down curve
○ SY2 up curve   ● SY2 down curve

Figure 2. Flow behaviour of the skimmed and fortified yoghurt samples. SY_1 – Skimmed yoghurt sample enriched with 2% skim milk powder and 2% lactose (w/v); SY_2 - Skimmed yoghurt sample enriched with 3% skim milk powder and 3% lactose (w/v)

Protein addition to the skimmed milk samples (SY_1 and SY_2) resulted in higher viscosity and shear stress values compared to the skimmed yoghurt with no added solids (SY) (Figure 1 and 2). Therefore, protein addition might be considered appropriate for improving yogurt structure by favoring a thicker gel network formation. These findings are in agreement with Bhullar et al. [16], who stated that supplementation of the yogurt samples with 2% (w/v) of whey protein concentrate led to increased viscosity and reduced syneresis. The lack of fat in yoghurt structure could affect EPS interaction with product components, resulting in higher hysteresis areas during flow (Figure 2). This phenomenon can be explained by the presence of higher number of protein-protein links, which result in a denser gel network and fewer protein-water links [17, 18, 15].

EPS presence into the samples highly influences the viscosity and other rheological properties of the yogurts. Patel *et al*. [19] stated that EPS exhibit remarkable thickening and shear-thinning properties, and display high intrinsic viscosities. Broadbent et al. [20] found that the amount of EPS produced in lactic fermented milk products is influenced by the environment composition (C:N ratio) and growing conditions. In our case the amount of synthesized EPS, reported by Vasilean et al. [21] when using the same yogurt preparation procedure, was relatively close in case of the samples obtained from whole fat and partially skimmed milk (71.46 and 71.07 mg/l respectively), and lower in case of the yogurt obtained from skimmed milk (63.65 mg/l). The addition of protein and lactose to the skimmed milk before fermentation did not favor the EPS amount from yoghurt samples (63.51 mg/l for SY_1 sample and 68.89 mg/l for SY_2). Thus the viscosity increment in fortified samples could not be necessarily attributed to EPS presence.

Analyzing oscillatory rheology results presented in Figure 3, the soft solid structure can be observed for all yoghurt samples. For the entire range of tested frequency, G' values overcame the G``, indicating that yoghurt samples behaved like elastoviscous fluids. The yoghurt sample with high fat content (FY) presented the highest value of elastic modulus. In agreement with the flow test observations, the SY sample presented a more elastic (solid like behaviour) structure with respect to NY sample. We appreciate that this phenomenon could be explained by different molecule distribution within the gel network and by the different bond type participating to network formation and stabilization. As indicated by Van Vliet et al. [22] the rheological properties of yoghurts are influenced by the strength of protein-protein interactions, the number of bonds per cross-section of the strand, relaxation times for the network bonds, and the orientation of the strands within the matrix. Thus presence of higher amount of protein-fat-protein links alowed higher fluidity in comparison to the samples where the protein-protein interactions are predominant.
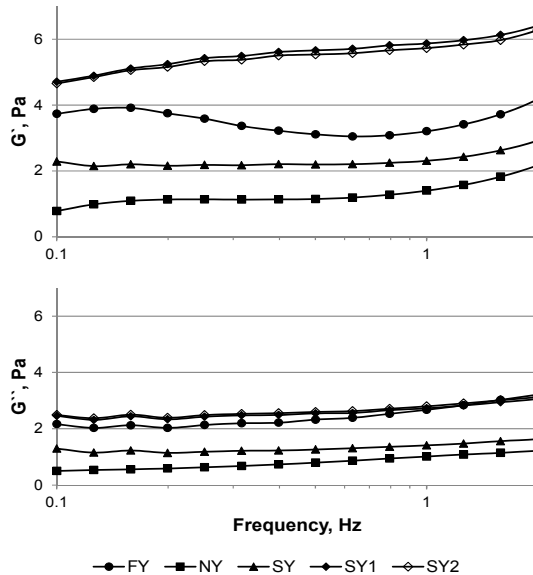
Figure 3. The influence of total fat content and milk fortification on viscoelastic moduli of set yoghurt samples. FY - Yoghurt with high fat content (3.5% fat w/w); NY – Partially skimmed yoghurt (1.5% fat w/w); SY – Skimmed yoghurt (0.1% fat w/w); SY_1 – Skimmed yoghurt enriched with 2% skim milk powder and 2% lactose (w/v); SY_2 - Skimmed yoghurt enriched with 3% skim milk powder and 3% lactose (w/v).

Addition of 2% skim milk powder together with 2% lactose to the skimmed yoghurt samples determined an increase of the gel network density. The fortification most probably led to the reduction of pores dimensions thus causing the increase of viscoelastic moduli values. There observations are in agreement with the literature [23, 24, 5, 4, 25]. Lee and Lucey [26] stated that the physical and sensory properties of yogurt gels are greatly influenced by the total solids content of the yogurt milk, especially the protein content, the G′ values of yogurt increasing with the increase of the total solids content. However, further increase of the total solids quantity in case of SY2 sample did not led to significant variation of G` and G`` values.

Sensorial analysis. The results of sensorial analysis of the yoghurt samples are represented in figure 4. As one can see fat content together with product fortification significantly influenced products sensorial characteristics (p<0.01).

The color of the samples with higher fat contents (3.5% and 1.5%) was better appreciated by the assessors probably because of their higher luminosity, and no significant differences between these two samples (p>0.05) was obtained. Concerning the samples with low fat content, regardless of the enrichment with skim milk powder and lactose, the color

264

was medium appreciated (Figure 4). The non-fat solid addition to the skimmed milk before fermentation with EPS producing lactic acid bacteria had no significant influence on the color attribute ($p > 0.05$).

Panelists found no odor for the yoghurt samples with 3.5 and 1.5% fat (FY and NY), with no significant differences between the two samples ($p > 0.05$). On the other hand, some unspecific smell was identified in case of the skimmed yogurt samples, regardless of non-fat solids supplementation ($p > 0.05$).

The same trend was observed in case of the syneresis attribute. No syneresis phenomenon was observed for FY and NY samples ($p > 0.05$). The highest amount of separated whey was obtained in case of skimmed yoghurt sample (SY), and the addition of skim milk powder and lactose resulted in the decrease of released whey, with significant differences between SY2 and SY or SY1 samples.

Regarding firmness, the most appreciated sample was FY, while the lowest score was obtained for SY sample. The firmness values ($p < 0.01$) varied significantly with the yogurt sample, except for NY and SY2 samples when no differences were registered ($p > 0.05$). The addition of higher amounts (3% w/v) of skim milk powder and lactose to the skimmed yoghurts determined the perception of firmness attribute similar to yoghurts with medium fat content. The same trend was observed in case of consistency.
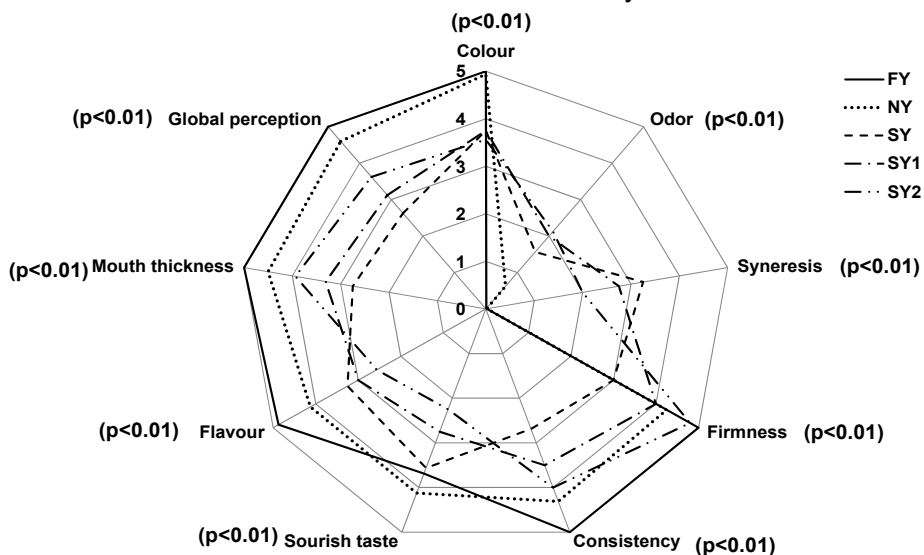
Figure 4. Sensorial characteristics of set yoghurt types fermented with EPSs releasing starter culture, as a function of fat and total solids content. FY - Yoghurt with high fat content (3.5% fat w/w); NY – Partially skimmed y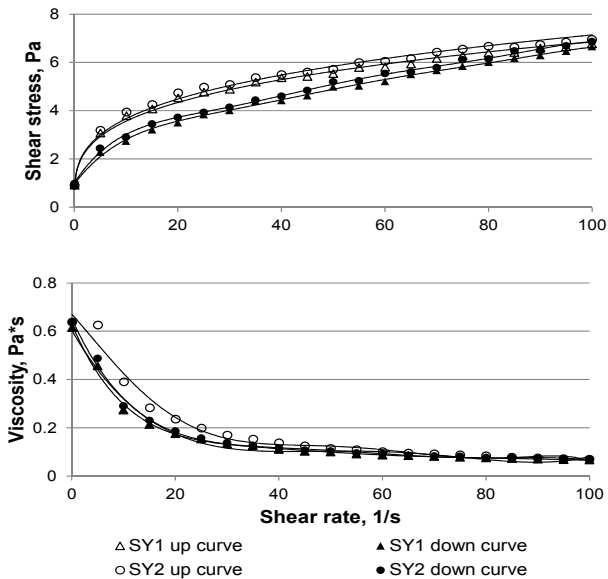oghurt (1.5% fat w/w); SY – Skimmed yoghurt (0.1% fat w/w); SY_1 – Skimmed yoghurt enriched with 2% skim milk powder and 2% lactose (w/v); SY_2 - Skimmed yoghurt enriched with 3% skim milk powder and 3% lactose (w/v).

The sourish taste of the yogurt was masked by the fat content and lactose addition, being perceived with similar intensity for FY, NY and SY samples ($p > 0.05$). The SY_1 with SY_2 samples registered the lowest scores with no significant differences between values ($p > 0.05$), but with significant differences with respect to FY, NY and SY samples ($p < 0.01$).

The flavour of the fat containing yogurt samples (FY and NY) was better appreciated, whereas the addition of lactose and skim milk powder had no contribution to flavour attribute.

Regarding mouth thickness, the skimmed yoghurt got the lowest appreciation scores. The addition of non-fat solids to the skimmed milk before lactic fermentation led, to some extent, to the improvement of the yogurt thickness.

When considering the global perception, the yogurt samples with fat in composition (FY and NY) the most appreciated by the panelists, while with the skimmed yoghurt sample got the lowest scores (Figure 4). The same conclusion was drawn based on the real score values estimated by taking into account the importance coefficient of every attribute as seen in Figure 5.
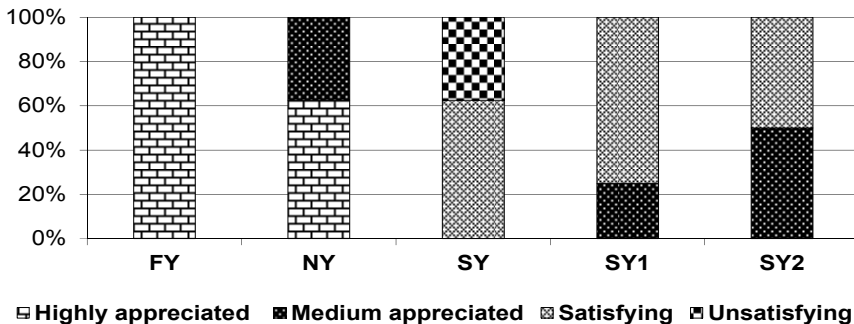
Figure 5. Global perception of yoghurt samples as indicated by importance coefficient of every assessed sensory attribute.

CONCLUSIONS

Yogurt samples with different fat contents were obtained through fermentation with EPS producing lactic acid bacteria. Rheological tests showed that all yoghurt samples behave like viscoelastic gels. We appreciate that the interactions between EPS released by lactic acid bacteria and other macromolecular components, such as proteins, allowed formation of viscoelastic network with proper flow characteristics. Better

rheological properties were obtained in case of the yogurts with high fat levels. When considering the skimmed yoghurt, increasing the total solids level proved to be an appropriate method of improving the rheological characteristics of the gel. This observation is in good agreement with sensorial appreciation showing that increasing the non-fat solid content of yogurts support denser and firmer gel structure formation. However, sensorial characteristics were better appreciated in case of the samples with 3.5% and 1.5% fat with respect to the skimmed yogurts.

EXPERIMENTAL SECTION

Yoghurt preparation. Commercial UHT treated milk with different fat contents was used for yogurt preparation: whole milk with 3.5% (w/w) fat and 11.82% (w/w) total solids; partially skim milk with 1.5% (w/w) fat and 10.67 % (w/w) total solids and skim milk with 0.1% (w/w) fat and 9.02% (w/w) total solids.

In order to increase the total solids content, the skim milk was fortified with skim milk powder (2 and 3% w/w) and lactose (2 and 3% w/w). The addition of lactose to the milk is favorable for lactic acid bacteria growth [21]. Set yoghurt was produced using mixed culture of thermophilic lactic acid bacteria containing *Streptococcus termophilus* and *Lactobacillus delbrueckii* ssp. *Bulgaricus* (commercial name YF-L 812, Chr. Hansen). This lactic acid bacteria mixture was shown previously to produce EPS in yoghurt samples [21].

The milk was first tempered at 45°C and afterwards was inoculated with the starter culture according to producer specifications. The inoculated milk was immediately poured in plastic containers and was incubated at 43°C until pH 4.6 was reached. Yoghurt samples were subsequently cooled and were stored in refrigeration at 4°C before analysis. All samples were obtained in triplicate.

Rheological analyses. The rheological behaviour of the yogurt samples was determined after 24h of storage 4°C with an AR2000ex rheometer (TA Instruments, Ltd). Analyses were performed using a cone - plate geometry with 40 mm in diameter and 2° cone angle, and a gap of 1000 µm. Prior to analyses yoghurt samples were stirred in order to homogenize composition with released whey if any.

In order to observe flow behaviour of tested samples, a stepped flow step was applied and shear rate was increased from 0.1 to 100 s^{-1}, and then decreased back to 0.1 s^{-1}. Temperature was set to 20 ^{o}C. Tests were performed in triplicate and mean values were represented in graphs.

The viscoelastic domain was determined by performing strain sweep test and a critical strain of 5% was estimated. The frequency sweep

tests were further performed at a controlled strain of 0.5% and the elastic modulus (G') and viscous modulus (G'') were monitored while increasing the oscillation frequency from 0.1 to 2 Hz.

The rheology data were analyzed using TA Rheology Advantage Data Analysis Software V 4.8.3 and the mathematical models of Power Low and Bingham were used to fit the experimental results.

Sensory evaluation. The sensory analysis of the yoghurt was performed after 24 hours of storage at 4°C by a panel consisting on twenty trained assessors, equally distributed by gender, aged between 20 to 30 years in proportion of 70 % the other 30 % were aged between 30 to 40 years old. The samples (~100 mL of yoghurt) were purred in plastic cups and tempered at 10÷12 °C before testing.

The ten attributes assessed are listed and defined in Table 2. Products quality was appreciated by a 5 points system. The Importance Coefficients (Table 2) for each attribute was decided based on the relevance to the global quality of the yogurt. The real/final sensory score was estimated by multiplying the score of each attribute by its importance coefficient [27]. The importance coefficient is established individually, depending on the research aim so that the most significant characteristics for the study could be followed.

Table 2. Attributes used by the sensory panel for describing the sensory properties of yoghurt samples

Attribute	Definition	Importance coefficient
Odor	Identification of characteristic smell or any flavour defects as unspecific, foreign or masked odor	0.05
Flavour	General evaluation of flavour and identification of any defects	0.05
Colour	Colour evaluation (white, whitish, yellow or yellowish)	0.1
Syneresis	Visual observation of separated whey on the surface of the set yoghurt	0.15
Gel firmness	Estimation of gel fragility, hardness, gelatinous or gumminess structure	0.15
Consistency	Evaluation of gel viscosity by stirring the yoghurt sample with a spoon	0.15
Sourish taste	Evaluation of the sour taste intensity	0.05
Sweetness	Evaluation of the sweet taste intensity	0.05
Mouth thickness	Perceived as the degree of thickness when swallowing the yogurt at normal-high eating rate	0.1
Global perception	Global appreciation of the product considering the above mentioned attributes	0.15

REFERENCES

1. G. Campbell-Platt, *Food Research International*, **1994**, *27(3)*, 253.
2. S. Otles, O. Cagindi, *Pakistan Journal of Nutrition*, **2003**, *2(2)*, 54.
3. J. M. Aguilera, *Food Technology*, **2000**, *11*, 56.
4. I. Sodini, F. Remeuf, S. Haddad, G. Corrieu, *Critical reviews in food science and nutrition*, **2004**, *44(2)*, 113.
5. A. Skriver, J. Holstborg, K. B. Qvist, *Journal of Dairy Research*, **1999**, *66*, 609.
6. M. N. Oliveira, I. Sodini, F. Remeuf, G. Corrieu, *International Dairy Journal*, **2001**, *11(11)*, 935.
7. L. Ramchandran, N. P. Shah, *LWT-Food Science and Technology*, **2010**, *43(5)*, 819.
8. G. M. Costin, T. Florea, *BIIL*, **2004**, *19 (1)*,1.
9. L. De Vuyst, F. De Vin, F. Vaningelgem, B. Degeest, *International Dairy Journal*, **2001**, *11*, 687.
10. P. Raus-Mediedo, J. Hugenholtz, P. Zoon, *International Dairy Journal*, **2002**, *12*, 163.
11. A. Laws, Y. Gu, V. Marshall, *Biotechnology Advances*, **2001**, *19*, 597.
12. P. A. Laws, M. V. Marshall, *International Dairy Journal*, **2001**, *11*, 709.
13. A. D. Welman, I. S. Maddox, *Trends in biotechnology*, **2003**, *21(6)*, 269.
14. L. De Vuyst, B. Degeest, *FEMS Microbiology Reviews*, **1999**, *23*, 153.
15. T. Amatayakul, A. L. Halmos, F. Sherkat, N. P. Shah, *International Dairy Journal*, **2006**, *16*, 40.
16. Y. S. Bhullar, M. A. Uddin, N. P. Shah, *Milchwissenschaft*, **2002**, *57(6)*, 329.
17. A. N. Hassan, J. F. Frank, K. A. Schmidt, S. I. Shalabi, *Journal of Dairy Science*, **1996**, *79(12)*, 2098.
18. V. M. Marshall, H. L. Rawson, *International Journal of Food Science and Technology*, **1999**, *34*,137.
19. A. K. Patel, P.Michaud, R. R. Singhania, C. R. Soccol, A. Pandey, *Food Technology and Biotechnology*, **2010**, *48(4)*, 451.
20. J. R. Broadbent, D. J. McMathon, D. L. Welker, C. J. Oberg, S. Moineau, *Journal of Dairy Science*, **2003**, *86*, 407.
21. I. Vasilean, R. Segal, A. Vasile, *Annals of the University Dunarea de Jos of Galati-Fascicle VI: Food Technology*, **2011**, *35(1)*, 92.
22. T. Van Vliet, H. J. M. Van Dijk, P. Zoon, P. Walstra, *Colloid and Polymer Science*, **1991**, *269(6)*, 620.
23. C. G. Biliaderis, M. M. Khan, G. Blank, *International Dairy Journal*, **1992**, *2(5)*, 311.
24. C. Wacher-Rodarte, M. V. Galvan, A. Farres, F. Gallardo, V. M. Marshall, M. Garcia-Garibay, *Journal of Dairy Research*, **1993**, *60(02)*, 247.
25. Y. Peng, M. Serra, D. S. Horne, J. A. Lucey, *Journal of Food Science*, **2009**, *74*, 666.
26. W. J. Lee, J. A. Lucey, *Asian-Aust. Journal of Animal Science*, **2010**, *23(9)*, 1127.
27. M. Bulancea, G. Iordachescu, "*Textura produselor alimentare*", Ed. Aius, Craiova, **2006**.

ASSESSMENTS OF ELECTRONIC PROPERTIES IN PHENOTHIAZINE CARBALDEHYDE REGIOISOMERS SERIES

**BALASZ BREM[a], EMESE GAL[a], TÁMAS LOVÁSZ[a],
CASTELIA CRISTEA[a,*], LUIZA GĂINĂ[a] AND
LUMINIŢA SILAGHI-DUMITRESCU[a]**

ABSTRACT. Regioselective C-formylation of phenothiazine using N,N-dimethylformamide is revisited and optimized synthesis of 10-methyl-10*H*phenothiazine-carbaldehyde regioisomers are presented. Recorded NMR and UV-Vis spectroscopic data are compared in the regioisomers series. Fluorescence emissions in the visible range are described. Density Functional Theory (DFT) computational results regarding structural characteristics in the regioisomers series are supporting the recorded spectral properties.

Keywords: Phenothiazine carbaldehyde, UV-Vis absorption, Fluorescence, DFT.

INTRODUCTION

Phenothiazine is a redox-active compound well known as a potent pharmacophoric group for medicinal applications [1], but also a suitable building block for new materials mainly based on UV-Vis absorption and fluorescence emission properties modulated by carrefully selected substitution patterns [2]. In this context, phenothiazine carbaldehide derivatives appear as versatile substrates for extending the functionalization of the parent heterocyclic unit. Literature survey indicate the phenothiazine-3-carbaldehyde as the most widely employed precursor mainly because it can be readily prepared by rather simple Vilsmeyer [3], or Duff [4] formylation procedures. Even though the preparation of phenothiazine-1-, 2-, and 4-carbaldehyde regioisomers was also previously reported, these regioisomers were less employed as precursors for further functionalization of phenothiazine unit.

---

[a] *"Babes-Bolyai" University, Faculty of Chemistry and Chemical Engineering, RO-400028, Cluj-Napoca, Romania*
[*] *Corresponding author: castelia@chem.ubbcluj.ro*

The Vilsmeier-Haack formylation of a phenothiazine substrate is based on aromatic electrophilic substitution reaction directed by the electron donor effect of the heterocyclic N atom mainly increasing the electron density in the *para* position of the adjacent aromatic ring. This procedure was first applied to 10-methyl-phenothiazine substrate and generated 3-formyl-10-methyl-phenothiazine in up to 50% yields [5]. Convenient formylation conditions were described for the preparation of 3-formyl-10-methyl-phenothiazine and 3,7-diformyl-10-methyl-phenothiazine using N,N-dimethylformamide (DMF) and phosphorous(V)oxychloride for generating the electrophile [6]. A modified procedure gave 97% yield 10-ethyl-3-formyl-phenothiazine when using chloroform solvent [7]

The microwaves assisted Duff formylation procedure using urotropine in acetic acid showed regioselectivity for position 3 and gave satisfactory results in the formylation of both phenothiazine and 10-methyl-phenothiazine substrates with less environmental burden [8].

Lithiation and subsequent formylation using DMF as electrophile is another method designated to the preparation of heteroaromatic aldehydes bearing a formyl group adjacent to the heteroatom. When subjected to this procedure, phenothiazine may generate both C^1 (*ortho* to the N directing atom) and C^4 (*ortho* to the S directing atom) substitution products [9]. However a preference for substitution in the position *ortho* to the heterocyclic nitrogen atom was observed in the case of 10*H*-phenothiazine. A double lithiation experiment indicate the C^1 substited product in the presence of DMF, but other electrophiles such as acetyl chloride gave the N substited product [10]. An ingenious two step procedure was developed based on the formation of an unstable carbamate intermediate which favorize C^1-lithiation and generate the electrophilic substitution product exclusively at the carbon center [11] When sterically hindred N-methylformanilide was employed, 4-formyl-phenothiazine was preferentially formed [12]. 10-alkyl-phenothiazines appeared to undergo lithiation at position C^4 when using butyl lithium in the presence of TMEDA [13]. This strategy can be applied for the introduction of a formyl group at position C^3 of the phenothiazine core only based on a halogen-litium exchange reaction applied to a halogenated phenothiazine substrate followed by subsequent treatment with DMF electrophyle [14].

In this work, the regioselective C-formylation of phenothiazine substrate in the presence of DMF was achieved by modulating the chemical reactivity of the heterocycle towards electrophilic substitution and optimal experimental conditions are described. The electronic properties of the prepared C-formyl-N-methyl-phenothiazine regioisomers were discussed based on NMR and UV-Vis absorption/emission spectroscopic data recorded in solution. Theoretical computational data were employed in supporting the fine tunable electronic properties in the regioisomers series.

RESULTS AND DISCUSSIONS

Synthesis of 10-Methyl-phenothiazine carbaldehyde regioisomers

10-Methyl-10*H*phenothiazine-1-, 2- and 4-carbaldehyde regioisomers **1, 2, 4** were successfully obtained by a two-steps procedure involving a phenothiazine-lithium intermediate further trapped by the treatment with dimethylformamide (DMF) electrophile. A careful selection of the reaction conditions (substrate, lithium reagent, reaction temperature) was required in order to obtain satisfactory yields of each target regioisomer (scheme 1). Thus, when starting with N-methyl-phenothiazine substrate and *n*-BuLi reagent a hydrogen lithium exchange occurred at 0 °C preferentially under the *orto* directing effect of the heterocyclic sulfur atom (affording phenothiazine-4-carbaldehyde **4** in 43% yields). At 0 °C the nitrogen *orto* directing effect was prevalent in the 10H-phenothiazine substrate and the sterically hindered 10-methyl-phenothiazine-1-carbaldehyde **1** was obtained in 25% yield after a subsequent alkylation of the 1-formyl-10Hphenothiazine intermediate. The preparation of phenothiazine 2-carbaldehyde **2** was best achieved by subjecting 2-chloro-10-methyl-phenothiazine substrate to halogen-lithium exchange using metallic lithium under sonochemical conditions in the presence of DMF. 10-Methyl-10*H*phenothiazine-3-carbaldehyde was obtained in 80% yields by an adapted Vilsmeyer procedure using 1,2-dichloroethane solvent.

R=H,   X=H,   i) *n*BuLi/Et$_2$O 0°C,
                     ii) NaH/THF, H$_3$C-I   **1** *1*-CHO 22%
R=Me, X= Cl   i) Li/Et$_2$O,))), 30 °C, 6h   **2** *2*-CHO 43%
R=Me, X=H   i) POCl$_3$/DCE, 90 °C, 6h   **3** *3*-CHO 80%
R=Me, X=H   i) TMEDA/*n*Bu-Li,r.t.,20 min   **4** *4*-CHO   61%
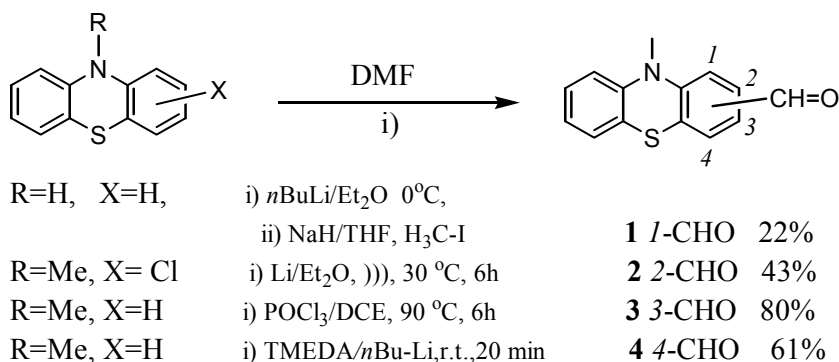
Scheme 1. *Regioselective C-formylation of 10Hphenothiazine derivatives.*

The recorded ^{1}H-NMR spectra are collectively presented in figure 1 for regioisomers **1-4**, thus giving the possibility of inspecting the key signals and comparing the deshielding effects induced by electronic conjugation, steric hindrance and magnetic anisotropy of the aldehyde group.
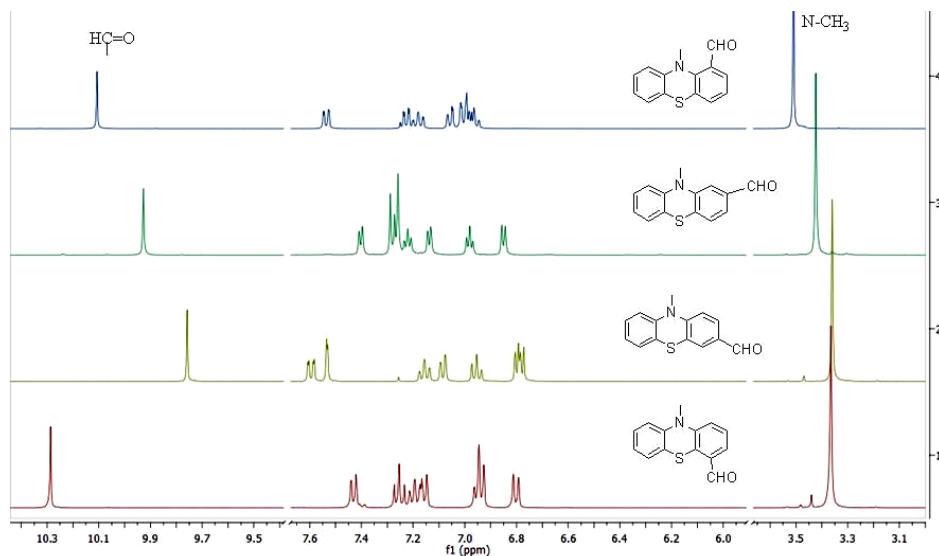
Figure 1. 400 MHz ^{1}H-NMR spectra of 10-methyl-10-*H*phenothiazine-carbaldehyde regioisomers in CDCl$_3$ (from top to bottom: **1, 2, 3, 4**) in CDCl$_3$

Electronic properties

The molecular structures of the regioisomesr **1-4** have been studied by using density functional theory. The energies corresponding to the optimized geometries (E) in ground states and frontier molecular orbitals (E_{HOMO}, E_{LUMO}) were computed at the using Spartan programme [15] and the results are presented in Table 1.

Taking into consideration the calculated E values (Table 1) the stability of regioisomers **1-4** may be correlated to the substitution pattern of the phenothiazine unit and falls in the order: phenothiazin-1-< 4-< 2-< 3-yl in concordance with a steric hindrance in positions 1 of the heterocycle and favourable extended n-π conjugation in position 2, or 3 respectively.

The frontier molecular orbital plots presented in figure 2 show a participation to the HOMO of all the atoms joint in the heterocyclic system, while LUMO appears localized on the formyl substituent and its adjacent benzene ring with a selective participation of the heteroatoms according to the substitution pattern (N atomic orbitals participates to LUMO in the case of **1** and **3**, while S atomic orbitals participates to LUMO in the case of **2** and **4** regioisomers).
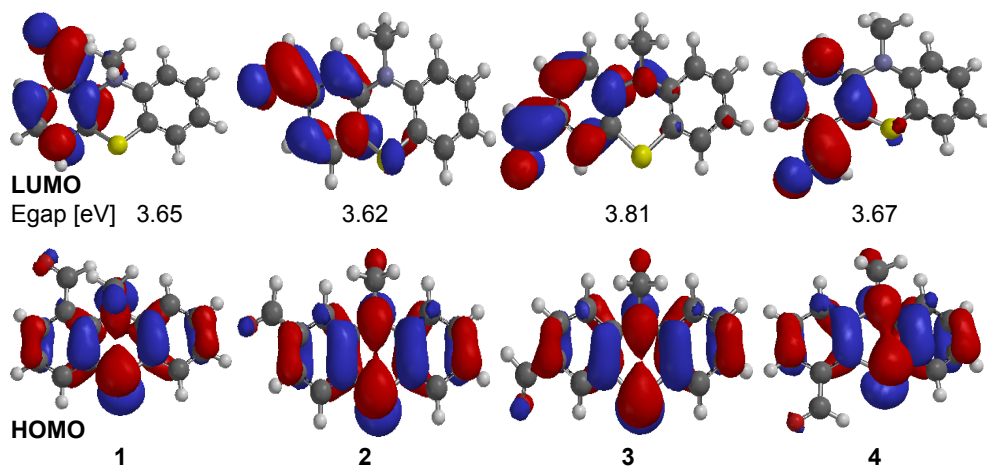
Figure 2. Frontier molecular orbital plots of
10-methyl-phenothiazine-carbaldehyde regioisomers

Each phenothiazine carbaldehyde **1-4** show two absorption bands, situated in the UV region (Table 1) with larger extinction coefficients for the higher frequency band which can be assigned to allowed π→π* transitions involving the excitation of the electrons from the aromatic rings; the forbidden n→π* transitions may be responsible for the low intensity band situated at longer wavelengths. These absorption bands appear slightly affected by the position of the auxochrome formyl group, except for the case of **3** which reveals a hypsochromic shift of aprox. 30 nm for the band situated at longer wavelength (Table 1); in agreement with this experimental evidence **3** is also characterized by the largest computed HOMO-LUMO energy gap of the series (figure 2).

Upon excitation with either of the two UV absorption maxima, each regioisomer **1-4** exhibited emission bands in solution with maxima situated in the visible region (figure 3). A correlation between the position of the emission band and the substitution pattern of the heterocycle indicate a red shift of the emission maxima according to the auxochrome position in the following order: phenothiazine-1yl-<2-yl<-3-yl<-4-yl-carbaldehyde. Larger Stokes shift values are noticeable in the case of **1** and **3** which can be correlated to geometrical changes upon excitation, from a non-planar ground-state of the phenothiazine moiety to a largely planarized excited state [16] and corroborated with computational results regarding LUMO electron distribution (figure 2).
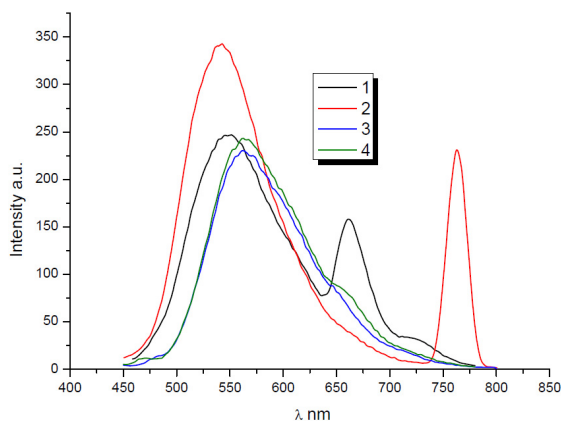
Figure 3. Fluorescence emission spectra of 10-methyl-10*H*phenothiazine carbaldehyde regioisomers **1-4** in 0.02mM in DCM.

Table 1. Electronic properties of phenothiazine carbaldehyde **1-4** determined by UV-Vis absorption/emission spectroscopy 10^{-4} M in DCM and molecular modelling

Cpd	$\lambda_{max, abs}$ (ε) [nm]	$\lambda_{max, em}$ [nm]	Stokes shift [cm^{-1}]	E_{HOMO} [eV]	E_{LUMO} [eV]	E [hartree]
1	277 (54400)	543	9400	-5.25	-1.60	-1068.264
	411 (3180)	670				
2	282 (109200)	551,	5700	-5.35	-1.73	-1068.274
	418 (4730)	730				
3	282 (60950)	567	8600	-5.37	-1.56	-1068.275
	381 (5900)					
4	277 (58600)	571	6300	-5.37	-1.70	-1068.269
	419 (6170)					

CONCLUSIONS

Adequate experimental conditions for regioselective C-formylation of 10-methyl-10*H*-phenothiazine substrate were described.

Evidences of photophysical properties of phenothiazine carbaldehyde regioisomers were brought by means of UV-Vis absorption/emission spectroscopy which indicated fine tunable absorptions in the UV region and fluorescence emission in visible region according to the position of the formyl auxochrome.

EXPERIMENTAL SECTION

10-methyl-10Hphenothiazin-1-carbaldehyde (1).

a) To a solution of phenothiazine (4 g, 20 mmol) in 150 ml of dry ethyl ether *n*-BuLi (31 ml 25 mmol, 1.6 M in hexane) was added under argon atmosphere at 0°C. The reaction mixture was stirred 10 hours at room temperature and then DMF (1.5 g, 20 mmol, 0.944 g/cm³) was added drop wise at 0°C. After it was stirred one hour at room temperature, the reaction mixture was hydrolyzed with ice cold aqueous HCl 0.5 N. The mixture was shaken vigorously and the organic layer was then separated. The aqueous phase was extracted three times with ethyl ether (50 ml). The organic phases were collected, washed with water and dryed ower magnesium sulfate. After the evaporation of the solvent under vacuum, the red viscous residue was purified by column chromatography (silica gel, hexane/ethyl acetate= 10/1) to give 10Hphenothiazin-1-carbaldehyde 1.14g (25%) m.p.= 81-82°C, (lit. 81-83°C [12])

b) To a suspension of NaH (0.174 g, 4.4 mmol) in dry THF (20 ml) was added under continuous stirring, a solution of 10H-phenothiazine-1-carbaldehyde (1g 4.4 mmol) in 10 ml dry THF (under inert atmosphere). The mixture was stirred for 4h, at 0-5°C. To the obtained solution, was added methyl iodide (0.62g, 4.4 mmol 2.28 g/cm³) and the mixture was stirred at room temperature for 10 hours. The reaction mixture was treated with 100 ml water and extracted three times with ethyl ether (30ml). The organic phase was collected and dryed over magnesium sulfate. After evaporation of the organic solvent the crude product was purified by column chromatography (silica gel, hexane/ethyl acetate= 10/1) to give (0.95 g 90%) yellow powder m.p.= 75-77°C, (lit. 70-71°C [17])

δ_H (300 MHz, CDCl$_3$) 3.62 (3H, s, CH$_3$), 6.85 (1H, d, *J* 7.8 Hz, H$_9$), 7.00 (1H, td, *J* 7.5, 1.9 Hz, H$_7$), 7.07-7.13 (2H, m, H$_6$, H$_8$), 7.14 (1H, dd, *J* 2.0, 7.8 Hz, H$_4$,), 7.28 (1H, t, *J* 7.8 Hz, H$_3$,), 7.43 (1H, dd, *J* 2.0, 7.6 Hz, H$_2$), 9.56 (1H, s, CHO); δ_C (75 MHz, CDCl$_3$) 43.9, 118.4, 122.6, 124.1, 125.6, 126.5, 126.6, 127.6, 130.6, 131.1, 131.3, 146.4, 146.8, 189.7; MS m/z (EI, 70eV) 241 (M$^+$).

10-methyl-10Hphenothiazin-2-carbaldehyde (2).

10-methyl-2-chloro-10*H*phenothiazine (247 mg, 1 mmol) was solved in dry diethyl ether (25ml) under inert atmosphere, metallic lithium (7 mg, mmol) and dry dimethylformamide (146 mL, 2 mmol) were added. The reaction mixture was sonicated in an ultrasonic bath at 30°C for 6h. The mixture was poured into ice (50 g), and then extracted with dichloromethane and the two layers were separated; after evaporation of the organic solvent the crude product was purified by column chromatography with toluene as eluent. Yellow-brown powder (103.6 mg, 43%), mp 69-71°C, (lit bp 220°C/3 torr [18]);

δ_H (600 MHz, CDCl$_3$) 3.39 (3H, s, CH$_3$), 6.82 (1H, d, *J* 8.1Hz, H$_9$), 6.95 (1H, t, *J* 7.4Hz, H$_7$), 7.11 (1H, d, *J* 7.5Hz, H$_6$), 7.19 (1H, t, *J* 7.4 Hz, H$_8$), 7.23-7.24 (2H, m, H$_1$, H$_4$), 7.37 (1H, d, *J* 7.6 Hz, H$_3$), 9.89 (s, 1H, CHO); δ_C (150 MHz) 35.5, 112.2, 114.6, 121.9, 123.0, 125.8, 127.2, 128.1(2C), 132.6, 135.9, 144.9, 146.4, 191.6; MS m/z (EI, 70eV), 241 (M$^{+\cdot}$).

10-methyl-10Hphenothiazin-3-carbaldehyde (3)

DMF (24 mmol) was cooled to 0ºC, then POCl$_3$ (24 mmol) was added drop wise and the mixture was stirred at room temperature for one hour. A solution of 10-methyl-10*H*-phenothiazine (20 mmol) dissolved in 1,2-dichloroethane (30 ml) was added slowly and the reaction mixture was stirred at 90°C for 6 hours. After cooling, an ice cold saturated solution of sodium acetate (30 ml) was added drop wise to the reaction mixture. The product was extracted with ethyl acetate, and the extract was dried over magnesium sulfate and then concentrated to dryness.

Yellow precipitate recrystallized from toluene (3.85g, 80%), mp 88°C lit 81-82 [19]; δ_H (600 MHz, CDCl$_3$) 3.36 (s, 3H), 6.78 (1H, d, *J* 8.0 Hz, H$_9$), 6.80 (1H, d, *J* 8.4 Hz, H$_1$), 6.95 (1H, t, *J* 8.4 Hz, H$_7$), 7.08 (1H, dd, *J* 1.4, 7.6 Hz, H$_6$), 7.15 (1H, td, *J* 1.4, 8.4 Hz, H$_8$),7.53 (1H, d, *J* 2 Hz, H$_4$), 7.60 (1H, dd, *J* 2.0, 8.4 Hz, H$_2$), 9.76 (1H, s, CHO); δ_C (150 MHz, CDCl$_3$) 35.8, 113.7, 114.8, 122.4, 123.6 123.8, 127.2, 127.8, 130.5, 131.1, 144.0, 150.9, 190.0; m/z (EI, 70eV) 241 (M$^{+\cdot}$).

10-methyl-10Hphenothiazin-4-carbaldehyde (4)

10-methylphenothiazine (2 g, 8.8 mmol) was dissolved in dry ethyl ether (50 cm^3). After 10 min under argon atmosphere, TMEDA (3.32 cm^3, 22 mmol) was added followed by *n*-butyllithium (13.8 cm^3 of a 1.6 M solution in hexane, 22 mmol). The mixture was kept at room temperature for 0.5 h, then cooled at 0ºC before dry DMF (1.6 g, 0.948 g/cm^3, 22 mmol) was added. The mixture was stirred for 20 min at room temperature. The reaction mixture was poured into cooled aqueous HCl (4.5% w/v; 180 cm^3) and further stired for 30 min. The organic phase was separated and the aqueous phase was extracted with chloroform (3x100 cm^3). The combined organic phases were dried and evaporated to give an orange oil. The crude product was subjected to column chromatography (silica gel, hexane/ethyl acetate=8/1), yellow crystals (1.38 g, 61%) mp 110-112°C (lit. 110-111ºC [20])

Yellow crystals, (0.97g, 43%), mp 110-112°C (lit[13], 110-111°C); δ_H (600 MHz, CDCl$_3$) δ 3.46 (s, 3H, CH$_3$), 6.89 (1H, d, *J* 8.1 Hz, H$_9$), 6.95 (1H, t, *J* 7.8 Hz, H$_7$), 7.03 (1H, d, *J* 7.8 Hz, H$_1$), 7.17-7.21 (2H, m, H$_6$, H$_8$), 7.28 (1H, t, *J* 7.8 Hz, H$_2$), 10.31 (1H, s, CHO); δ_C (150 MHz, CDCl$_3$) 36.5, 115.3, 119.8, 122.8, 123.6, 124.5, 126.7, 127.7, 127.9, 130.4, 133.0, 145.2, 145.9, 190.4. m/z (EI, 70eV) 241 (M$^{+\cdot}$), 226.

AKNOWLEDGMENTS

REFERENCES

1. K. Pluta, B. Morak-Młodawska, M Jeleń, *Eur. J. Med. Chem*., **2011**, *46*, 3179.
2. a) C. Garcia, R. Oyola, L.E. Pinero, R. Arce, J. Silva, V. Sanchez, *J. Phys. Chem. A.* **2005**, *109*, 3360; b) Meyer T., Ogermann D., Pankrath A., Kleinermanns K., Müller T.J.J., *J. Org. Chem.* **2012**, *77*, 3704; c) Zhang X., Qiu X., Lu R., Zhou H., Xue P., Liu X., *Talanta*, **2010**, *82*,1943.
3. A. Vilsmeier, A. Haak, *Ber. Dtsch. Chem. Ges.*, **1927**, *60(1)*, 119.
4. J.C. Duff, *J. Chem. Soc*., **1941**, 547.
5. Ng.Ph. Buu-Hoï, N.G. Hoán, *J. Chem. Soc.*, **1951**, 1834.
6. V. Fărcăşan, I. Oprean, C. Bodea, *Rev. Roum. Chim*., **1968**, *13*, 647; (b) V. Fărcăşan, I. Oprean, C. Bodea, *Rev. Roum. Chim*., **1970**, *15*, 1433.
7. Y. Tian, M. Zhang, X. Yu, G. Xu, Y. Ren, J. Yang, J. Wu, X. Zhang, X. Tao, S. Zhang, M. Jiang, *Chem. Phys. Lett.,* **2004**, *388*, 325.
8. L. Gaina, D. Porumb, I. Silaghi-Dumitrescu, C. Cristea, L. Silaghi-Dumitrescu, *Can. J. Chem*., **2010**, *88*(1), 42.
9. a) G. Gauquil, A. Cassadavall, E. Cassadavall, *Bull. Soc. Chim. Fr.*, **1960**, 1049; b) H.W. Gschwend, H.R. Rodriguez, *Org. React.*, **1979**, *26*, 47; c) A. Halberg, A.R. Martin, *J. Heterocycl. Chem.*, **1982**, *19*, 433; d) A. Halberg, A.R. Martin, *Synth. Commun.*, **1983**, *13*, 467; e) A. Halberg, I. Al-Showaier, A.R. Martin, *J. Heterocycl. Chem.*, **1983**, *20*, 1435.
10. J. Mortier, T.H. Nguyen, D. Tilly, A.S. Castanet, *ARKIVOC*, **2007**, *vi*, 47.
11. A.R. Katritzky, L.M. Vazquez de Miguel, G.W. Rewcastle, *Synthesis*, **1988**, *3*, 215.
12. A. Hallberg, A. Martin, *J. Heterocyclic Chem.*, **1982**, *19*, 433.
13. a) H. Gilman, P.R. Van Ess, D.A. Shirley, *J. Am. Chem. Soc.*, **1944**, *66*, 1214; b) R.D. Nelson, *Iowa State Coll. J. Sci.*, **1953**, *27*, 229.
14. S. Ebdrup, *J. Chem. Soc., Perkin Trans.,* **1998**, *1,* 1147.
15. SPARTAN 06 Wavefunction, Inc. Irvine, CA.
16. L. Yang, J.K. Feng, A.M. Ren, *J. Org. Chem.,* **2005**, *70*, 5987.
17. G. Cerbai, L.Turbanti, *Bollettino chimico farmaceutico*, **1969**, *108* (7), 433.
18. G. Cauquil, A. Casadavall, *Bull. Soc. Chim.Fr.*, **1955**, 768.
19. H. Spreitzer, M. Scholz, G. Gescheidt, J. Daub, *Liebigs Annales*, **1996**, *12*, 2069.
20. J. Bergman, L. Renstrom, B. Sjoberg, *Tetrahedron,* **1980**, *36* (17), 2505.

DIRECT AND SIMULTANEOUS QUANTIFICATION OF ATORVASTATIN AND AMLODIPINE IN TABLETS BY NIR SPECTROSCOPY

**ANDREEA LOREDANA VONICA-GLIGOR[a,b,c],
TIBOR CASIAN[a], ANDRA REZNEK[a], IOAN TOMUȚĂ[a*],
FELICIA GLIGOR[b]**

ABSTRACT. Near infrared spectroscopy (NIRS) is a technique widely used for direct and non-destructive analysis of solid samples. A NIRS method for the simultaneous quantification of atorvastatin and amlodipine in fixed-dose combination tablets was developed and fully validated. The PLS calibration model was developed based on the 26 samples prepared according to a D-optimal experimental design with 2 factors and 5 levels. The best predictive model for atorvastatin was developed using standard normal variate pre-processing method, 7 PLS factors; the best predictive model for amlodipine was developed using first derivate followed by standard normal variate pre-processing method and 7 PLS factors. The method was validated in terms of linearity, trueness, precision and accuracy. The validation results show that the method is reproducible, precise and has good accuracy and linearity profiles. Furthermore, comparative data obtained on independent samples shows no statistical difference ($p > 0.05$) between the results predicted by the NIRS method and the values obtained using HPLC reference method. So, NIRS based on PLS multivariate calibration could be a suitable tool for the non-destructive, direct and simultaneous prediction of the chemical composition of a fixed-dose combination that includes two APIs in a single tablet and is helpful in achieving the goals of Process Analytical Technology (PAT).

---

[a] *University of Medicine and Pharmacy Iuliu Haţieganu, 41 V. Babeş str., RO-400023, Cluj-Napoca, Romania*
[b] *Lucian Blaga University, 2A L. Blaga str., RO-550169, Sibiu, Romania*
[c] *S.C. Polipharma INDUSTRIES, 156 Alba Iulia str., RO-550052, Sibiu, Romania*
* Corresponding author: tomutaioan@umfcluj.ro

A. L. VONICA-GLIGOR, T. CASIAN, A. REZNEK, I. TOMUȚĂ, F. GLIGOR

INTRODUCTION

A single-pill combination drug is a fixed-dose combination (FDC) that includes two or more active pharmaceutical ingredients (APIs) combined in a single dosage form. FDC can benefit patients through the potential increase in efficacy and/or a reduced incidence of adverse effects, the convenience in terms of administration and compliance and potentially lower costs of manufacturing compared to the costs of producing separate products administered concurrently [1]. The amlodipine/atorvastatin single pill has been shown to improve patients' achievement of national-guideline-recommended blood pressure and lipid target levels and exhibits a safety profile consistent with its parent compounds. This combination pill is now available in Europe in formulations containing either 5 or 10 mg amlodipine and 10 mg atorvastatin [2,3].The combination is indicated for patients suffering from both high blood pressure and high levels of cholesterol and has had worldwide sales of more than $600 million in 2013.

The manufacturing process typically involves several unit operations, such as blending, granulation, tableting, and coating, all of which can have critical influences on the final quality of the product. Process monitoring is a methodology that guarantees a high-predefined quality standard and offers the possibility to react during the process if any parameters drift from the normal operating range, but it requires quick methods. Process monitoring is the goal of Process Analytical Technology (PAT). PAT is defined by the Food and Drug Administration (FDA) and European Medicines Agency (EMA) as a concept which implies the design and control of pharmaceutical processes through real time measurements of critical process parameters that could affect quality assurance [4,5]. Direct analysis of intact solid dosage forms as whole tablets is considered to be a very important goal for NIRS analysis in the pharmaceutical industry, with increasing needs of on-line or in-line testing for process monitoring according to PAT [6,7].

In the field of APIs quantification in tablets, including fixed-dose combinations, the high performance liquid chromatography (HPLC) technique is widely used due to good selectivity, specificity and linear range [8]. Until now, only HPLC methods were developed and validated for the simultaneous quantification of both APIs (atorvastatin and amlodipine) in fixed-dose combinations [9,10]. However, this requires sample preparation, chromatographic separation of the analytes and takes hours, so therefore it is currently only done off-line [6,7,11]. Near InfraRed Spectroscopy (NIRS) is a non-destructive technique that allows the direct quantification of chemical properties such as the active pharmaceutical ingredients content [6,7,12] or physical characteristics as pharmaceutical properties [13,14] of tablets and powder blends for tableting

[11,15,16]. NIRS can be used to perform quantitative analysis of one, two or more compounds in different matrices, like pharmaceutical powder blends for tableting or tablets. The advantages of the NIRS method are numerous: non-invasive and non-destructive techniques, no sample preparation, high frequency of spectrum acquisition, as well as a large number of molecules which could be quantified [6]. Many papers are reporting the determination of API content in tablets by NIRS methods [12,17], but only a few are focusing on the prediction of two or more APIs and/or excipients in the composition of powder blends or tablets [6,7,18].

The aim of this work was to develop and validate a NIRS method for direct and simultaneous quantification of amlodipine and atorvastatin in tablets, using a direct, fast, non-invasive and non-destructive technique that requires no sample preparation.

RESULTS AND DISCUSSION

The NIR spectra of tablets contain both chemical information related with APIs and excipients contents and physical information related with tablet compaction. Therefore, pre-processing methods and wavelength selection ranges should be carefully chosen to extract the chemical information that is mainly correlated with the APIs concentration, in order to develop robust calibration models.

Spectra investigation

The calibration model was built after recording twenty spectra of each tablet formulation. Overall 520 tablets spectra were recorded and analyzed for the calibration model development (Figure 1). The NIR spectra of pure APIs is also presented (a1 – atorvastatincalcium; b1 – amlodipinebesilate) in the same figure.

Development of calibration models

The development of calibration models for APIs assay is an iterative technique and consisted in checking the predictive ability of several spectral pre-processing methods in association with different spectral regions with high NIR absorbance of the APIs of interest. By applying different spectra pre-processing methods in combination with different spectral regions a large number of models was generated. Among these, the most potentially interesting 6 models for each API were selected and presented in Table 1.

A. L. VONICA-GLIGOR, T. CASIAN, A. REZNEK, I. TOMUȚĂ, F. GLIGOR

Table 1. Statistical parameters and number of principal components for atorvastatincalcium and amlodipinebesilate, without data pre-processing as well as after different spectra pre-processing

Atorvastatincalcium						
Pre-processing method*	none a	SLS b	SNV C	FD d	SLS-4 e	**SNV-4 f**
Spectral range (cm^{-1})**	R1	R1	R1	R1	R4	**R4**
Number of PLS factors	8	7	7	7	7	**7**
R^2	0.9408	0.9411	0.9423	0.9349	0.9586	**0.9588**
RMSECV (% w/w)	0.353	0.352	0.348	0.374	0.295	**0.292**
Bias	-0.00015	-0.00026	0.000301	-0.00010	-0.000477	**-0.00025**
Amlodipinebesilate						
Pre-processing method*	none g	MSC h	SLS i	SNV j	FD+SLS k	**FD+SNV l**
Spectral range (cm^{-1})**	R1	R1	R1	R1	R1	**R1**
Number of PLS factors	9	8	8	8	7	**7**
R^2	0.9675	0.9737	0.9733	0.9738	0.9757	**0.9768**
RMSECV (% w/w)	0.353	0.318	0.320	0.318	0.306	**0.299**
Bias	-0.000073	-0.00074	-0.00054	-0.00034	-0.000592	**-0.000551**
*none-no pre-processing, SLS-straight light substraction, SNV-standard normal variate, FD-first derivate, MSC-multiplicative scattering correction, FD+MSC – first derivative followed by multiplicative scattering correction, FD+SNV – first derivative followed by standard normal variate **R1-Spectra range 1 region: 10000-4200cm^{-1}; R4-Spectra range 4 region: 10000-8270; 7700-7120; 6800-5616; 5400-4243 cm^{-1}.						

In the case of the atorvastatincalciumcalibration, based on the analysis of different calibration models, the models generated using 4 spectra range had the best results. As the R^2 values of the models are very close, this parameter does not allow any clear differentiation between the models. Regarding RMSECV, the (f) model seems to be slightly better than the (b), (c) and (e) models: its RMSECV is the smallest. Thus, (f) was the selected model which was the most fitted for this purpose, and the model candidate for method validation according to current pharmaceutical requirements. The shape of the spectra after pre-processing according to this model is presented in Figure 1, a$_2$. In the case of the amlodipine besilatecalibration, the results look very similar, R^2 values of the models are very close, so the models were selected based on RMSECV values. Regarding RMSECV, the (l) model seems to be slightly better than the (h), (i), (j) or (k) models: its RMSECV is the smallest. The shape of the spectra after pre-processing according to this model is presented in Figure 1, b$_2$. The predictive ability of the chosen models was checked on independent samples in the validation step.
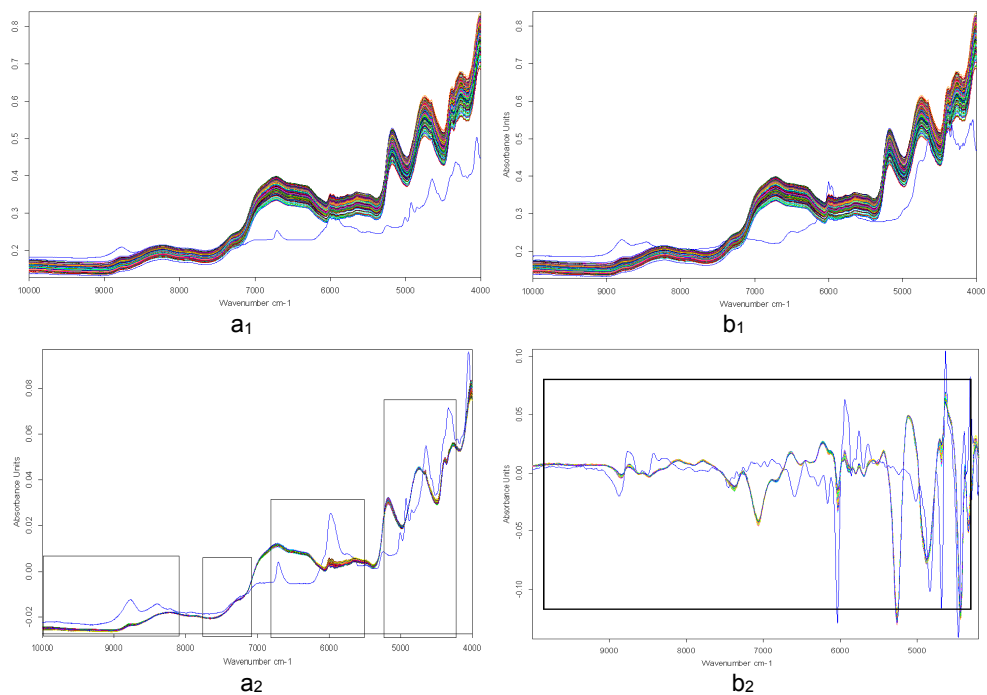
Figure 1. NIR spectra of tablets without preprocessing (a_1, b_1) and pre-processed using SNV-4 method (a_2) for atorvastatin calcium and FD+SNV method for amlodipine besilate (b_2); blue line in a_1, a_2– atorvastatincalcium; blue line in b_1, b_2 - amlodipine besilatespectrum

Validation of the method

Validation was based on ICH Q2 guidance and included linearity, range of application, accuracy, precision (repeatability and intermediate precision), and was done on validation samples. Independent validation samples similar to the calibration samples were prepared at 3 different active content levels (corresponding to 80, 100 and 120% concentrations) of each API (formulation N7, N13, N19, Table 4). The predictive performance of the chosen models was evaluated based on accurate profiles computed on the external validation samples. Accuracy represents the total error concept which is the sum of the trueness (systematic error) and precision (random error) and was evaluated by determining the accuracy profile following the methodology proposed by Hubert *et all* [23, 24]. Table 2 shows the validation results obtained with the developed NIR model (f, SNV-4) for atorvastatincalcium (standard normal variate pre-processing, 7 PLS factors and 4 spectral regions: 10000-8270; 7700-

7120; 6800-5616; 5400-4243cm⁻¹) and model (l, FD+SNV) for amlodipine besilate (first derivative followed by standard normal variate pre-processing, 7 PLS factors and 1 spectral regions: 10000-4200cm⁻¹).

Table 2. Validation results of the NIRS method

for the quantification of **atorvastatin calcium (f, SNV – 4)**

Conc. level (mg/tablet)	Trueness		Precision		Accuracy	
	Relative bias (%)	Recovery (%)	Repeatability (RSD %)	Intermediate precision (RSD %)	Relative tolerance limits (%)	Tolerance limits (mg/tablet)
9.31	-0.568	99.43	1.54	1.65	[-4.50, 3.37]	[8.89, 9.62]
10.34	1.475	101.48	0.99	1.09	[-1.13, 4.08]	[10.22, 10.77]
11.37	-0.091	99.91	0.50	0.80	[-2.57, 2.38]	[11.08, 11.64]

for the quantification of **amlodipine besilate (l, FD+SNV)**

Conc. level (mg/tablet)	Trueness		Precision		Accuracy	
	Relative bias (%)	Recovery (%)	Repeatability (RSD %)	Intermediate precision (RSD %)	Relative tolerance limits (%)	Tolerance limits (mg/tablet)
12.48	-0.823	99.18	1.33	1.49	[-4.48, 2.84]	[11.92, 12.83]
13.87	0.498	100.50	1.03	1.17	[-1.84, 2.83]	[13.61, 14.26]
15.26	-0.257	99.74	1.83	2.11	[-4.40, 3.88]	[14.59, 15.85]

The trueness of the method was evaluated by calculating the relative bias and the recovery. The recovery had very good values (close to 100%) for both APIs at all three concentration levels. The minimum value was 99.18 at a low concentration level of amlodipine besilate and maximum 101.48 at a medium concentration level of atorvastatincalcium. The precision evaluated as repeatability (intra-day precision) and intermediate precision (repeatability over different days) shows also good values for both APIs and at all concentration levels. The best repeatability and intermediate precision values were obtained at medium concentration levels for both APIs.

Figure 2 shows the linearity profile and the accuracy profiles of the NIRS method. The linearity profile of the method was evaluated by plotting the determinate concentration of APIs in validation samples by NIRS method as a function of introduced concentration. The linearity profile of the NIRS method for both APIs is shown in Figure 2 (left).The dashed limits on the graph correspond to the accuracy profile and the dotted curves represent the acceptance limits at ±5% expressed in the concentration unit per tablet. As seen in the Figure 2, the R^2 and the slope values are close to 1 for both APIs, confirming the linearity of the method for the direct and simultaneous quantification of atorvastatin and amlodipine in tablets.

For the accuracy profile the acceptance limits were set at ±5%, as required for the determination of API in pharmaceutical products [13].The β-expectation tolerance limits should be included in the acceptance limits. As seen in Figure 2, the β-expectation tolerance limits are fully included within the ±5% acceptance limits for both APIs, so it can be concluded that the NIRS method provides results with adequate accuracy for simultaneous atorvastatin and amlodipine assay, in tablets without any sample preparation over the range of 9.31-11.37 mg/tablet for atorvastatincalcium and 12.48-15.26 for amlodipinebesilate. The largest relative tolerance limits for atorvastatin calcium (-4.50%, 3.37%) were at the lowest concentration level and the largest relative tolerance limits for amlodipine besilate (-4.40%, 3.88%) were at the highest concentration level. The best accuracy was obtained at the medium concentration level for both APIs.
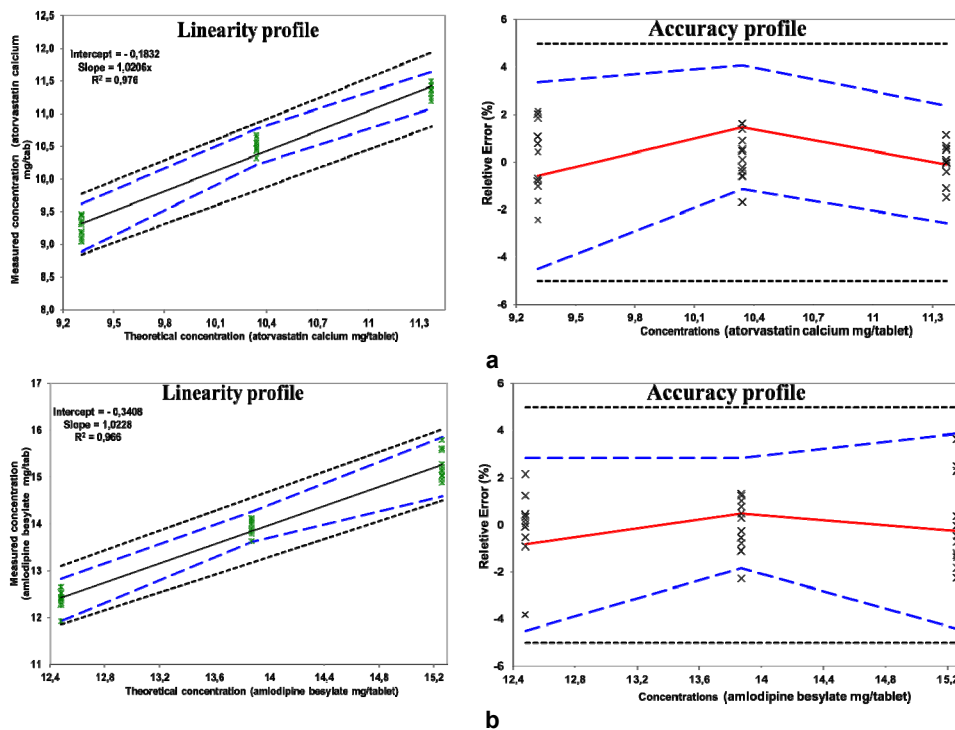
Figure 2. The linearity profiles (left) and accuracy profiles (right) the obtained for the NIRS method of simultaneous quantification of atorvastatincalcium (a) and amlodipine besilate (b).

According to the data presented above in Table 2 and Figure 2, the NIRS method using model (f, SNV-4) for atorvastatincalcium (standard normal variate pre-processing, 7 PLS factors and 4 spectral regions: 10000-8270; 7700-7120; 6800-5616; 5400-4243cm^{-1}) and model (l, FD+SNV) for amlodipine besilate (first derivative followed by standard normal variate pre-processing, 7 PLS factors and 1 spectral region: 10000-4200cm^{-1}) is reproducible, accurate and linear (has an accuracy profile and a linearity profile within the acceptance limits set at ±5%,). So, it can be concluded that the NIRS method is linear, sufficiently precise and accurate for the direct (without any sample preparation) and simultaneous quantification of both APIs (atorvastatin and amlodipine) in tablets.

Application of the method

The results presented in the validation section indicated that the method could be used for the direct and simultaneous determination of atorvastatin and amlodipine content in tablets with active content 10 mg APIs/table (over the range of 9.31-11.37 mg/tablet for atorvastatin as atorvastatin calcium and over the range of 12.48-15.26 for amlodipine as amlodipine besylate). The NIRS method has been applied for the simultaneous quantification of both APIs in 4 control samples of tablet batches containing 10 mg APIs/tablet, strength which is the expected in the tablets available on the market. A reference HPLC method has also been used for APIs assay in the same control samples. The results obtained with the NIRS method and reference HPLC methods are shown in Table 3.

Table 3. Results obtained on control samples by NIRS method and HPLC reference method

Control samples	Atorvastatin			Amlodipine		
	HPLC*	NIRS	Recovery** (%)	HPLC*	NIRS	Recovery** (%)
P1	10.22	10.64	104.15	13.91	13.63	97.95
P2	10.29	10.45	101.56	13.81	14.01	101.43
P3	10.34	10.51	101.65	13.54	13.90	102.71
P4	10.60	10.43	98.39	13.80	14.11	102.24
Mean	10.36	10.51	101.44	13.77	13.91	101.08
SD		0.09			0.21	
t_{exp}		1.519			1.133	
P (type 1 error)		0,179			0.301	
*HPLC reference method ** Calculated as 100 ×NIR/HPLC						

The NIRS predicted values for APIs content in control samples were compared with values obtained by the reference HPLC method, in terms of active content recovery, and the Student t test has been used for comparison of the methods. As presented in Table 3, similar results were obtained by both methods (NIRS and reference HPLC method). The average recovery was 101.44 for atorvastatin and 101.08 for amlodipine. The results did not show any statistical difference (p>0.05) between the results obtained using NIRS method and results obtained using the reference HPLC method.

CONCLUSIONS

In this work a NIRS method was explored for the direct, fast, non-destructive and non-invasive quantitative analysis of two APIs in a fixed-dose combination tablet. The two components were determined simultaneously using pre-processed spectra (standard normal variate, first derivative followed by standard normal variate) together with PLS multivariate calibration. The method was validated in terms of trueness, precision and accuracy, for active contents of 90-100-110%. The validation shows good statistical results and furthermore, application of the method and on real samples similar with the tablets on the marked proved that results obtained with NIRS are similar with those obtained by HPLC, used as reference method.

According to the data presented in this paper, NIRS based on PLS multivariate calibration could to be a suitable tool for non-destructive, direct and simultaneous prediction of the chemical composition of a fixed-dose combination that includes two active pharmaceutical ingredients (atorvastatin and amlodipine) combined in a single dosage form and is helpful in achieving the goals of Process Analytical Technology (PAT).

EXPERIMENTAL SECTION

Materials

Atorvastatin calcium (Hetero, India), amlodipine besylate (Hetero, India), microcrystalline cellulose (JRS Pharma, Germany), calcium carbonate (SPI Pharma, France), sodium croscarmellose (JRS Pharma, Germany), corn starch (Colorcon, UK) silicon dioxide (RohmPharma Polymers, Germany), magnesium stearate (Union Derivan, Germany).

Sample preparation for NIR analysis

A protocol was followed for calibration and validation, in order to develop and validate a robust NIRS method for the simultaneous quantification of two APIs. The protocol included batches and days as sources of variability. A training calibration set consisting in 26 different formulations of tablets containing different amounts of atorvastatincalcium and amlodipine besilate was prepared according to a D-optimal experimental design with 2 variables and 5 levels generate by Modde 10 software (Umetrics, Sweden) (Table 4).

Table 4. Composition of calibration/validation set according to an D-optimal experimental design

Exp Name	X_1 mg/tablet	X_2 mg/tablet	Exp Name	X_1 mg/tablet	X_2 mg/tablet
N1	8,27	11,09	N14	11,37	13,87
N2	9,31	11,09	N15	12,41	13,87
N3	10,34	11,09	N16	8,27	15,26
N4	11,37	11,09	N17	9,31	15,26
N5	12,41	11,09	N18	10,34	15,26
N6	8,27	12,48	N19*	11,37	15,26
N7*	9,31	12,48	N20	12,41	15,26
N8	10,34	12,48	N21	8,27	16,64
N9	11,37	12,48	N22	9,31	16,64
N10	12,41	12,48	N23	10,34	16,64
N11	8,27	13,87	N24	11,37	16,64
N12	9,31	13,87	N25	12,41	16,64
N13*	10,34	13,87	N26	12,41	16,64

X_1– atorvastatincalcium, X_2 - amlodipinebesilate * - validation samples

Table 5. Qualitative and quantitative composition of calibration and validation samples

Concentration level	1[a] 80%	2[a,b] 90%	3[a,b] 100%	4[a,b] 110%	5[a] 120%
Tablets composition (mg/tablet)					
Atorvastatin calcium	**8.27**	**9.31**	**10.34**	**11.37**	**12.41**
Amlodipine besylate	**11.09**	**12.48**	**13.87**	**15.26**	**16.64**
Microcrystalline Cellulose	78.26	75.84	73.42	71.00	68.58
Calcium carbonate	30.00	30.00	30.00	30.00	30.00
Croscarmellose sodium	6.00	6.00	6.00	6.00	6.00
Corn starch	15.00	15.00	15.00	15.00	15.00
Silicon dioxide	0.38	0.38	0.38	0.38	0.38
Magnesium stearate	1.00	1.00	1.00	1.00	1.00
	150.0	150.0	150.0	150.0	150.0

[a] calibration samples for API assay; [b] validation samples for API assay;

In the tablets the amount of APIs was between 8.27 – 12.41 mg/tablet for atorvastatin calcium and between 11.09–16.64 mg/tablet for amlodipine, respectively. This amount results from the preparation of atorvastatincalcium and amlodipine tablets with 10mg of each API/tablet and 150 mg tablet weight. The amount of API/tablet was 8.27, 9.31, 10.34, 11.37, 12.41 mg atorvastatin calcium and 11.09, 12.48, 13.87, 15.26, 16.64 mg amlodipine besilate respectively, corresponding to 80, 90, 100, 110 and 120% API content in the formulations (Table 5).

Tablets were prepared by direct compression. In detail, atorvastatincalcium, amlodipinebesilate, microcrystalline cellulose, calcium carbonate, sodium croscarmellose, corn starch and silicon dioxide were mixed using a planetary mixer (PRS type, Erweka, Germany) for 5 min. The powder blend for tableting was passed through the 0.8 mm sieve and remixed for 3 minutes in the same mixer. Subsequently, magnesium stearate was added to the mixture and mixed for 1 minute. A total of 150 mg of powder for tableting was filled in a die (Ø 7mm) and compressed using an eccentric tablet press (Riva, UK).

NIR analysis

NIR spectra were recorded using a Fourier-transform NIRS analyser (Antaris, TermoElectron, SUA) in Reflectance Sampling configuration. Each reflectance spectrum was acquired via OMNIC software (Termo Scientific, USA) by integrating 32 scans taken over a wave number between $4000cm^{-1}$ to $10000cm^{-1}$ with $8cm^{-1}$ resolution. Twenty different NIR measurements on twenty different tablets of the same batch tablets sample were recorded.

Model calibration

For the development of calibration models the PLS (Partial Least Squares) regression method from the OPUS Quant 6.5 (Bruker Optics, Germany) was used. Different pre-processing methods were applied in combination with the whole spectra or different spectral regions in order to find models with high predictive ability [19]. The predictive ability of a model was evaluated according to the following classical criteria: RMSECV (root mean square error of cross-validation), high correlation coefficient (R^2), low number of PLS factors and low bias [20,21]. The optimal numbers of factors for PLS were determined by a cross-validation procedure with groups of two spectra (each side of the sample being represented by a spectrum) [22].

Method validation

For validation, external independent sets of samples are needed. In order to validate the NIRS methods, the formulations from calibration sets corresponding to 90, 100 and 110% APIs content, (formulations N7, N13 and N19) were prepared using the same methodology presented previously. Four replicates for each concentration level were prepared in three different days as validation samples. There are several validation parameters that must be determined in order to be consistent with the recommendations of International Conference of Harmonization (ICH) and other regulatory (EMA, FDA) guidelines: accuracy, precision (repeatability and intermediate precision), linearity and range of application. The validation was performed according to the strategy proposed by Hubert *et al* [23] with slight modification according with a recent review on NIRS methods validation [24]. Calculation of the validation parameters (trueness, precision, accuracy) was performed in Microsoft Office Excel 2010 (Microsoft Corporation, USA)

Reference methods

Atorvastatin and amlodipine assay in tablets were performed using a reference HPLC-UV validated method. The chromatographic parameters were: column Phenomenex Luna C18 (2) 150 x 4,6mm x5μm; mobile phase acetate buffer (0.025M, pH 4.5): acetonitrile in gradient (0-2min, 55:45v/v; 2-5min 75:25vv); flow rate of 1.5 ml/min. The detection was performed at 236nm for atorvastatin and 246nm for amlodipine. Under the given chromatographic conditions the retention time was 2.01 minutes for atorvastatin and 4.01 minutes for amlodipine.

ACKNOWLEDGMENTS

REFERENCES

[1]. C.S. Gautam, L. Saha, *British Journal of Clinical Pharmacology*. **2008**, *65*, 795.

[2]. R. Blank, F.D. Hobbs, J. Zamorano, X. Girerd, *Drugs Today* (Barc). **2007**, *43*, 157.

[3]. S.G. Chrysant, *Clin Drug Investig.* **2008**, *28*, 713.

[4]. ***EMA Reflection Paper: Chemical, pharmaceutical and biological information to be included in dossiers when Process Analytical Technology (PAT) is employed. http://www.ema.europa.eu/docs/en_GB/document_library/Other/2009/10/WC500004890.pdf (accessed 02/03/2015).

[5]. ***FDA Guidance for Industry: PAT – A Framework for Innovative Pharmaceutical Development, Manufacturing, and Quality Assurance. http://www.fda.gov/downloads/Drugs/GuidanceComplianceRegulatoryInformation/ Guidances/ ucm070305.pdf (accessed 02/03/ 2015).

[6]. M. Jamrógiewicz, *J Pharm Biomed Anal.* **2012**, *66*, 1.

[7]. T. De Beer, A. Burggraeve, M. Fonteyne, L. Saerens, J.P. Remon, C. Vervaet, *Int J Pharm.* **2011**, *417*, 32.

[8]. I.A. Tuhuţiu, D. Casoni, C. Sârbu, *Studia UBB Chemia,* **2012**, *LVII (2)*, 83.

[9]. A. Jena, M. Madhu, S. Latha, *IJPSR*, **2010**, *1*, 100.

[10]. D.A. Shah, K.K. Bhatt, M.B. Shankar, R.S. Mehta, T.R. Gandhi, S.L. Baldania *Indian J Pharm Sci.* **2006**, *68(6)*, 796.

[11]. C. Sîrbu, I. Tomuţă, L. Vonica, M. Achim, L.L. Rus, E. Dinte, *Farmacia,* **2014**, *62*, 48.

[12]. I. Tomuta, R.Iovanov, A.L. Vonica, S.E. Leucuta, *Sci Pharm.* **2011**, *79*, 885.

[13].I. Tomuta, R. Iovanov, E. Bodoki, L. Vonica, *Drug Dev Ind Pharm.* **2014**, *40*, 549.

[14]. M. Donoso, E.S. Ghaly, *Pharm Dev Technol.* **2005**, *10,* 211.

[15]. L.B. Marić, B.D. Jović, S.D. Petrović, A.M. Nikolić, I.J. Homšek, *J. Serb. Chem. Soc.* **2014**, *79*, 331.

[16]. P.F. Chavez, P. Lebrun, P.Y. Sacré, C. Bleye, L. Netchacovitch, S. Cuypers, J. Mantanus, H. Motte, M. Schubert, B. Evrard, P. Hubert, E. Ziemons, *Int J Pharm.* **2015**, *486*, 13.

[17]. C.V. Liew, A.D. Karande, P.W. Heng, *Int J Pharm.* **2010**, *386*, 138.

[18]. K. Järvinen, W. Hoehe, M. Järvinen, S. Poutiainen, M. Juuti, S. Borchert, *Eur J Pharm Sci.* **2013**, *48*, 680.

[19]. A. Porfire, L. Rus, A.L. Vonica, I. Tomuţă, *J Pharm Biomed Anal.* **2012**, *70*, 301.

[20]. J. Mantanus, E. Ziémons, P. Lebrun, E. Rozet, R. Klinkenberg, B. Streel, B. Evrard, P. Hubert,*Talanta* **2010**, *80*, 1750.

[21]. I.A. Sima, R.D. Naşcu-Briciu, C. Sârbu, *Rev. Roum. Chim.*, *2013*, *58*(7-8), 705.

[22]. T. Naes, T. Isaksson, T. Fearn, T. Davies, A User-Friendly Guide to Multivariate Calibration and Classification. NIR Publications. Chichester, 2002, chapter 1.

[23]. P. Hubert, J.J. Nguyen-Huu, B. Boulanger, E. Chapuzet, P. Chiap, N. Cohen, P.A. Compagnon, W. Dewé, M. Feinberg, M. Lallier, M. Laurentie, N. Mercier, G. Muzard, C. Nivet, L. Valat, E. Rozet, *J Pharm Biomed Anal.* **2007**, *45*, 82.

[24]. C. De Bleye, P.F. Chavez, J. Mantanus, R. Marini, P. Hubert, E. Rozet, E. Ziemons, *J Pharm Biomed Anal.* **2012**, *69*, 125.

MINOXIDIL AND NEOPTIDE TOPICAL APPLICATION REINFORCED BY LOW-LEVEL LASER THERAPY ON AN ANIMAL MODEL OF ALOPECIA

**MEDA SANDRA ORĂSAN[a], ANDREI CONEAC[b*],
CARMEN MIHAELA MIHU[b], CODRUŢA MARE[c], ADRIANA MURESAN[d]**

ABSTRACT. This study investigated on a rat model the hair regrowth effects of Low-Level Laser Therapy as monotherapy or concomitant therapy with topical application of two chemical treatments that are used in human patients with hair loss: Minoxidil 2% - Hairgrow (Dar Al Dawa Pharma/Amman, Jordan) and Neoptide (Ducray/ Boulogne, France).
 Results of hair regrowth evaluated by macroscopical images (photographs), trichoscopy (with a dermatoscope) and grown hair weight (from a surface area of 1cm²) revealed that Minoxidil 2% therapy was more efficient than Neoptide. Topical treatments were less efficient than LLLT exposure alone. Both combined therapies: LLLT plus Minoxidil 2% and LLLT with Neoptide induced better hair regrowth than topical applications. Our study proves that not all the products recommended for human use have the same hair regrowth efficiency on an animal model and that a combined therapy (laser plus topical substance) may bring supplementary benefits.

Keywords: hair regrowth, low-level laser therapy, combined treatment, Minoxidil 2%, Neoptide, trichoscopy

INTRODUCTION

More than half of the population worldwide suffers from a hair loss disorder [1]. Androgenetic alopecia (AGA) is the most common cause of hair loss, affecting more than half of the males over 40 years old and females over

---

[a] *"Iuliu Hatieganu" University, Faculty of General Medicine, Physiopathology Department, 8 Victor Babes str., RO-400012, Cluj-Napoca, Romania*
[b] *"Iuliu Hatieganu" University, Faculty of General Medicine, Histology Department, 8 Victor Babes str., RO-400012, Cluj-Napoca, Romania*
[c] *"Babes-Bolyai" University, Faculty of Economics and Business Administration, Department of Statistics – Forecasts - Mathematics, 58-60 Teodor Mihali str., RO-400591, Cluj-Napoca, Romania*
[d] *"Iuliu Hatieganu" University, Faculty of General Medicine, Physiology Department, 8 Victor Babes str., RO-400012, Cluj-Napoca, Romania*
* *Corresponding author: andrei.coneac@gmail.com*

65 [1]. AGA is a chronic dermatological disorder defined as thin diffuse hair loss over the vertex and frontal area of the scalp in females and it is accompanied by hairline recession at the temples in males. The disease is caused by androgen excess (testosterone and its derivate dihydrotestosterone) and it is due to the susceptibility of hair follicles to androgen miniaturization. Heredity also plays a part [1].

Minoxidil 2% topical therapy in female patients, as well as Minoxidil 5% and Finasteride treatment in males represent the only FDA approved drugs for AGA. As currently used therapies proved not to be effective in all patients, scientists focused on finding new quality therapies for hair loss and treatment. Laser has thus become an interesting and encouraging field of research as it has already been demonstrated that red or near-infrared light determines tissue repair. Low Level Laser Therapy (LLLT) may provide a promising treatment option for patients who do not respond to classical treatment. LLLT represents a type of laser which produces low power, coherent monochromatic red light, promotes regeneration and stimulates cellular activity [2]. The device was previously tested and recorded positive results on wound healing, nerve regeneration, joint pain relief, stroke recovery and mucositis treatment [3,4,5,6,7,8,9]. LLLT delivers fluences of 1-10J/cm² with a power density of 3-90mW/cm² and has demonstrated beneficial effects in various skin conditions as well [10].

In the late 1960's the usual wavelengths ranged from 500-1100 nm, therefore Endre Mester used a low-power ruby laser (694nm) on a mice animal model. During his study on cargiogenic potential of lasers, he discovered that the therapy applied determined an unexpectedly significant hair regrowth on the test areas [11,12]. LLLT was since considered a potential treatment for hair loss [13]. The photobiomodulation produced by LLLT stimulates epidermal stem cells in the follicle bulge and determines the shifting of the follicles from telogen (resting phase) to the anagen (active) phase of the hair growth cycle [1]. Laser phototherapy is thought to prolong the duration of anagen and prevent premature catagen development (hair falling phase) [14,15]. LLLT alters cell metabolism through photodissociation of inhibitory nitric oxide (NO), leading to increase adenosine triphosphate (ATP) production and modulation of reactive oxygen species (ROS) [16]. It also determines induction of transcription factors that cause protein synthesis, triggering cell proliferation, alteration of cytokine levels, growth factors, inflammatory mediators and significant tissue oxygenation [17]. LLLT has been proved to produce vasodilation and increased blood flow with important therapeutic effect in alopecia [17-19].

Recently, a large number of commercial devices using LLLT have been promoted with increased media attention and significant marketing budgets.

Professional and home-based LLLT devices may have a hand-held design or consist of a therapy helmet for hands-free use. Most of the studies claim that LLLT of the scalp at 655nm significantly improves the hair counts in males with AGA, with an increase in the number of terminal hairs and in shaft diameter, together with a decrease of vellus hairs [20, 21]. Few clinical trials have been conducted on these LLLT devices and results are controversial. The therapeutic effect remains unclear due to the lack of independent long-term placebo-controlled clinical studies and due to analyzing issues [21, 22]. Further research is required to establish the efficacy on hair regrowth in comparison to classic topical solutions [22, 23].

The objective of our study was to determine whether treatment with a low-level laser device, the US FDA-cleared HairMax Lasercomb, is efficient in inducing hair growth in vivo, on an animal model in single usage (standard parameters, 3 minutes therapeutic exposure) and in combination with topical therapy: Minoxidil 2% (Hairgrow, Dar Al Dawa Pharma/Amman, Jordan) and Neoptide (Laboratoires Dermatologiques Ducray/ Boulogne, France).

RESULTS AND DISCUSSION

A) Macroscopic and Microscopic Evaluation

Macroscopic examination of the skin surface on day 30 of treatment enabled us to assess the *in vivo* hair regrowth effect induced by topical daily application of Minoxidil 2% in Group I. We comparatively evaluated the test area and the control area of each rat from this group and the majority of rats showed positive hair regrowth under this therapy. Regarding the macroscopic score, 4 rats had Type 4 hair regrowth on the test area (marked increased hair regrowth, full, thick fur), 2 rats had Type 3 (moderately increased hair growth with no visible skin area), one rat showed Type 2 (low hair density, with the visualization of the skin) and another one Type 1 (uneven hair growth on the test area, skin easily seen). Trichoscopic examination of the same study group revealed an equal distribution (3:3 ratio) between Type 4 and Type 3 hair regrowth pattern.

Group II (treated with Neoptide 0.3 ml topical daily application) had a moderate hair growth effect, as the test area presented Type 3 hair regrowth in 4 rats, Type 2 hair regrowth in 3 rats and only 1 rat recorded a maximum hair regrowth result (Type 4 hair regrowth pattern). Tricoscopy evaluation however showed that Type 4 pattern was misinterpreted and, in fact, it was a case of moderately increased hair growth.

LLLT laser therapy in Group III (applied for 3 minutes, three times per week) enhanced hair regrowth. Both microscopic and macroscopic assessment revealed that half of the rats in the study group had Type 4, marked increased hair regrowth on the test area. Type 3 pattern was diagnosed in 2 rats and an equal number had Type 2 pattern.

When evaluated by macroscopic aspect, the majority of animals in Group IV (LLLT plus Minoxidil 2%) revealed marked increased hair regrowth (Type 4 in 5 rats), suggesting a powerful therapeutic effect. Moderately increased hair regrowth (Type 3) was encountered in 2 rats on the test area, and only one had low hair density (Type 2). Tricoscopy evaluation enabled us to correctly assess the hair regrowth result and to notice that one Type 3 pattern was misinterpreted as marked increased hair growth. 75% of the animals in this group recorded an efficient hair growth effect induced by this combined therapy.

Group V, treated with LLLT plus Neoptide, recorded similar results to LLLT laser Group III: 4 rats with Type 4 hair regrowth, 2 rats with Type 3 and 2 with Type 2. The results were arrived at by macroscopic and trichoscopic assessments.

The comparative evaluation of the experimental groups show that the lowest hair regrowth effect was noticed in Group II (Neoptide) ($p>0.05$). As far as topical treatment is concerned, we found out that topical Minoxidil 2% application (in Group I) was significantly better in inducing hair regrowth, even thought the p-value was over 0.05 (Table 1, Table 2).

Table 1. The macroscopic score from the treated area and the control area, expressed in the 0-5 scale described in literature. Results are expressed with Exact Wilcoxon-Signed-Rank Test * = $p<0.05$.

Treatment	Macroscopic score Median Percentile (25th-75th)	Mean ± SD	P value
Group 1 **Minoxidil 2%**	3.00 (2.25-3.75)	2.88±0.991	0.102
Control	2.50 (1.25-3.00)	2.38±1.061	
Group 2 **Neoptide**	3.00 (2.00-3.00)	2.75±0.707	0.257
Control	2.00 (1.25-3.75)	2.38±1.188	
Group 3 **HairMax**	3.00 (2.25-3.75)	3.00±0.756	0.034*
Control	2.00 (1.25-3.00)	2.25±1.035	
Group 4 **HairMax + Minoxidil 2%**	4.00 (3.00-4.00)	3.50±0.756	0.038*
Control	2.50 (2.00-3.00)	2.50±0.926	
Group 5 **HairMax + Neoptide**	3.50 (2.25-4.00)	3.25±0.886	0.023*
Control	2.00 (1.25-3.00)	2.25±1.035	

By comparing the outcomes of LLLT performed with HairMax Laser Comb, we noticed that in Group III (treated only with the laser device) it had a significant hair growth effect (p<0.05). Still, LLLT monotherapy was less efficient on hair regrowth than the combined treatment regimen with daily topical application of the Minoxidil or Neoptide compounds.

LLLT plus Minoxidil 2% (in group IV) and LLLT with Neoptide (in Group V) seem to be equally successful therapies in inducing hair regrowth, facts revealed both by macroscopic and trichoscopic assessment (p<0.05). Out of the five study groups, the best hair regrowth effect was noticed by macroscopic and trichoscopic assessment in Group IV (Laser + Minoxidil 2%) (p<0.05) (Table 1, Table 2).

Table 2. Trichoscopy score from the treated area and the control area, expressed in the 0-5 scale defined by using a dermatoscope. Results are expressed with Exact Wilcoxon-Signed-Rank Test. * = p<0.05.

Treatment	Trichoscopic score Median Percentile (25th-75th)	Mean ± SD	P value
Group 1 Minoxidil 2%	3.00 (2.25-4.00)	3.00±1.069	0.102
Control	2.5 (1.25-3.00)	2.38±1.061	
Group 2 Neoptide	3.00 (2.25-3.00)	2.75±0.463	0.157
Control	2 (1.25-3.00)	2.25±1.035	
Group 3 HairMax	3.00 (2.25-3.75)	3.00±0.756	0.034*
Control	2 (1.25-3.00)	2.25±1.035	
Group 4 HairMax + Minoxidil 2%	4.00 (3.25-4.00)	3.63±0.744	0.024*
Control	2.5 (2.00-3.00)	2.50±0.926	
Group 5 HairMax +Neoptide	3.50 (2.25-4.00)	3.25±0.886	0.023*
Control	2 (1.25-3.00)	2.25±1.035	

B) HAIR WEIGHT DETERMINATION

Regarding the hair growth differences recorded between the test area and control area of the same animal, hair weight evaluation showed that the sum of differences in the Minoxidil study group was of 40.6 mg/cm². The weight of newly grown hair was the lowest in the Neoptide treatment protocol (Group II), the difference in hair weight being of 38,3 mg/cm². Both Minoxidil and Neoptide topical compounds induced a statistically significant hair regrowth on the test areas (p<0.05) (Table 3).

Compared to the control area from the same rat, the hair weight increased significantly in the LLLT treated groups (Group III, IV and V). Group III had a hair weight difference of 45.4mg/cm² between the test and control area of the rats. The highest hair weight was recorded for LLLT plus Minoxidil treated animals (Group IV), with a sum of hair weight differences of 57.1mg/cm². Group V (LLLT and Neoptide) has a lower, but still significant hair growth result, with a total of hair increase, (evaluated by hair weight difference) of 51.8 mg/cm². Statistic analysis enabled us to say that LLLT therapy (in monotherapeutic regimen or in combination with Minoxidil or Neoptide) has induced a better regrowth effect than topical therapy alone ($p < 0.05$) (Table 3).

Table 3. The hair weight removed from one cm^2 in the treated area and the control area, expressed in mg/cm^2. Results are expressed with Exact Wilcoxon-Signed-Rank Test. * = $p < 0.05$.

Treatment	Hair weight (mg/cm²) Median Percentile (25th-75th)	Mean ± SD	P value
Group1 Minoxidil 2%	42.40 (38.37-48.15)	42.53±6.03	0.012*
Control	38.25 (31.25-42.47)	37.46±6.09	
Group 2 Neoptide	44.10 (42.02-47.15)	44.51±2.83	0.012*
Control	39.25 (36.00-42.95)	39.72±3.99	
Group 3 HairMax	44.25 (42.30-51.62)	45.48±5.68	0.012*
Control	38.85 (35.5-43.47)	39.81±5.47	
Group4 HairMax + Minoxidil 2%	48.50 (44.87-52.3)	48.70±4.77	0.012*
Control	40.35 (36.87-45.82)	41.56±5.29	
Group5 HairMax +Neoptide	45.15 (41.82-49.27)	44.80±5.01	0.012*
Control	39.00(34.37-42.22)	38.32±5.74	

In the attempt to discover an effective treatment for hair loss, new therapies for alopecia have been studied on rats, hamsters and even stump-tailed macaque [24, 25].

LLLT has been tested on animal models and significant hair regrowth has been reported, but the optimum wavelength and dosimetric parameters still need to be determined [26]. According to literature LLLT stimulates hair regrowth in mice under chemotherapy-induced alopecia. LLLT applied on a rat animal model determined a significant hair regrowth in the HairMax treated groups, 5 days earlier than in the control and sham-control animals, as reported by a Satino study [27].

HairMax Laser Comb Professional 12 was screened for safety and received the US-FDA approval for medical use since 2007 [28]. In clinical use it is recommended for the scalp, 8 minutes, three times per week and its good compliance is due to the fact that it does not leave residue on the scalp, as topically applied substances do [10].

The incidence of adverse effects of LLLT is rather low: dry skin (5.1%), pruritus (2.5%), skin tenderness (1.3%), irritation (1.3%) and warm sensation at the site of application (1.3%) [1,10]. In our study no side effects were recorded in the LLLT treated groups (III, IV and V).

Minoxidil 2%, that we used in two of our study groups (I and IV) was not specially devised for hair loss problems and its hair growing effect has accidentally been discovered as a side effect.

The mechanism underlying the hair growth effect is therefore not completely clear yet. The drug action is directed to the mesenchymal cells from the follicular dermal papilla of the hair follicle (DP) which controls the growth and differentiation of hair matrix cells [26]. DP associated stem cells are the site of expression of genes related to hair growth, being under the negative effect of androgen mediated events, and under the positive stimulation of Wnt proteins and wound growth factors [29].

Possible indirect drug action is represented by the vasodilation produced by Minoxidil that generates an increased blood flow to the DP [26]. Minoxidil contains an N-oxide group able to release NO, an important cellular signaling molecule, also functioning as a vasodilator [30]. Minoxidil is also a potassium channel blocker, which also leads to vasodilation of the scalp blood vessels. This direct mechanism of action involving the ATP sensitive K+ channels was highly investigated [31]. New hair growth induced by Minoxidil can also be due to local irritation related to it or some components of the vehicle [26]. Researchers also suspect that Minoxidil may act in inducing hair regrowth through the immune system, as it stimulates prostaglandin synthethase-1 and the subsequent production of PGE(2) [32,33].

Literature did not mention any dysplastic or atypical changes in follicular germinal epithelium during or after application of topical minoxidil, and did not reveal the development of new follicles (follicular neogenesis) [26]. Studies performed on animal models with Minoxidil topical therapy described the shortening of telogen (resting phase), a premature entry in anagen phase (active) of the resting follicles, an action meant to prolong the anagen and leading to hair regrowth [34,35]. Larger hair follicles were reported in the morphometric evaluation of human scalp biopsies after treatment with topical minoxidil in a vehicle made up of propylene glycol, water and ethanol [26]. The alcohol and propylene glycol present in topical preparations can dry the scalp, causing dandruff and contact dermatitis. Nanosome formulation reduces the rate of contact dermatitis from the vehicle [36,37].

A systemic review of the side-effects of Minoxidil as hair loss treatment for AGA patients, done by Cochrane, underlined significant differences between 2% and 5% formulation, the latter determining an increased rate of general side-effects, such as: pruritus, skin irritation, dermatitis with a slightly elevated rate of hair growing in places other than the scalp, burning or irritation of the eye, redness, unwanted hair growth elsewhere on the body and even temporary hair loss or exacerbation of hair loss [38,39,40]. Serious side effects such as: severe allergic reactions, chest pain, dizziness, fainting, tachycardia, unexplained weight gain, or swelling of the hands and feet, were rarely reported [41]. Our study findings are in agreement with literature reports as no side effects were recorded in the Minoxidil 2% treated animal groups (I and IV).

The three types of evaluation methods applied in our study support the idea that Minoxidil 2% has a good hair growth inducing effect in the topical application regimen on animal model. Our results correlate with other literature data on Minoxidil efficacy. An Uno and Kurata study, performed on fuzzy rats in 1993, reported that topical application of Minoxidil, Diazoxide and Copper peptide produced a conversion from short vellus to long terminal hairs, an enlargement of the follicular size and a prolongation of anagen phase [31,42]. In human studies, hair loss reduction and growth of new hair is noticed after 4 months of 1 ml application/day Minoxidil topical treatment and after 6 months there was an increased in hair count with 13.2% [43,44,45]. Unfortunately, even though Minoxidil is the most commonly used topical hair growth compound, the monotherapy has a positive response rate in just 20-56% of the cases and AGA continues to progress [31,45].

Neoptide, on the other hand, is a promising topical treatment for hair regrowth as some human studies revealed. With a proper blend of vitamin B3, amino acids and botanicals, it significantly reduces the hair loss in female patients, simultaneously boosting the hair mass. The association of Neoruscine, Nicotinamide and GP4G facilitates optimal nutritional exchange in the hair bulb and provides an energy-activating role.

In agreement with this, our own study data revealed that just the topical therapy does not offer a proper therapeutic response. We also noticed that LLLT is a powerful hair growth promoter by itself. Our results showed that hair density was increased when topical treatment and LLLT therapy were associated. The combination of the two induced a statistically significant hair regrowth which suggests that LLLT reinforces the chemical compound. Another possible hypothesis is that through the vasodilation created by LLLT the substance applied topically on the scalp has a better absorption rate which eases the active compounds delivery to the hair bulb. It will be our purpose, in a next research, to determine through high affinity chromatography, the absorption rate of the topical treatment.

The originality of our study research relies on the fact that LLLT was applied in conjunction with the gold standard treatment of AGA (Minoxidil 2%) and also with a new compound (Neoptide) which is thought to be an effective hair growth inducer in clinical practice. Another innovative aspect is Neoptide application on an animal model of alopecia, which was not done before.

CONCLUSIONS

An overall improvement of the test area with higher hair density was reported in all our study groups, though the results did not reach statistical significance for groups I and II when evaluation by macroscopical images (photographs) or trichoscopy (with a dermatoscope) was performed.

Results of the hair weight assessment (from a surface area of 1cm²) revealed that treatment with Minoxidil 2% induced significant hair regrowth. The lowest hair growth effect was noticed after treatment with Neoptide. Thus our study proves that not all the products recommended for human use are having the same hair regrowth efficiency on an animal model.

We also found a statistically significant difference in the increase of hair density between LLLT treated areas and control areas. Our results suggest that low-level laser treatment is more efficient than single use of topical therapy while the combined therapy (laser plus topical application) brings even supplementary benefits. The applied therapy was well tolerated as no adverse effects were reported on the animal model used.

Research on prevention and reversal hair loss continues to be a challenging subject. Further studies are required not only to compare efficiency of different therapies but also to identify the optimal length of laser treatment, the duration of the response and more importantly the long term safety of the newly implemented LLLT.

EXPERIMENTAL SECTION

Study design

40 adult Wistar-Bratislava rats were preselected for their telogen (resting) phase of the hair cycle according to age (around 120 days) from the Animal Facility of UMF "Iuliu Hatieganu" Cluj-Napoca. The Wistar albino rats of either sex, weighing about 200 g, were acclimatized to the experimental room in the Physiology Department of UMF Cluj, at a temperature of 23 Celsius degrees, in controlled humidity conditions with a 12:12 h light and dark cycle for 14 days prior to the experiment. We housed maximum 2 animals

per cage, offering them free access to standard pellets as basal diet and water ad libitum. Following the experiment they were euthanized according to the current regulations.

The study has obtained ethical committee clearance from the Institutional Animal Ethics Committee (IAEC) of Iuliu Hatieganu University of Medicine and Pharmacy Cluj-Napoca.

In order to create the alopecia animal model we induced general anesthesia and used electric hair clippers for the dorsal animal fur, followed by shaving which allowed us to create two rectangular areas, each of 2 cm width and 4 cm length. The denuded areas were symmetrically situated on both sides of the mid dorsal line, the right area provided for testing and the left as control.

We randomly assigned the animals to 5 experimental groups, each consisting of 8 rats. The treatment was performed for 1 month (Table 4).

Table 4. Experimental groups and treatments

GROUP	PRODUCT	MANUFACTURER/ CITY, COUNTRY	DETAILS	EXPOSURE DOSE	TREATMENT FREQUENCY
I	Minoxidil 2%, HairGrow	Dar Al Dawa Pharma / Amman, Jordan	topical application	0.3 ml	daily
II	Neoptide, Traitement antichute	Laboratoires Dermatologiques Ducray/Boulogne, France	topical application	0.3 ml	daily
III	HairMax Laser Comb 12	Lexington International LLC/ USA	laser exposure 655nm, <5mW	3 minutes	three times/ week
IV	Minoxidil 2% + HairMaxLaser	Dar Al Dawa Pharma,	topical	0.3 ml	daily
		Lexington International LLC	laser exposure	3 minutes	three times/ week
V	Neoptide + HairMaxLaser	Laboratoires Dermatologiques,	topical	0.3 ml	daily
		Lexington International LLC	laser exposure	3 minutes	three times/ week

The Lasercomb device

LLLT was applied by exposing the test area of each rat in Group III to HairMax Laser, at standard parameters (<5mW, continuous emission) for 3 minutes, with a frequency of three times/week. Group IV received daily

application of 0.3 ml Minoxidil 2% plus LLLT exposure three times per week, while Group V had 0.3 ml Neoptide daily topical application associated with 3 minutes LLLT, three times per week (Monday, Wednesday, Friday).

The HairMax Laser Comb Professional 12 is a hand-held Class 3R lower level laser therapy device. It contains a single laser module that emulates 12 beams: 6 of them at a wavelength of 635nm (±5%) and 6 beams at 655nm (±5%) [10].The device uses a technique of parting the subject's hair by special combs that are attached to it. By aligning the teeth with the laser beams, the hair can be parted, excluding possible obstruction and improving the delivery of distributed laser light energy to the skin surface.

The topical therapy

Topical therapy consisting of 0.3 ml solution was applied on the denuded test area of the rats daily in all test groups, except Group III, restricted to LLLT exposure. Group I received Minoxidil 2% daily application, while Group II was topically treated with Neoptide. Group IV had Minoxidil 2% topical application associated with LLLT for 3 minutes, three times per week (Monday, Wednesday, Friday). Group V also received combined therapy with Neoptide daily application together with laser therapy exposure, in the same specified regimen.

The systematic (IUPAC) name of Minoxidil is 6-Piperidin-1-ylpyrimidine-2,4-diamine 3-oxide. The chemical formula is a Chemical data formula $C_9H_{15}N_5O$, with a molecular mass of 209.251 g/mol. The Pharmacokinetic data include: its biotransformation (metabolism) primarily hepatic (90%), a half-life of 4.2 h and renal excretion [24].

Neoptide (Laboratoires Dermatologiques Ducray/Boulogne, France) is a hair growth promoter containing a peptide complex: Tetrapeptide, Neoruscine, Niconamid and guanosine (5') tetraphospho (5') guanosine abbreviated as GP4G.

Efficacy evaluation

On day 0, during the hair removal procedure with electric clippers, we defined a surface of 1 cm² and gathered the cut hairs in an aluminum foil. The hairs were then weighed with an analytical balance in the Chemistry Experimental Laboratory of the Physiology Department. Once the alopecia animal model was prepared, we photographed the macroscopic aspect and stored the images for each experimental group in electronic folders. We also used a hand held Dermatoscope (Dermlite DL3) to visualize the denuded area of the rats, followed by the capturing of the trichoscopy images and storage in electronic folders.

At the completion of 1 month treatment, the assessment of hair regrowth was evaluated in all study groups. We used both qualitative and quantitative methods, to ensure a correct evaluation process. For qualitative assessments of macroscopic and trichoscopic stored images, an observer, blind to the experiment, was used.

Macroscopic aspect and Trichoscopy are two qualitative assessments with results expressed on a scale of clinical aspect, subjectively perceived. The scale may be either defined in percentage according to the examples provided by literature, or devised by the researcher. We applied an evaluation scoring system based on the comparison of the treated area with the control of the same animal, as it has been successfully used before. The 4 stages of our scoring system were defined as: Type 1 (uneven hair growth on the tested area, skin can be easily seen), Type 2 (low hair density, with the visualization of the skin), Type 3 (moderately increased hair growth with no visible skin area), Type 4 (marked increased hair regrowth, full, thick fur). Both methods are approximations of hair growth that do not provide the possibility of precise measurement of the new grown hairs, as counting the number of hairs per unit and the determination of their diameter are not possible. Macroscopic aspect and Trichoscopy cannot quantify minor increases in hair density, which are considered a reliable sign of hair regrowth.

On the other hand, hair weight evaluation is able to determine slight increases in hair density. Hair weight is a quantitative and objective evaluation technique, based on precise measurement of hair from a predetermined area.

Statistic analysis

Descriptive statistics of the variables were expressed through mean and standard deviations. As variables are either ordinal or scale, but not normally distributed, the median value and the first and third quartile are also presented. Comparison between the treated area and the control one was based on the Wilcoxon Rank Test, a non-parametric test applied for two related samples. Significant effect of the treatment applied was considered when a p-value < 0.05 was obtained.

ACKNOWLEDGMENTS

REFERENCES

[1]. P. Avci, G.K. Gupta, J. Clark , N. Wilkonkal, M.R. Hamblin, *Lasers Surg Med*, **2014**, *46*(2), 144.

[2]. A Schindl, M. Schindl, H. Pernerstorfer-Schon, L. Schindl, *J Investig Med*, **2000**, *48*(5), 312.

[3]. J.M. Bjordal, C. Couppe, R.T. Chow, J. Tuner, E.A. Ljunggren, *Aust J Physiother*, **2003**, *49*(2), 107.

[4]. L. Brosseau, V. Welch, G. Wells, et al, *Cochrane Database Syst Rev*, **2000**, *2*, CD002049

[5]. R. G. Cauwels, L.C. Martens. *Eur Arch Paediatr Dent*, **2011**, *12*(2), 118.

[6]. A. Christie, G. Jamtvedt, K.T. Dahm, R.H. Moe, E.A. Haavardsholm, K.B. Hagen, *Phys Ther*, **2007**, *87*(12), 1697.

[7]. G. Jamtvedt, K.T. Dahm, I. Holm, S. Flottorp, *BMC Health Serv Res*, 2008, *8*, 145.

[8]. M.M Schubert, F.P. Eduardo, K.A. Guthrie, et al, *Support Care Cancer*, **2007**, *15*(10), 1145.

[9]. G.B. Silva, E.F. Mendonca, C. Bariani, H.S. Antunes, M.A. Silva, *Photomed Laser Surg,* **2011**, *29*(1), 27.

[10]. J.J. Jumenez, T.C. Wikramanayake, W. Bergfeld, et al, *Am J Clin Dermatol*, **2014**, *15*(2), 115.

[11]. E. Mester, G. Ludany, M. Sellyei, B. Szende, G. Gyenes, G.J. Tota, *Langenbecks Arch Chir*, **1968**, *322*, 1022.

[12]. D. Barolet, *Semin Cutan Med Surg*, **2008**, *27*(4), 227.

[13]. A.I. Metelitsa, J.B. Green, *Semin Cutan Med Surg*, **2011**, *30*(3), 144.

[14]. T.C. Wikramanayake, R. Rodriguez, S. Choudhary, et al, *Lasers Med Sci*, **2012**, *27*(2), 431.

[15]. M. Leavitt, G. Charles, E. Heyman, D. Michaels, *Clin Drug Investig*, **2009**, *29*(5), 283.

[16]. J.T. Eells, M.T. Wong-Riley, J. Verhoeve, et al, *Mitochondrion*, **2004**, *4*(5–6), 559.

[17]. H. Chung, T. Dai, S.K. Sharma, Y.Y. Huang, J.D. Carroll, M.R. Hamblin, *Ann Biomed Eng*, **2012**, *40*(2), 516.

[18]. N.L. Lohr, A. Keszler, P. Pratt, M. Bienengraber, D.C. Warltier, N. Hogg, *J Mol Cell Cardiol*, **2009**, *47*(2), 256.

[19]. E. Makihara, S. Masumi, *Nihon Hotetsu Shika Gakkai Zasshi*, **2008**, *52*(2), 167.

[20]. R.J. Lanzafame, T.T. Blanche, A.B. Bodian, R.P. Chiacchierini, A. Fernandez-Obregon, E.R. Kazmirek, *Lasers Surg Med*, **2013**, *45*(8), 487.

[21]. M.R. Avram, N.E. Rogers, *J Cosmet Laser Ther*, **2009**, *11*(2), 110.

[22]. A.K. Gupta, D. Daigle, *J Dermatol Treat*, **2014**, *25*(2), 162.

[23]. A.K. Gupta, D.C. Lyons, W. Abramovits, *Skinmed*, **2014**, *12*(3), 145.

[24]. P. Balakrishnan, S. Shanmugam, W.S. Lee, et al, *Int J Pharm*, **2009**, *377*(1), 1.

[25]. R.C. Wester, et al, *J Invest Dermatol*, **1984**, *82*(4), 353

[26]. J.T. Headington, *Dermatologica*, **1987**, *175* (2), 19.

[27]. J.L. Satino, M. Markou, *Int J Cos Surg Aest Dermatol*, **2003**, *5*, 113.

[28]. M. Leavitt, G. Charles, E. Heyman, D. Michaels, *Clin Drug Investig*, **2009**, *29*(5), 283.

[29]. M.P. Zimber, C. Ziering, F. Zeigler, et al, *J Drugs Dermatol*, **2011**, 10, 1308.

[30]. P.H. Proctor, *Arch Dermatol*, **1989**, *125*(8), 1146.

[31]. K. Shorter, N.P. Farjo, S.M. Picksley, V.A. Randall, *FASEB J*, **2008**, *22*(6), 1725.

[32]. J.F. Michelet, S. Commo, N, Billoni, Y.F. Mahe, B.A. Bernard. *J Invest Dermatol*, **1997**, *108*(2), 205.

[33]. R. Wolf, H. Matz, M. Zalish, A. Polack, E. Orion. *Dermatol Online J*, **2003**, *9*(3), 7.

[34]. A.G. Messenger, J. Rundegren, *Br J Dermatol,* **2004**, *150*, 186.

[35]. R. Dhurat, M.S. Sukesh, G. Avhad, A. Dandale, A. Pal, P. Pund, *Int J Trichology*, **2013**, *5*(1), 6.

[36]. Dandruff and Seborrheic Dermatitis". Medscape.com. Retrieved 2009-10-09.

[37]. P. Balakrishnan, S. Shanmugam, W.S. Lee, *Int J Pharmaceutics*, **2009**, *377*(1-2), 1.

[38] E.J. van Zuuren, Z. Fedorowicz, B.Carter, R.B. Andriolo, J. Schoones, *Cochrane Database Syst Rev*, **2012**, *16*, 5.

[39]. E.J. van Zuuren, Z. Fedorowicz, B. Carter, *Br J Dermatol*, **2012**, *167*(5), 995.

[40]. M. Hordinsky, A. Donati, *Am J Clin Dermatol*, **2014**, *15*(3), 231.

[41]. Minoxidil Official FDA information, side effects and uses". Drugs.com. Retrieved 2015-04-01.

[42]. M. Li, A. Marubayashi A, Y. Nakaya, K. Fukui, S. Arase, *J Invest Dermatol*, **2001**, *117*(6), 1594.

[43]. A. Tosti, B. Duque-Estrada, *Expert Opin Pharmacother*, **2009**, *10*, 1017.

[44]. J.M. Mella, M.C. Perret, M. Manzotti, H.N. Catalano, G. Guyatt, *Arch Dermatol*, **2010**, *146*, 114.

[45]. U. Blume-Peytavi, K. Hillmann, E Dietz, D. Canfield, N. Garcia Bartels, *J Am Acad Dermatol*, **2011**, *65*(5), 1126.

RAPID SIMULTANEOUS LC/MS[2] DETERMINATION OF RIFAMPICIN AND 25-DESACETYL RIFAMPICIN IN HUMAN PLASMA FOR THERAPEUTIC DRUG MONITORING

CRISTINA MIHAELA GHICIUC[a], NICOLETA RADUCANU[b], FARCZÁDI LÉNÁRD[c], LAURIAN VLASE[d,*], CĂTĂLINA ELENA LUPUȘORU[a], CONSTANTIN MIRCIOIU[e], BRINDUSA TILEA[f]

ABSTRACT. A rapid and sensitive liquid chromatography coupled with tandem mass spectrometry (LC/MS[2]) method for the simultaneous quantification of rifampicin and its main active metabolite 25-desacetyl rifampicin in human plasma was developed and validated. The separation was performed on a Gemini NX C18 column under isocratic conditions using a mobile phase of 40:60 (V/V) methanol and 2mM ammonium formate in water, at 40 ºC, with a flow rate of 0.6 mL/min. The detection of rifampicin and its metabolite was performed in multiple reaction monitoring mode using an ion trap mass spectrometer with positive electrospray ionization. The human plasma samples (0.1 mL) were deproteinized with methanol and aliquots of 0.3 µL from supernatants obtained after centrifugation were directly injected into the chromatographic system. The method shows a good linearity (r > 0.993), precision (CV < 8.2%) and accuracy (bias < 6.3%) over the range of 411 - 19737 ng/mL for rifampicin and good linearity (r > 0.992), precision (CV < 10.1%) and accuracy (bias < 8.2%) over the range of 70 - 3379 ng/mL for 25-desacetyl rifampicin. The lower limit of quantification (LLOQ) was 411 ng/mL and recovery was between 90.3-108.2% for rifampicin, whereas for 25-desacetyl rifampicin the LLOQ was 70 ng/mL and recovery between 93.1-107.5%, respectively. The developed and validated method is simple, rapid

[a] *Department of Pharmacology, School of Medicine, "Gr.T. Popa" University of Medicine and Pharmacy Iasi, 16 Universitatii Str., Iasi, RO-700115, Romania*
[b] *PhD Student, "Carol Davila" University of Medicine and Pharmacy Bucharest, 7 Traian Vuia Str., Bucharest, sector 1, RO-020955, Romania*
[c] *Vim Spectrum SRL, Sighisoarei 409, RO-547367, Corunca, Targu-Mures, Romania*
[d] *Department of Pharmaceutical Technology and Biopharmacy, Faculty of Pharmacy, University of Medicine and Pharmacy "Iuliu Hațieganu", Cluj-Napoca, 8 Victor Babeş Str., RO-400012 Cluj-Napoca, Romania*
[e] *Department of Pharmaceutical Technology and Biopharmacy, Faculty of Pharmacy, "Carol Davila" University of Medicine and Pharmacy Bucharest, 7 Traian Vuia Str., Bucharest, sector 1, RO-020955, Romania*
[f] *Infectious Diseases Department M4, Clinical Scineces, Faculty of Medicine, University of Medicine and Pharmacy, 38 Gh. Marinescu Str., RO-540139, Târgu Mures, Romania*
* Corresponding author: Laurian.vlase@umfcluj.ro

and specific for the high throughput simultaneous determination of rifampicin and 25-desacetyl rifampicin in human plasma and was successfully applied in therapeutic drug monitoring of rifampicin in patients with tuberculosis.

Keywords: *rifampicin, 25-desacetyl rifampicin, LC/MS^2, human plasma*

INTRODUCTION

Rifampicin, a semisynthetic antibiotic produced from *Streptomyces mediterranei* (Fig. 1) is used as first-line therapy for the treatment of tuberculosis in combination with at least one other anti-tuberculosis drug. As the incidence of infections is increasing, rifampicin is also preferred in combination therapy in the treatment of infections associated with prosthetic devices (e.g., implantable cardiac electronic devices) or in antimicrobial-resistant infections, especially methicillin-resistant Staphylococcus aureus (MRSA) [1,2].

Rifampicin is characterized by wide inter- and intra-individual variability in healthy volunteers, but also in tuberculosis patients [3]. Although the majority of patients respond to a standardized therapy, low drug concentrations are commonly associated with treatment failure or bacteria resistance, resulting in poor clinical outcomes [4,5]. 25-desacetyl-rifampicin is the main active metabolite of rifampicin, thus it is also responsible on the clinical efficiency of the treatment [3]. Rifampicin stimulates the metabolism of isoniazid and of other concomitant administered drugs and also induces its own metabolism over the first few weeks of treatment. In most patients with reduced renal or hepatic function, the doses should be reduced to prevent toxicity, but for rifampicin doses might need to be increased to avoid under-dosing due to enzyme induction. The determination of rifampicin and its metabolite in biological samples is useful for the evaluation of rifampin pharmacokinetics in combination therapy, facilitating early screening of therapeutic failure and preventing adverse effects [6,7]. Pharmacokinetic/pharmacodynamic studies are needed to evaluate the interrelation between the free plasma drug concentration and microbiological and clinical outcomes of the treatment with rifampicin [5].

Several chromatographic analytical methods have been reported for the determination of rifampicin and 25-desacetyl rifampicin involving various techniques such as high performance thin layer chromatography (HTPLC) [7], high performance liquid chromatography (HPLC) [11], liquid chromatography coupled with mass spectrometry (LC-MS/MS) [10,12,13].
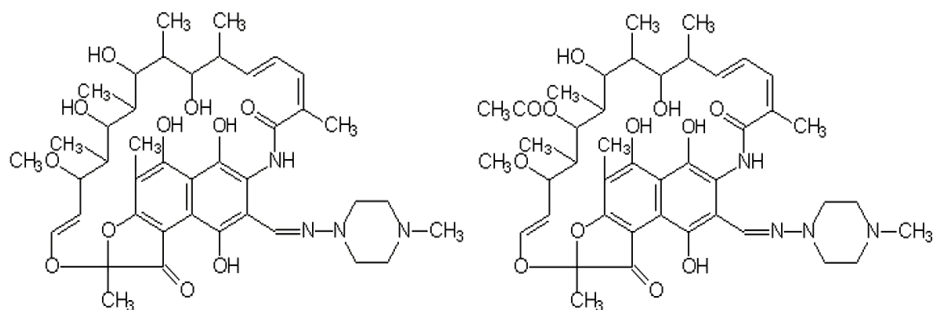
Figure 1. Chemical structures of rifampicin (left) and 25-desacetyl rifampicin (right)

Rifampicin can be determined using HPTLC [7], which is a quick and cheap method, however LC/MS methods are much more sensitive and more selective. HPLC methods have also been used for the determination of rifampicin [11], but we decided to develop a new LC/MS method due to its better selectivity in comparison to HPTLC and HPLC methods.

For analysis of biological samples using chromatographic methods, the samples must first undergo an extraction / purification process. A purification process often used is solid phase extraction (SPE) [9]. Although it is a very effective purification method, it is time consuming and raises the cost of analysis significantly. A fast, simple and inexpensive method for biological sample purification is protein precipitation (PP) method, widely used especially when LC/MS analysis is employed [10,12,13].

RESULTS AND DISCUSSION

Sample preparation

Although the MS detection type and parameters greatly influence the sensitivity of LC/MS assay methods, the sample preparation method can also have an influence on the chromatographic background noise level and can create suppression effects. Generally the analyte is extracted from the matrix prior to analysis using SPE or LLE for reasons such as sample purification and sample pre-concentration. The extraction processes (both SPE and LLE) are tedious, time and resource consuming, and will usually require the use of internal standards in order to reduce extraction variability. For these reasons PP as a sample processing technique is recommended whenever high-throughput and low extraction variability are required. The

disadvantage of PP is the fact that the samples are not highly purified as in the case of SPE or LLE, samples get diluted in the process, thus reducing sensitivity. The sample preparation technique must be chosen in a way to assure the best performance needed for a given analysis, whether reduced time and costs are needed, or a high sensitivity is needed.

The range of the calibration curves was adapted to the expected concentration levels of biological samples to be analyzed, 411.2 - 19737.6 ng/mL for rifampicin and 70.4 - 3379.2 ng/mL for 25-desacetyl rifampicin, respectively. As the developed analytical method shows good sensitivity for both analytes, the PP extraction method (which implies sample dilution) was considered a good alternative to SPE or LLE providing shorter processing times and high reproducibility.

The method developed by us requires samples of only 0.1 mL plasma, processed by PP with methanol (0.3 mL), the supernatant being injected into the HPLC system directly after centrifugation. The sensitivity obtained meets the requirements in order for the method to be usable for the given drug monitoring application and absolute recoveries were close to 100%.

LC-MS assay

The detection parameters were optimized in order to achieve best sensitivity and specificity for both rifampicin and 25-desacetyl rifampicin. Both compounds were ionized in ESI source by proton addition, giving pseudomolecular ions with m/z 824 for rifampicin and m/z 750 for 25-desacetyl rifampicin. By fragmentation, these ions are broken down to ions with m/z 792 for rifampicin and m/z 732 for 25-desacetyl rifampicin respectively (Fig. 2 and Fig 3). The extracted ion chromatograms (EIC) of m/z 792 from m/z 824 for rifampicin and m/z 732 from m/z 750 for 25-desacetyl rifampicin were analyzed for quanfication purposes. In the chromatographic conditions of the method the retention times were 1.1 minutes for rifampicin and 0.6 minutes for 25-desacetyl rifampicin, with a run-time per sample of 1.4 minutes. Typical chromatograms of human plasma samples spiked with rifampicin and 25-desacetyl rifampicin at LLOQ are shown in Fig. 3. No interfering peaks attributed to plasma components were observed at the retention times of rifampicin and 25-desacetyl rifampicin (Fig.3).

Assay validation

Validation of the method was carried out in accordance with international regulations [14]. Calibration curves prepared in human blank plasma were linear for both rifampicin and 25-desacetyl rifampicin over their concentration ranges of 411.2 - 19737.6 ng/mL, and 70.4 - 3379.2 ng/mL respectively.

Correlation coefficients were greater than 0.993 for rifampicin and greater than 0.992 for 25-desacetyl rifampicin. The lower limit of quantification (LLOQ) was established at 411.2 ng/mL for rifampicin and 70.4 ng/mL for 25-desacetyl rifampicin. Results for within-day and between-day precision and accuracy determined during the validation are shown in Tables 1 and 2 for rifampicin, and Tables 3 and 4 for 25-desacetyl rifampicin, respectively. All values for accuracy and precision were within acceptance criteria (< ±15%) [14]. Recovery values were between 90.3-108.2% for rifampicin and 93.1-107.5% for 25-desacetyl rifampicin.
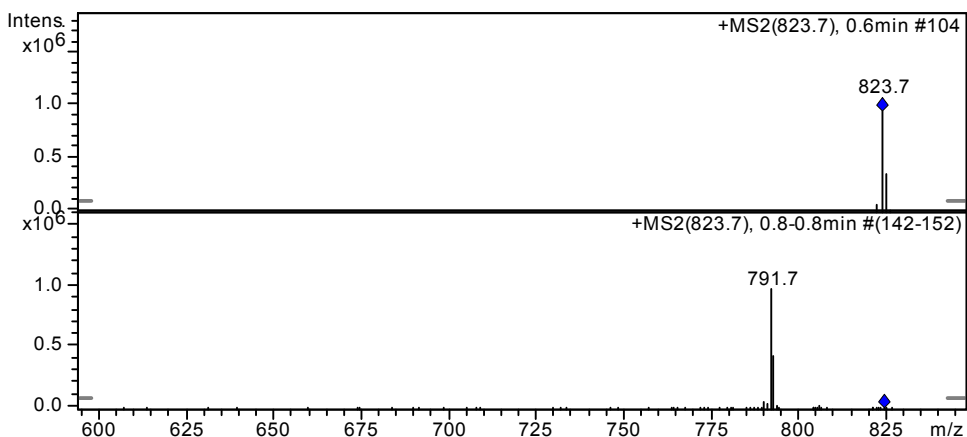
Figure 2. MS spectra of rifampicin – MS spectra (upper image), MS/MS spectra (lower image)
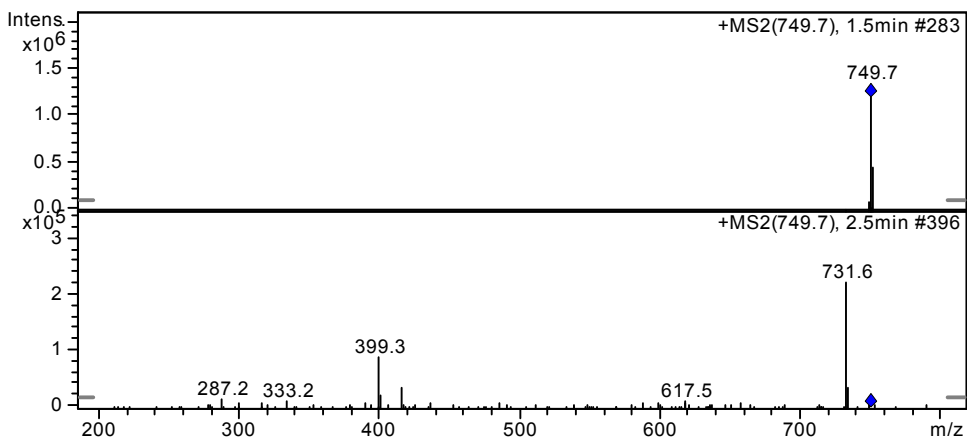
Figure 3. MS spectra of 25-desacetyl rifampicin – MS spectra (upper image), MS/MS spectra (lower image)

Method application

The validated method for simultaneous determination of rifampicin and 25-desacetyl rifampicin in human plasma was successfully applied in therapeutic drug monitoring and pharmacokinetic assessment of rifampicin and 25-desacetyl rifampicin in tuberculosis patients. Typical chromatograms of rifampicin and 25-desacetyl rifampicin in a tuberculosis patient plasma sample is shown in Fig. 3 and the overlapped plasma profiles obtained in the whole study (spaghetti plot chart) are presented in Fig. 4.
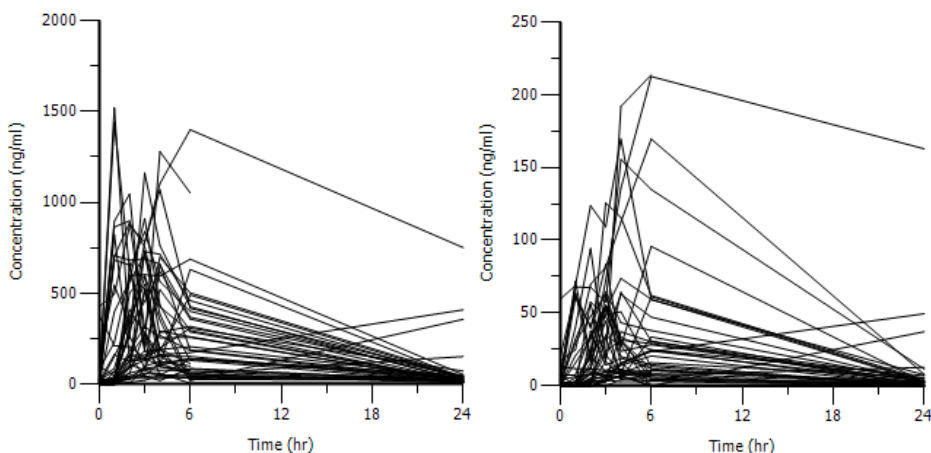
Figure 4. Overlapped plasma profiles of rifampicin (left) and 25-desacetyl rifampicin (right) administrated to patients with tuberculosis (600 mg rifampicin/day)

CONCLUSION

Antimicrobial therapeutic drug monitoring could be an important tool in clinical practice if the administered drug shows large inter-subject variability in pharmacokinetics or when the patient's compliance is poor. Therefore, quantification of drug in plasma is an important issue in clinical practice to enhance efficacy and to reduce toxicity.

The LC/MS^2 method developed by us for the quantification of rifampicin and 25-desacetyl rifampicin is specific, accurate, fast and inexpensive, as long as the analytical technology used (LC/MS) is available. It is one of the fastest analytical methods for simultaneous determination of rifampicin and 25-desacetyl rifampicin in biological matrices published, also having the advantage of using a simple, high throughput sample preparation technique. The method has a runtime of 1.4 minutes. Compared to other methods described in literature with runtimes of 2.1 minutes [10], 3.5 minutes [12] and 6 minutes [13]. This allows for shorter analysis times and higher throughput,

especially when large batches of samples need to be analysed. The faster runtimes were achieved without loss of accuracy or precision of the method. For rifampicin the within-day precision ranged from 1.0% to 7.7%, with an accuracy (bias, %) of -6.3% to 5.3%, while between-day precision ranged from 3.0% to 8.2%, with an accuracy (bias, %) of -3.2% to 4.7%. For 25-desacetyl rifampicin the within-day precision ranged from 1.8% to 4.2%, with an accuracy (bias, %) of 0.1% to 8.2%, while between-day precision ranged from 5.3% to 10.1%, with an accuracy (bias, %) of -2.5% to 1.0%. These values are similar to those of other methods described in literature [10,12,13]. The sample preparation using protein precipitation is simple and fast, ideal for high throughput LC-MS methods, and is also used in other methods described in literature [10, 12, 13]. The lower limit of quantification was 411 ng/mL for rifampicin and 70.4 ng/mL for 25-desacetyl rifampicin, higher than other methods described for the quantification of rifampicin [10, 12, 13] and 25-desacetyl rifampicin [10]. However, the purpose of our analytical method was its suitability for therapeutic drug monitoring, when steady-state plasma concentrations are much higher than after single-dose administration and a shorter analysis time is more desirable than a higher sensitivity.

The method was successfully applied in therapeutic drug monitoring of rifampicin and 25-desacetyl rifampicin in patients with tuberculosis.
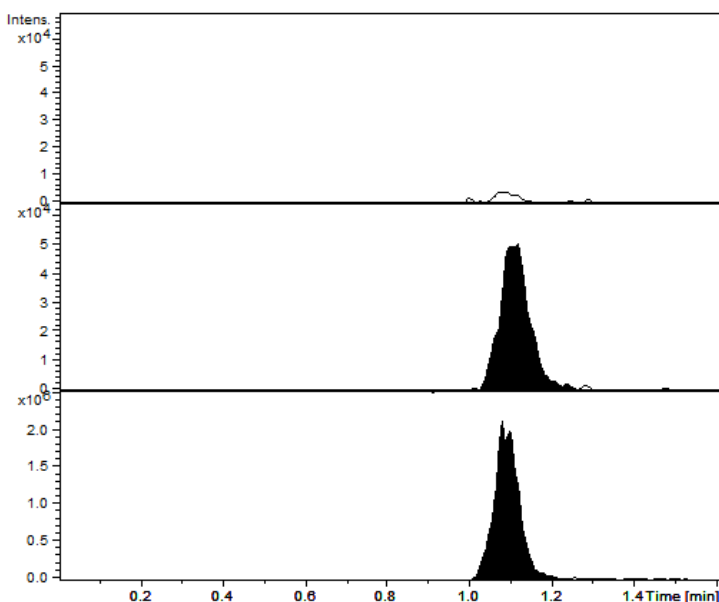
Figure 5. Representative chromatograms of blank sample (upper image); plasma spiked with rifampicin at lower limit of quantification (411 ng/mL, middle image); and a plasma sample from a patient under treatment with 600 mg rifampicin/day, sample taken after 2h from administration, concentration found 13672 ng/mL (lower image).
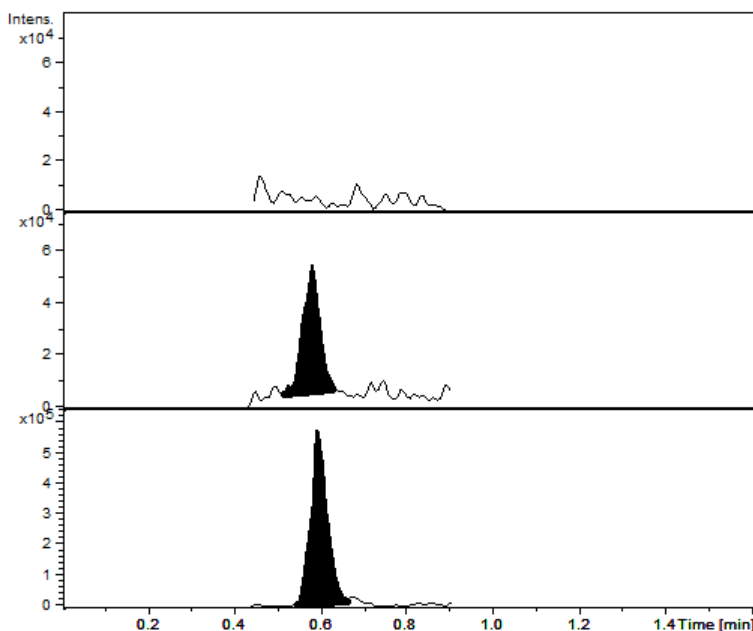
Figure 6. Representative chromatograms of blank sample (upper image); plasma spiked with 25-desacetyl rifampicin at lower limit of quantification (70 ng/mL, middle image); and a plasma sample from a patient under treatment with 600 mg rifampicin/day, sample taken after 2h from administration, concentration found 645 ng/mL (lower image).

Table 1. Within-day precision, accuracy and recovery (n = 5) for rifampicin

$c_{nominal}$ ng/mL	Mean c_{found} ng/mL (± S.D.)	CV %	Bias %	Recovery % (± S.D.)
411.2	436.5±33.6	7.7	6.2	94.8±8.6
822.4	770.4±13.5	1.8	-6.3	100.8±10.2
3289.6	3241.0±67.8	2.1	-1.5	108.2±11.6
9868.8	10390.5±101.6	1.0	5.3	96.6±9.6

Table 2. Between-day precision, accuracy and recovery (n = 5) for rifampicin

$c_{nominal}$ ng/mL	Mean c_{found} ng/mL (± S.D.)	CV %	Bias %	Recovery % (± S.D.)
411.2	430.3±35.4	8.2	4.7	96.2±12.8
822.4	804.6±44.2	5.5	-2.2	100.1±12.9
3289.6	3182.8±203.3	6.4	-3.2	90.3±4.7
9868.8	10191.6±304.1	3.0	3.3	102.2±12.7

Table 3. Within-day precision, accuracy and recovery (n = 5)
for 25-desacetyl rifampicin

$c_{nominal}$ ng/mL	Mean c_{found} ng/mL (± S.D.)	CV %	Bias %	Recovery % (± S.D.)
70.4	74.0±2.7	3.7	5.1	99.4±6.6
140.8	152.3±2.7	1.8	8.2	102.1±4.9
563.2	577.8±24.5	4.2	2.6	97.3±6.3
1689.6	1691.8±61.3	3.6	0.1	99.4±7.0

Table 4. Between-day precision, accuracy and recovery (n = 5)
for 25-desacetyl rifampicin

$c_{nominal}$ ng/mL	Mean c_{found} ng/mL (± S.D.)	CV %	Bias %	Recovery % (± S.D.)
70.4	71.13±4.9	7.0	1.0	99.6±9.2
140.8	140.33±14.1	10.1	-0.3	96.4±2.3
563.2	549.35±29.0	5.3	-2.5	93.1±0.9
1689.6	1659.9±126.2	7.6	-1.8	107.5±3.2

EXPERIMENTAL SECTION

Reagents

Rifampicin and 25-desacetyl rifampicin reference standards were from USP (Rockville, MD, USA). Gradient grade methanol for liquid chromatography and ammonium formate of analytical-reagent grade were supplied by Merck KGaA (Darmstadt, Germany). Bidistilled deionised water for injections was supplied by the Infusion Solution Laboratory of the University of Medicine and Pharmacy Cluj-Napoca (Cluj-Napoca, Romania). Human blank plasma was obtained from healthy volunteers, both male and female.

Apparatus

The apparatus and equipment used were: Sigma (Osterode am Harz, Germany) 204 series Centrifuge; Mettler-Toledo (Greifensee, Switzerland) Analytical Plus Balance and Mettler-Toledo (Greifensee, Switzerland) Precision Standard Balance; Scientific Industries (New York, USA) Vortex Genie 2 mixer; Elma (Singen, Germany) Transsonic 700/H Ultrasonic bath. An Agilent Technologies (Darmstadt, Germany) 1100 series LC/MS system was used consisting of: G1312A binary pump, G1379A in-line degasser, G1329A autosampler, G1316A column thermostat and an 1100 SL Ion Trap Detector.

Chromatographic and spectrometric conditions

A Phenomenex (Torrance, California, USA) Gemini NX C18 (50 x 2.0 mm i.d., 3.0 µm) chromatographic column was used for separation, using a mobile phase of a 40:60 (V/V) mixture of methanol and 2mM ammonium formate in water under isocratic conditions, kept at 40 ºC with a flow rate of 0.6 mL/min. Detection of rifampicin and 25-desacetyl rifampicin was carried out using multiple reaction monitoring (MRM) mode of the ion trap mass spectrometer with electrospray ionization (ESI) source, positive ionization (capillary exit 175 V, nebulizer 60 psi (nitrogen), dry gas (nitrogen) at 11 L/min, dry gas temperature 350ºC). The column effluent was diverted to waste for the first 0.4 minutes in order to keep the ESI source clean of contamination. The extracted ion chromatograms (EIC) of m/z 792 from m/z 824 for rifampicin and m/z 732 from m/z 750 for 25-desacetyl rifampicin were analyzed (MS^2 mode).

Standard solutions

Stock solutions of 1.028 mg/mL rifampicin and 0.440 mg/mL 25-desacetyl rifampicin were prepared by dissolving the appropriate quantity of substance in methanol. Working solutions of rifampicin (41.12 µg/mL) and 25-desacetyl rifampicin (7.04 µg/mL) were prepared by appropriate dilution of stock solutions in human blank plasma. The working solutions were then used to prepare seven plasma calibration standards and three quality control standards for both rifampicin and 25-desacetyl rifampicin. Concentrations of calibration standards for rifampicin were between 411.2 ng/mL and 19737.6 ng/mL, and quality control standards had concentrations of 822.4 ng/mL (low), 3289.6 ng/mL (medium) and 9868.8 ng/mL (high). For 25-desacetyl rifampicin the calibration standards were between 70.4 ng/mL and 3379.2 ng/mL, and quality control standards had concentrations of 140.8 ng/mL (low), 563.2 ng/mL (medium) and 1689.6 ng/mL (high). All calibration standards and quality control standards were prepared by diluting the appropriate volumes of the working solutions with blank plasma.

Sample preparation

0.1 mL of standard and plasma sample respectively were added to a 1.5 mL plastic tube and precipitated with 0.3 mL methanol. The samples were then vortex-mixed (10 seconds) and centrifuged (3 minutes at 12000 rpm), and 0.15 mL of the supernatants were transferred to autosampler vials and 0.3 µL were injected into the HPLC system.

Method validation

Rifampicin and 25-desacetyl rifampicin concentrations were determined automatically by the instrument's QuantAnalysis data system using the peak areas, using the external standard method. The calibration curve model was determined to be $y = b + ax$, weighted $(1/y^2)$ linear regression, where y is the peak area and x is the concentration of the analyte (μg/mL).

Within-day precision and accuracy were determined analyzing five different samples (n = 5) of each of the QC standards (low, medium, high) in the same run. The between-day precision and accuracy were determined analyzing five different samples (n = 5) of each of the QC standards (lower, medium, higher), each on one of five different days. Precision was expressed as the coefficient of variation (CV %) of five samples, while accuracy was expressed as relative difference between mean of measured and the calculated concentrations (bias %). The lowest calibration standard with an accuracy and precision within the 20% acceptance was established as the lower limit of quantification (LLOQ). Relative recovery values (at LLOQ and low, medium, high QC levels) were determined by comparing chromatographic peak areas of spiked plasma samples with peak areas of samples in pure solvent, both having the same concentration of rifampicin and 25-desacetyl rifampicin respectively [15-16].

ACKNOWLEDGMENTS

REFERENCES

1. G.N. Forrest, K. Tamura. *Clin Microbiol Rev,* **2010**, *23*, 14-34.
2. A.L. Stavrakis, J.A. Niska, J.H. Shahbazian, A.H. Loftin, R.I. Ramos, F. Billi, K.P. Francis, M. Otto, N.M. Bernthal, D.Z. Uslan, L.S. Miller*, Antimicrob Agents Chemother*. **2014**, *58*, 2377-2386.
3. D. Marchidanu, N. Raducanu, D.S. Miron, F.S. Radulescu, V. Anuța, I. Mircioiu, I. Prasacu. *Farmacia,* **2013**, *61,* 398-410.
4. F. Fahimi, P. Tabarsi, F. Kobarfard, B.D. Bozorg, A. Goodarzi, F. Dastan, N. Shahsavari, S. Emami, M. Habibi, J. Salamzadeh. Int J Tuberc Lung Dis, **2013**, *17,* 1602-1606.
5. M. Regazzi, A.C. Carvalho, P. Villani, A. Matteelli. *Clin Pharmacokinet*, **2014**, *53,* 489-507.
6. B.C. Moldoveanu, C.M. Ghiciuc, C.E. Lupuşoru. *Arch. Balk. Med. Union*. **2011**, *46,* 299-302.

7. D.H. Shewiyoa, E. Kaale, P.G. Risha, B. Dejaegher, J. Smeyers-Verbeke, Y. Vander Heyden, *Journal of Chromatography A*, **2012**, *1260*, 232– 238.
8. D.H. Vu, R.A. Koster, M.S. Bolhuis, B. Greijdanus, R.V. Altena, D.H. Nguyen, J.R.B.J. Brouwers, D.R.A. Uges, J.W. Calffenaar. *Talanta,* **2014**, *121*, 9–17.
9. K.H. Hee, J.J. Seo, L.S. Lee. *Journal of Pharmaceutical and Biomedical Analysis*, **2015**, *102*, 253–260
10. L.C. Winchester, A.T. Podany, J.S. Baldwin, B.L. Robbins, C.V. Fletcher. *Journal of Pharmaceutical and Biomedical Analysis,* **2015**, *104,* 55–61.
11. C. Magis-Escurra, J. van den Boogaard, D. Ijdema, M. Boeree, R. Aarnoutse. *Pulmonary Pharmacology & Therapeutics,* **2012**, *25*, 83-86.
12. J. Xu, H. Jin, H. Zhu, M. Zheng, B. Wang, C. Liu, M. Chen, L. Zhou, W. Zhao, L. Fu, Y. Lu, *Clinical Therapeutics,* **2013,** *35(2),* 161-168.
13. A. Srivastava, D. Waterhouse, A. Ardrey, S.A. Ward. *Journal of Pharmaceutical and Biomedical Analysis,* **2012**, *70*, 523–528.
14. Guidance on the Investigation of Bioavailability and Bioequivalence. The European Agency for the Evaluation of Medicinal Products, Committee for Proprietary Medicinal Products, **2001**, CPMP/EWP/QWP/1401/98.
15. D. Mihu, L. Vlase, S. Imre, C.M. Mihu, M. Achim, D.L. Muntean, *Studia UBB Chemia*, **2009**, *54(3)*, 151.
16. M. Achim, D. Muntean, L. Vlase, I. Bâldea, D. Mihu, S. E. Leucuţa, *Studia UBB Chemia*, **2009**, *54(3)*, 7.

SYNTHESIS AND STRUCTURAL CHARACTERIZATION OF STRONTIUM CONTAINING BIOACTIVE GLASSES

MARIA STEINER[a], ROZALIA VERES[a,*], VIORICA SIMON[a]

ABSTRACT. Bioactive glasses of SiO_2-CaO-SrO-P_2O_5 system, wherein SrO progressively replaced up to 4 mol% CaO, were produced using the sol–gel route. Their structural properties and bioactivity were tested using differential thermal analysis (DTA), X-ray diffraction (XRD) and Fourier transform infrared spectroscopy (FT-IR). Based on the DTA results, the 110 ºC dried gels were subjected to heat treatment at 600 ºC. X-ray diffractograms show a predominant amorphous character for all samples. FT-IR results indicate few changes in the local structure by progressive addition of strontium. The soaking of samples for 14 days in biological fluid resulted in the formation of hydroxyapatite layer that delivered characteristic infrared absorption band sensitive to strontium content.

Keywords: bioactive glasses; sol-gel; strontium; in vitro bioactivity.

INTRODUCTION

Osteoporosis is a skeletal disorder characterized by compromised bone strength predisposing to an increased risk of fracture [1]. In osteoporotic bone, osteoclasts resorb too much bone, while osteoblastic bone formation is not sufficient to counterbalance this, resulting in reduced bone mineral density, weak and brittle bones [2].

Therefore, in last decades there has been large amount of work on developing synthetic materials for bone regeneration and replacing. Bioactive glasses are a group of synthetic materials with bone bonding properties first discovered by Hench [3, 4]. They have the ability of direct bonding to bone via formation of a surface carbonated hydroxyapatite layer when exposed to simulated body fluid (SBF) [5, 6]. Many bioactive glass compositions including copper [7], silver [8] magnesium [9], zinc [10, 11] and strontium as dopants have been studied and have shown considerable efficacy in bone regeneration [12-15].

---

[a] *Babeş-Bolyai University, Faculty of Physics & Institute of Interdisciplinary Research in Bio-Nano-Sciences, Cluj-Napoca RO-400084, Romania*
* *Corresponding author: rozalia.veres@ubbcluj.ro*

It was reported that the introduction of strontium ions into silicate matrix leads to bone formation and inhibits bone resorption by osteoclasts, promoting the increase of bone density and resistance [16, 17]. The advantages of strontium-doped bioactive glasses are based on the controlled release of the Sr ions that stimulate the activity of osteoblast cells. Strontium can substitute for calcium in bioactive glasses, and this replacement may induce few structural changes [14] that influence the gradual degradation of the bioactive material, with effects on new bone formation on the implant surface [18, 19].

The objective of the present study was to produce new sol–gel derived bioactive glasses of SiO_2-CaO-SrO-P_2O_5 system and to characterize their structural properties and bioactivity.

RESULTS AND DISCUSSION

In the investigated $65SiO_2 \cdot 5P_2O_5 \cdot (30-x)CaO \cdot xSrO$ glass system (0≤x≤4 mol%) we explored five compositions, i.e. x = 0, 0.5, 1, 2 and 4 mol%. The corresponding samples were noted Sr0, Sr0.5, Sr1, Sr2 and Sr4, respectively.

The TGA curves for all samples present several regions of weight loss (Figure 1). The first weight loss is associated with an endothermic peak in DTA curve that occurs around 80 °C and can be ascribed to the loss of free water molecules. A second weight loss can be observed until 400 °C. This loss can be associated with the elimination of water caged in pores and the decomposition of residual nitrates. The peaks observed around 550 °C arise from dehydroxylation [20]. Based on these results, a thermal treatment at 600 °C was considered.

The X-ray diffraction patterns for all samples treated at 600 °C for 2 hours (Figure 2) indicate a predominant amorphous structure, without significant crystalline phases. The large diffraction peaks at about 32º might show a tendency to calcium strontium phosphate crystals (JCPDS 34-0484), excepting the sample without strontium oxide.

The structural properties of the glasses treated at 600ºC were also analyzed through Fourier Transform Infrared Spectroscopy (FTIR). The absorption band recorded at 3512 cm^{-1} (Figure 3) can be assigned to silanol groups linked to molecular water through hydrogen bonds and the band appeared at 1648 cm^{-1} to the bending mode of adsorbed molecular water [21]. The bands occurring in the spectral region 1560-1370 cm^{-1} correspond to carbonate species arising from the slight reaction between the glass samples and carbon dioxide from the atmosphere and might be also due to the formation of small quantities of calcium/strontium carbonates [22]. The broad band located in 1300-800 cm^{-1} range is present in all the samples and is specific for silica-based bioactive glasses [23-24]. The shoulder at 1234 cm^{-1} is attributed to

bending mode of Si–O–Si group. The peak observed at 1062 cm^{-1} can be assigned to the Si-O-Si asymmetric stretching mode of bridging oxygen (BO), whereas the shoulder situated at 939 cm^{-1} can be attributed to the Si-O asymmetric stretching mode of the non-bridging oxygen bonds (NBO) [25, 26]. A decrease of this signal intensity is noticed with the increase of SrO content. Withal, a shift of the absorption band assigned to Si–O–Si vibrations to lower wavenumbers is observed, suggesting the shortening of Si–O–Si bonds in the vicinity of large Sr cations [27, 28]. In all the investigated glasses is observed around 551 cm^{-1} a band which corresponds to bending vibration of amorphous P-O bond [29]. Furthermore, the band situated in the range 510-460 cm^{-1} can be ascribed to the Si–O–Si bending mode.
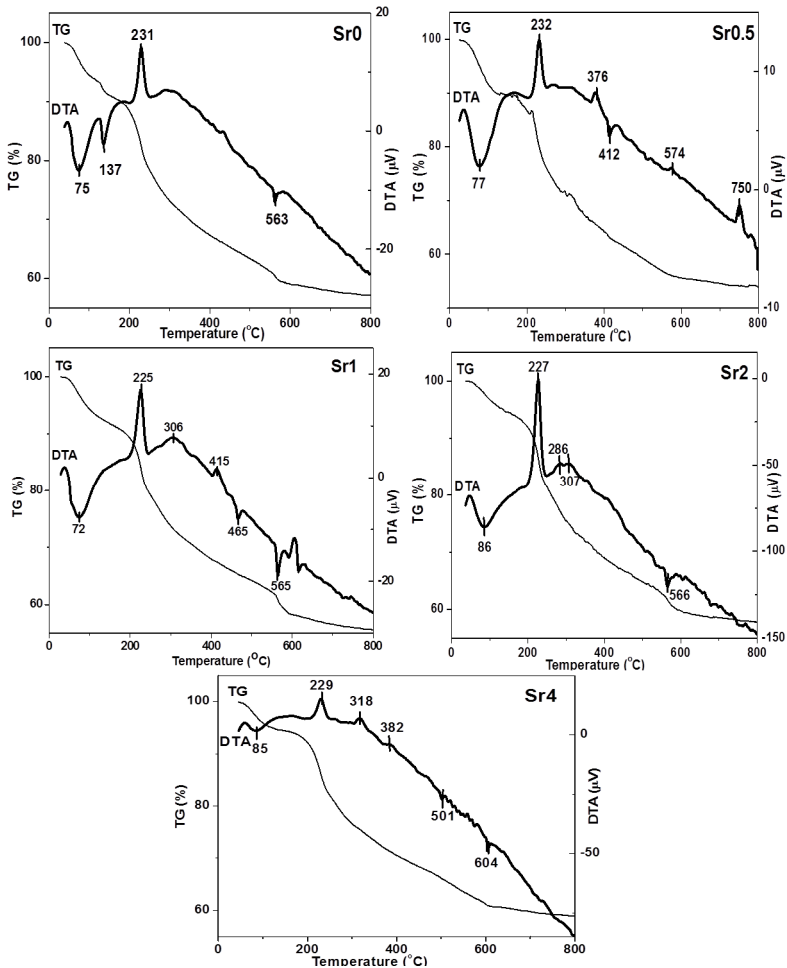
Figure 1. The DTA and TGA curves for xerogel samples dried at 110 ºC.
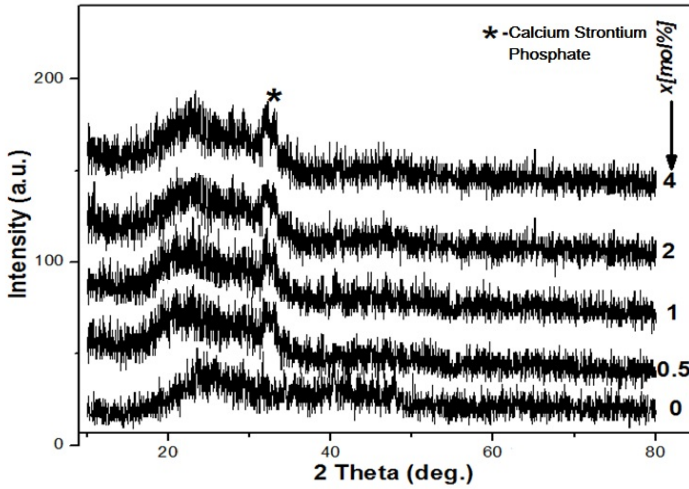
Figure 2. XRD patterns of 65SiO$_2$·5P$_2$O$_5$·(30-x)CaO·xSrO glass samples.
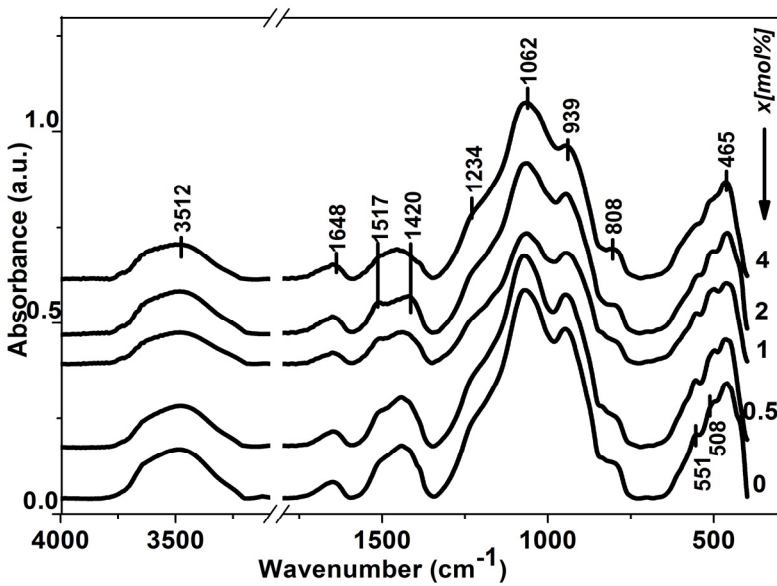
Figure 3. FT-IR spectra of 65SiO$_2$·5P$_2$O$_5$·(30-x)CaO·xSrO glasses treated at 600 ºC.

The bioactivity of the glasses was evaluated by soaking the samples during 14 days in SBF solution and characterizing them by XRD and FTIR techniques.

The XRD patterns for the immersed samples indicate the formation of a crystalline layer on the surface of the glasses (Figure 4), being observed one peak well developed at value $2\theta=32.2°$ which corresponds to the formation of hydroxyapatite (HA) crystals. This characteristic peak of apatite is observed in all specimens having lower peak intensity with the increase of strontium amount. It can be observed that for all the Sr concentrations, the glasses still indicate a good bioactivity.
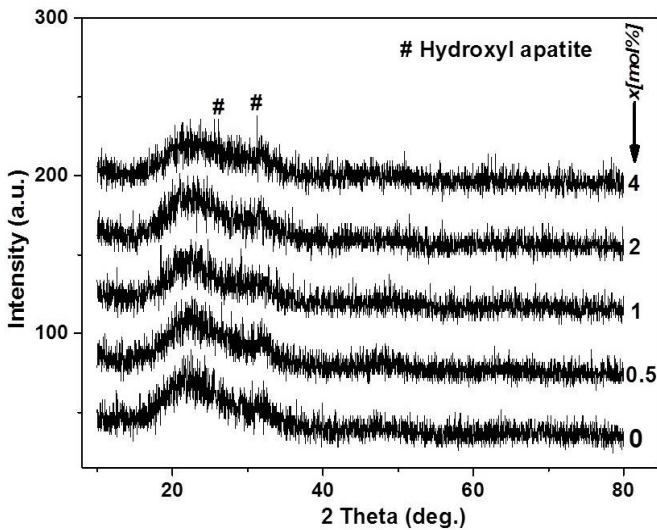
Figure 4. XRD patterns of $65SiO_2 \cdot 5P_2O_5 \cdot (30-x)CaO \cdot xSrO$ samples after immersion in SBF for 14 days.

FTIR spectra of all glasses show few changes after immersion in SBF (Figure 5) in comparison with the spectra before immersion.

All the spectra clearly show as the non-bridging oxygen Si-O band situated at 920 cm^{-1} decreased in intensity after immersion. The band from 790 cm^{-1} appeared in the spectra after immersion being assigned to Si-O-Si between the two adjacent silicates tetrahedra [30-32] which is an indicator for the formation of a silica gel layer. Furthermore, the band situated at 878 cm^{-1} appeared in all the glasses and might correspond to the formation of complex carbonate species connected with the presenceof Ca^{2+} ions on the surface [33]. Very clear changes can be seen in the region 520–620 cm^{-1}, being the characteristic area for apatite. The doublet observed at 567 and 614 cm^{-1} in all the investigated glasses corresponds to P–O bending vibrations in a PO_4^{3-} tetrahedron in hydroxyapatite [33] and denotes the glasses bioactivity.
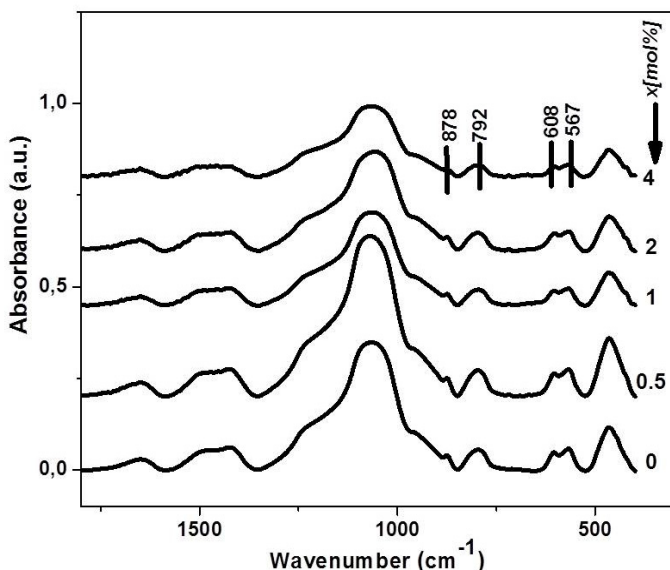
Figure 5. FTIR spectra of $65SiO_2 \cdot 5P_2O_5 \cdot (30-x)CaO \cdot xSrO$ glasses after immersion in SBF for 14 days.

CONCLUSIONS

Bioactive glasses based on SiO_2-CaO-SrO-P_2O_5 system were obtained by sol–gel method. The structure of the samples thermally stabilized at 600 ºC has a predominant amorphous character. The substitution of CaO with SrO up to 4 mol % does not inhibit the samples bioactivity, but the progressive increase of SrO content leads to the decrease of the absorption band assigned to the bioactive self-assembling hydroxyapatite layer. The samples can be considered for further investigation with respect to their bioactivity required for biomaterials used as scaffolds in bone tissue regeneration.

EXPERIMENTAL SECTION

Samples of $65SiO_2$-$5P_2O_5$-$(30-x)CaO$-$xSrO$ bioactive glass system (x= 0, 0.5, 1, and 4 mol%) were prepared following the sol-gel route. The precursors of SiO_2, P_2O_5, CaO and SrO used for the synthesis of the glasses were tetraethylorthosilicate (TEOS), triethylphosphate (TEP), calcium nitrate tetrahydrate and strontium nitrate, respectively. All reagents were of analytical grade purity. In the first stage TEOS was mixed with HNO_3 aqueous solution

having molar ratios TEOS:H_2O:HNO_3=1:9:0.1 and stirred for 1h, then was added TEP and the stirring was continued for more 1h. In the second stage both strontium and calcium nitrates were dissolved in water. Finally the solutions were mixed together under continuous stirring for 1 h for the completion of hydrolysis reaction. The obtained sols were left 7 days at 37 ºC for gelation and maturation, then the samples were dried for 24 h at 110 ºC, and thermally treated at 600 ºC for 2 h.

Differential thermal analysis and thermogravimetric analysis

DTA/TG analysis were performed on Shimadzu type derivatograph DTG-6OH SHIMADZU equipment, with a heating rates of 10 ºC/min using alumina open crucibles, in order to investigate the thermal behavior of the dried sample.

X-ray diffraction

The 600 ºC treated samples were analyzed using an X-ray Shimadzu XRD-6000 diffractometer with a monochromator of graphite for CuKα radiation (λ=1.5418Å) with Ni-filter. The diffractograms were recorded in 2θ range from 10º to 80º with a speed of 2°/min. The operation voltage and current were 40kV and 30mA, respectively.

FT-IR spectroscopy

The FT-IR spectra were recorded at room temperature in the 400-4000 cm^{-1} spectral range in absorbance mode with a JASCO FT/IR-6200 spectrometer, with an instrumental resolution of 4 cm^{-1}. An amount of 2 mg of powder sample was thoroughly mixed with 200 mg of KBr and compressed to form pellets.

Assessment of the bioactivity

Hydroxyapatite forming ability of the bioactive glasses was studied by immersing the samples in simulated body fluid (SBF) that has the ion concentrations and pH nearly equal to that of human blood plasma [34]. The samples immersed in SBF were kept in an oven at 37 ºC for 14 days. The weight of glass per volume of SBF was 10 mg/ml for each sample. After 14 days the powders were filtrated, rinsed several times with distillate water and dried at room temperature.

REFERENCES

1. Osteoporosis Prevention, Diagnosis, and Therapy, *National Institutes of Health Consens Statement,* **2000**, March 27-29; *17*, 1.
2. Y.C. Fredholm, N. Karpukhina, D.S. Brauer, J.R. Jones, R.V. Law, R.G. Hill, *Journal of the Royal Society*, **2012**, *7*, 880.
3. L.L. Hench, R.J. Splinter, W. C. Allen, T. K.Greenlee, *Journal Biomedical Materials Research Symposium*, **1971**, *2*, 117.
4. L.L. Hench, H.A. Paschall, *Journal of Biomedical Materials Research*, **1973**, *7*, 25.
5. P.J. Marie, P. Ammann, G. Boivin, C. Rey, *Calcified Tissue International*, **2001**, *69*, 121.
6. P. J. Marie, *Current opinion in pharmacology*, **2005**, *5*, 633.
7. V. Timar, R. Ciceo-Lucacel, O. Hulpus, I. Ardelean, *Modern Physics Letters B* **2009**, *23*, 747.
8. K. Magyari, R. Stefan, D.C. Vodnar, A. Vulpoi, L. Baia, *Journal of Non-Crystalline Solids*, **2014**, *402*, 182.
9. P.I. Riti, A. Vulpoi, O. Ponta, V. Simon, *Ceramics International*, **2014**, *40*, Part B, 14741.
10. R. Ciceo Lucacel, O. Ponta, V. Simon, *Journal of Non-Crystalline Solids*, **2012**, *358*, 2803.
11. R. Veres, E. Vanea, C. Gruian, L. Baia, V. Simon, *Composites: Part B*, **2014**, *66*, 83.
12. M.D. O'Donnell, R. G. Hill*, Acta Biomaterialia*, **2010**, *6*, 2382.
13. G. Boivin, P. Deloffre, B. Prrat, G. Panezer, M. Boudeull, Y. Mauras, P. Allain, Y. Tsouderos, P.J. Meunier, *Journal of Bone and Mineral Research*, **1996**, *11*, 1302.
14. J.R. Jones, E. Gentleman, J. Polak, *Elements*, **2007**, *3*, 393.
15. S. Hesaraki, M. Gholami, S. Vazehrad, S. Shahrabi*, Materials Science and Engineering*, **2009**, *30*, 383.
16. E. Gentleman, Y.C. Fredholm, G. Jell, N. Lotfibakhshaiesh, M.D. O'Donnell, R.G. Hill, M.M. Stevens, *Biomaterials*, **2010**, *31*, 3949.
17. Y. Fredholm, N. Karpukhina, R.V. Law, R.G. Hill, *Journal of Non-Crystalline Solids*, **2010**, *356*, 2546.
18. A. Merolli, P.T. Leali, P.L. Guidi, C. Gabbi, *Journal of Materials Science: Materials in Medicine*, **2000**, *11*, 219.
19. Y. Fredholm, M.M. Stevens, R. Hill, *Proceedings of the 8th World Biomaterials Congress 28 May-1 June* **2008**, Amsterdam RAI.
20. L. Lefebvre, J. Chevalier, L. Gremillard, R. Zenati, G. Thollet, D. Bernache Assolant, A. Govin, *Acta Materialia*, **2007**, *55*, 3305.
21. S. Jehabi, H. Oudadesse, J. Elleuch, S. Tounsi, H. Keskes, P. Pellen, T. Rehai, A. El Feki, H. El Feki, *Journal of the Korean Society for Applied Biological Chemistry*, **2013**, *56*, 533.

22. M.D. O'Donnell, P.L. Candarlioglu, C.A. Miller, E. Gentleman, M.M. Stevens, *Journal of Materials Chemistry*, **2010**, *20*, 8934.
23. M. Sitarz, M. Handke, W. Mozgawa, *Spectrochimica Acta Part A*, **2000**, *56*, 1819.
24. V. Aina, G. Malavasi, A. Fiorio Pla, L. Munaron, C. Morterra, *Acta Biomaterialia*, **2009**, 5, 1211.
25. K. Omori, *Am Mineral*, **1971**, *56*, 1607.
26. A. Aronne, *Journal of Non-Crystalline Solids,* **2005**, *351*, 3610.
27. C. Chen, D. Huang, W. Zhu, X. Yao, *Applied Surfaces Science*, **2006**, *252*, 7585.
28. R. Veres, C. Ciuce, V. Simon, *Studia UBB Chemia,* **2011**, *3,* 193.
29. Z. Hong, R.L. Reis and J.F. Mano, *Journal of Biomedical Materials Research Part A*, **2009**, *88*, 304.
30. D.S. Brauer, N. Karpukhina, M.D. O'Donnell, R.V. Law, R.G. Hill, *Acta Biomaterialia*. **2010**, *6*, 3275.
31. C.Y. Kim, A.E. Clark, L.L. Hench, *Journal of Non-Crystalline Solids*, **1989**, *113*, 195.
32. X. Chen, X. Chen, D.S. Brauer, R.M. Wilson, R.G. Hill, N. Karpukhina, *Materials*, **2014**, *7*, 5470.
33. A. Goel, R.R. Rajagopal, J.M.F. Ferreira, *Acta Biomaterialia*, **2011**, *7*, 4071.
34. T. Kokubo, H. Kushitani, S. Sakka, T. Kitsugi, T. Yamamuro, *Journal of Biomedical Materials Research*, **1990**, *24*, 721.

DEVELOPMENT OF MULTIWALLED CARBON NANOTUBES BASED SOLID PHASE EXTRACTION FOR THE DETERMINATION OF TRACE LEVEL OF Mn(II) AND Sn(IV) IN RIVER WATER SAMPLES

SHAHRAM NEKOUEI[a,*], FARZIN NEKOUEI[a]

ABSTRACT. This paper reports a multiwalled carbon nanotubes (MWCNTs) modified with 3-amino-7-dimethylamino-2-methylphenazine (Neutral Red, NR) as a new solid phase extractor for determination of ultra trace amounts of Mn(II) and Sn(IV). The metal ions were retained on -column filled with the solid phase at a flow rate of 3.0 mL/min. The retained metal ions were eluted with 3 mol L^{-1} solution of HCl and measured by flame atomic absorption spectroscopy (FAAS). The effect of different variables such as, sample pH, concentration of 3-amino-7-dimethylamino-2-methylphenazine (Neutral Red, NR), sample flow rate, eluting solution and the effect of interfering ions have been investigated systematically. The calibration graph was linear in the range of 0.4-100 µg L^{-1} and 0.6-150 for Mn(II) and Sn(IV), respectively. Under optimized conditions, the limit of detections (LOD) were 0.12 and 0.16 µg L^{-1} for Mn(II) and Sn(IV), respectively. The method was used for determination of target metal ions in some water samples from rivers located in industrial and nonindustrial areas.

Keywords: Solid phase extraction; 3-amino-7-dimethylamino-2-methylphenazine (Neutral Red, NR); Multiwalled carbon nanotubes; river water samples; Flame atomic absorption spectrometry, Mn(II) AND Sn(IV)

INTRODUCTION

Natural processes as well as antropogenic activities are both sources of metals and their compounds into the environment. Since exposure to heavy metals is potentially harmful their monitoring in environmental, biological and clinical samples even at trace levels is nowadays required by law and other regulations in many cases [1]. Mining operations and heavy industry in the developing world is leading to the accumulation of high concentrations of

---

[a] *Young Researchers and Elite Club, Science and Research Branch, Islamic Azad University, Tehran, Iran*
* *Corresponding author: sh.nekouei@hotmail.com*

toxic heavy metals in natural waters. Today, it is understood that exposure to heavy metals may seriously affect human health. [2]

Manganese is an essential element for human life, however, excessive levels of manganese are detrimental to the organism. Humans exposed to very high levels of manganese over a long time can develop mental and emotional disturbances and slow, clumsy body movements. Therefore, the determination of trace amounts of manganese in samples from various matrices is very important for certain areas of study. [3]

Tin is widely used in industry due to features such as low melting point, affinity to form alloys, and corrosion resistance. Exposure to Sn and its compounds can produce several effects such as neurological, hematological and immunological. Inhalation of inorganic compounds of Sn can induce to pneumoconiosis and ingestion may lead to gastrointestinal effects. Exposure to organic compounds of Sn inhibits the synthesis of hemeoxygenase and may be genotoxic, while its skin contact may cause severe irritation and burning. Other effects include kidney and liver damage [4].

Solid-phase extraction (SPE) is one of the most employed preconcentration methods that can be applied in off-line or online systems, with the advantage of possible automatization. SPE consists of the retention of metal species (or its derivatives) on the appropriate solid sorbent packed in a column or microcolumn and the later desorption with the adequate solvent. Thus, the concentration and separation of the analyte from the rest of sample matrix is achieved. [5] Solid-phase extraction (SPE), owing to its flexibility, absence of emulsion, simplicity, sampling in the field, safety, and ease of automation, is a preferred method for separation and enrichment of the target. SPE requires that the adsorbent possess a stronger selective adsorption ability. [6]

Carbon nanotubes (CNTs) are one of the most commonly used building blocks of nanotechnology. With one hundred times the tensile strength of steel, thermal conductivity better than all but the purest diamond, and electrical conductivity similar to copper, but with the ability to carry much higher currents, they seem to be a very interesting material. Carbon nanotubes (CNTs) have been proposed as a novel solid phase extractor for various inorganic and organic materials at trace levels. [7]

Carbon nanotubes (CNTs) have become attractive materials, since its discovery in 1991, because of their novel structure characteristics. [8-18] Recently, Carbon nanotubes as an adsorbent for the preconcentration of traces heavy metals have become very popular. [19-29]

In this article, we have modified MWCNTs using NR and applied this functionalized material to SPE coupled with FAAS for simultaneously determination of Mn(II) and Sn(IV) in the water samples from rivers located in industrial and nonindustrial areas. Also for the validity of the method the Mn(II) and Sn(IV) levels in the final solutions were determined by ICP-AES using the general procedures.

RESULTS AND DISCUSSION

To obtain a sufficiently high efficiency of a SPE procedure, the study was focused on optimization of the extraction parameters containing, pH, amounts of NR and adsorbent, sample volume, elution conditions such as volume and concentration of eluent, flow rate of solution and matrix ions.

Effect of pH

The pH value plays an important role with respect to the adsorption of different ions on CNTs.[25] To evaluate the effect of pH on the extraction efficiency of Mn(II) and Sn(IV) as NR chelates adsorb on multiwalled carbon nanotubes, the pH of the sample solutions, were adjusted to fit in the range of 2–10. It is observable in Fig. 1, quantitative recoveries (>95%) were obtained for all studied ions at the pH range of 6–8. So, the pH 7 was selected for all subsequent studies.
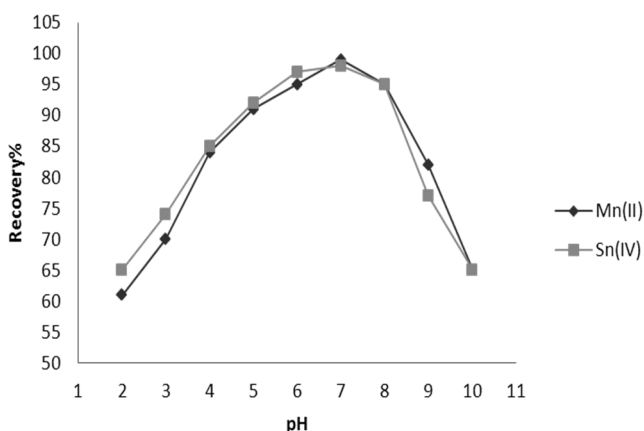
Figure 1. The effect of pH on the recoveries of the metal ions (N= 3.0.)

Effect of eluent type

The elution of the absorbed analytes could be achieved by using an appropriate eluent solution capable of effectively striping them from the MWCNTs and bring them into the solution [26]. Thus, the effects of various eluents (nitric acid, hydrochloric acid and acetic acid) on the recoveries of Mn(II) and Sn(IV) ions from multiwalled carbon nanotubes modified with NR were also investigated. The results are shown in Table 1. The results indicated that 3 mol L^{-1} HCl was sufficient for quantitative elution (>95%). Furthermore, the influence of eluent volume (1–5 mL) on the recoveries was studied by using 3 mol L^{-1} HCl. By adding 2 mL of 3 mol L^{-1} HCl, quantitative recoveries

were obtained for all analyte ions. The recoveries were not quantitative for the other eluents listed in Table 1. Therefore, 2 mL of 3 mol L^{-1} HCl was used as eluent for further work.

Table 1. The effect of various eluents on the analyte ion recoveries.

Eluent Recovery %		
	Mn(II)	Sn(IV)
1 mol L^{-1} HCl	92±0.4	91±1.3
2 mol L^{-1} HCl	95±3.0	95±2.4
3 mol L^{-1} HCl	99±2.2	98±1.6
1 mol L^{-1} HNO$_3$	85±2.8	88±1.2
2 mol L^{-1} HNO$_3$	89±1.1	91±1.1
3 mol L^{-1} HNO$_3$	91±3.0	90±2.0
1 mol L^{-1} CH$_3$COOH	67±2.6	73±3.1
2 mol L^{-1} CH$_3$COOH	73±1.2	78±2.5
3 mol L^{-1} CH$_3$COOH	77±1.3	68±2.5

Effect of amount of chelating agent

To evaluate the effect of ligand on the recovery of metal ions, different amounts of NR solution (3×10^{-4} mol L^{-1}) in the range of 0-5 mL was investigated. As presented in Fig. 2, the recoveries of analyte ions increased with increasing amounts of NR added and reached a constant value over 95% with at least 3 mL. The recovery values of analytes were quantitative at the amounts of ligand range of 3-5 mL. Hence, 3 mL of ligand was selected for subsequent studies. At lower concentrations, the amount of ligand is insufficient to extract all the analyte in the solution. But at higher concentrations, all the analyte species were used, thus, process of complex formation was stop and the percentage of recoveries remained nearly constant, in other words, the limiting factor is analyte concentration.
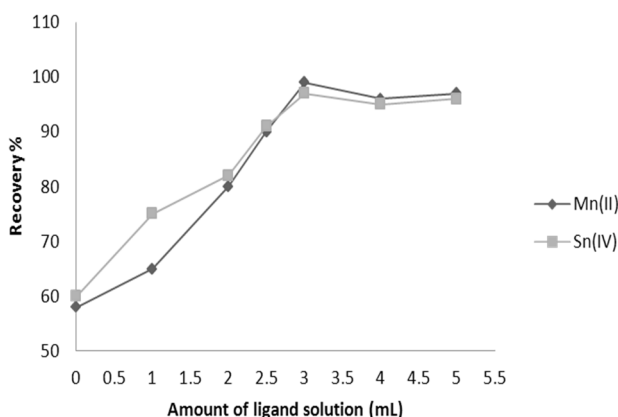
Figure 2. Effect of amount of ligand solution on the recoveries of analytes.

Effect of amounts of adsorbent (MWCNTs)

The amount of solid phase extraction material is another important factor on the column studies to obtain quantitative recoveries. On the other hand, an excess amount of the adsorbent can also prevent the quantitative elution of the retained metals by a small volume of the eluent. To estimate the impact of adsorbent mass on the recovery of metal ions, different amounts of adsorbent (50-400 mg), packed into an SPE column, were investigated, following the preconcentration procedure. The recoveries of metal ions increased with increasing amounts of adsorbent. For less than 200 mg of adsorbent, the recoveries amounts are not quantitative and it is due to by-passing of the liquid in the SPE column [19]. Thus absorbent weight of 200 mg was found to be suitable for this purpose.

Effect of the sample volume

The preconcentration and separation of the analytes are usually performed at a lower concentration. In order to improve the relative sensitivity of the procedure when determining very low concentration of analytes, a relative large sample volume is usually suggested. Therefore, the maximum volume of sample solution was investigated by increasing the volume of metal ion solution by passing 100–600 mL of sample solutions. The effects of sample volumes on the recoveries of the two analytes are shown in Figure 3. The results showed that the maximum sample volume could be up to 500 mL with the recovery >95%. Therefore, 500 mL of sample solution was adopted for the preconcentration of analytes from sample solutions. The preconcentration factor (PF) is calculated by the ratio of the highest sample volume (500 mL) and the lowest eluent volume (2 mL). The preconcentration factor was calculated as 250.
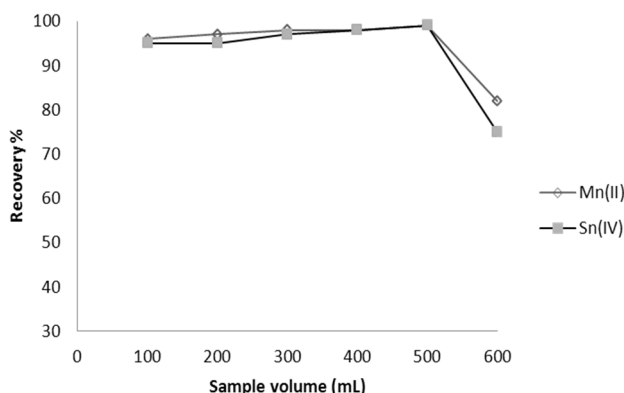
Figure 3. Effect of sample volume on the recoveries of analytes (N= 3.0)

Flow rates of sample and eluent solutions

The influences of the flow rates of sample and eluent solutions on the retentions of Mn(II) and Sn(IV) were also investigated keeping other conditions constant. Low flow rates can be time consuming. The flow rates were investigated in the range of 1–5 mL min−1 and under the optimum conditions (pH and eluent type). It was found when the flow rates of the sample and eluent solutions were at the range of 1.0-3.0 and 1.0-4.0 mL min^{-1}, The recoveries of analytes were quantitative. At higher flow rates, there was a decrease in the recovery in that there was not sufficient contact time between MWCNTs and sample solution. Therefore, all the studies were carried out for flow rates of sample and eluent solutions at a flow rate of 3.0 mL/min.

Effect of foreign ions

The influences of possible matrix ions in the environmental samples and some transition metals on the recoveries of analytes on multiwalled carbon nanotubes were also examined.

The obtained results were presented in Table 2. The tolerance limit is defined as ions had no significant interferences in the preconcentration and determination of the analyses. This is due to the low adsorbing capacity or rates for interfering ions. These results demonstrate that the method has a good tolerance to interference and is suitable for Mn(II) and Sn(IV) detection.

Table 2. Effect of interfering ions on the recoveries of the analytes (N= 3).

Ion	Concentration (mg L^{-1})	Recovery (%)[a]	
		Mn(II)	Sn(IV)
Ag^+, K^+, Na^+, Cl^-, Li^+, I^-	10000	98±1	95±1
SO_4^{-2}, Ca^{2+}, CO_3^{-2}, Br^-, $C_2O_4^{-2}$	8000	98±1	97±2
Mg^{2+}, F^-	6000	96±2	98±1
HCO_3^{-2}, NO_3,	3000	99±1	97±2
PO_4^{-3}, CH_3COO^-	1500	95±2	96±3
Ni^{2+}, Pb^{2+}	500	96±3	95±1
Cd^{2+}, Mo^{5+}	250	98±2	98±2
Pd^{2+}	100	95±1	98±3
Hg^{2+}, Al^{3+}, Cr^{3+}	10	97±2	99±2

[a] Mean ± standard deviations.

Adsorption capacity

For investigation of the adsorption capacity of multiwalled carbon nanotubes, 0.1 g MWCNTs was added to 50 ml of solution containing 1.0 mg of metal ion at pH 7.0. After shaking for 30 min, the mixture was filtered. Ten milliliters of the supernatant solution was diluted to 100 ml and determined by flame atomic absorption spectrometry. This procedure was repeated for each analyte ions separately. The capacity of modified MWCNTs for Mn(II) and Sn(IV) was found to be 86.6 and 77.8 mg g^{-1}, respectively.

Analytical performance

Using the optimized experimental conditions, calibration curves of enrichment process were linear in the range of 0.4-100 µg L^{-1} and 0.6-150 µg L^{-1} for Mn(II) and Sn(IV), respectively. The detection limits, based on three times the standard deviation of 10 runs of blank solution, were found to be 0.12 and 0.16 µg L^{-1} for Mn(II) and Sn(IV), respectively. The relative standard deviation (RSD), nine determinations of 1.0 µg L^{-1} of Mn(II) and Sn(IV) were 4.0 and 2.6%, respectively (N=9). The correlation coefficients for Mn(II) and Sn(IV) were 0.9997, 0.9995, respectively. The preconcentration factor for the proposed method was 250.

Analytical applications

A solid phase extraction method was applied to determination of trace Mn(II) and Sn(IV) in water samples from river located in industrial and nonindustrial areas. Various amounts of analytes were also spiked to these water samples. The results are given in Table 3 and Table 4. A good agreement was obtained between the added and measured Mn(II) and Sn(IV) amounts. The accuracy of the method was verified by the analysis of samples spiked with known amounts of the analytes. These results indicated the suitability of NR-MWCNT for selective SPE and determination of trace Mn(II) and Sn(IV) in environmental samples. The river water samples were also analysed by (ICP-AES). As Table 3 and Table 4. shows there is a good agreement between the results obtained by the proposed method with those obtained by the ICP-AES. This reveals the capability of the method for determination of Mn(II) and Sn(IV) in all real samples without considerable error. In Table 5, the relative comparison of analytical performance with those reported in the literature [26-29].

Table 3. The results for determination of Pd(II) and Cd(II)
in various river water samples by FAAS

Sample	Added (µg L^{-1})		Found [a] (µg L^{-1})		Recovery (%)		RSD(%)	
	Mn(II)	Sn(IV)	Mn(II)	Sn(IV)	Mn(II)	Sn(IV)	Mn(II)	Sn(IV)
River Water[b]	-	-	71.48±0.06	84.28±0.02	-	-	1.1	2.3
	100	100	173.93±0.02	182.52±0.03	101.43	99.04	1.1	1.4
	200	200	275.12±0.04	285.65±0.05	101.34	100.48	1.3	1.3
River Water[c]	-	-	65.25±0.05	50.65±0.04	-	-	3.0	2.1
	100	100	164.79±0.07	153.56 ±0.09	99.72	101.93	2.9	2.7
	200	200	265.61±0.05	241.41±0.09	100.51	96.31	3.1	2.5
River Water[d]	-	-	61.14±0.01	67.19±0.02	-	-	1.9	2.6
	100	100	162.22±0.02	164.74±0.01	100.67	98.53	1.5	2.2
	200	200	263.16±0.04	260.11±0.03	100.77	97.35	2.8	1.5
River water[e]	-	-	5.31±0.05	12.61±0.05	-	-	1.8	2.1
	100	100	103.31±0.03	109.64 ±0.07	98.10	97.36	2.6	1.5
	200	200	205.16±0.09	211.51±0.09	99.92	99.48	1.5	2.3

[a] $\bar{x} \pm ts \sqrt{n}$ at 95% confidence (N = 5)
[b] From karoon river, located in a industrial area
[c] From zayande rood river, located in a industrial area
[d] From khour musa, located in a industrial area
[e] From pole zohre located in a nonindustrial area

Table 4. The results for determination of Pd(II) and Cd(II)
in various river water samples by ICP-AES.

Sample	Added (µg L^{-1})		Found [a] (µg L^{-1})		Recovery (%)		RSD(%)	
	Mn(II)	Sn(IV)	Mn(II)	Sn(IV)	Mn(II)	Sn(IV)	Mn(II)	Sn(IV)
River Water[b]	-	-	71.35 ±0.01	84.15±0.01	-	-	2.1	2.1
	100	100	173.62±0.05	181.85±0.03	101..32	98.75	1.1	1.9
	200	200	275.12±0.04	285.65±0.05	101.51	100.79	1.2	2.1
River Water[c]	-	-	65.25±0.05	50.65±0.04	-	-	1.2	2.1
	100	100	164.79±0.07	153.56 ±0.09	99.56	100.89	2.4	2.7
	200	200	265.61±0.05	241.41±0.09	100.04	99.18	1.2	1.7
River Water[d]	-	-	61.14±0.01	67.19±0.02	-	-	1.8	2.1
	100	100	162.22±0.02	164.74±0.01	102.47	99.14	1.5	2.2
	200	200	263.16±0.04	260.11±0.03	101.99	97.17	1.2	2.9
River water[e]	-	-	5.31±0.05	12.61±0.05	-	-	1.0	2.0
	100	100	103.31±0.03	109.64 ±0.07	97.66	101.03	2.2	2.9
	200	200	205.16±0.09	211.51±0.09	99.89	100.27	1.6	3.1

[a] $\bar{x} \pm ts \sqrt{n}$ at 95% confidence (N = 5)
[b] From karoon river, located in a industrial area
[c] From zayande rood river, located in a industrial area
[d] From khour musa, located in a industrial area
[e] From pole zohre located in a nonindustrial area

Table 5. Comparison of the proposed method with recent studies reported in literature using solid phase extraction

Analytes	Medium	Eluent (mol L^{-1})	PF[a]	LOD[b] (µg L^{-1})	Reference
Cu^{2+} , Cd^{2+} , Mn^{2+}	pH=9	1 (HNO_3)	28.9	0.13–0.58	26
Mn^{2+}	pH=10	0.5 (HCl)	17	0.7	27
Sn^{2+}, Sn^{4+}	pH=2	1.0 (HNO_3)	100	0.7-1.1	28
Mn^{2+}, Pb^{2+}	pH=9	2.0 (HNO_3)	-	0.6-1	29
Mn^{2+}, Sn^{4+}	pH=7	3 (HCl)	250	0.12-0.16	This work

[a] PF: Preconcentration factor
[b] LOD: Limit of detection

EXPERIMENTAL

Apparatus

A Metrohm pH-meter (model 691, Switzerland) was used in order to adjust the pH at desirable values. A Chemtech Analytical Instrument model CTA-3000 atomic absorption spectrometer (Bedford, England) equipped with a flame burner was used for analysis of the understudy metals, including lamp currents and wavelength were those recommended by the manufacturer. All metals were measured under optimized operating conditions by FAAS with an air–acetylene flame. Inductively coupled plasma (ICP) model Varian Liberty 150AX Turbo was used for the validity of concentration determination of the analyte.

Standard solutions and reagents

Analytical reagent-grade chemicals were used in this work. All the plastic and glassware were cleaned by soaking in 10% HNO_3 solution and then rinsed with distilled water prior to use. Standard solutions (1000 mg L^{-1}) of Mn(II) and Sn(IV) ions were prepared from high purity compounds, supplied by E. Merck (Darmstadt, Germany). The working standard solutions were prepared by diluting stock standard solution. A 3×10^{-4} mol L^{-1} solution of (NR) reagent was prepared by dissolving 0.008 gr of it it in 100 mL water. McIlvaine's buffer solution in the pH range of 2-10 was used to adjust pH values by adding 16.47 mL of Na_2HPO_4 and 3.53 mL of acid citric. Multiwalled carbon nanotube was purchased from Aldrich, (Milwaukee, WI, USA). The BET (Brunauer–Emmett-Teller) surface area and density of nanotubes were 300 m^2 g^{-1} and 2.1 g mL^{-1}, respectively.

Preparation of the column

Two-hundred milligrams of multiwalled carbon nanotubes was loaded into an SPE column (10 mm × 150 mm). A polypropylene frit was placed at each end of the column to prevent loss of the adsorbent. Before use, 3 mol L^{-1} HCl were passed through the column to clean it.

Recommended procedure

A standard solution containing 0.4-100 µg L^{-1} of Mn (II) and 0.6-150 µg L^{-1} of Sn(IV) and the pH value was adjusted to 7 with McIlvaine's buffer solution. then NR was added to form the [metal-(NR)] chelates. After that, the solutions passed through the column gravitationally. Subsequently, metal ions retained on the MWCNT, were eluted with the desired volume and concentration of eluent. The eluent was analyzed for the determination of metal concentrations by flame atomic absorption spectrometry and inductively coupled plasma atomic emission spectrometry (ICP-AES).

Sample preparations

The river water samples were collected from the rivers located in industrial and non industrial areas. The water samples were filtered through a 0.45 µm PTFE Millipore filter. After adjusting to the desired pH values, the solutions were passed through the column gravitationally.

CONCLUSION

The proposed method offers a simple, inexpensive, selective and sensitive method for the enrichment of Mn(II) and Sn(IV) using MWCNTs modified by NR as a solid-phase extractant for SPE coupled with FAAS. The proposed method was proved to be simple, rapid and reliable and could be used for studied metal ions determination in environmental samples. The high accuracy of the proposed method was confirmed by recovery test with standard addition method. The possible interference of some important ions was investigated and no important interference was encountered. The MWCNTs has great potential as an adsorbent for the preconcentration and determination of trace metal ions in complex samples. The accuracy and validity of the method is provable by the comparison among the resultant results of the proposed method and those obtained by ICP-AES method (Table 3 and Table 4). High sensitivity and selectivity, and also the good detection limits and high preconcentration factor (PF=250.0) which is comparable or higher than the other solid-phase extraction methods in literature (mentioned at section 2.10)

REFERENCES

1. L. Prusa, J. Dedina, J. Kratzer, *Anal. Chim. Acta*, **2013**, *804,* 50.
2. I. Hagarová, M. Bujdoš, P. Matúš, J. Kubová, *Spectrochim. Acta. A*, **2013**, *88*, 75.
3. A. Khajeh, E. Sanchooli, *J. Food. Compos. Anal*, **2010**, *23*, 677.
4. S.V. De Azevedo, F.R. Moreira, R.C. Campos, *Anal. Chim. Acta*. **2013**, *46*, 245.
5. C.H. Latorre, J.A. Méndez, J.B. García, S.G. Martín, R.M.P. Crecente, *Anal. Chim. Acta*. **2012**, *749*, 16.
6. L. Xi, Zh. Zhao-Hui, Zh. Hua-Bin, H. Yu-Fang, Y. Xiao, N. Li-Hua, *Chin. J. Anal. Chem*, **2011**, *39*, 839.
7. M. Tuzen, K.O. Saygi, C. Usta, M. Soylak, *Biores. Technol*, **2008**, *99*, 1563.
8. S. Iijama, *Nature*, **1991**, *354*, 56.
9. S. Iijama, T. Ichihashi, *Nature*, **1993**, *363*, 603.
10. C. Pan, S. Xu, H. Zou, Zh. Guo, Y. Zhang, B. Guo, *J. Am. Soc. Mass. Spectrom*. **2005**, *16*, 263.
11. N. Pourreza, K. Sheikhnajdi, *Talanta*, **2012**, *99*, 507.
12. M. Soylak, Y.M, Unsal, *Food. Chem. Toxicol,* **2010**, *48*, 1511.
13. Y. Liu, Y. Li, Zh. Q. Wu, X.P. Yan, *Talanta*, **2009**, *79*, 1464.
14. N. Rastkari, R. Ahmadkhaniha, *J. Chromatogr. A*, **2013**, *1286*, 22.
15. A. Duran, M. Tuzen, M. Soylak, *J. Hazard. Mater.* **2009**, *169,* 466.
16. J. Li, Q. Su, K.Y. Li , Ch. F. Sun, W.B. Zhang, *Food. Chem*, **2013**, *141*, 3714.
17. E. Zakharchenko, O. Mokhodoeva, D. Malikov, N. Molochnikova, Y. Kulyako. G. Myasoedova, *Proc. Chem,* **2012**, *7*, 268.
18. L. Guo, H.K. Lee, *J. Chromatogr. A*, **2011**, *1218*, 9321.
19. M. Moazzen, R. Ahmadkhaniha, M. Es'haghi Gorji. M. Yunesian, N. Rastkari. *Talanta*, **2013***, 115*, 957.
20. Sh. K. Wadhwa, M. Tuzen, K. Gul Kazi, M. Soylak, *Talanta*. **2013**, *116*, 205.
21. P. Kueseng, J. Pawliszyn, *J. Chromatogr*. A, **2013**, *1317*, 199.
22. B. Dai, M. Cao, G. Fang, B. Liu, X. Dong, M. Pan, Sh. Wang, *J. Hazard. Mater,* **2012**, *219–220*, 103.
23. X. Liu, X. Wang, F. Tan, H. Zhao, X. Quan, J. Chen, L. Li, *Anal. Chim. Acta*, **2012**, *727*, 26.
24. X. Chen, Zh. Zhang, X. Yang, J. Li, Y. Liu, H. Chen, W. Rao, Sh. Yao, *Talanta*, **2012**, *99*, 959.
25. Zh. Zang, Zh. Hu, Zh. Li, Q. He, X. Chang, *J. Hazard. Mater*, **2009**, *172*, 958.
26. C. Karadas, T. Turhan, D. Kara, *Food. Chem*, **2013**, *141,* 655.
27. V.A. Lemos, C.G. Novaes, M.A. Bezerra, *J. Food Compos. Anal*, **2009**, *22*, 337.
28. R. Caldorin, A.A. Menegario, *Microchim. Acta*, **2007**, *157*, 201.
29. Gh. Daneshvar Tarigh, F. Shemirani, *Talanta*. **2013**, *115*, 744.

CLOUD POINT EXTRACTION AND SPECTRO-PHOTOMETRIC DETERMINATION OF As(III) USING BRILLIANT BLACK BN AS AN EXTRACTION AGENT IN WATER SAMPLES

SHAHRAM NEKOUEI[a,*], FARZIN NEKOUEI[a]

ABSTRACT. Cloud point methodology was successfully used for the extraction of trace amounts of arsenic (III) s a prior step to their determination by spectrophotometry. For the proposed method, Brilliant Black BN (BBB), trioctylamine (TOA), Triton X-114, and NaCl were applied as chelating, sensitizing agent, extraction and co-extraction agents, respectively. A linear calibration curve in the range of 8-1000 µg L^{-1} of Brilliant Black BN (BBB) was acquired. Under the optimized conditions, the limit of detection (LOD) was 2.4 µg L^{-1} and the relative standard deviation (RSD) for 2.4,100 and 400 µg L^{-1} were 1.26, 2.05 and 1.18, respectively (n = 11). The application of the work is determination of arsenic (lll) quantities in the various samples by spectrophotometric method. In addition, in this work TOA plays the same role of cationic surfactant and as a novel ion pairing reagent that was innovatively used instead of common cationic surfactants such as cetyltrimethylammonium bromide (CTAB).

Keywords: Cloud point extraction; Brilliant Black BN (BBB); trioctylamine (TOA); water samples; Spectrophotometry, As(III)

INTRODUCTION

Arsenic (As) is widely distributed in the environment, water, soils, sediments and rocks in its different forms (As(III), As(V) and organic species) [1]. Occupational exposure and arsenic poisoning may occur in persons working in industries involving the use of inorganic arsenic and its compounds, such as wood preservation, glass production, nonferrous metal alloys, and electronic semiconductor manufacturing. Inorganic arsenic is also found in coke oven emissions associated with the smelter industry [2]. It was ranked as the No. 1 of

---

[a] *Young Researchers and Elite Club, Science and Research Branch, Islamic Azad University, Tehran, Iran*
* *Corresponding author: sh.nekouei@hotmail.com*

hazardous element and has serious effects on plants, animals and human health [3]. Millions of people worldwide are exposed to arsenic in their drinking water and ingested arsenic is an established cause of bladder, lung, and skin cancer. In addition to cancer, arsenic in water has also been associated with cardiovascular disease, skin lesions, diabetes, reproductive disorders, cognitive deficits in children and other health effects [4]. The linkage between arsenic contamination in water, arsenic concentration and accumulation in various biological samples, and oxidative DNA damage, has been proved [5]. Exposing to arsenic induces increases in DNA double strand breaks in both cell lines [6]. Because of the importance of this issue, a lot of researchers have done studies regarding measuring of Arsenic by various methods [7]. Also there are some works previously reported regarding determination of arsenic by spectrophotometric methods in the literature [13-16].

Cloud point extraction (CPE) is an outstanding alternative to conventional solvent extraction method because it produces high extraction efficiencies and pre-concentration factors, by using inexpensive and non-toxic reagents [3].

In the last decade, the increase of attention and interest upon the use of aqueous micellar solution has been found in field of separation science [17]. The cloud point extraction (CPE) technique has also been applied as a procedure for determination and removal of dyes and pigments as well as analyzing metals. [18,19]. In the present work, we applied CPE for the determination of arsenic (III) quantities in the various samples by BBB as the ligand which has made the work as a novel method.

RESULTS AND DISCUSSION

In this study, As (III) ion interacted with Brilliant Black BN, an anionic dye, which led to the formation of (As-Brilliant Black BN) complex. This complex was extracted by mixed-micelle mediated extraction through the ion pairing reagent (TOA) and non-ionic (Triton-X114) surfactants. The absorption spectra of As-BBB-TOA complexation showed a maximum absorption band at 616 nm. To obtain the maximum absorbance and sensitivity, we need to optimize various conditions which can affect the extraction. Hence, the effects of various operating conditions have been investigated and the optimum concentrations have been established for CPE.

In the present work, in order to study As (III) ion, a procedure is adopted which As (III) was used in the presence of BBB ion as a chelating agent. The interaction between arsenic and BBB that has four anionic sites to interaction with target metals led to the formation of [As-BBB]$^{1-}$ anionic complex. With regard to the fact that, hydrophobic ion-associated complexes could be more

efficiently extracted into surfactant-rich phase than ionic ion-associated complexes, small amount of ion pairing reagent (TOA) also as the sensitizing agent and a cationic auxiliary ligand was added. The addition of ion pairing reagent (sensitizing agent) improves the selectivity and sensitivity of the metal determinations. So, TOA+ as sensitivity enhancement agent was added, producing a neutral and stable ion-pair complex (ternary ion-association system), [As-BBB-TOA]. Most importantly, a colored ligand such as BBB takes the solution to visible area and as a matter of fact, in spectrophotometric method, the study of visible absorption area would be the most convenient and accurate type of detection because numerous solvents and reagents used in CPE and liquid-liquid extraction (LLE) have adsorption spectra in UV area which interfere in the determination of the goal analytes. After that, we used TOA as the ion pairing reagent, cationic surfactant, sensitizing agent and a cationic auxiliary ligand. ion pairing reagent can interact with dye and/or the metal–dye complex as an individual molecule or aggregates. With regard to the fact that, hydrophobic ion-associated complexes could be more efficiently extracted into surfactant-rich phase than ionic ion-associated complexes, small amount of ion pairing reagent (TOA) was added. The addition of sensitizing agent improves the selectivity and sensitivity of the metal determinations. In the last step, NaCl was used as the electrolyte to increases the efficient extraction.

Effect of pH

pH is an important analytical parameter that significantly influence the formation of metal–ligand complex. Therefore, in order to acquire the favorable preconcentration efficiencies, the pH values were studied in the ranges of 1.0–8.0. For this range we studied the various values of Na_2HPO_4 with acid citric to make the buffer to reach the desired pH.
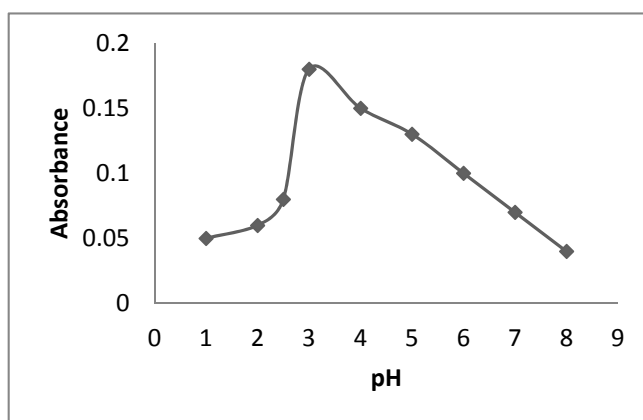
Figure 1. The concentration effect of pH on CPE

Thus the highest absorbance was obtained at pH 3. It is shown in Fig. 1. Probably, at lower pH values the rate of complex formation is low and at higher pH values the complex decomposes. Hereby, pH 3 was selected for the further experiments by 1.5 mL of *McIlvaine's buffer* solution.

Effect of Brilliant Black BN dye concentration

For studying the effect of Brilliant Black BN on extraction of Arsenic (50 µg L^{-1}), a solution containing Arsenic and various amounts of Brilliant Black BN was provided. The extraction efficiency was the highest when 1.33×10^{-5} mol L^{-1} (2ml) of Brilliant Black BN was applied. Thus, it was chosen for subsequent experiment. As it is observable in Fig. 2, at higher concentrations the absorbance declined, because the excessive Brilliant Black BN could be co-extracted into the surfactant rich phase, thus decreased the extraction efficiency of target complex.
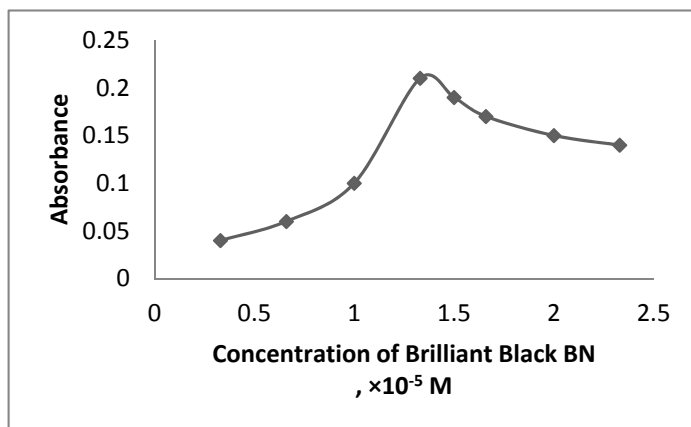
Figure 2. The concentration effect of Brilliant Black BN on CPE

Effect of ion pairing reagent concentration

With regard to the fact that, hydrophobic ion-associated complexes could be more efficiently extracted into surfactant-rich phase than ionic ion-associated complexes, small amount of TOA$^+$ was added in the presence of 50 µg L^{-1} of arsenic.

Amines lead to aminium salts in the presence of acids like HCl, HBr and HI due to protonation.

$$TOA + HCl \longrightarrow TOA^+ Cl^- \tag{1}$$

The result was the formation of [As-(BBB)-TOA] hydrophobic complex. Also, in order to improve the sensitivity and selectivity as well as increasing the efficiency of CPE, initially, three amines such trioctylamine (TOA), triethyamin (TEA) and tripropylamine (TPA) were considered and investigated in the range of 0.05-0.4% v/v. The best extraction yield was obtained in presence of TOA. Therefore, to the use of TOA was decided for further studies. The effect of TOA concentration, used as sensitive improving auxiliary ligand, on the extraction yield of As(III) was studied in range of 0.05-0.4% v/v. The effect of concentration of TOA as well as TEA and TPA on extraction yield is shown in Fig. 3. The extraction yield gradually increased by increasing TOA concentration up to 0.2% v/v, and quickly declined at higher concentrations. This is probably because of an increase in the blank absorbance and decrease the absorbance of ternary ion association also, excessive presence of TOA^+ in the solution can act as a competitor for As(III) in complexation with BBB. As a result, the 0.2% v/v TOA solution was selected as the optimal ion pairing reagent concentration.
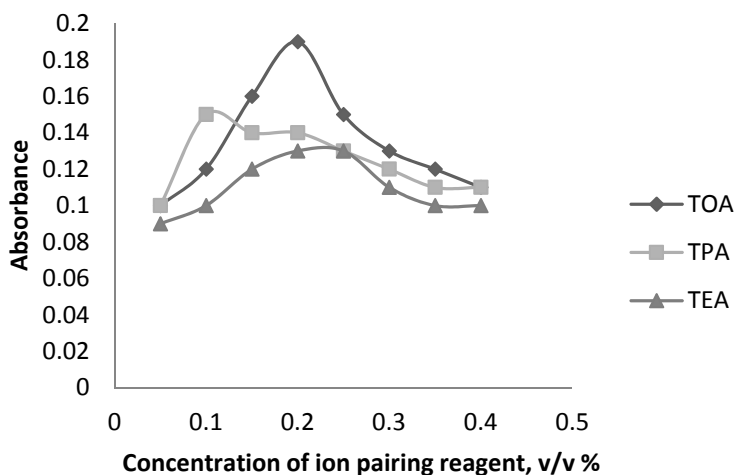
Figure 3. The concentration effect of ion pairing reagent on CPE

Effect of non-ionic surfactants

Optimization of this parameter was carried out in order to accomplish a minimum desirable surfactant concentration with maximum extraction efficiency. some non-ionic surfactants including Triton X-114, Triton X-100 and Triton X- 45 (0.1-0.45% (v/v)) were applied to CPE. Among them Triton X-114 was selected due to its higher extraction efficiency. Triton X-114 was chosen as

a surfactant due to its low cloud point temperature and high density of surfactant-rich phase, this facilities phase separation by centrifugation. So, for further studies it was chosen. With increasing the surfactant concentration up to 0.3% (v/v) the signal increased. Thus, it was used as optimum concentration. At lower concentrations, the extraction efficiency of the complexes is low, probably because of an inadequacy in the assemblies to entrap the hydrophobic complex quantitatively. The preconcentration was decreased at higher concentrations due to increase in the volume of the surfactant-rich phase. Therefore, the measured absorbance as a result of sensitivity is decreased. The results are shown in Fig. 4.
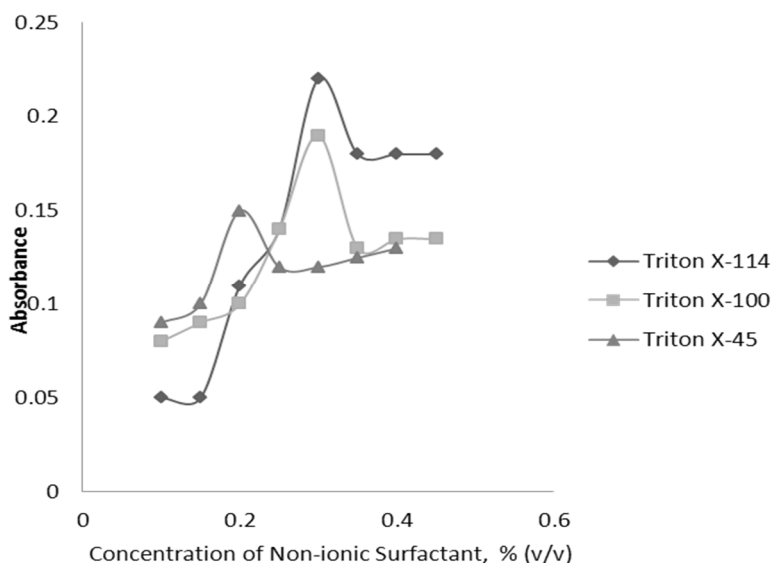
Figure 4. The concentration effect of Non-ionic Surfactant on CPE

Effect of ionic salt concentration

To investigate the influence of electrolyte concentration on the extraction efficiency, 0.1 mol L^{-1} NaCl and KCl were surveyed to solution in various amounts as the co-extraction agents. NaCl showed a more increase on the absorbance of solution. Thus, it was chosen for the further studies. It increased the extraction efficiency of arsenic up to 1.0×10^{-2} mol L^{-1} and was chosen to next studies. The salting-out ability of the cations follows the Hofmeister series ($Na^+ > K^+$) and can be related to the ions from Gibbs' free energy of hydration. (Fig. 5)

348
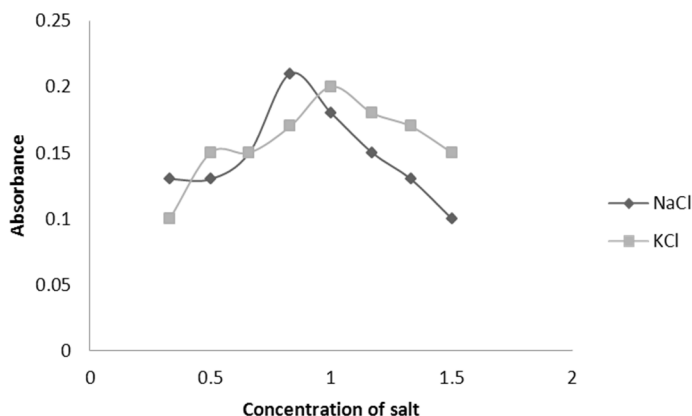
Figure 5. The concentration effect of salt on CPE

Effect of incubation time and centrifuge time and rate

For investigation of effective preconcentration and easy phase separation, the centrifugation time, equilibration temperature and incubation time were optimized. The results demonstrated that centrifuging for 5 min at 3500 rpm leading to the highest extraction of As(III). Additionally, the influence of time on the extraction of As(III) was surveyed in the time range of 5-20 min which the maximum absorbance was acquired 10 min. The influence of equilibration temperature in the range of 20-60 °C was investigated. It was established that 45 °C is sufficient for the quantitative analysis.

Analytical performance

Analytical characteristic data of the proposed CPE for As(III) was studied. In the range of 8 to 1000 µg L^{-1} the calibration curve for arsenic was linear. The limit of detection (LOD) was 2.4 µg L^{-1} and was calculated according to 3 S_{blank} /s, where S blank was obtained from the standard deviation for 10 replicate measurements of a blank solution, and s is the slope of the calibration graph. The regression equation was acquired by the least square method is $A = 2.19 \times 10^{-3} C_{As} + 1.75 \times 10^{-2}$ for 8-1000 µg L^{-1} of As(III) with a correlation coefficient of 0.998 (n = 10), where A is the absorbance and C_{As} shows the concentration of As(III) in µg L^{-1}. The relative standard deviation (RSD) at 2.4 and 100 and 400 µg L^{-1} were 1.26, 2.05 and 1.18, respectively (n = 11). The preconcentration factor was 21.4.

Interference studies

The validity of the method was assessed by investigating the effect of various foreign ions which are likely to interfere in the determination.

Usually coexisting ions may influence on objective determination of As(III) by CPE. To verify this assumption, solutions containing 100 µg L^{-1} of As(III) were taken with different amounts of foreign ions and recommended procedure was followed. The results were summarized in Table 1.

Table 1. The effect of other species on the determination of 100 µg L^{-1} of As(III)

Foreign ions	Tolerance limit (µg mL^{-1})
Cl$^-$, Na$^+$, K$^+$, NH$_4^+$, NO$_3^-$	1000
Cu^{2+}, Pb^{2+},Li$^+$, Ca^{2+}	800
Ag$^+$, HCO$_3^-$, Cd^{2+}	500
Br$^-$, HPO$_4^{2-}$	250
Ni^{2+}, Sn^{2+}, Co^{2+}	100
Al^{3+} , Fe^{3+}, Cr^{6+}, Sb^{3+}	50

APPLICATION

The proposed method was employed for the determination of As(III) in various water samples. Five replicates determinations were carried out and the obtained results (Table 2) were satisfactory. The high percentage recovery was confirmed the accuracy, precision and the independence of the procedure from the matrix interference.

Table 2. Determination of Arsenic in different Water samples and recovery tests

Sample	As (III) added (µg L^{-1})	As (III) Found [a] (µg L^{-1})	Recovery (%)	RSD (%)
River water [b]	-	61.17 ± 0.12	-	2.1
	50	110.58 ± 0.16	99.47	1.6
	100	159.15 ± .080	98.75	2.9
River water [c]	-	14.96 ± 0.51	-	1.1
	50	62.76 ± 0.17	96.61	3.0
	100	112.50 ± 0.11	97.86	2.5
Tap water	-	8.21 ± 0.16	-	2.1
	50	58.14 ± 0.10	99.88	2.1
	100	110.51 ± 0.19	102.12	2.3
Well water	-	20.15 ± 0.03	-	2.1
	50	71.81 ± 0.17	102.37	1.7
	100	118.60 ± 0.04	98.81	1.8
Spring water	-	22.17 ± 0.09	-	2.0
	50	70.84± 0.18	98.16	2.5
	100	121.15 ± 0.04	99.16	3.0

[a] $\bar{x} \pm ts\sqrt{n}$ at 95% confidence (n = 5)
[b] zayande rood river, Esfahan (located in an industrial area)
[c] beshar river-tang-e-sorkh village branch(located in a nonindustrial area)

EXPERIMENTAL

Apparatus

Absorption spectra and absorbance measurements were made by a Shimadzu UV-1800, UV–Vis spectrophotometer using 1 cm quartz cells (1.0 mL). A Metrohm digital pH meter (model 691) with a combined glass electrode was applied to measure pH values. A Hettich universal 320 centrifuge was used to hasten the phase separation.

Standard solutions and reagents

The non-ionic surfactant Triton X-114 (3%, v/v) (Sigma-Aldrich, Steinheim, Germany) was used without further purification. Stock standard solution of Arsenic was prepared from the 1000 mg L^{-1} As(III) standard by dissolving appropriate amount of As$_2$O$_3$ (Merck, Darmstadt, Germany) in 3 M NaOH and pH 7.0 with 5 M HCl solution. The 1.0×10^{-4} mol L^{-1} of Brilliant Black BN(Merck, Germany), solution was obtained by dissolving 0.0086 g of it in 100 ml water. A 3% v/v stock solution of trioctylamine (TOA) (Sigma-Aldrich) was attained by diluting 3.0 mL of the reagent to 100 mL water containing 1 mL of HCl (0.1 mol L^{-1}) in a volumetric flask. The McIlvaine's buffer solution was provided by 4.11 ml of 0.2 M Na$_2$HPO$_4$ in 15.89 ml of 0.1 M citric acid. Stock solution of NaCl (1.0×10^{-1}) was prepared by dissolving 0.584 gr of it in distilled water and diluting to 100 mL in a flask.

Procedure

An aliquot of the solution containing As(III) (in the range of 8-1000 µg L^{-1}), 2 mL of Brilliant Black BN (1.0×10^{-4} mol L^{-1}), 1.5 mL of 3% (v/v) of Triton X-114, 1 mL of 3% TOA, 1.75 mL of 0.1 mol L^{-1} of NaCl and 1.5 mL of *McIlvaine's buffer* (pH =3) was transferred into a 15 mL tube, and equilibrated at 45 $^{\circ}$C in a thermostat bath for 10 min. The separation into two phases was accelerated by centrifuging at 3500 rpm for 5 min. The contents of tubes were cooled in an ice-bath for 6 minutes, the surfactant-rich phase became viscous, and the upper aqueous phase was decanted. The surfactant-rich phase of this procedure was dissolved and diluted to 0.7 mL with the methanol and transferred into a quartz cell. The absorbance spectrum of the solution was measured at the 616 nm. A blank solution that was prepared in the same way except that distilled water was used instead of As(III) was also submitted to the same course of action and its spectrum was measured.

Sample preparation

Different water samples were preconcentrated. All the collected samples were spiked with a suitable amount of standard solution of As(III). All the aforementioned samples were filtered through a 0.44µm membrane to remove the suspended and floated particles. Standard addition method was applied so as to calculate recovery values and check accuracy of results.

CONCLUSION

The proposed work was found to be very simple, direct, very selective and sensitive. The limit of detection of the proposed method seems to be satisfactory. The possible interference of some important ions was investigated and no important interference was encountered. The Simplicity in operation, good precision, being economical, low extraction time and the lack of the toxic solvents presence in the method are from other benefits of the work. The proposed method formed hydrophobic ion-associated complex, and the hydrophobic complexes are more extractable by Triton X-114 than the non hydrophobic complexes. Spectrophotometry of such colored ternary complexes probably provides the most sensitive, relatively simple and fast approach to trace metal analysis. This reason is extendable to contrast among the ligandless extractions and those have one or more ligands. In addition, the percentage recoveries were higher than 96% confirming the accuracy. Considering the achieved results, the arsenic quantities, in water samples of the river located in industrial area is considerably higher than the nonindustrial one. And well water and spring water (as unpurified samples) have more quantities of arsenic as compared to tap water (as purified sample). This method gives reasonably good detection limit, wide linearity and also good standard deviations.

ACKNOWLEDGEMENT

REFERENCES

1. J.A. Baig, T.G. Kazi, A.Q. Shah, M.B. Arain, H.I. Afridi, G.A. Kandhro, Sumaira Khan, *Anal. Chim. Acta*, **2009**, *651*, 57.
2. E. Priha, I. Ahonen, P. Oksa, *Am. J. Ind. Med,* **2010***, 39*, 402*.*

3. Baig J.A., Kazi T.G., Shah A.Q., Arain M., Afridi H.I., Kandhro G.A., Sumaira Khan, Naeemullah, A.S. Soomro, **2010**, *Food. Chem. Toxicol*, *48*, 3051.
4. D. Melak, C. Steinmaus, C. Ferreccio, K. Kalman, R. Parra, J. Acevedo, L. Pérez, S. Cortés, A.H.Y. Smith, Yuan, J. Liaw, *Toxical. Appl. Pharm*, **2014**, *274*, 225.
5. P. Hinhumpatch, M. Ruchirawat, P. Navasumrit, K. Chaisatra, J. Promvijit, C. Mahidol, *Toxical. Appl. Pharm*, **2013**, *273*, 569.
6. H. Xie, S. Huang, S. Martin, Sr J.P. Wise, *Mutat. Res-Gen. Tox. En*, **2014**, *760*, 33.
7. G. Yang, W. Xiao-Ru, C. Xuan, Y. Jing-Jing, F. Sen-Chun Lee, *Chinese J Anal Chem*, **2009**, *37*, 1738.
8. Y. Zhang, S. Qiang, J. Sun, T. Hang, M. Song, *J. Chromatogr. B*., **2013**, *917-918*: 93.
9. P. Thambidurai, A.K. Chandrashekhar, D. Chandrasekharam; *Procedia Earth Planet. Sci*, **2013**, *7*, 834.
10. A.H. Pétursdóttir, J. Feldmann, G. Gunnlaugsdóttir, E.M. Krupp, *Food. Chem*, **2014**, *150*, 353.
11. W.R. Cullen, K.J. Reimer, M.M. Moriarty, W.M. Lai, I. Koch, L. Cui, C. Combs, E.M. Krupp, J. Feldmann; *Sci. Total. Environ*, **2014**, *466-467*, 90.
12. C.M.M. Santos, M.A.G. Nunes, I.S. Barbosa, G.L. Santos, M.C. Peso-Aguiar, M.G.A. Korn, E.M. Flores, V.L. Dressler, *Spectrochim. Acta. B*, **2013**, *86*, 108.
13. B. Narayana, T. Cherian, M. Mathew, C. Pasha, *Ind. J. Chem. Tech.* **2006**, *13*, 36.
14. S.F.P. Pereira, S.L.C. Ferreira, G.R. Oliveira, D.C. Palheta, B.C. Barros. *Eclet. Quim.* **2008**, *33*, 23.
15. A. Pillai, G. Sunita, V.K. Gupta, *Anal. Chim. Acta*. **2000**, *408*, 111.
16. T. Cherian, B. Narayana, *Anal. Lett*. **2005**, *38*, 2207.
17. J.H. Harwell, J.F. Scamehorn, "Surfactant Based Separation Processes", Marcel Dekker Inc, New York, 1989: Chapter 1.
18. Sh. Abedi, F. Nekouei, *E. J. Chem*, **2011**, *8*, 1588.
19. R. Mousavi, F. Nekouei, *E. J. Chem*, **2011**, *8*, 1606.

ANTIOXIDANT CONTENT IN ROMANIAN TRADITIONAL DISTILLED ALCOHOLIC BEVERAGES

BIANCA MUREŞAN[a], CLAUDIA CIMPOIU[a], ANAMARIA HOSU[a], CRISTINA BISCHIN[a], EMESE GAL[a], GRIGORE DAMIAN[b], EVA FISCHER-FODOR[c], RADU SILAGHI-DUMITRESCU[a,*]

ABSTRACT. Reported here is a first detailed analysis of the antioxidant activity in traditional fruit-derived distilled alcoholic beverages from Romania ("ţuica"). A distinctly highest activity, paralleled by Folin-Ciocalteu data and UV-vis absorbances, was seen in the most common type of such brandy, made of plums; other samples included brandies made of apples, pears, fruit mixtures, wine, and cereals. In fact, the values seen for the plum brandy were, even before maturation with wood, similar to those of commercially-available wood-matured whisky. Increases of up to one order of magnitude in antioxidant activity were seen in all brandies upon maturation with various types of wood – with mulberry tree by far the most efficient, followed by oak and cherry – and with lowest values seen for acacia. Attempts to identify anticancer activity in concentrated extracts prepared from plum brandy, failed. Copper electron paramagnetic (EPR) signals are shown for the first time in such brandy samples.

Keywords: brandy; antioxidant; polyphenol; hemoglobin; EPR

INTRODUCTION

The beneficial effects on human health and disease prevention (cardiovascular, neurodegenerative, colon cancer) of moderately consumed wine and brandy are correlated with their antioxidant capacity, especially due to the higher ability of the polyphenolic compounds to quench free radical species [1-14].

[a] *Faculty of Chemistry and Chemical Engineering, Babeş-Bolyai University, 11 Arany Janos str., RO-400028, Cluj-Napoca, Romania*
[b] *Faculty of Physics, Babeş-Bolyai University Cluj-Napoca, Romania*
[c] *Tumor Biology Laboratory, The I. Chiricuta Oncology Institute, Cluj-Napoca, Romania*
* *Corresponding author: rsilaghi@chem.ubbcluj.ro*

Polyphenols and antioxidant capacity are almost absent in the case of vodka, gin and rum. However, whisky and brandy have an intermediate antioxidant capacity between red and white wine. In this case, polyphenols come from the wood of the storage container during the maturation process [15,16]. Numerous studies show that storage of wine or other alcoholic beverage, especially in oak barrels, may lead to significant changes in the polyphenolic composition, due to the transformation of native compounds as well as to the hydrolysis of tannins or lignin from the woods [7,17-25]. Recently, new technologies have been developed in order to simplify the aging process and to decrease the cost of preservation of brandy in wood barrels. Thus, one potential alternative technology consists in adding of wood pieces to the beverage kept in stainless steel tanks [26,27].

Although there are numerous studies regarding the antioxidant capacities of some distilled alcoholic beverages (cognac, liquor, whisky) [9,28,29], limited data have been obtained in the case of traditionally-produced brandies in Romania (tuica or palinca). As opposed to the use of cereals in other European countries (Scotland, Ireland, Northern Europe), traditional Romanian distilled beverages are based on processing of various autochthonic of fruits such as plums, apples, pears, cherries, apricots, berries. The distillation of the fermented fruit pulp is typically performed in cooper stills, with open fire, followed by a maturation phase in oak barrels [30].

According to the alcoholic concentration (37 vol % cf. current legislation), Romanian fruit brandies are classified as superior distilled drinks palinca (the name is a translation of the similar Hungarian product, palinka), obtained by a mixture of fruits, or slibovita, obtained by distillation and redistillation of plum marc, and inferior assortments known as spirits. The tuica, other traditional beverage obtained typically exclusively from plums, is produced at various alcohol concentrations, depending on region [31,32].

The purpose of this study was to investigate the relationship between polyphenolic content of various types of traditional distilled Romanian beverages and the antioxidant capacities under the influence of different types of wood used during the maturation process. Herein, besides traditional methods used to investigate antioxidant capacities of food and drinks (ABTS, DPPH) [16,33,34], a new physiologically relevant method based on hemoglobin ascorbate peroxidase activities is applied.

RESULTS AND DISCUSSION

General features

There are only a few data regarding the quality of Romanian distilled fruit beverages, mainly focused on technical analyses such as relative density, alcohol concentration, total and volatile acidity, pH, total dry extract, total polyphenol index and volatile compounds [31,32,35]. However, a detailed analysis of the antioxidant character has not been reported. By contrast, it is known that several kinds of polyphenolic compounds such as ellagic acid, gallic acid and lyoniresinol could be detected in whisky; nevertheless, a majority of them come from oak barrels, due to the higher concentration of alcohol, in the maturation process [36]. Here, some traditional and new methods for the characterization of antioxidant capacities were applied for the analysis of 5 types of Romanian brandy; additionally, the effect of maturation in the presence of different species of wood was also examined.

All studied brandy samples have an alcoholic concentration between 47 and 52 % very close to the commercial distilled beverage, whisky. Copper is the only detected metal in all samples, having a concentration between 0.1627-0.377 ppm; this is an acceptable level according to the current legislation (5 ppm legal limit (Monitorul oficial al Romaniei, part I, Nr. 268.11 VI 1999)). The metals found in alcoholic beverage may have different sources including raw materials, brewing, process type and equipment, bottling, aging/storage and adulteration [37]. The presence of Cu in the studied alcoholic distilled beverage was detected here for the first time, in our knowledge, using not only elemental analysis but also EPR spectroscopy (Supplementary Information, Figure S1).

UV-vis spectra

All analyzed brandy samples display UV-vis absorbance between 200 and 320 nm (Figure 1 A) - a region specific for the absorption of aromatic and unsaturated compounds. The difference in the absorption intensity of spectra suggests the diversity of the compounds found in these brandies. The highest intensity was obtained for plum brandy and the lowest for wine and corn ones. Considering that antioxidants present here are organic compounds, presumably polyphenolic compounds, one would expect a good correlation between the intensity of the spectra and the antioxidant activity of the samples. Compared to other distilled beverages (Fig. 1 B), the spectrum of the Romanian tuica has a visible difference in the intensity of absorbance at 250 nm. At 275 nm, the tuica appears to be more similar to whisky and tequila; in fact, below 300 nm, its absorbance (and, hence, its organic content – implying antioxidant activity) are the highest among all samples tested.
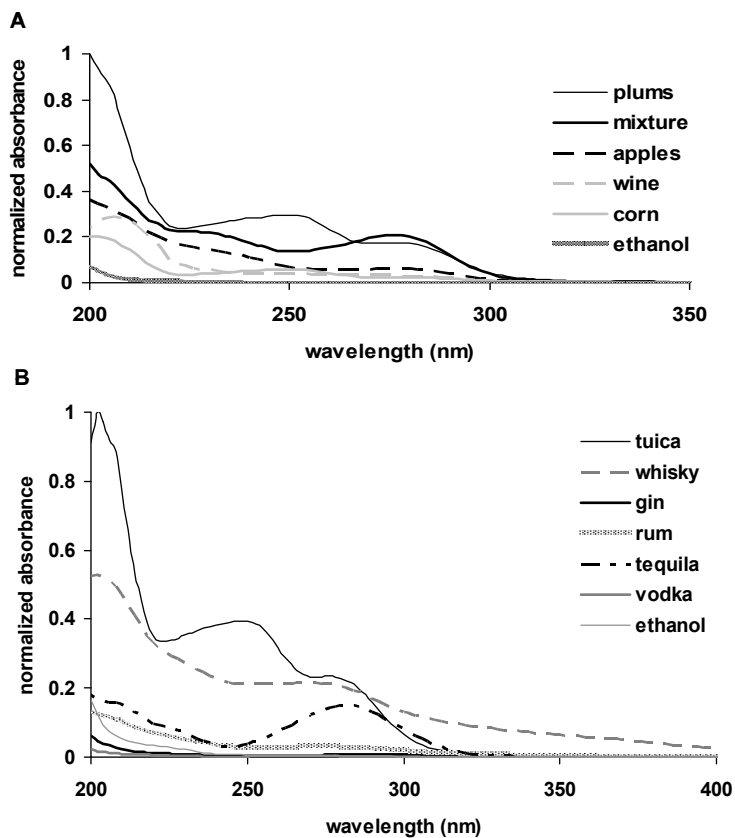
Figure 1. UV-vis spectra of Romanian brandy samples (A)
and other commercial distilled beverage (B).

Chromatographic analyses

The attempts to detect antioxidant compounds from tested Romanian brandies by TLC were, unfortunately, unsuccessful even in the case of concentrated samples. This may suggest that part of the responsible compounds for antioxidant activity were also volatile (as seen in the following sections, chemical analysis does reveal a certain polyphenolic content). On the other hand, the chromatogram obtained for the maturated brandies (Fig. 2) indicates specific and obvious differences in the type and content of compounds: the highest amounts were in mulberry tree (1), cherry (3) and oak (2) samples. It must be specified that in the case of maturated brandies the sample pre-concentration is not necessary.
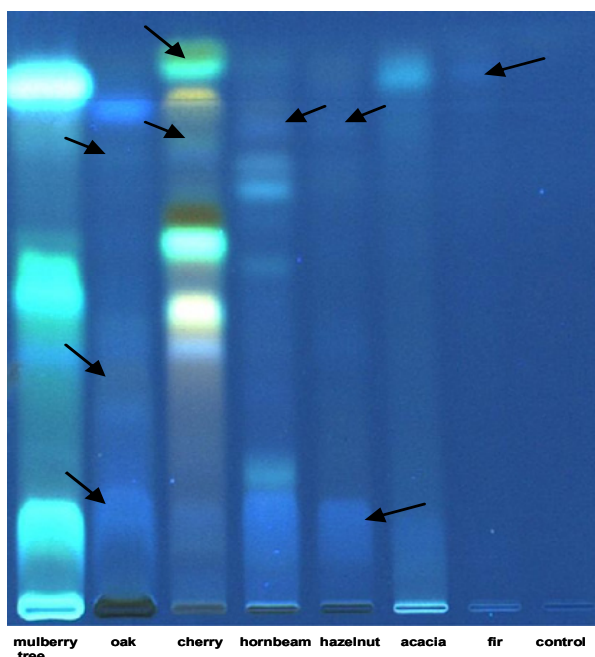
Figure 2. TLC separation of maturated brandies on silica gel 60 F_{254} with ethyl acetate: methanol: water (7.7: 1.3: 1, v/v/v) as mobile phase. Derivatization with NP/PEG, UV 366nm. Control sample is represented by plums brandy before maturation, obtained by concentration of initial extracts 20 times by evaporation, lyophilization and suspension of the residue in ethanol.

The separation shows that the largest number of separated compounds are found in the brandy maturated in mulberry, followed by brandies maturated in oak and cherry. Furthermore, a distinction regarding the number of separated compounds and their concentration can be done. The specific compounds presented only in the particular brandy are marked with arrow on the chromatogram. All these characteristics of TLC separation allow the differentiation of analyzed samples according to the wood and can be used as fingerprinting of maturated brandies.

DPPH and Folin-Ciocalteu reagent based assays

Figure 3 reveals a close correlation between the DPPH assay, which is widely used for biologically relevant antioxidant capacity evaluation, due to its simplicity and low cost, and total polyphenolic content, determined by Folin-Ciocalteu assay. Both methods are based on electron transfer mechanisms and are suitable for aqueous systems.

The simple end-time measurement of DPPH percentage bleached used for the analyses of the 5 Romanian types of brandy indicates that the highest polyphenolic contents appears to be in the case of the plum brandy. No significant differences were obtained between the apple brandy and the mixed sample (apple + plum mixture); the lowest concentration of polyphenols was found in the corn brandy. Also, kinetic measurements were employed to compare a plum brandy sample (not maturated with wood) and commercial whisky. Similar results were obtained measuring the area under the curve (described in Methods section) between plum brandy (553±5) and whisky (551±1) and a slight difference was shown in the case of end point experiments (0.048±0.006 for the plum brandy and 0.075±0.001 for whisky). Taking into account that plum brandy samples had not been maturated yet with wood, the antioxidants in this brandy originate mainly from consumable plant materials, not from wood hydrolysis – which may in principle be considered an advantage over other European distilled beverages such as whisky or vodka.
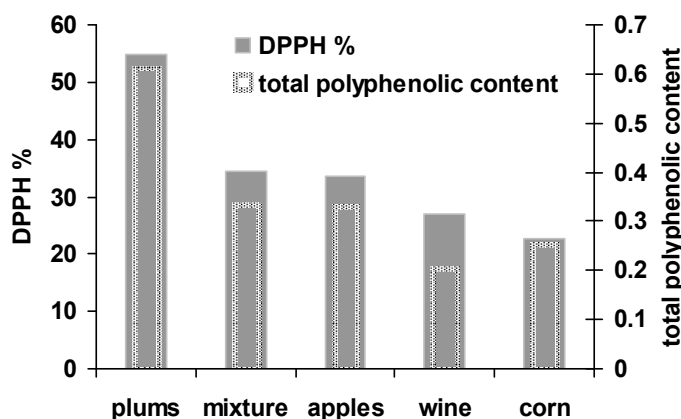
Figure 3. DPPH based assay and Folin-Ciocalteu data
for the 5 types of Romanian brandy.

TEAC assay

In Fig. 3 the antioxidant capacity of the aqueous and ethanolic extracts of the brandies is analyzed, using the simplest and cheaper test TEAC, which is based on the ability of antioxidants to react directly with ABTS˙ radical. The extracts, obtained after lyophilization and resuspension in 20-time smaller volumes of solvent (either water or alcohol) would be expected to contain a higher concentration of antioxidants (10-20 times) than the original brandy samples.

Kinetic measurements were performed measuring both the difference of the absorbance, which is directly correlated with the antioxidant capacities of the samples and area under the curve, which is inversely correlated with the antioxidant capacities. Thus, for the first case, (Fig. 4 A) the ethanolic extract displayed measurable amounts (in line with DPPH and Folin-Ciocalteu assays on the intact brandy), much larger than the water extracts.

A

B
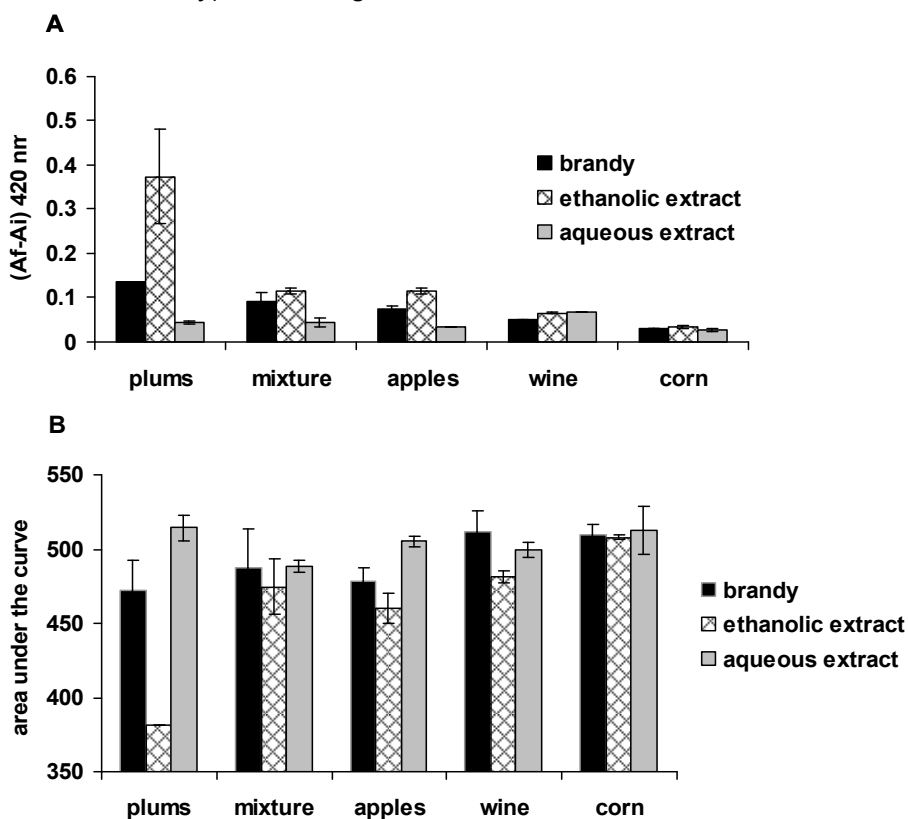
Figure 4. ABTS assay reflected in total change in absorbance (A) and area under the curve (B), obtained for aqueous and ethanolic extract of 5 types of Romanian brandy.

A good correlation could be observed between the difference of absorbance and the second parameter used for the characterization of antioxidant capacities - area under the curve shown in Figure 4 B. Although one may have expected a higher antioxidant capacity of the ethanolic extract, due to the increased concentration of original solution (20 times), this could not be observed - most probably due to loss of antioxidant content during the

lyophilization process. Indeed, one must consider that since these brandies are obtained via distillation, the majority of the compounds would also be volatile (of the type illustrated in Table S3 in Supporting Information) – or at least predisposed to being carried by vapors of the volatile compounds. Reference [35] does in fact list a few compounds that, while volatile, may also be targets for free radicals and hence act as antioxidants.

The characteristic parameters of the kinetic curve, fitted using a bi-exponential function, are described in Tab. S1 (Supporting Information). Thus, two concomitant processes of different rates occur during this reaction, most probably due to the structure of the antioxidants, reflected in a different rate consuming of ABTS$^{\cdot}$ radicals.

Kinetics data of the consumption of ABTS radical by polyphenols, obtained by EPR measurements fitted using a mono-exponential function (due to the different time scales between this experiment and UV-vis experiment), show a good correlation with UV-vis experiments for plums and corns brandy (Figure 5).
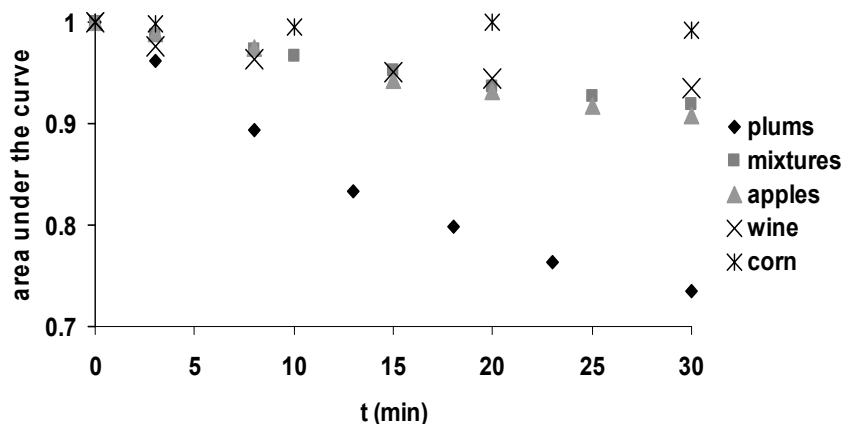
Figure 5. Kinetic of the consumption of ABTS$^{.+}$ radical during an EPR experiment for 5 type of Romanian brandy. Area under the curve was normalized and corresponded to the integration of each EPR spectrum.

Effects of maturation

UV-vis spectra of maturated brandies with wood show an increase in the intensity of absorbance, especially in the case of mulberry tree, compared with original sample (Figure 6). A good similarity can be observed for oak and cherry spectra. One would expect a correlation between the UV-vis characteristics and the antioxidant capacity.
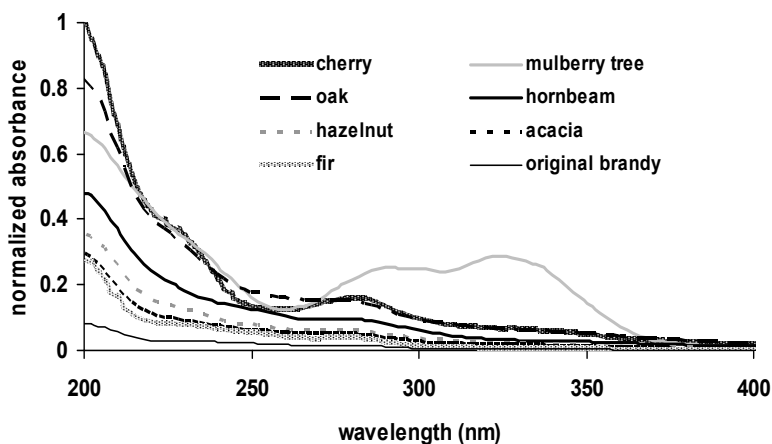
Figure 6. UV-vis spectra of the maturated brandies.
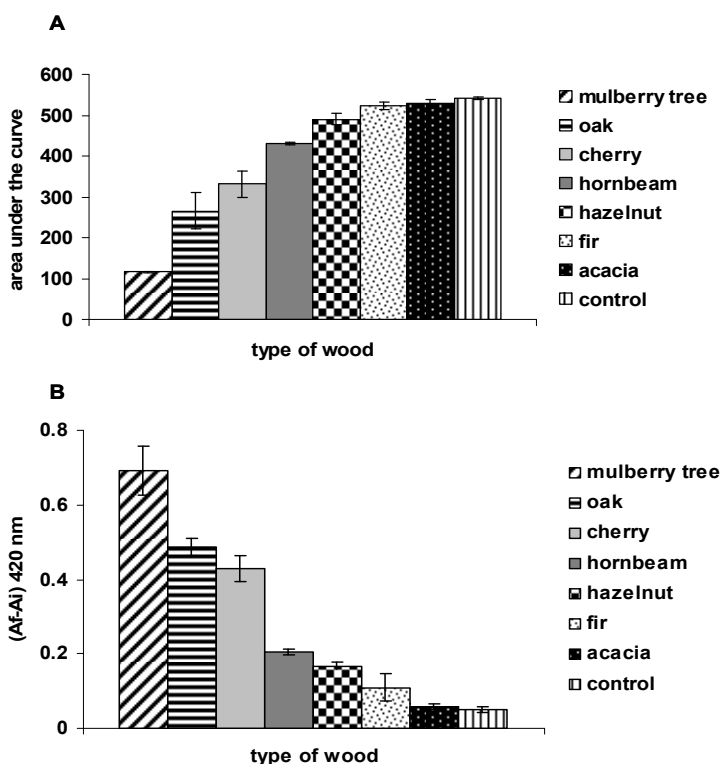
Figure 7. The effect of different wood used in the maturation process of plums brandy, reflected in the ABTS parameters: total change in absorbance (A) and area under the curve (B).

Indeed, a significant improvement of the antioxidant capacity (compared to original samples) was achieved after the maturation of brandies using different pieces of wood species. The results presented in Fig. 7 (kinetic parameters fitted using a bi-exponential function are presented in Supplementary Information, Table S2) show that the best improvement, in agreement with the chromatogram shown in Figure 2 and UV-vis spectra shown in Figure 6, was obtained for mulberry tree followed by oak. Acacia and fir woods proved to have the lowest influence on this process.

HAPX assay

A new physiologically relevant method proposed for the evaluation of antioxidant capacities is based on the ascorbate peroxidase activity of hemoglobin, as described in detail in [38-44]. Under some natural (physical effort) or pathological conditions such as haemolytic anaemias, subarachnoid
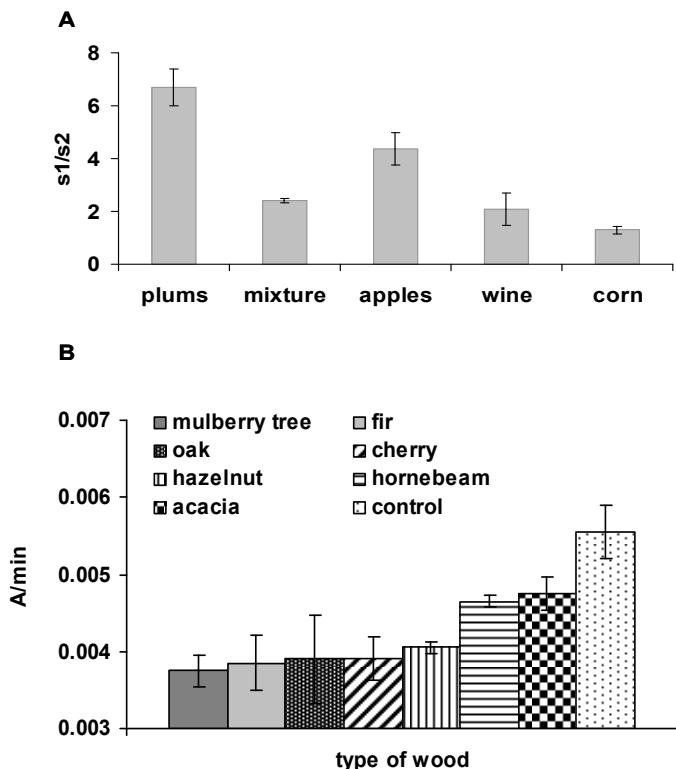
Figure 8. A. HAPX results reflected in the change of slope at 290 nm, for the Romanian analyzed brandies. S1/s1 represents the ratio between slope 1 and slope 2. B. HAPX assay results reflected in the change of slope at 290 nm, for the plums brandy maturated with different types of wood.

haemorrage and rhabdomyolysis, globins can initiate free radical chemistry, in particular by interaction of the ferric form of hemoglobin (met) with peroxide yielding two strong oxidants: ferryl iron and a protein-bound free radical. Ascobate has the ability to reduce plasma methhemglobin, ferryl hemoglobin and globin radicals. Other antioxidants compounds present in the sample can also interact with these highly oxidant species during the catalytic cycles of these reaction; these easily could be observed in the inhibition of ascorbate hemoglobin dependent oxidation [45].

HAPX applied for Romanian brandy shows a good correlation with traditional methods used for evaluation of antioxidant capacity (ABTS, DPPH) (Figure 8 A). Plums sample was proved to have the best antioxidant capacity, and corn brandy the lowest. The results obtained using this method for the maturated samples are shown in Figure 8 B. With some few exceptions, a good correlation can be observed between the results obtained here and in the ABTS test. Thus, the higher antioxidant capacity was achieved for the brandy maturated in the presence of a piece of mulberry tree species, followed, unlike on the ABTS results, by the fir wood, oak and cherry. The lowest antioxidant capacity was observed, as in the ABTS experiments, for the acacia wood.

Cell culture tests

The antioxidant contents of various foodstuffs is often cited as indicative of health-promoting effects; alcoholic beverages make no exception, as reviewed in the Introduction. Biological tests were in this context performed on 20-fold concentrated extracts of the plum brandy, following methodologies described elsewhere [46]. Unfortunately, no anticancer effect was detected – nor was any other protective or toxic effect noticed.

CONCLUSIONS

Reported here is a first detailed analysis of the antioxidant activity in traditional fruit-derived distilled alcoholic beverages from Romania ("ţuica"). By far, the highest activity is seen in the most common type of such brandy, made of plums. In fact, these values are, even before maturation with wood, similar to those of commercially-available wood-maturated whisky. Increases of up to one order of magnitude in antioxidant activity were seen in all brandies upon maturation with various types of wood – with mulberry tree by far the most efficient, followed by oak. Attempts to identify anticancer activity in concentrated extracts prepared from plum brandy were not successful. Copper electron paramagnetic (EPR) signals are shown for the first time in such brandy samples.

EXPERIMENTAL SECTION

5 types of brandy (from plums, mixture of plums and apples, apples, wine and corn) produced simultaneously with a similar alcoholic concentration were collected directly from a producer originating from the Bistrita-Nasaud county in Romania. From the same region, 7 pieces of different species of wood were collected from mulberry tree, oak, hazelnut, acacia, fir, cherry and hornbeam. Whisky (commercial brand, 40 vol % alcohol) was obtained from a local store.

ABTS (2,2'-azino-bis(3-ethylbenzothiazoline-6-sulphonic acid), DPPH, and ascorbic acid were purchased from Sigma-Aldrich (Germany). The Folin-Ciocalteu reagent (standard solution 2 N, 1: 10 dilution) was obtained from Merck KGaA (Germany). Bovine hemoglobin, purified according to the Antonini and Brunori procedure [47], was oxidized to met hemoglobin (metHb) by ferricyanide treatment.

Silica gel $60F_{254}$ thin layer chromatographic (TLC) plates (10x10cm) were purchased from Merck, Darmstadt (Germany). NP (Natural Product) was prepared by dissolution of 1 g of diphenylboronic acid aminoethyl esther in 200 mL ethyl acetate; PEG solution was prepared by dissolution of 10 g polyethylene glycol 400 (Macrogol) in 200 mL dichloromethane.

Brandy aging (maturation) occurred in the presence of a piece of wood ($3 cm^3$), in plastic containers, at 4ºC, during 24 hours. Then, the samples were decanted and analyzed. Selected samples of brandies were concentrated on a water bath at 40ºC under mild vacuum (water suction), until the final volume of sample was decreased 20-fold. The obtained extracts were lyophilized and then, the residues were suspended in ethanol and water, respectively.

Thin layer chromatography

20 μL of each concentrated brandy samples and those obtained by maturation with different types of wood were applied as 8mm bands with a rate of 30nL/s to the TLC plate using a semi-automatic applicator device (Linomat V, Camag). The plates were developed in normal chromatographic twin trough chamber (Camag) pre-saturated for 30 minutes with mobile phase - ethyl acetate: methanol: water (7.7: 1.3: 1, v/v/v). The dried developed plate was heated at 1000C for 3 min, dipped while still hot in the NP solution, dried in cold air and then immersed in the PEG solution. The plates dipping were performed using an immersion device (Camag). The detection was performed under UV light (254 nm and 366 nm) and under visible light, before and after the dipping of the plates in the NP/PEG solutions and the documentation of the plates was performed using a TLC vizualizer device (Digistore 2 - Camag).

The total polyphenolic content was determined using the Folin-Ciocalteu assay, described in [45]. For each sample, 1.5 mL Folin-Ciocalteu reagent were added to 1 mL brandy, and samples were incubates in the dark for 5 minutes. Then, 1.2 mL sodium carbonate (0.7 M) were added and samples were incubated in the dark for 2 h, at which point the solution turned deep blue to various degrees, depending the sample. The absorbance of the blue samples was recorded at 760 nm, on a Cary 50 UV-vis spectrometer (Varian).

DPPH assay

A stock solution of 0.09 mg/mL was prepared. 1 mL of DPPH solution was added to the 2 mL brandy and the samples were incubated for 15 minutes at room temperature, followed by measurement of the absorbance at 517 nm. Besides the end-point experiment, kinetics measurements were also performed for 30 minutes, at 517 nm. Typical decay curves were obtained for every sample, allowing one to calculate the total change in absorbance (ΔA), which is directly correlated with antioxidant capacities of the samples, as well as the calculation of the area under the curve, which is inverse correlated with the antioxidant capacities.

Trolox equivalent antioxidant capacities (TEAC) assay

The ABTS radical was enzymatically obtained by 2 hours of incubation of 2 mM reduced ABTS solution in 5 mM sodium acetate pH 5.5, with 50 nM horseradish peroxidase and 1.3 mM hydrogen peroxide. The radical was separated from the enzyme using a 10 kDa cut-off amicon filter. For this assay, kinetic measurements were performed. In a quartz cuvette, 50 µl ABTS radical was added to the 900 µl PBS buffer and 10 µl brandy. The decrease of the ABTS radical absorbance was monitored at 420 nm. As in the DPPH methods, the evaluation of the antioxidant capacities of the sample can be obtained using the total change in absorbance as well as via the calculation of the area under the curve.

The inhibition of hemoglobin ascorbate peroxidase activity (HAPX) assay was conducted as in [45]. For this experiment, kinetic measurements were performed. Thus, in a quartz cuvette, 14 µl metHb of 1mM, 13 µl peroxide of 60 mM and 10 µl were added to 952 sodium acetate buffer, pH 5.5 - after which the absorbance changes were monitored at 290 nm. After absorbance stabilization, the reaction was triggered by the addition of 50 µl ascorbate of 50 mM. The kinetic profile for ascorbic acid degradation after the addition of met-Hb, was linear for least 100 s. For the evaluation of the hemoglobin ascorbate peroxidase activity, the slope of the linear decrease was calculated (corresponding to the oxidation of ascorbate).

EPR measurements were performed as described in [46].

ACKNOWLEDGMENTS

REFERENCES

1. F. Cimino,V. Sulfaro, D. Trombetta, A. Saija, A. Tomaino, *Food Chem.,* **2007**, *103*, 75-81
2. D. Di Majo, M. La Guardia, S. Giammanco, L. La Neve, M. Giamanco, *Food Chem.*, **2008**, *111*, 45-49
3. N. Paixao, R. Perestrelo, J.C. Marques, J.S. Camara, *Food Chem.*, **2007**, *105*, 204-214
4. I.G. Roussis, I. Lambropoulous, P. Tzimas, A. Gkoulioti, V. Marinos, T. Tsoupeis, I. Boutaris, *J. Food Compost Anal.*, **2008**, *21*, 614-621
5. F. Que, L. Mao, X. Pan, *Food Res. Int.*, **2006**, *39*, 581-587
6. M. Scwartz, M.C. Rodriguez, C. Martinez, V. Bosquet, D. Guillen, C.G. Barroso, *Food Chem.*, **2009**, *116*, 29-33
7. S. Canas, V. Casanova, A.P. Belchior, *J. Food Compost Anal.*, **2008**, *21*, 626-633
8. A. Stasko, V. Brezova, M. Mazur, M. Certik, M. Kalinak, M. Gesheid, *Food Sci. Techol.*, **2008**, *41*, 2126-2135
9. G.G. Duthie, M.W. Pedersen, P.T. Gardner, P.T. Morrice, A.M. Jenkinson, D.B. McPhail, G.M. Steele, *Eur. J. Clin. Nutr.*, **1998**, *52*, 733-736
10. M. Gronbaek, U. Becker, D. Johansen, A. Gottschau, P. Schohr, H.O. Hein, G.S. Jensen, T.I. Sorensen, *Ann. Intern. Med.*, **2000**, *133*, 411-419
11. E.N. Frankel, A.L. Waterhouse, P.L. Teissedre, *J. Agric. Food Chem.*, **1995**, *43*, 890-894
12. S. Yoshioka, T. Terashita, H. Yoshizumi, N. Shirasaka, *Biosci. Biotechnol. Biochem.*, **2011**, *75*, 2278-2282
13. L.B. Mann, J.D. Folts, *Pathophysiology*, **2004**, *10*, 105-112
14. D.M. Goldberg, B. Hoffman, J. Yang, G.J. Soleas, *J. Agr. Food Chem.*, **1999**, *47*, 3978-3985
15. D.M. Goldberg, B. Hoffman, J. Yang, G.J. Soleas, *J. Agric. Food Chem.*, **1999**, *47*, 3978-3985
16. H. Aoshima, H. Tsunoue, H. Koda, Y. Kiso, *Food Chem.*, **2004**, *52*, 5240-5244

17. A.B. Cerezo, W. Tesfaye, M.E. Soria-Diaz, M.J. Torija, E. Mateo, M.C. Garcia-Parrilla, A.M. Troncoso, *J. Food Comp. Anal.*, **2010**, *23*, 175-184

18. D. Matejicek, O. Mikes, B. Klejdus, D. Sterbova, V. Kuban, *Food Chem.*, **2005**, *90*, 791-800

19. S. Kallinthraka, M.I. Salacha, I. Tzourou, *Food Chem.*, **2009**, *113*, 500-505

20. V.T. Karathanos, C. Syrimbei, A. Chiou, A. Karathanos, D.P. Makris, *J. Food Compost. Anal.*, **2008**, *21*, 667-671

21. J.A. Avila-Reyes, N. Almaraz-Abarca, E.A. Delgado-Alvarado, L.S. Gonzalez-Valdez, G.V. Del Toro, E.D. Paramo, *Food Res. Int.*, **2010**, *43*, 296-300

22. M.R.G.B.S. Valles, Y.D. Garcia, P. Del Valle Arguelles, P.L. Lobo, *Food Sci. Biotechnol.*, **2010**, *19*, 1129-1134

23. S. Pecic, M. Veljovic, S. Despotovic, I. Leskosek-Cukalovic, M. Jadranin, V. Tesevic, M. Nikdic, Nikicevic, *Eur. Food Res. Technol.*, **2012**, *235*, 479-487

24. R.R. Madrera, D.B. Gomis, J.J.M. Alonso, *J. Agric. Food Chem*, **2003**, *51*, 7969-7973

25. J.R. Mosedale, *Forestry*, **1995**, *68*, 204-230

26. S. Canas, I. Caldeira, A.P. Belchior, *Food Chem.*, **2013**, *138*, 2460-2467

27. I. Caldeira, O. Anjos, V. Portal, A.P. Belchior, S. Canas, *Anal. Chim. Acta*, **2010**, *660*, 43-52

28. A.M. Alonso, R. Castro, M.C. Rodriguez, D.A. Guillen, C.G. Barroso, *Food Res. Int.*, **2004**, *37*, 715-721

29. W. Li, T. Beta, *Food Chem.*, **2011**, *127*, 968-975

30. N.I. Pohomaci, *Tuica and natural brandies (in Romania)*; Ed, Ceres: Bucharest, 2002.

31. D. Beceanu, M. Niculaua, *Cercetari Agronomice in Moldova*, **2009**, *XLII*, 49-61

32. D. Beceanu, M. Niculaua, I. Moraru, R.M. Anghel, *Cercetari Agronomice in Moldova*, **2010**, *XLIII*, 61-77

33. J. Tabart, C. Kevers, J. Pincemail, J.O. Defraigne, J. Dommes, *Food Chem.*, **2009**, *113*, 1226-1233

34. M.D. Rivero-Perez, M.L. Gonzalez-Sanjose, M. Ortega-Heras, P. Muniz, *Food Chem.*, **2008**, *111*, 957-964

35. T.E. Rusu Coldea, C. Socaciu, M. Parv, D. Vodnar, *Not. Bot. Horti. Agrobo.*, **2011**, *39*, 109-116

36. K. Koga, A. Taguchi, S. Koshimizu, Y. Sua, Y. Yamada, N. Shirasaka, H. Yoshizumi, *J. Food. Sci.*, **2007**, *72*, S212-S217

37. J.G. Ibanez, A. Carreon-Alvarez, M. Barcena-Soto, N. Casillas, *J. Food Compost. Anal.*, **2008**, *21*, 672-683

38. J. Dunne, D.A. Svistunenko, A.I. Alayash, M.T. Wilson, C.E. Cooper, *Adv. Exp. Med. Biol.*, **1999**, *471*, 9-15

39. C.E. Cooper, R. Silaghi-Dumitrescu, M. Rukengwa, A.I. Alayash, P.W. Buehler, *Biochim Biophys Acta*, **2008**, *1784*, 1415-20

40. B.J. Reeder, D.A. Svistunenko, C.E. Cooper, M.T. Wilson, *Antioxidant & Redox Signaling*, **2004**, *6*, 954-966

41. B.J. Reeder, M. Grey, R.L. Silaghi-Dumitrescu, D.A. Svistunenko, L. Bulow, C.E. Cooper, M.T. Wilson, *J. Biol. Chem.*, **2008**, *283*, 30780-7

42. R. Silaghi-Dumitrescu, B.J. Reeder, P. Nicholls, C.E. Cooper, M.T. Wilson, *Biochem. J.*, **2007**, *403*, 391-5
43. N.B. Vollaard, B.J. Reeder, J.P. Shearman, P. Menu, M.T. Wilson, C.E. Cooper, *Free Radic Biol. Med.* **2005**, *39*, 1216-28
44. N.B. Vollaard, B.J. Reeder, J.P. Shearman et al., *Spors Med.*, **2005**, *35*, 1045-1062
45. A.C. Mot, G. Damian, C. Sarbu, R. Silaghi-Dumitrescu, *Redox Rep.*, **2009**, *14*, 267-74
46. J.D. Tamokou, J.R. Chouna, E. Fischer-Fodor, G. Cherches, O. Barbos, G. Damian, D. Benedect, M. Duma, A.P. Efouet, H.K. Wabo, J.R. Kuiate, A. Mot, R. Silaghi-Dumitrescu, *PLoS One*, **2013**, *8*
47. E. Antonini, M. Brunori, *Hemoglobin and Myoglobin in their Reaction with Ligands*; North-Holland: Amsterdam, 1971

SYNTHESIS OF NEW
BENZOTHIAZOLYL-PHENOTHIAZINE DERIVATIVES

**BALASZ BREM[a], EMESE GAL[a], CASTELIA CRISTEA[a],
LUIZA GĂINĂ[a], ADRIANA GROZAV[b,*], VALENTIN ZAHARIA[b]
AND LUMINIŢA SILAGHI-DUMITRESCU[a]**

ABSTRACT. A series containing 1-, 2-, 3- and 4-(benzothiazol-2yl)-10*H*phenothiazine derivatives was advantageously prepared by the condensation of each corresponding phenothiazine-carbaldehyde regioisomer with 2-amino-benzenethiol. The reaction conditions were optimized and the structures of the new compounds were unambiguously assigned based on high resolution nuclear magnetic resonance spectroscopy and mass spectrometry.

Key words*: phenothiazine, benzothiazole, NMR*

INTRODUCTION

Benzothiazole derivatives consisting of a cumulative structural motif formed by the 5-membered heteroaromatic ring, the fused benzene unit and diverse substituents attached in various positions (especially mercapto groups) already found important industrial applications in anti-oxidant formulations, components in metal finishing liquors [1], vulcanization accelerators in the rubber industry [2] and fungicides [3]. Various 2-substituted benzothiazoles (2-aryl benzothiazole) received much attention due to potential uses as imagining agents [4] and anticancer agents [5].

Several procedures were developed for the synthesis of benzothiazoles (scheme 1). One method involves the condensation of 2-aminothiophenols with carboxylic acids [6] or aldehydes [7, 8] respectively, under oxidative conditions (reported oxidants: bromine, iodine, quinine, metal salts). Another method involves the transition-metal-catalyzed intramolecular cyclization of thioanilides [9]. Most

[a] *"Babes-Bolyai" University, Faculty of Chemistry and Chemical Engineering, RO-400028, Cluj-Napoca, Romania*
[b] *"Iuliu Haţieganu" University of Medicine and Pharmacy, Faculty of Pharmacy, RO-400012, Victor Babes 41, Cluj-Napoca, Romania*
* Corresponding author: adriana.ignat@umfcluj.ro

efforts were focused on noble metal catalysts, such as Ru, Rh, Pd, but the iron-catalysed [10] synthesis may benefit from the low toxicity and large availability of iron derivatives. Metal-free methods starting from alkyl amines [11] or aryl ketones [12] at high temperature under oxidative conditions were also reported. The third method involves the condensation of 2-aminothiophenols with β-ketonitriles [13], β-ketoesters [14] or β-diketones [15] under microwave activation at high temperature or in the presence of catalytic ammounts of Bronsted acids.
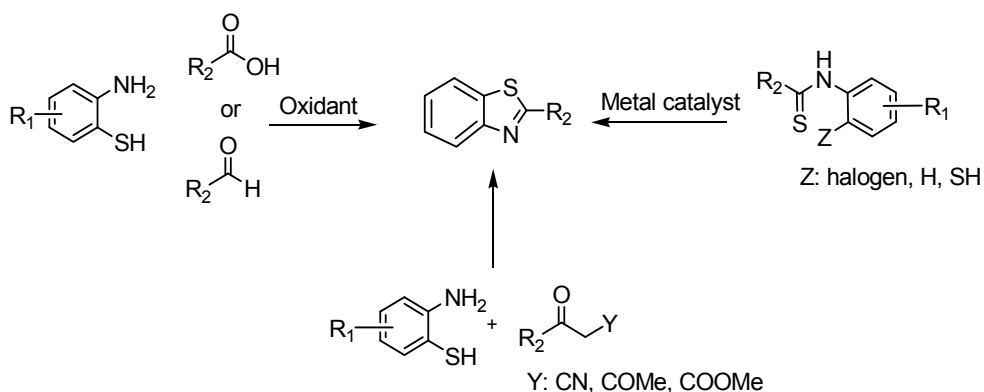
Scheme 1

        Continuing our investigations dedicated to the synthesis of new polyheteroaromatic structures containing phenothiazine and thiazole units assembled in the same molecular structure [16], in this work we described an advantageous procedure for the synthesis of new derivatives with joint phenothiazine and thiazole units.

RESULTS AND DISCUSSIONS

        The synthetic strategy applied in this work is based on the condensation of aldehydes with o-aminobenzenethiols under thermal activation conditions. A series of benzothiazolyl-phenothiazine derivatives was prepared starting with a phenothiazine-carbaldehyde derivative (10*H*-phenothiazin-1-carbaldehyde, 10-methyl-10*H*-phenothiazin-1-, 2-, 3-, and 4-carbaldehyde regioisomers, 10-methyl-7-bromo-10*H*-phenothiazin-3-carbaldehyde and 10-methyl-10*H*-phenothiazin-3,7-dicarbaldehyde respectively) and *ortho*-aminobenzenethiol which were severely heated in DMSO solvent (Scheme 2). No other oxidant was required when working-up in the presence of atmospheric oxygen.

R = -H, -CH₃
X = -H, -CHO, -Br

1 *1*-thiazolyl, R=H,   x= H
2 *1*-thiazolyl, R=CH₃, x= H
3 *2*-thiazolyl, R=CH₃, x= H
4 *3*-thiazolyl, R=CH₃, x= H
5 *4*-thiazolyl, R=CH₃, x= H
6 *3*-thiazolyl, R=CH₃, x= Br
7 *3*-thiazolyl, R=CH₃,   x=thiazolyl
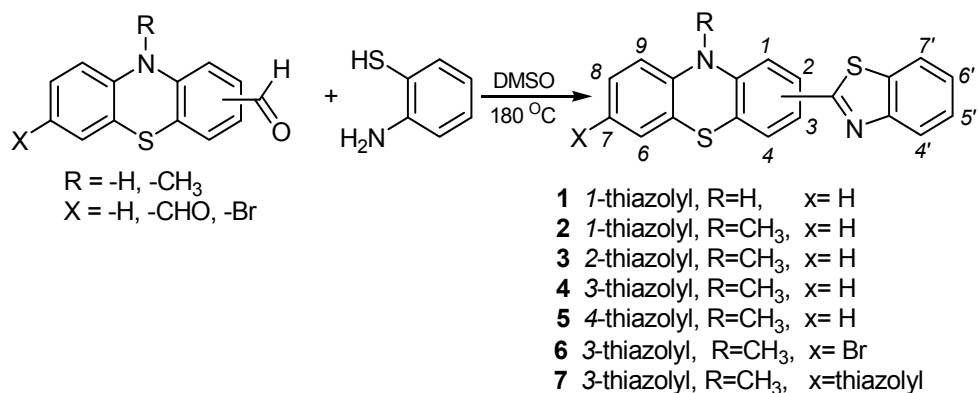
Scheme 2

This convenient procedure gave satisfactory yields even in the case of sterically hindered substrates such as 10-methyl-10*H*-phenothiazin-1-carbaldehyde or 10*H*-phenothiazin-1-carbaldehyde Best yields were obtained in the preparation of 2-benzotiazolyl-phenothiazine. The products are stable crystalline compounds with a yellow colour.
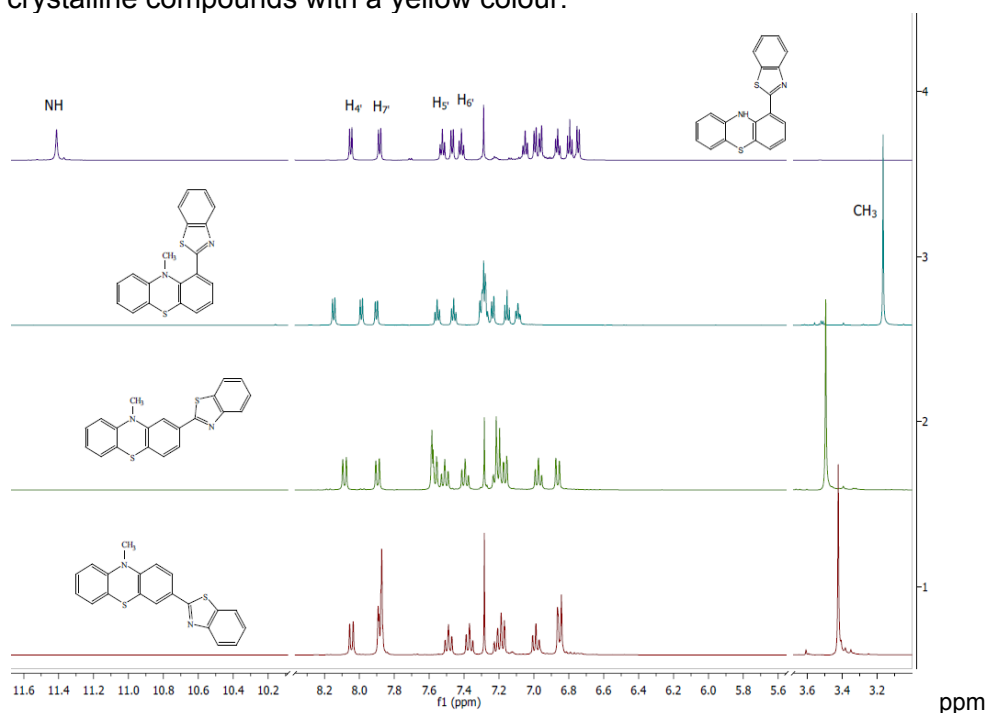
Figure 1. 600 MHz ¹H-NMR spectra of benzothiazol-2-yl-phenothiazine regioisomers in CDCl₃

The structures of the new compounds were unambiguously assigned based on HRMS and NMR spectroscopic data. 2D-NMR 1H-1H homocorrelation and ^{1}H-^{13}C-heterocorrelation experiments were performed in order to completely assign the signals of the nuclei present in the two heterocyclic units. As it may be seen from figure 1 which collectively presents the ^{1}H-NMR spectra of the series of regioisomers **1-5**, the benzothiazolyl moiety is responsible for generating the most deshielded signals, accompanied by the protons of the phenothiazine unit situated in the closest neighboring position. An inspection of the chemical shifts recorded in the case of sterically hindered structures **1** and **2** suggest a preferred bisectional orientation of the benzothiazolyl substituent in respect to the aromatic ring of the phenothiazine unit. The ring current of the benzothiazolyl unit induces a magnetic anisotropy observable in the chemical shifts of the substituents situated in the *peri* position (a deshielding of the NH signals in **1** and a shielding of –CH$_3$ signals in **2** respectively).

CONCLUSIONS

A convenient procedure for the preparation of new heteroaromatic compounds with joint phenothiazine and thiazole units was developed based on thermal activated condensation of *ortho*-aminobenzenethiol with phenothiazine carbaldehydes.

EXPERIMENTAL SECTION

HRMS spectra were recorded using Thermo LTQ *Orbitrap XL* mass spectrometer.

NMR spectra were recorded at room temperature on 400 or 600 MHz Bruker Avance instruments. Chemical shifts are expressed in δ (ppm) relative to standard tetramethylsilane (TMS).

O-amino-benzenethiol was purchased from Sigma_Aldrich.

Phenothiazine carbaldehydes were prepared according to previously reported procedures.

General procedure for the synthesis of benzothiazol-2yl-phenothiazine derivatives

Ortho-Aminobenzenethiol (4mmol, 0.5g) and the corresponding phenothiazinyl aldehyde (4mmol) dissolved in 50 ml DMSO were heated at 180 °C on oil bath for 6 h. After cooling down to room temperature, the mixture was poured in water and extracted with ethyl acetate. The

organic phase was dried over Mg_2SO_4 and the solvent was removed under vacuum. The residue was purified by recrystallisation from ethanol or by column chromatography (eluent toluene).

1-(benzo[d]thiazol-2-yl)-10H-phenothiazine (1)
Purification by flash chromatography, gave 0.9 g, 68 % as orange solid.

HRMS (ESI+): [M+H$^+$] found 333.0454, $C_{13}H_{13}N_2S$ requires 333.0515.

^{1}H-NMR (600MHz, CDCl$_3$): δ (ppm) = 6.72 (d, 1H, H$_9$, ^3J =7.62Hz), 6.76 (t, 1H, H$_7$, ^3J = 7.8 Hz), 6.83 (t, 1H, H$_8$, ^3J = 7.2 Hz), 6.93 (d, 1H, H$_4$, ^3J = 7.62Hz), 6.96 (d, 1H, H$_6$, ^3J =7.44 Hz), 7.02 (td, 1H, H$_3$, ^3J = 7.8 Hz, ^4J = 0.9 Hz), 7.39 (t, 1H, H$_{6'}$, ^3J = 7.44 Hz), 7.44 (dd, 1H, H$_2$, ^3J =7.86Hz, ^4J = 0.66Hz), 7.49 (t, 1H, H$_{5'}$, ^3J = 7.32 Hz), 7.85 (d, 1H, H$_{7'}$, ^3J =8.1 Hz), 8.01 (d, 1H, H$_{4'}$, ^3J =8.1 Hz), 11.38 (s, 1H, NH)

^{13}C-NMR (125 MHz, CDCl$_3$): δ (ppm) = 115.5 (C$_q$, C$_1$), 115.8 (C$_H$, C$_7$), 117.7 (C$_q$, C$_{4a}$), 120 (C$_q$, C$_{5a}$), 121.1 (C$_H$, C$_{4'}$), 121.3 (C$_H$, C$_7$), 122.6 (C$_H$, C$_{7'}$), 123 (C$_H$, C$_8$), 125.5 (C$_H$, C$_6$), 126.4 (C$_H$, C$_{6'}$), 127.5 (C$_H$, C$_2$), 128.2 (C$_H$, C$_6$), 128.5 (C$_q$, C$_3$), 133.2 (C$_q$, C$_{7a'}$), 140.8 (C$_q$, C$_{9a}$), 141.7 (C$_q$, C$_{10a}$), 153 (C$_q$, C$_{4a'}$), 168.3 (C$_q$, C$_{2'}$);

1-(benzo[d]thiazol-2-yl)-10-methyl-10H-phenothiazine (2)
Purification by recrystallisation, gave (0.8g, 58 %) as orange solid.

HRMS (ESI+): [M+H$^+$] found 347.0611, $C_{13}H_{13}N_2S$ requires 347.0671.

^{1}H-NMR (600MHz, CDCl$_3$): δ (ppm) = 3.16 (s, 3H, N-CH$_3$), 7.09 (td, 1H, H$_4$, ^3J = 8 Hz, ^4J = 1.74 Hz), 7.15 (t, 1H, H$_3$, ^3J = 7.7 Hz), 7.23 (d, 1H, H$_9$, ^3J =7.56Hz), 7.26-7.31 (m, 3H, H$_8$, H$_7$, H$_6$), 7.45 (t, 1H, H$_{6'}$, ^3J = 7.5 Hz), 7.55 (t, 1H, H$_{5'}$, ^3J = 7.5 Hz), 7.90 (dd, 1H, H$_2$, ^3J = 7.68 Hz, ^4J = 1 Hz), 7.99 (d, 1H, H$_{7'}$, ^3J = 8 Hz), 8.15 (d, 1H, H$_{4'}$, ^3J = 8.1 Hz);

^{13}C-NMR (125 MHz, CDCl$_3$): δ (ppm) = 43.3 (CH$_3$, **C$_a$**), 121 (C$_H$, **C$_7$**), 121.6 (C$_H$, **C$_{7'}$**), 123.3 (C$_H$, **C$_{4'}$**), 124.3 (C$_H$, **C$_3$**), 124.6 (C$_H$, **C$_4$**), 125.4 (C$_H$, **C$_{6'}$**), 126.2 (C$_H$, **C$_{5'}$**), 126.9 (C$_H$, **C$_9$**), 127 (C$_q$, **C$_{4a}$**), 127.7 (C$_H$, **C$_8$**), 128.7 (C$_H$, **C$_6$**), 128.8 (C$_q$, **C$_{5a}$**), 129.8 (C$_H$, **C$_2$**), 132.8 (C$_q$, **C$_1$**); 136.4 (C$_q$, **C$_{7a'}$**), 144 (C$_q$, **C$_{9a}$**), 147 (C$_q$, **C$_{10a}$**), 152.8 (C$_q$, **C$_{4a'}$**), 165.5 (C$_q$, **C$_{2'}$**);

2-(benzo[d]thiazol-2-yl)-10-methyl-10*H*-phenothiazine (3)
Purification by recrystallisation, gave 1.1 g, 81 % as yellow solid.

HRMS (ESI+): [M+H$^+$] found 347.0616, $C_{13}H_{13}N_2S$ requires 347.0671.

^{1}H-NMR (400MHz, CDCl$_3$): δ (ppm) = 3.47 (s, 3H, N-CH$_3$), 6.84 (d, 1H, H$_9$, ^3J = 7.8 Hz), 6.95 (td, 1H, H$_3$, ^3J = 7.48 Hz, ^4J = 0.8 Hz), 7.14 (dd, 1H, H$_6$, ^3J = 7.6 Hz, ^4J = 1.3 Hz), 7.17-7.21 (m, 2H, H$_4$, H$_8$), 7.37 (td, 1H, H$_{6'}$, ^3J = 8 Hz, ^4J = 0.9 Hz), 7.48 (td, 1H, H$_{5'}$, ^3J = 8.2 Hz, ^4J = 1 Hz), 7.53-7.56 (m, 2H, H$_1$, H$_7$), 7.87 (d, 1H, H$_{7'}$, ^3J = 8 Hz), 8.06 (d, 1H, H$_{4'}$, ^3J = 8.2 Hz);

¹³C-NMR (100 MHz, CDCl₃): δ (ppm) = 35.6 (CH₃, C_a), 112.2 (CH, C_1), 114.4 (CH, C_9), 121.6 (CH, $C_{7'}$), 122 (CH, C_7), 122.6 (CH, C_{4a}), 122.8 (CH, C_3), 123.1 (CH, $C_{4'}$), 125.3 (CH, $C_{5'}$), 126.4 (CH, $C_{6'}$), 127.2 (CH, C_1), 127.3 (CH, C_6), 127.5 (C_q, C_{5a}), 127.8 (CH, C_8), 132.9 (C_q, C_2), 135 (C_q, $C_{7a'}$), 145.3 (C_q, C_{9a}), 146.4 (C_q, C_{10a}), 154.1 (C_q, $C_{4a'}$), 167.8 (C_q, $C_{2'}$);

3-(benzo[d]thiazol-2-yl)-10-methyl-10H-phenothiazine (4)
Purification by recrystallisation, gave 0.9 g, 65 % as yellow solid (m.p. = 160-161°C).

HRMS (ESI+): [M+H⁺] found 347.0610, $C_{13}H_{13}N_2S$ requires 347.0671.

¹H-NMR (400MHz, CDCl₃): δ (ppm) = 3.39 (s, 3H, N-CH₃), 6.82 (d, 2H, H_9, H_1, ^3J = 8.2 Hz), 6.95 (td, 1H, H_7, ^3J = 7.4 Hz, ^4J = 0.8 Hz), 7.14-7.20 (m, 2H, H_8, H_6), 7.34 (td, 1H, $H_{6'}$, ^3J = 8 Hz, ^4J = 0.84 Hz), 7.46 td, 1H, $H_{5'}$, ^3J = 8.2 Hz, ^4J = 1 Hz), 7.84-7.86 (m, 3H, $H_{7'}$, H_2, H_4), 8.02 (d, 1H, $H_{4'}$, ^3J = 8 Hz);

¹³C-NMR (100 MHz, CDCl₃): δ (ppm) = 35.6 (CH₃, C_a), 114.1 (CH, C_1), 114.5 (CH, C_9), 121.6 (CH, $C_{7'}$), 122,7 (C_q, C_{4a}), 122.9 (CH, C_7), 123.1 (CH, $C_{4'}$), 124.2 (C_q, C_{5a}), 124.9 (CH, C_2), 125.96 (CH, $C_{5'}$), 126.4 (CH, $C_{6'}$), 127.1 (CH, C_1), 127.36 (CH, C_6); 127.7 (CH, C_8), 128 (C_q, C_3), 134.9 (C_q, $C_{7a'}$), 144.8 (C_q, C_{9a}), 148.2 (C_q, C_{10a}), 154.2 (C_q, $C_{4a'}$), 167.1 (C_q, $C_{2'}$);

4-(benzo[d]thiazol-2-yl)-10-methyl-10*H*-phenothiazine (5)
Purification by recrystallisation, gave 0.8 g, 60 % as yellow solid.

HRMS (ESI+): [M+H⁺] found 347.0615, $C_{13}H_{13}N_2S$ requires 347.0671.

¹H-NMR (400MHz, CDCl₃, ppm): δ (ppm) = 3.15 (s, 3H, N-CH₃), 6.57 (d, 1H, H_9, ^3J = 8 Hz), 6.63 (t, 1H, H_7, ^3J = 7.5 Hz), 6.68 (d, 1H, H_1, ^3J = 8.04 Hz), 6.8 (d, 1H, H_6, ^3J = 7.3 Hz), 6.92 (m, 1H, H_8), 7.01 (t, 1H, H_2, ^3J = 8 Hz), 7.18 (m, 2H, $H_{6'}$, H_3), 7.29 (m, 1H, $H_{5'}$), 7.7 (d, 1H, $H_{7'}$, ^3J = 7.92 Hz), 7.89 (d, 1H, $H_{4'}$, ^3J = 8.08 Hz);

¹³C-NMR (100 MHz, CDCl₃): δ (ppm) = 35.3 (CH₃, C_a), 113.5 (CH, C_9), 115.5 (CH, C_1), 121 (CH, $C_{7'}$), 122 (CH, C_7), 122.9 (CH, $C_{4'}$), 123.2 (C_q, C_{4a}), 123.7 (CH, $C_{6'}$), 124.9 (C_q, C_{5a}), 125.7 (CH, C_3), 126.5 (CH, $C_{5'}$), 127.2 (CH, C_6), 127.6 (CH, C_2); 128.4 (CH, C_8), 131 (C_q, $C_{7a'}$), 135 (C_q, C_4), 145.9 (C_q, C_{9a}), 145.95 (C_q, C_{10a}), 152.8 (C_q, $C_{3a'}$), 164.8 (C_q, $C_{2'}$);

3-(benzo[d]thiazol-2-yl)-7-bromo-10-methyl-10H-phenothiazine (6)
Purification by recrystallisation, gave 1.1 g, 68 % as greenish-yellow solid.

HRMS (APCI⁺): [M+H⁺] found 426.9755, $C_{20}H_{14}N_2S_2Br$ requires 424.9776.

¹H NMR (400MHz, CDCl₃): δ (ppm) = 3.38 (s, 3H, N-CH₃), 6.71 (d, 1H, H₉, ^3J = 9.24 Hz), 6.89 (d, 1H, H₁, ^3J = 8.5 Hz), 7.23-7.26 (m, 2H, H₆, H₈), 7.36 (t, 1H, H₆', ^3J = 6.24 Hz), 7.47 (t, 1H, H₅', ^3J = 7.3 Hz), 7.81-7.85 (m, 2H, H₂, H₄), 7.87 (d, 1H, H₇', ^3J = 8.2 Hz), 8.02 (d, 1H, H₄', ^3J = 8.2 Hz);

¹³C NMR (100 MHz, CDCl₃): δ (ppm) = 35.7 (CH₃), 114.3 (C_H, C₁), 115.4 (C_q, C₇), 115.6 (C_H, C₉), 121.6 (C_H, C₇'), 123 (C_H, C₄'), 125 (C_q, C₄ₐ), 125.1 (C_H, C₆'), 126 (C_H, C₄), 126.4 (C_H, C₅'), 127.3 (C_H, C₂), 128.4 (C_q, C₅ₐ), 129.5 (C_H, C₆); 130.4 (C_H, C₈), 134.9 (C_q, C₃), 144.1 (C_q, C₇ₐ'), 147.7 (C_q, C₉ₐ), 154.2 (C_q, C₃ₐ'), 166.9 (C_q, C₂');

3,7-bis(benzo[d]thiazol-2-yl)-10-methyl-10*H*phenothiazine (7)
Purification by recrystallisation, gave 0.6 g, 63 % as yellow solid.

HRMS (APCI⁺): [M+H⁺] found 480.0653, C₂₇H₁₈N₃S3 requires 480.0653.

¹H-NMR (400MHz, CDCl₃): δ (ppm) = 3.42 (s, 3H, N-CH₃), 6.93 (d, 2H, H₁, H₉, ^3J = 8.32 Hz), 7.36 (t, 2H, H₆', ^3J = 7.6 Hz), 7.48 (t, 2H, H₅', ^3J = 7.6 Hz), 7.81-7.86 (m, 4H, H₂, H₄), 7.88 (d, 2H, H₇', ^3J = 8.2 Hz), 8.03 (d, 2H, H₄', ^3J = 8.2 Hz);

¹³C-NMR (100 MHz, CDCl₃): δ (ppm) = 35.5 (CH₃, Cₐ), 114.9 (C_H, C₉), 121.5 (C_H, Cₐ), 122.8 (C_H, C₇'), 123.9 (C_H, C₇), 124.9 (C_q, C₄ₐ), 126 (C_H, C₄'), 126.3 (C_H, C₅'), 126.9 (C_H, C₆'), 128.3 (C_q, C₃), 134.7 (C_q, C₇ₐ'), 145.9 (C_q, C₉ₐ), 154 (C_q, C₃ₐ'), 166.7 (C_q, C₂').

ACKNOWLEDGMENTS

REFERENCES

1. J.K. Reichert, J. Lochtman, R. Miiller, I. Kanen, *Jahrestagung der FG Wasserchemie in der GdCh, Badenweiler*, **1993**.
2. R.B. Spies, B.D. Andresen and D.W. Rice Jr., *Nature*, **1987**, *327*, 697.

3. I. Liska, E.R. Brouwer, A.G.L. Ostheimer, H. Lingeman, U.A.T. Brinkman, R.B. Geerdink and W.H. Mulder, *Int. J. Environ. Anal. Chem.*, **1992**, *47*, 267.
4. P. Reddy, Y. Lin, H. Chang, *Arivoc.,* **2007**, *XVI*, 113.
5. Y. Heo, Y. Song, B. Kim, J. Heo, *Tetrahedron Lett.,* **2006**, *47,* 3091.
6. (a) H. Sharghi, O. Asemani, *Synth. Commun.*, **2009**, *39*, 860. (b) X. Wen, J. El Bakali, R. Deprez-Poulain, B. Deprez, *Tetrahedron Lett.,* **2012**, *53*, 2440. (c) V.K. Tandon, M. Kumar, *Tetrahedron Lett.* **2004**, *45*, 4185. (d) K. Yamamoto, H. Watanabe, *Chem. Lett.* **1982**, 1225.
7 (a) A.J. Blacker, M.M. Farah, M.I. Hall, S.P. Marsden, O. Saidi, J.M. Williams, *J. Org. Lett.,* **2009**, *11*, 2039. (b) C. Mukhopadhyay, P.K. Tapaswi, *Tetrahedron Lett.,* **2008**, *49*, 6237. (c) M.A. Chari, D. Shobha, T. Sasaki, *Tetrahedron Lett.,* **2011**, *52*, 5575. (d) S.S. Patil, V.D. Bobade, *Synth. Commun*., **2010**, *40*, 206. (e) S.M. Inamdar, V.K. More, S.K. Mandal, *Tetrahedron Lett.,* **2013**, *54*, 579.
8. S.P.G. Costa, A.M.F. Oliveira-Campos, J.A. Ferreira, G. Kirsch, *J. Chem. Res. (S)*, **1997**, 314, *J. Chem. Res. (M)*, **1997**, *9,* 2001.
9. (a) P. Saha, T. Ramana, N. Purkait, A.M. Ashif, R. Paul, T.J. Punniyamurthy, *Org. Chem.,* **2009**, *74*, 8719. (b) G. Evindar, R.A. Batey, *J. Org. Chem*., **2006**, *71*, 1802. (c) D. Yang, H. Fu, L. Hu, Y. Jiang, Y. Zhao, *J. Org. Chem.,* **2008**, *73*, 7841. (d) J. Peng, M. Ye, C. Zong, F. Hu, L. Feng, X. Wang, Y. Wang, C. Chen, *J. Org. Chem.,* **2011**, *76*, 716. (e) E.A. Jaseer, D.J.C. Prasad, A. Dandapat, G. Sekar, *Tetrahedron Lett.,* **2010**, *51*, 5009. (f) T. Itoh, T. Mase, *Org. Lett.,* **2007**, *9*, 3687. (g) D. Ma, S. Xie, P. Xue, X. Zhang, J. Dong, Y. Jiang, *Angew. Chem., Int. Ed.,* **2009**, *48*, 4222.
10. H. Wang, L. Wang, J. Shang, X. Li, H. Wang, J. Guia, A. Leiab, *Chem. Commun.,* **2012**, *48,* 76.
11. T.B. Nguyen, L. Ermolenko, W.A. Dean, A. Al-Mourabit, *J. Org. Lett*., **2012**, *14*, 5948.
12. Y. Liao, H. Qi, S. Chen, P. Jiang, W. Zhou, G. Deng, *J. Org.Lett.,* **2012**, *14*, 6004.
13. K. Sukanta, B. Koh, E.R. Biehl, *J. Heterocycl.Chem.,* **2006**, *43*, 1609.
14. (a) K. Sukanta, H. Zhang, E.R. Biehl, *Heterocycles,* **2005**, *65*, 2119.(b) L. Cai, X. Ji, Z. Yao, F. Xu, Q. Shen, *Chin. J. Chem.*, **2011**, *29*, 1880.
15. (a) Z.-X. Wang, H.-L. Qin, *J. Heterocycl. Chem.,* **2005**, *42*, 1001. (b) M.S. Mayo, X. Yu, X. Zhou, X. Feng, Y. Yamamoto, M. Bao, *Org. Lett*., **2014**, *16*, 764.
16. A. Ignat, T. Lovasz, M. Vasilescu, E. Fischer-Fodor, C.B. Tatomir, C. Cristea, L. Silaghi-Dumitrescu, V. Zaharia, *Arch. Pharm. Chem. Life Sci.,* **2012**, *345*, 574.

CELL@CELL HIGHER DIMENSIONAL STRUCTURES

ATENA PARVAN-MOLDOVAN[a] AND MIRCEA V. DIUDEA[a*]

ABSTRACT. Local domains of *n*-spaces surrounded by the common Euclidean 3D-space may exist in complex chemical (mineral or synthetic) structures. In this paper, two classes of the simplest clusters embedded in n-dimensional spaces higher than three are designed by operations on maps and their properties discussed.

Keywords: graph, n-dimensional space, n-cube, torus, cluster

INTRODUCTION

The gravitational theory (general relativity) describes our universe having the geometry of three-dimensional space with the fourth-dimension being the time. The so-called 3 + 1 space gives an accurate description of the universe we observe. A stellar black hole is believed to be formed by the gravitational collapse of a massive star (from five to several tens of the solar mass). Understanding the universe led us to the need of learning about spaces of dimensions higher than three. The aim of finding domains of *n*-spaces surrounded by the common Euclidean 3D-space, in complex chemical (mineral or synthetic) structures promoted our efforts towards a systematic design of n-dimensional hyper-structures. Let, for the beginning, introduce to some basic mathematical notions.

A ***convex hull*** (envelope) [1-3] of a set *X* of points in the Euclidean space is the smallest convex set that contains *X*. A set of points is called convex if it contains all the line segments connecting each pair of its points. The convex hull of a finite set *S* of points is the set of all its convex combinations; in a convex combination, each point x_i is weighted by a coefficient α_i such that the coefficients are all non-negative and their sum is one. For each choice of coefficients, the resulting convex combination is a point in the convex hull, and the whole convex hull can be generated by choosing coefficients in all possible ways. One can write the convex hull as the set:

[a] *Department of Chemistry, Faculty of Chemistry and Chemical Engineering, Babes-Bolyai University, 400028 Cluj, Romania*
* *Corresponding author: diudea@chem.ubbcluj.ro*

$$\left\{ \sum_{i=1}^{|S|} \alpha_i x_i \mid (\forall_i : \alpha_i \geq 0) \wedge \sum_{i=1}^{|S|} \alpha_i = 1 \right\} \tag{1}$$

The convex hull of a finite point set $S \in \mathbf{R}^n$ forms a convex polygon, for $n = 2$, or, in general, a convex polytope in $\mathbf{R}^n$. Every convex polytope in $\mathbf{R}^n$ is the convex hull of its vertices.

There are six regular 4D-polytopes, also called polychora: 5-Cell {3,3,3}; 8-Cell {4,3,3}; 16-Cell {3,3,4}; 24-Cell {3,4,3}; 120-Cell {5,3,3} and 600-Cell {3,3,5}. Five of them can be associated to the Platonic solids but the sixth, the 24-cell has no close 3D equivalent; it consists of 24 octahedral cells, 6 cells meeting at each vertex. Among them, 5-Cell and 24-Cell are self-cage-dual while the others are pairs: (8-Cell & 16-Cell); (120-Cell & 600-Cell). In the above, {p, q, r,…} are the Schläfli symbols: the symbol {p} denotes a regular polygon for integer p, or a star polygon for rational p; the symbol {p, q} denotes a 3D-object tessellated by p-gons while q is the vertex-figure (i.e. the number of p-gons surrounding each vertex); the symbol {p, q, r} describes a 4D-structure, in which r 3D-objects join at any edge (r being the edge-figure) of the polytope, and so on. The Schläfli symbol has the nice property that its reversal gives the symbol of the dual polyhedron. The 4D polytopes have been first described by Schläfli [4].

In dimensions 5 and higher, there are only three kinds of convex regular polytopes no non-convex regular polytopes exists. Let us give some details, in the following.

The **n-simplex**[1], with Schläfli symbol $\{3^{n-1}\}$, and the number of its k-faces$\binom{n+1}{k+1}$, is a generalization of the triangle or tetrahedron to arbitrary dimensions. A simplex is an n-dimensional polytope, which h is the convex hull of its $n+1$ vertices. For example, a 0-simplex is a point, a 1-simplex is a line segment, a 2-simplex is a triangle, a 3-simplex is a tetrahedron, and a 4-simplex is a 5-cell. A simplex may be defined as the smallest convex set containing the given vertices. A regular n-simplex may be constructed from a regular $(n − 1)$-simplex by connecting a new vertex to all original vertices by the common edge length.

The convex hull of any nonempty subset of $k+1$ points that define an n-simplex is called a *face* of the simplex; faces are simplexes themselves. In particular, the convex hull of a subset of size $k+1$ (of the $n+1$ defining points) is a k-simplex and is called a k-face of the n-simplex. The 0-faces (i.e., the points themselves) are called the *vertices*, the 1-faces are called the *edges*, the $(n − 1)$-faces are called the *k-faces* (or *facets)*, and the sole n-face is the whole n-simplex itself.

The **hypercube** [1] is a generalization of the 3-cube to n-dimensions; it is also called an n-cube and commonly denoted Q_n. It is a regular polytope with mutually perpendicular sides, thus being an orthotope. It has the Schläfli symbol $\{4,3^{n-2}\}$ and k-faces given by $2^{n-k}\binom{n}{k}$. Figure 1 illustrates the 4-cube, i.e., 8-Cell or Tesseract, as painted by the Italian painter Juseppe Zaccuri, Milano.

Figure 1. HyperCube by Juseppe Zaccuri, Milano

The **n-orthoplex or cross-polytope** [1] has the Schläfli symbol $\{3^{n-2},4\}$ and k-faces $2^{k+1}\binom{n}{k+1}$; it exists in any number of dimensions and is the dual of n-cube. The cross-polytope is the convex hall of its vertices; its facets are simplexes of the previous dimensions, while its vertex figures are other cross-polytopes of lower dimensions.

To investigate an n-dimensional polytopes, a formula, also due to Schläfli [4], is used

$$\sum_{i=0}^{n-1}(-1)^i f_i = 1-(-1)^n \tag{2}$$

For n=4, eq (2) reduces to the well-known Euler [5] relation

$$v - e + f = 2(1-g) \tag{3}$$

with v, e, f and g being the vertices, edges, 2-faces and the genus, respectively; g=0 for the sphere and g=1 for the torus.

RESULTS AND DISCUSSION

The n-dimensional spaces may be locally present in minerals or artificial chemicals [6]. Some 4-dimensional 13-atom clusters: MaMb12 or M13, M=Fe, Pd, Ru, Rh was found to show giant magnetic moments [7]. Other simple molecules as B4Cl4, $Co(CO)_4^-$, etc. may be described in dimensions higher than three. In this respect, two simplest classes of clusters showing dimensionality higher than three will be introduced as follows.

P-Centered Clusters

Body centered clusters derived from the Platonic solids are easily drawn, as shown in Figure 2; their figure count is given in Table 1. These small clusters, excepting DoP.21, were next transformed by operations on maps [8-10] in their 2-dual, medial (i.e. rectified) and truncated derivatives (Figures 3 to 6). P-centered clusters represent cell-duals of polyhedra with the same number of cells around a central one; they are objects of Euclidean 4D-space, as shown by the figure count (Tables 2 to 5) cf. eq (2). This idea can be extended to objects other than Platonics.

The name of clusters can be made in at least three ways, as shown in the bottom of figures and tables; the "endohedral" @ symbol was used, starting from the core and going radially, to the exterior, the suffix number counting the points/atoms in the whole structure.

TP.5	OctP.7	CP.9	DoP.21	IcoP.13
P@T.5	P@Oct.7	P@C.9	P@Do.21	P@Ico.13
P@T4@T.5	P@T8@Oct.7	P@(Py4)6@C.9	P@(Py5)12@Do.21	P@T20@Ico.13
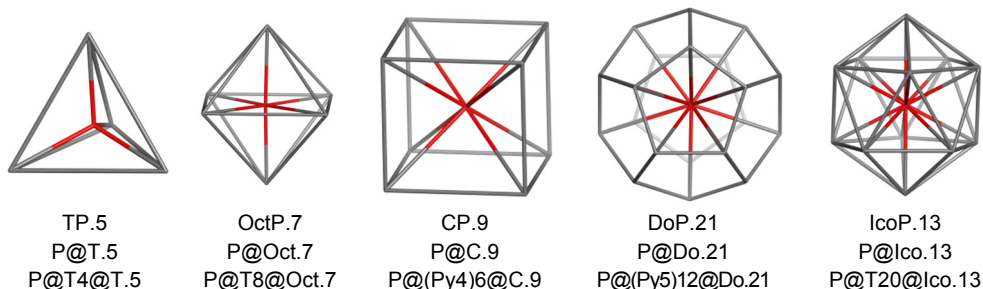
Figure 2. Body centered clusters derived from the Platonic solids

Table 1. Figure count for clusters in Figure 2

Cluster	v	e	f_3	f_5	f_6	f	p1	p2	p3	M	c	Sum(f)	Sym	p_k; (M)
TP	5	10	10	0	0	10	4	0	0	1	5	0	3	T; 0; 0 (T)
OctP	7	18	20	0	0	20	8	0	0	1	9	0	4	T;0;0 (Oct)
CP	9	20	12	6	0	18	0	0	0	1	7	0	4	0;Py4; 0 (C)
DoP	21	50	30	0	12	42	0	12	0	1	13	0	5	0;Py5;0 (Do)
Icop	13	42	50	0	0	50	20	0	0	1	21	0	5	T; 0; 0 (Ico)

| Du(TP).10 | Med(TP).10 | Tr(TP).20 |
| T@Oct.10 | T@Oct.10 | T@(TT4;T4)@TT.20 |
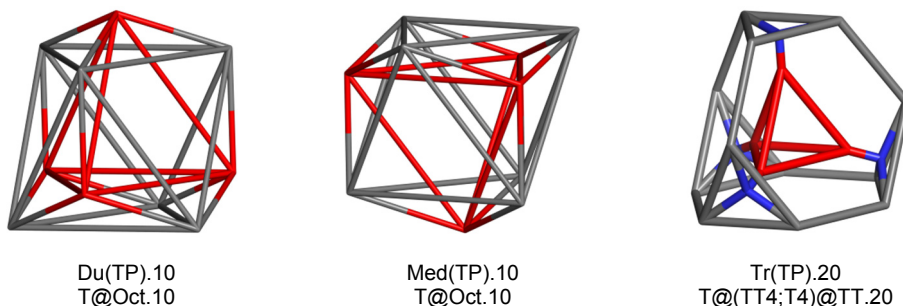
Figure 3. TP-derived structures

Table 2. Figure count for clusters derived from TP cluster

T-structure	v	e	f₃	f₅	f₆	f	p1	p2	p3	M	c	Sum(f)	Sym	p_k; (M)
TP.5	5	10	10	0	0	10	4	0	0	1	5	0	3	T; 0; 0 (P; T)
Du(TP).10	10	30	30	0	0	30	4	4	0	2	10	0	3	T; Oct= AP₃; 0 (T;Oct)
Med(TP).10	10	30	30	0	0	30	4	4	0	2	10	0	3	T; Oct= AP₃; 0 (T;Oct)
Tr(TP).20	20	40	20	0	10	30	4	4	0	2	10	0	3	T;TT; 0 (T; TT)

| Du(OctP).20 | Med(OctP).18 | Tr(OctP).36 |
| CO@((AP4)6;T8)@C.20 | Oct@(Oct8;(Py4)6)@CO.18 | Oct@(TT8;(Py4)6)@TO.36 |
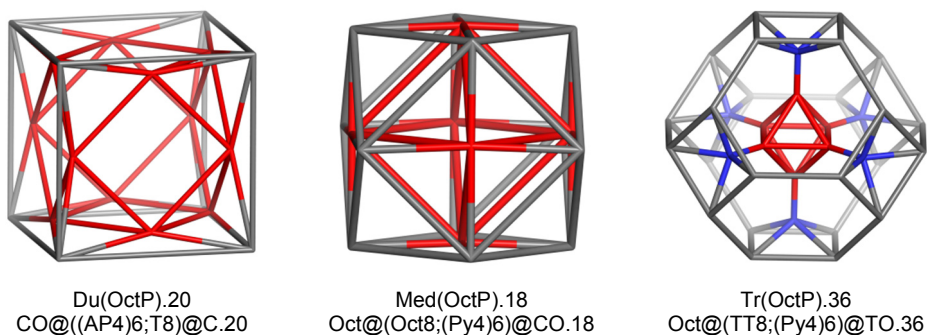
Figure 4. OctP-derived structures

Table 3. Figure count for clusters derived from OctP cluster

Oct-structure	v	e	f₃	f₅	f₆	f	p₁	p₂	p₃	M	c	Sum(f)	Sym	p_k; (M)
OctP.7	7	18	20	0	0	20	8	0	0	1	9	0	4	T;0;0 (P;Oct)
Du(OctP).20	20	60	44	12	0	56	8	6	0	2	16	0	4	T;Ap4;0 (CO;C)
Med(OctP).18	18	60	52	6	0	58	8	6	0	2	16	0	4	Oct; Py4 (Oct; CO)
Tr(OctP).36	36	78	32	6	20	58	8	6	0	2	16	0	4	TT;Py4;0 (Oct;TO)

Du(CP).18
Oct@(Oct8;(Py4)6)@CO.18

Med(CP).20
C@((AP4)6;T8)@CO.20

Tr(CP).40
C@((HTO)6;T8)@TC.40
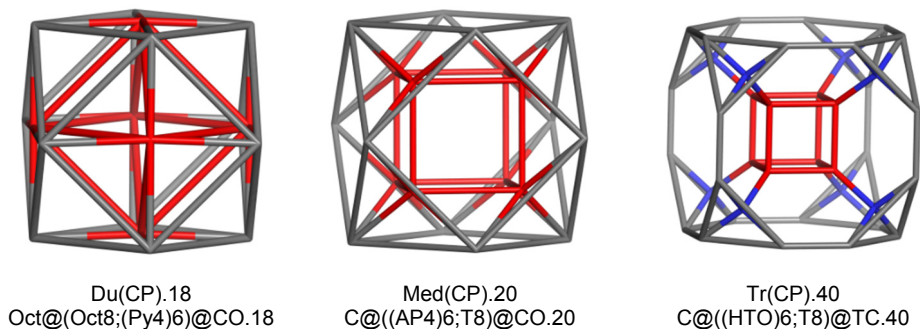
Figure 5. CP-derived structures

Table 4. Figure count for clusters derived from CP cluster

C-structure	v	e	f_3	f_5	f_6	f	p_1	p_2	p_3	M	c	Sum(f)	Sym	p_k; (M)
CP.9	9	20	12	6	0	18	0	6	0	1	7	0	4	0;Py4; 0 (P;C)
Du(CP).18	18	60	52	6	0	58	8	6	0	2	16	0	4	Oct; Py4 (Oct; CO)
Med(CP).20	20	60	44	12	0	56	8	6	0	2	16	0	4	T;Ap4;0 (C; CO)
Tr(CP).40	40	80	32	6+6	12	56	8	6	0	2	16	0	4	T;HTO;0 (C; TC)

Du(IcoP).50
ID@((AP5)12;T20)@Do.50
Med(DoP).50=Do@((AP5)12;T20)@ID.50

Med(Icop).42
Ico@(Oct20;(Py5)12)@ID.42

Tr(Icop).84
Ico@(TT20;(Py5)12)@C60.84
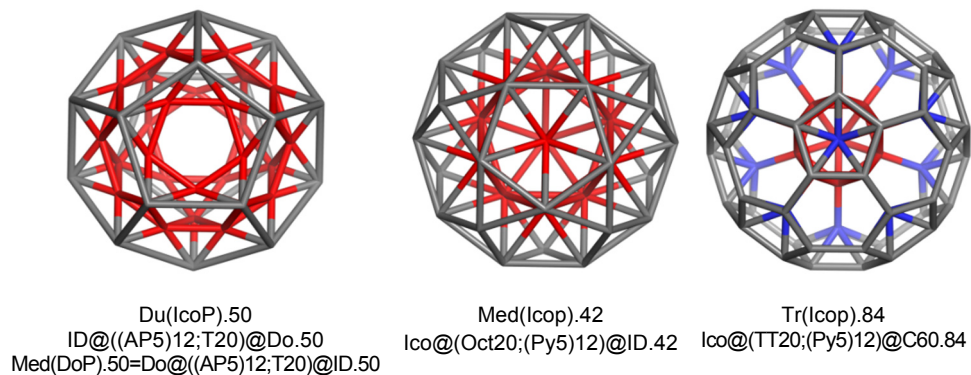
Figure 6. IcoP-derived structures

Table 5. Figure count for clusters derived from IcoP cluster

Ico-structure	v	e	f_3	f_5	f_6	f	p_1	p_2	p_3	M	c	Sum(f)	Sym	p_k; (M)
IcoP.13	13	42	50	0	0	50	20	0	0	1	21	0	5	T; 0; 0 (P; Ico)
Du(IcoP).50	50	150	110	24	0	134	20	12	0	2	34	0	5	T;AP5;0 (ID30;Do20)
Med(Icop).42	42	150	130	60	12	142	20	12	0	2	34	0	5	Oct; Py5;0 (Ico;ID30)
Tr(Icop).84	84	192	80	0	62	142	20	12	0	2	34	0	5	TT; Py5; 0 (Ico;C60)

Note that Tr(Icop).84 is related to the Samson cluster, that consists of twenty truncated tetrahedra TT (Friauf polyhedra), icosahedrally arranged, with a central atom inside each TT, all together counting 104 points/atoms [11-13]; the central shell forms an icosahedron. It is related to intermetallic phases. Intermetallics [14] represent compounds involving two or more metals, e.g. Laves phases (AB_2), e.g., $MgCu_2$, $MgZn_2$ and $MgNi_2$, size packing phases, such as Frank-Kasper, phases, etc. They can display desirable magnetic, superconducting and chemical properties, due to their strong internal order and mixed (metallic and covalent/ionic bonding, respectively). Intermetallics have promoted novel materials development.

Cell-in-Cell Clusters

Let now introduce the selective truncation operation (for general map operations, the reader is invited to consult refs [8-10, 15]: it leaves unchanged the non-marked points/atoms. In this simple way, cell-in-cell clusters can be designed (Figure 7); the figure count for these structures is listed in Table 6.

Further examples are shown in Figures 8 and 9 while their figure count is given in Table 7. Observe the double-shell torus T(4,12)Q4T5.96 (Figure 9, left), with a square tube section; every sector can be counted as an n-cube (see Figure 9, right). It was proposed by Diudea [16] as a model for the galactic black holes.

| T@T.8 | Oct@Oct.12 | C@C.16 | Do@Do.40 | Ico@Ico.24 |
| T@(P3)4@T.8 | Oct@(P3)8@Oct.12 | C@C6@C.16 | Do@((P5)12@Do.40 | Ico@((P3)20@Ico.24 |
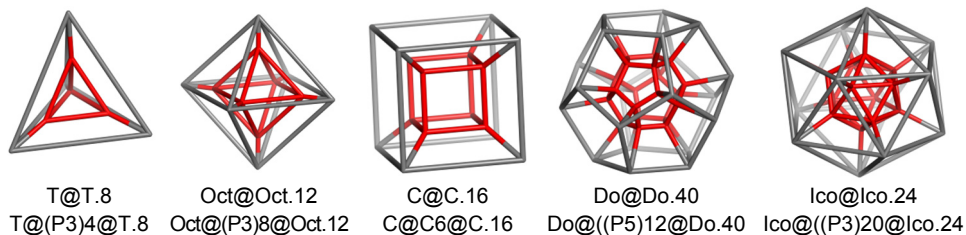
Figure 7. Selectively truncated body centered clusters of the Platonic solids

Table 6. Figure count for selectively truncated body centered clusters
Trs(P@M); M= Platonic solids

	Trs(P@M)	v	e	f_3	f_4	f_5	f	p_k	M	Cell	Sum(f)	Sym	p_k; M
1	.T@T.8	8	16	8	6	0	14	4	2	6	0	3	P3 (T;T)
2	Oct@Oct_12	12	30	16	12	0	28	8	2	10	0	4	P3 (Oct;Oct)
3	C@C.16	16	32	0	24	0	24	6	2	8	0	4	P4 (C;C)
4	Do@Do.40	40	80	0	30	24	54	12	2	14	0	5	P5 (Do;Do)
5	Ico@Ico.24	24	72	40	30	0	70	20	2	22	0	5	P3 (Ico;Ico)

ID@ID.60
ID@((P5)12;(P3)20)@ID.60

C$_{60}$@C$_{60}$.120
C$_{60}$@((P5)12;(P6)20)@C$_{60}$.120
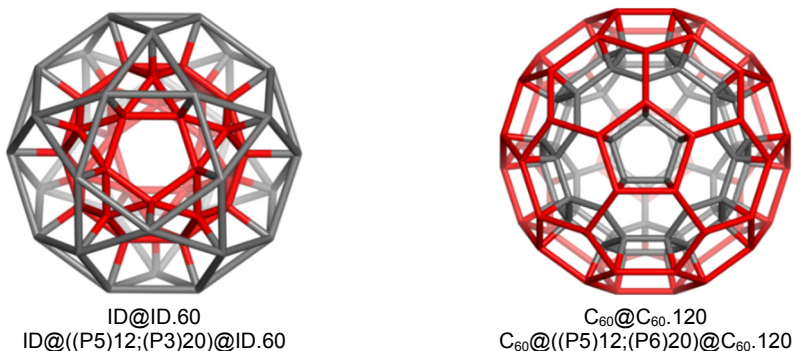
Figure 8. Other "cell-in-cell" structures

T(4,12)Q4T5.96

Q6(TU(4,8)Q6T7.64
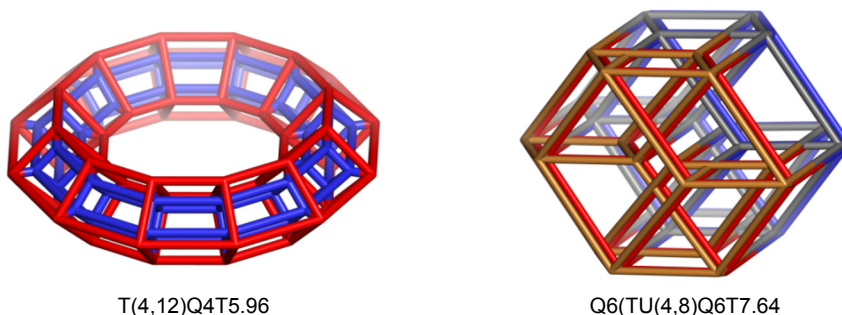
Figure 9. A double-wall torus with the square section and 12 units Q4 (left);
a detailed Q6 unit (right)

Table 7. Figure count for the objects in Figures 4 and 5

Structure	0	1	f3	f4	f5	f6	2	p3	p5	p6	m	3	4	5	Sum(f)
ID@ID.60	60	150	40	60	24	0	124	20	12	0	2	34	0	0	0
C$_{60}$@C$_{60}$.120	120	240	0	90	24	40	154	0	12	20	2	34	0	0	0
T(4,12)Q$_4$T$_5$.96	96	240	0	216	0	0	216	0	0	0	0	84	12	0	0*
Q6.64	64	192	0	240	0	0	240	0	0	0	0	160	60	12	0

* in case of Torus, the right member of (2) gives all time zero, because the torus is a surface of genus *g*=1.

It is the time to show a lower bound for the clusters existing in dimensions higher than three:

Theorem. A cluster of points/atoms with at least two (concentric) shells belongs to *n*-spaces higher than tridimensional.

Proof. A polytope is convex if any of its *k*-facets is shared by at least two *k*+1-facets. In particular, for *n*=4, *k* =2 while *k*+1 is a 3-facet, i.e. a cell. In other words, any 2-facet must share at least two 3-facets: the actual cell and the whole envelope. Next, the cluster is bound by 3-facets, thus the polytope is of dimension 3+1=4. This condition is already reached in P-centered clusters (Figure 2; Table 1), as much as in the "cell-in-cell" double-shell clusters (Figure 7). This is a lower bound condition and the theorem is demonstrated.

At the end, two pairs of clusters are presented: Med(CP).20 & Du(OctP).20 (Figure 10, left) and Med(DoP).50 & Du(IcoP).50 (Figure 10, right); they illustrate the sphere inversion event and is equivalent to tesseract moving on the fourth dimension (i.e. the time), a proof in addition that double-shell clusters belong to higher-dimensional spaces.

CO@C.20	C@CO.20	ID@Do.50	Do@ID.50
CO@((AP4)6;T8)@C	C@((AP4)6;T8)@CO	ID@((AP5)12;T20)@Do	Do@((AP5)12;T20)@ID
Med(CP).20	Du(OctP).20	Med(DoP).50	Du(IcoP).50
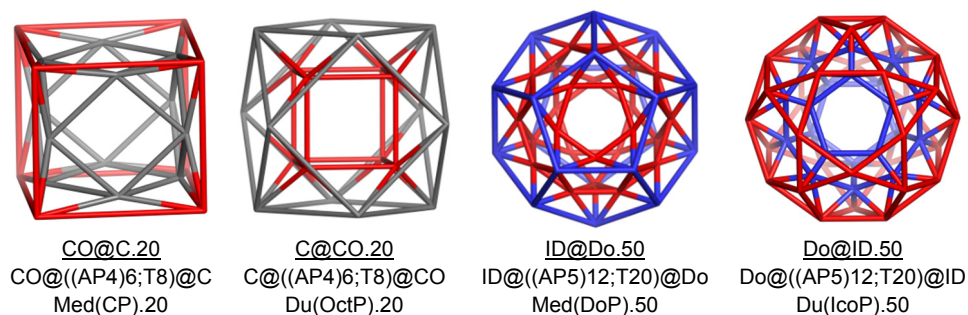
Figure 10. Sphere inversion by 4D-clusters: moving on the fourth dimension

COMPUTATIONAL DETAILS

The design and properties of the studied structures was performed by our original CVNET [17] and Nano Studio [18] software programs.

CONCLUSIONS

Some 4D-and higher-dimensional structures have been designed by using operations on maps, and their topological properties discussed. Multi-shell clusters appear frequently in minerals/chemicals and such analysis as we performed here could help in structure elucidation efforts.

There is a trend in Chemistry, Physics and even Astronomy to consider the *n*-dimensional spaces locally mixed/interlaced with the actually perceptible 3-dimensional Euclidean space. It seems that 3D-space and nD-spaces

simultaneously exist, as a manner of highly organizing the matter. The difficulty of visualization of the higher dimensions arises from the fact that only projections of the whole nD-structure can be seen in 3D- or even 2D-spaces.

ACKNOWLEDGEMENTS

REFERENCES

1. *http://en.wikipedia.org/wiki/Convex_hull; http://en.wikipedia.org/wiki/Simplex*; *http://en.wikipedia.org/wiki/Cross-polytope; http://en.wikipedia.org/wiki/Hypercube.*
2. H.S.M. Coxeter, *Regular Polytopes, 3rd ed.* New York: Dover, **1973**.
3. B. Grünbaum, *Convex Polytopes*, Graduate Texts in Mathematics (2nd ed.), Springer, **2003**.
4. L. Schläfli, *Theorie der vielfachen Kontinuität Zürcher und Furrer*, Zürich, 1901 (Reprinted in: Ludwig Schläfli, 1814-1895, Gesammelte Mathematische Abhandlungen, Band 1, 167–387, Verlag Birkhäuser, Basel, **1950**).
5. L. Euler, *Novi Comm. Acad. Scient. Imp. Petrop*. **1758**, *4*, 109-160.
6. V. Ya. Shevchenko, G.V. Zhizhin, A.L. MacKay, in: M.V. Diudea, C.L. Nagy (Eds.), *Diamond and Related Nanostructures*, Springer, Dordrecht, **2013**, Chap.17, p. 311.
7. B.V. Reddy, S.N. Khanna and B.I. Dunlap, *Phys. Rev. Lett.***1993**, *70*(21), 3323.
8. M.V. Diudea, M. Stefu, P.E. John and A. Graovac, *Croat. Chem. Acta,* **2006**, *79*, 355.
9. M.V. Diudea, *J.Chem.Inf.Model.*, **2005***, 45*,1002.
10. M.V. Diudea, *Studia UBB Chemia*, **2003**, *48* (2), 3.
11. S. Samson, *Acta Cryst.* **1965**, *19*, 401.
12. S. Samson, *Acta Cryst.* B, **1972**, *28*, 936.
13. M. de Boisieu, J. M. Dubois, M. Audier and B. Dubost, *J. Phys., Cond. Matter*, **1991**, *3*, 1.
14. *http://en.wikipedia.org/wiki/Intermetallic*
15. M.V. Diudea, in: M.V. Diudea, C.L. Nagy, Eds., Diamond and Related Nanostructures, Springer, Dordrecht, Heidelberg, New York, London, **2013**, Chap. 19, p. 333.
16. M.V. Diudea, *Int. J. Chem. Model.*, **2015**, *7*, 000.
17. M. Stefu and M.V. Diudea, CageVersatile_CVNET, *Babes-Bolyai Univ.* Cluj, **2005**.
18. Cs. L. Nagy, M.V. Diudea, NANO-Studio, *Babes-Bolyai Univ.* Cluj, **2009**.

ANTIOXIDANT AND HEPATOPROTECTIVE EFFECT OF CHITOSAN VERSUS VITAMIN E IN EXPERIMENTAL CARBON TETRACHLORIDE-INDUCED LIVER INJURIES

CRISTIAN CEZAR LOGIN[a,*], ANDRAS-LASZLO NAGY[b], ADRIANA MUREŞAN[a], REMUS MOLDOVAN[a], NICOLETA DECEA[a], DOINA DAICOVICIU[a], SIMONA CLICHICI[a]

ABSTRACT. The aim of our study was to assess the hepatoprotective and antioxidant effects of chitosan as compared with vitamin E in experimental toxic liver injury induced by carbon tetrachloride. Blood and liver samples were collected in order to assess hepatocytolisis (AST, ALT), oxidative stress (MDA, carbonyl proteins, GSH, SH groups, SOD and CAT), and histopathology examination was performed in order to asses inflammation and fibrosis. Liver enzymes level showed a significant, progressive increase after repeated exposure to CCl_4, first in liver tissue, then in the blood. Malondialdehyde and carbonyl proteins significantly increased, and GSH progressively decreased. Chitosan increased the GSH in the liver tissue to a value superior to that of the control group and decreased the AST and MDA level both in the liver and in the blood to values comparable to that of control group. Chitosan decreased carbonyl proteins level in the liver but slightly increased them in the blood. Vitamin E had similar effects concerning liver function and lipid peroxidation, but paradoxically, it induced protein peroxidation both in blood and in liver tissue. Histological modifications support the observed biochemical changes.

Keywords: chitosan, vitamin E, fibrosis, antioxidants

INTRODUCTION

The liver plays an essential role in the metabolism of a numerous toxic substances that enter the organism through the gastro-intestinal tract [1, 2]. Chronic exposure to small doses of carbon tetrachloride (CCl_4) leads

[a] *Iuliu Haţieganu University of Medicine and Pharmacy, Department of Physiology, 1 Clinicilor Street, Cluj-Napoca, Romania*
[b] *University of Agricultural Sciences and Veterinary Medicine, Department of Veterinary Toxicology, 3-5 Mănăştur Street, Cluj-Napoca, Romania*
[*] *Corresponding author: cezar.login@umfcluj.ro*

to formation of trichloromethyl and trichloromethyl peroxy radicals which, in turn, are able to oxidase the polyunsaturated fatty acids (PUFA) of the cell membrane and to induce oxidative injuries [3, 4]. Membrane injuries will lead to hepatocytes necrosis [5] and release of the liver enzymes. The oxidative stress will induce an increase in the activity of antioxidant enzymes (SOD, CAT, GPx) [5] and of the endogenous antioxidants level (GSH, SH), followed by a decrease, when the endogenous reserves will be depleted [6]. The use of synthetic and natural antioxidant substances have positive effects against oxidative stress induced liver injuries [3, 4, 7-9]. Vitamin E is capable to protect the PUFA against the reactive oxygen species (ROS) and can be used as an efficient antioxidant substance for the membranes [8, 9]. In toxic hepatitis induced by repeated experimental exposure to small amounts of carbon tetrachloride, vitamin E is able to scavenge free radicals, thus reducing the lipid peroxidation and protecting the endogenous antioxidants [10, 11]. Chitosan (CS) is a polymer obtained through the deacetylation of the chitin found in the exoskeleton of the marine shellfish. It has hemostatic [12], anti-inflammatory and antibacterial properties [13-15]. Recent studies also underlined its antioxidant and hepatoprotective properties and its ability to reduce the oxidative stress [16]. The aim of our study was to assess the antioxidant and hepatoprotective effects of chitosan as compared with vitamin E in experimental toxic liver injury induced by carbon tetrachloride.

RESULTS AND DISCUSSIONS

The mean values of the lipid and protein peroxidation products are presented in tables 1 and 2, of the non-enzymatic antioxidants in tables 3 and 4, and of the enzymatic antioxidants in table 5. Statistical significant differences (p<0.05) between groups are marked as follows: [a] (Ctrl-CCl4), [b] (Ctrl-VitE), [c] (Ctrl-CS), [d] (CCl4-VitE), [e] (CCl4-CS), [f] (VitE-CS).

Table 1. Mean values of the malondialdehyde in plasma and liver tissue

Group	Day 15		Day 30	
	Plasma (nmol/ml)	Tissue (nmol/mg prot.)	Plasma (nmol/ml)	Tissue (nmol/mg prot.)
Ctrl	2.37±0.36[a]	0.061±0.017[a]	1.26±0.17	0.078±0.009[a]
CCl4	2.82±0.31	0.092±0.015	1.30±0.60	0.101±0.023
CCl4+VitE	2.81±0.55	0.072±0.022	1.40±0.20	0.086±0.015
CCl4+CS	2.42±0.38	0.075±0.020	1.32±0.20	0.085±0.016

Table 2. Mean values of the carbonyl proteins in plasma and liver tissue

Group	Day 15		Day 30	
	Plasma (nmol/mg prot.)	Tissue (nmol/mg prot.)	Plasma (nmol/mg prot.)	Tissue (nmol/mg prot.)
Ctrl	1.13±0.32[b, c]	2.72±0.74[c]	1.21±0.14[b,c]	2.77±0.75
CCl$_4$	1.72±0.59	3.21±0.49[e]	1.44±0.45[d]	2.38±0.76
CCl$_4$+VitE	1.71±0.48	3.22±0.66	2.05±0.47	2.76±0.35
CCl$_4$+CS	2.10±0.50	1.75±0.61	1.73±0.34	2.82±0.84

Table 3. Mean values of the reduced glutathione (GSH)

Group	Day 15		Day 30	
	Plasma (nmol/ml)	Tissue (nmol/mg prot.)	Plasma (nmol/ml)	Tissue (nmol/mg prot.)
Ctrl	17.62±3.43[a,b]	0.63±0.28[a,b,c]	6.13±1.53[b,c]	1.42±0.36[b,c]
CCl$_4$	14.12±2.60[d]	2.20±0.70[e]	5.66±0.79[d,e]	0.93±0.51[d,e]
CCl$_4$+VitE	5.90±0.81[f]	2.41±1.09	10.16±1.64	2.16±0.34
CCl$_4$+CS	14.85±5.44	3.98±1.45	10.48±1.18	1.97±0.42

Table 4. Mean values of Sulfhydryl Groups (SH)

Group	Day 15		Day 30	
	Plasma (µmol/ml)	Tissue (µmol/mg prot.)	Plasma (µmol/ml)	Tissue (µmol/mg prot.)
Ctrl	0.081±0.015[c]	0.056±0.007	0.132±0.029[a,c]	0.078±0.013[a,c]
CCl$_4$	0.088±0.040[e]	0.052±0.007	0.084±0.022[d]	0.054±0.012[e]
CCl$_4$+VitE	0.069±0.028[f]	0.066±0.029	0.158±0.036[d]	0.062±0.013
CCl$_4$+CS	0.015±0.003	0.060±0.019	0.064±0.026	0.043±0.007

Table 5. Mean values of the enzymatic antioxidants plasma

Group	SOD (U/ml)		CAT (U/ml)	
	Day 15	Day 30	Day 15	Day 30
Ctrl	6848.57±984.86[a,b]	11344±1721.08[a,c]	5.26±0.49[a]	8.98±0.96
CCl$_4$	10418.16±1463.55	13606±1520.50[d,e]	6.53±0.40	8.52±0.43
CCl$_4$+VitE	9259.53±1046.89	10310±684.79[f]	7.62±1.46	8.23±1.10
CCl$_4$+CS	8897.06±2608.63	9306±576.22	6.56±1.75	8.57±0.46

After CCl$_4$ administration, our study identified a significant increase in MDA level both in plasma (day 30) and in liver tissue (day 15 and 30), which suggests the onset of the oxidative stress first in the liver and then in the blood. CCl$_4$ administration first stimulated the antioxidant enzymes levels (SOD, CAT) and induced a decreased of endogenous antioxidants (GSH,

SH). Good correlations between MDA and GSH have been identified ($\rho=0.57$). After vitamin E administration, our studied identified a significant increase of GSH level in the liver tissue to a level superior to that of the control group. After chitosan administration, a significant GSH increase was observed (day 15) in the liver tissue as compared with the CCl$_4$ exposed rats, and the level remained increased until the end of the experiment (day 30). Our results identified biochemical changes similar to those described in the literature [5, 17-21]. Both chitosan and vitamin E are able to decrease the oxidative stress level.

Carbon tetrachloride also induced an increase in carbonyl proteins level in the plasma, but not in the liver tissue. Neither vitamin E, nor chitosan protected the proteins against oxidative stress. Paradoxically, both substances demonstrated a slightly pro-oxidant effect on the proteins. Vitamin E administration induced protein peroxidation in the plasma, while the liver tissue values were not significantly modified as compared with the control group, changes that can be explained by the dual effect of vitamin E [11, 22, 23]. This effect was less visible concerning chitosan; its administration decreased protein oxidation in the liver tissue, while the plasma levels remained slightly increased. Anraku *et al.*, using a low molecular weight chitosan, also observed a decrease in plasma albumin peroxidation [24]. It is possible that the antioxidant effect on the proteins might be related to the molecular weight of the chitosan.

Table 6. Mean values of the liver enzymes

Group	AST (U/ml)		ALT (U/ml)	
	Day 15	*Day 30*	*Day 15*	*Day 30*
Ctrl	42.93±8.37[a,b,c]	58.46±16.15[a,b,c]	35.88±3.92[a,b,c]	45.48±13.10[a,b,c]
CCl$_4$	153.69±18.55[e]	229.82±41.09[d,e]	172.10±20.28[e]	220.61±54.68[d,e]
CCl$_4$+VitE	155.33±27.58[f]	186.37±18.95	147.00±34.39	152.24±19.45
CCl$_4$+CS	124.19±16.46	181.99±26.69	129.87±17.54	173.57±35.26

After the oxidative injuries, transaminases (AST, ALT) are released in the serum. AST is much more specific for liver injuries [25]. Our research identified a significant increase in liver enzymes levels after CCl$_4$ administration during the entire experiment, proportional with the duration of the exposure to CCl$_4$. AST serum level correlates with MDA level both in plasma ($\rho=0.792$) and in liver tissue ($\rho=0.493$). After vitamin E administration, some studies identified a decrease in the AST and ALT levels. We also identified a gradual decrease in AST level after vitamin E treatment, without arriving to values similar to those of the control group. The use of natural antioxidants in toxic liver injuries has hepatoprotective and antioxidant effects. Previous studies identified the antioxidant capacity of the chitosan in toxic liver pathology [16, 26]. Our study identified a decrease in AST levels after chitosan administration. Our results are

consistent with those found in the literature. Vitamin E and chitosan, administered simultaneously with CCl$_4$, have different effect of the oxidative stress and liver injuries. Both substances have the ability to decrease the transaminase levels, but none of them, in the used doses, completely protects against the action of CCl$_4$. In the context of our experiment, chitosan has superior antioxidant effects as compared with the vitamin.

Microscopic examination of the liver sections from animals of the control group revealed normal liver architecture. In the experimental groups at both sampling intervals, the most obvious lesions were represented by vacuolar dystrophy and hepatocellular necrosis, mainly in the central areas. Degenerated hepatocytes from the central areas presented clear cytoplasmic vacuoles of different size. Some of the hepatocytes presented numerous small vacuoles, the cytoplasm having a foamy aspect, other hepatocytes suffer hydropic change, characterized by hypertrophy and ballooning of the hepatocytes with a centrally located nucleus. Some hepatocytes presented granular degeneration. In some areas diffuse dilatation of the sinusoids was also evident (figures 1 and 2).
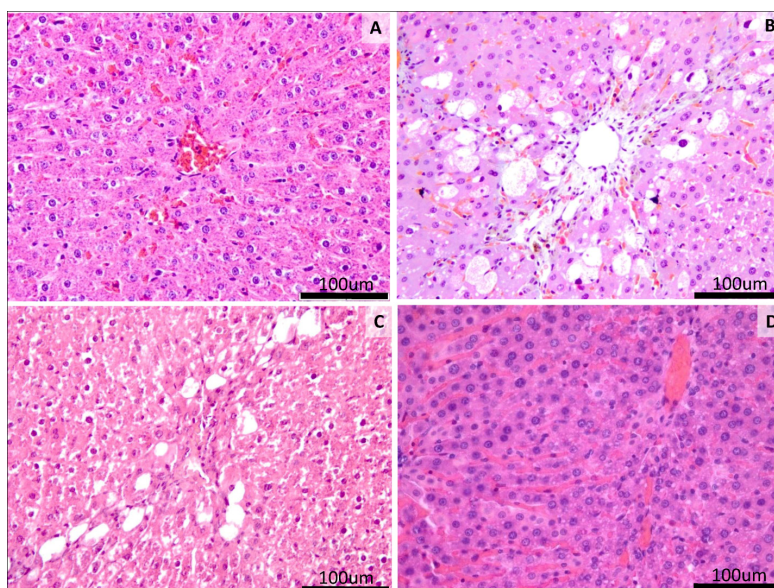

Figure 1. Histological changes in different experimental groups on the 15th day. Control group (A): central area, normal hepatic architecture; CCl$_4$ group (B): vacuolization of the hepatocytes from central areas; CCl$_4$+VitE group (C): hepatocellular vacuolization and necrosis; CCl$_4$+Chitosan group (D): discrete microvesicular steatosis, hepatocytes with a foamy aspect near the central areas, HE stain, original magnifications of 200×, Scale bar=100 μm.
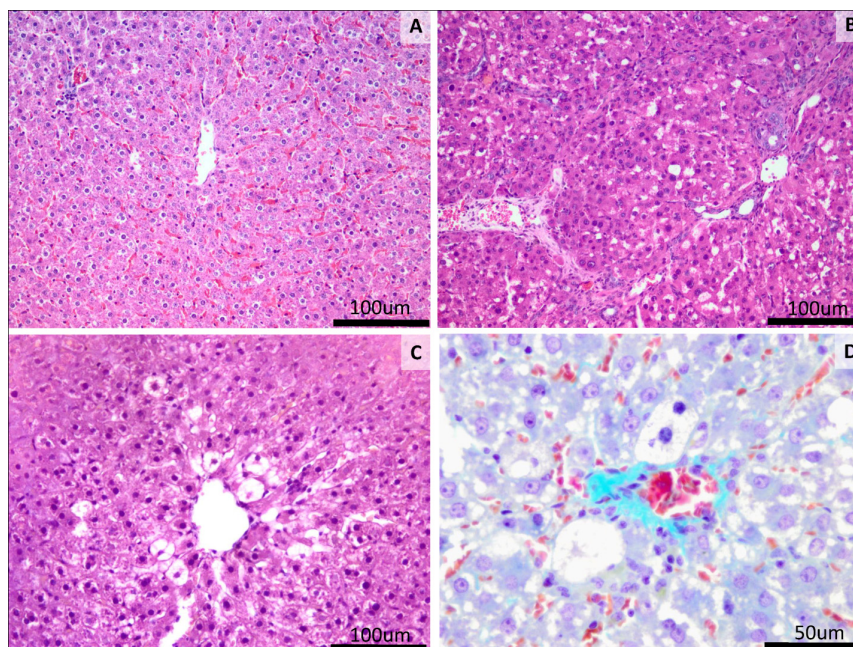
Figure 2. Histological changes in different experimental groups on the 30th day. Control group (A): central area, normal morphology, slight congestion; CCl_4 group (B): vacuolization of the hepatocytes from the central areas, centro-central bridges of degenerated and necrotic hepatocytes, oval cell hyperplasia; CCl_4+VitE group (C): hepatocellular vacuolization and necrosis in the central areas; CCl_4+Chitosan group (D): microvesicular steatosis and ballooning degeneration of the hepatocytes from central areas; HE stain (A,B,C), Masson's trichrome stain (D) original magnifications of 200× (A,B,C), 400x (D); Scale bar=100μm (A,B,C), Scale bar=50μm (D).

CONCLUSIONS

Our study confirmed the antioxidant effects of chitosan. Chitosan is able to decrease lipid peroxidation and to protect the endogenous antioxidant systems against the toxic effects of CCl_4. Only discrete histological liver injuries have been observed after chitosan administration. Vitamin E also demonstrates antioxidant properties, but the severity of the histological liver injuries was higher as compared to chitosan. In the used dose, the chitosan has a superior antioxidant and hepatoprotective effect as compared to vitamin E.

EXPERIMENTAL SECTION

Sixty four female Wistar rats, randomly distributed into four equal groups, have been used. The animals have been maintained at 23±2°C in the biobase of the Department of Physiology, Iuliu Haţieganu University of Medicine and Pharmacy Cluj-Napoca, Romania. The animals received standard food and water *ad libitum.* The experiment took place with the approval of the Ethical Committee of Iuliu Haţieganu University of Medicine and Pharmacy, Cluj-Napoca, and respected the Directive 86/609/EEC. Group I (Ctrl) received, by gavage, 0.9 ml/kg b.wt. sunflower oil, twice a week, for 30 days. Group II (CCl$_4$) received, by gavage, 1.2 ml/kg b.wt. CCl$_4$ 25%, diluted in sunflower oil, twice a week, for 30 days. Group III (CCl$_4$+vit E) received, in addition to the CCl$_4$, 5 mg/kg b.wt. vitamin E (Sicomed®, 30 mg/ml vials) daily, intramuscular injections. Group IV (CCl$_4$+CS) received, in addition to the CCl$_4$, daily intraperitoneal injection with 3 mg/kg b.wt. chitosan (Sigma-Aldrich®, molecular weight 190-310 kDa, deacetylation degree 75-85%). After 15 and 30 days, eight animals from each group were anesthetized with ketamine. Blood samples were taken from the retroorbitary sinus. Animals were euthanized by cervical dislocation. Liver samples were taken for biochemical assessment and a portion of the liver was fixed in formaldehyde for histological examination.

Malondialdehyde levels in the plasma and in the liver were assessed using the method of Conti [27]. Protein peroxidation was estimated through the measurement of the protein carbonyl groups using the method of Reznick [28]. The total amount of proteins was assed using Bradford method [29]. SOD activity was assessed using the method described by Flohe [30], and CAT activity using the method described by Pippenger *et al.* [31]. Sulfhydryl groups (SH) and reduced glutathione (GSH) were assessed using the method of Hu [32, 33]. Liver function was evaluated using the activity of ALT and AST enzymes in the blood with commercial assay kits (Diagnosticum Zrt. Budapest) [34].

Liver tissue samples were fixed in 10% buffered neutral formalin, embedded in paraffin; the sections were made at 4 micrometers with a microtome Leica RM 2125 RT and stained by Haematoxiline-Eosine and Masson's trichrome methods. The slides were examined under a microscope Olympus BX 51. The images were taken with Olympus DP 25 digital camera and processed by a special image acquisition and processing program: Olympus Cell B. Sections were scored by an independent observer blinded to the experimental protocol. The following lesions were scored according to Knodell Histological Activity Index (HAI): portal inflammation, periportal/bridging necrosis, intralobular degeneration/focal necrosis and fibrosis (Knodell) [35].

Statistical analysis was performed using non-parametric tests (Mann-Whitney, Kruskal-Wallis, Wilcoxon, Spearman non-parametric correlation). The analysis was done for every moment of the experiment and also concerning the dynamic of the parameters, using MedCalc 14.0 sofware. The results were expressed as mean±SD. *P* values were considered significant if <0.05.

ACKNOWLEDGEMENTS

REFERENCES

1. P.L. Wolf, *Indian journal of clinical biochemistry*. **1999**, *14*, 59.
2. J.A. Knight, *Journal of infusion nursing: the official publication of the Infusion Nurses Society*. **2005**, *28*, 108-117.
3. R. Joshi, J.P. Kamat, T. Mukherjee, *Chemico-biological interactions*. **2007**, *167*, 125.
4. N. Vargas-Mendoza, E. Madrigal-Santillan, A. Morales-Gonzalez, J. Esquivel-Soto, C. Esquivel-Chirino, Y.G.-R.M. Garcia-Luna, J.A. Gayosso-de-Lucio, J.A. Morales-Gonzalez, *World journal of hepatology*. **2014**, *6*, 144.
5. R. Simeonova, M. Kondeva-Burdina, V. Vitcheva, M. Mitcheva, *BioMed research international*. **2014**, 706302.
6. D.J. Reed, M.W. Fariss *Pharmacological reviews*. **1984**, *36*, 25s-33s.
7. Z.F. Zhang, Y. Liu, L.Y. Lu, P. Luo *Chinese journal of natural medicines*. **2014**, *12*, 488.
8. G.B. Kavishankar, S.S. Moree, N. Lakshmidevi, *Phytomedicine : international journal of phytotherapy and phytopharmacology*. **2014**, *21*, 1026.
9. Y.J. Li, L.Y. Li, J.L. Li, L. Zhang, F. Gao, G.H. Zhou, *Asian-Australasian journal of animal sciences*. **2015**, *28*, 374.
10. R. de Cabo, J.R. Burgess, P. Navas, *Journal of bioenergetics and biomembranes*. **2006**, *38*, 309.
11. H. Ochi, S. Takeda, *Gerontology*. **2015**, *61*, 319.
12. H. Hattori, M. Ishihara, *Biomedical materials*. **2015**, *10*, 015014.
13. Y. Wen, F. Yao, F. Sun, Z. Tan, L. Tian, L. Xie, Q. Song, *Materials science & engineering. C, Materials for biological applications*. **2015**, *48*, 220.
14. Y. Tang, L. Xie, M. Sai, N. Xu, D. Ding, *Materials science & engineering. C, Materials for biological applications*. **2015**, *48*, 1.
15. S. Ebrahimiasl, A. Zakaria, A. Kassim, S.N. Basri, *International journal of nanomedicine*. **2015**, *10*, 217.

16. P. Ramasamy, N. Subhapradha, V. Shanmugam, A. Shanmugam, *International journal of biological macromolecules*. **2014**, *65*, 559.
17. E. Al-Sayed, M.M. Abdel-Daim, *Planta medica*. **2014**, *80*, 1665.
18. M.M. Hafez, O.A. Al-Shabanah, N.O. Al-Harbi, M.M. Al-Harbi, S.S. Al-Rejaie, S. M. Alsurayea, M.M. Sayed-Ahmed, *Oxidative medicine and cellular longevity*. **2014**, 893212.
19. Y. Liu, Q. Liu, G. Ye, A. Khan, J. Liu, F. Gan, X. Zhang, S. Kumbhar, K. Huang, *Journal of agricultural and food chemistry*. **2015**, *63*, 242.
20. Y.H. Wang, X.J. Xu, H.L. Li, *International immunopharmacology*. **2014**, *22*, 126.
21. X. Pu, W. Fan, S. Yu, Y. Li, X. Ma, L. Liu, J. Ren, W. Zhang, *Canadian journal of physiology and pharmacology*. **2015**, *93*, 39.
22. S.M. Tabei, S. Fakher, M. Djalali, M.H. Javanbakht, M. Zarei, H. Derakhshanian, M.R. Sadeghi, E. Mostafavi, F. Kargar, *Bratislavske lekarske listy*. **2015**, *116*, 115.
23. M.F. Vrolijk, A. Opperhuizen, E.H. Jansen, R.W. Godschalk, F.J. Van Schooten, A. Bast, G.R. Haenen, *Redox biology*. **2015**, *4c*, 272.
24. M. Anraku, M. Kabashima, H. Namura, T. Maruyama, M. Otagiri, J.M. Gebicki, N. Furutani, H. Tomida, *International journal of biological macromolecules*. **2008**, *43*, 159.
25. S. Lores Arnaiz, S. Llesuy, J.C. Cutrin, A. Boveris, *Free radical biology & medicine*. **1995**, *19*, 303.
26. T.I. Jeon, S.G. Hwang, N.G. Park, Y.R. Jung, S.I. Shin, S.D. Choi, D.K. Park, *Toxicology*. **2003**, *187*, 67.
27. M. Conti, P.C. Morand, P. Levillain, A. Lemonnier, *Clinical chemistry*. **1991**, *37*, 1273.
28. A.Z. Reznick, L. Packer, *Methods in enzymology*. **1994**, *233*, 357.
29. M.M. Bradford, *Analytical Biochemistry*. **1976**, *72*, 248.
30. L. Flohe, F. Otting, *Methods in enzymology*. **1984**, *105*, 93.
31. C.E. Pippenger, R.W. Browne, D. Armstrong, *Methods in molecular biology*. **1998**, *108*, 299.
32. M.L. Hu, *Methods in enzymology*. **1994**, *233*, 380.
33. S. Mureşan, A. Filip, V. Simon, A.F. Gal, V. Miclăuş, N. Decea, R. Moldovan, A. Mureşan, *Studia UBB Chemia*. **2003**, *LVIII*, 7.
34. H.U. Bergmeyer, P. Scheibe, A. W. Wahlefeld, *Clinical chemistry*. **1978**, *24*, 58.
35. R.G. Knodell, K.G. Ishak, W.C. Black, T.S. Chen, R. Craig, N. Kaplowitz, T.W. Kiernan, J. Wollman, *Hepatology*. **1981**, *1*, 431.

MODELLING AND SIMULATION OF BOD AND COD FOR EFFLUENT LEVELS OF AN AERATION TANK FROM GHERLA WASTE WATER TREATMENT PLANT

MARIUS-DANIEL ROMAN[a*], RALUCA-ANDREEA FELSEGHI[a], MIRCEA-VLAD MUREŞAN[b]

ABSTRACT. The modelling results of BOD and COD for an aeration tank from Gherla's WWTP by Matlab/Simulink software program has no significant difference, because the results are close enough to the real ones that allow the user to make a good prediction regarding this parameters. A true validation of these results, including experimental validation of simulations of the entire collecting data was realistic. Validated process models can be used for dynamic simulations, for example, with different kinds of input data. In simulations the mathematical equations of process model are solved and the results given. Models and software for simulation have the possibility to control and evaluate the parameters. The presented control strategies use mainly ideal conditions, given the circumstances, for controllers and plant operations.

Keywords: simulation, modelling, Matlab, flow; BOD, COD.

INTRODUCTION

Simulation of activated sludge, is based on phenomena such as carbon oxidation, nitrification and denitrification, must necessarily account for a large number of reactions between of components. Mathematically is needed while to providing realistic predictions, the reactions must be representative of the most important fundamental processes occurring within the system. In this case the term process is used to mean a distinct event acting upon one or more system components. Furthermore, the model should quantify both the rate, concentration dependence and the relationship that one component has to another in a reaction, of each process [7].

[a] *Technical University of Cluj-Napoca, Building Services Engineering Department, 128-130 Boulevard December 21 Str., RO-400604, Cluj-Napoca, Romania*
[b] *Technical University of Cluj-Napoca, Engineering Materials and the Environment Department, 28 Memorandumului, 400114 Cluj-Napoca, Romania*
* *Corresponding author: Marius.ROMAN@insta.utcluj.ro*

In this case for a model is important to have something representative in the design and operation of wastewater treatment systems, it must be possible to evaluate parameter values which are wastewater specific and to estimate concentrations of important components in the influent [7]. The first step is to identify the components of relevance in the model. In this case these are BOD, COD, TN and others. The second step is to identify the biological processes occurring in the system, for example the transformations or the conversions that happen and write mathematical relations that describe the process. The third step is to use a simulation program. In this study were used Matlab/Simulink software. Although a number of environmental factors can influence the parameter values, these are specific factors in the wastewater, pH and temperature.

The two most common parameters used to recognize the composition of wastewater are the biochemical oxygen demand (BOD) and the chemical oxygen demand (COD). BOD_5 is a measure of how much dissolved oxygen is consumed by aerobic bacteria in 5 days at 20 ^{o}C. It is the broad measure of the strength of the organic matter in a waste stream. The typical range of BOD_5 in domestic wastewater ranges from 100 to 300 mg/L. COD is chemical oxygen demand and is measured chemically by digestion with acid. There exists a definite correlation between the COD and BOD under certain conditions and by determining the COD, the information about the BOD of the wastewater can be derived, but it is highly waste dependent [1], [2].

When a wastewater treatment system can be modelled, a certain number of simplifications and assumptions must be added in order to take the model tractable. Often this simplifications and assumptions are implicit, which may cause the user to overlook them. The system operates at constant temperature, because many of the coefficients are functions of temperature, their functionality would have to be explicitly expressed in the rate expressions, in order for time-variant temperature fluctuations to be considered.

It is known that the pH influences many of the coefficients. The inclusion of the alkalinity in the model allows the user to detect potential problems with pH control. The effects of limitations of nitrogen, phosphorus and other inorganic nutrients on the removal of organic substrate and on cell growth have not been considered. The coefficients for nitrification are assumed to be constant and to incorporate any inhibitory effects that other waste constituents are likely to have on them [3].

The purpose of this model is to find a mathematical model able to determine certain effluent levels, for BOD and COD concentrations depending on influent and effluent.

Khaled & Gina 2014 obtained in the case studies, for parameters COD and BOD in different plants of variable types and treatment capacities, that the correlation between BOD_5 and COD is generally linear, except in some rare cases where the relation was polynomial and sometimes doesn't have a definite pattern. However, this rare indefinite pattern might be due to inaccuracy in determination of the BOD_5 and COD parameters in such cases. Since the BOD and COD are correlated, the estimation of BOD_5 values using the quick COD test, and plant specific biodegradability index (which is the slope of the plotted correlation) became possible and relatively reliable. Thus, it can be used as a check parameter to evaluate performance for quick action. For existing wastewater treatment plants the BOD/COD correlation should be developed, to compromise the use of these parameters. In order to establish the BOD/COD correlation for a particular existing wastewater, one should have both COD and BOD5 values for several representative wastewater samples. From graphics the BOD_5 values versus the COD values then use the regression analysis to develop the correlation. The plotted BOD_5 and COD figures indicated that there is a clear linear positive correlation for most case studies, which differs from plant to another [2].

RESULTS AND DISSCUSIONS

Were performed 22 simulations for BOD to increasing values of inflow starting from 155.79 m³/h up to 400.54 m³/ h. Influent flow values and the influent concentrations were taken from experimentally determined data from treatment plant using the analysis method according to STAS 6560-82 [5].

Table 1. Experimental values for BOD

| Probes	Influent flow	Influent BOD	Effluent BOD	Probes	Influent flow	Influent BOD	Effluent BOD
	m³/h	mg/l	mg/l		m³/h	mg/l	mg/l
1	155.79	179.00	9.00	12	220.46	261.50	12.35
2	156.92	264.00	12.00	13	221.04	275.60	12.82
3	165.67	219.00	11.00	14	236.51	82.00	3.00
4	179.67	114.00	4.80	15	255.92	132.00	9.00
5	184.71	155.00	8.10	16	258.10	88.00	3.50
6	190.58	121.20	5.26	17	276.45	127.00	5.33
7	193.33	195.50	9.84	18	282.21	123.00	5.10
8	195.08	203.00	10.78	19	297.42	93.00	3.78
9	199.42	308.00	6.00	20	302.60	118.00	4.90
10	201.08	269.50	12.55	21	394.80	106.00	4.00
11	215.07	83.00	3.10	22	400.54	158.00	8.20
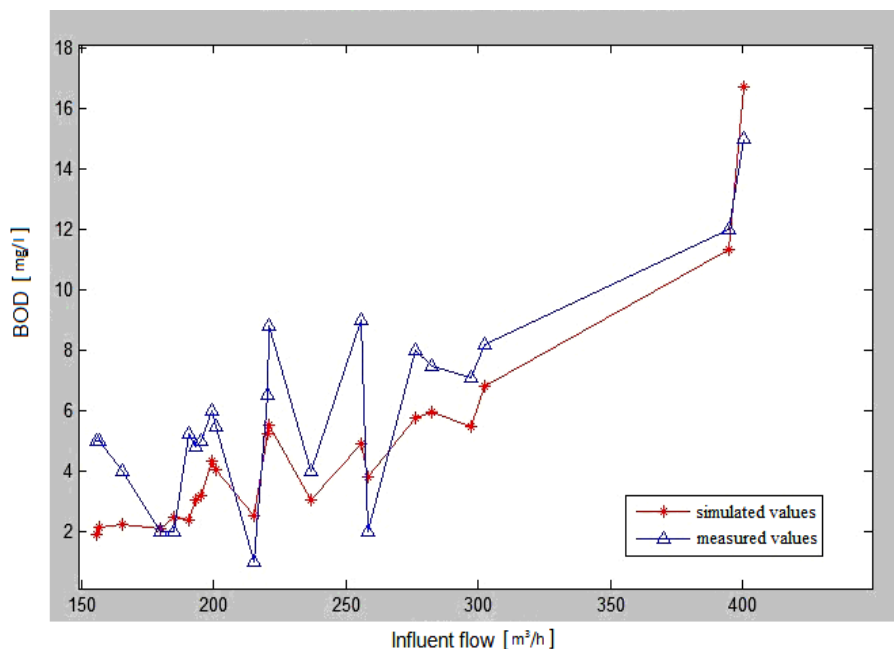
Figure 1. Simulated and measured values of BOD from Gherla's WWTP

Simulation results from data obtained were compared with those determined experimentally. In the case of biochemical oxygen demand after 5 days was obtained the graph from figure 1. It may be noted that the data obtained from simulation and the data obtained experimentally keeps tendency, which otherwise have no trend. The data measured at the plant can vary widely from day to day even for the same rate, this being also very difficult to simulate. But with this mathematical model results are close enough to the real ones that allow the user to make a good prediction of biochemical oxygen demand after 5 days, knowing the inflow of water and oxygen concentration standard.

As was shown in the graphic all data were simulated in according to standard NTPA-001/2005, below 25 mgO_2/l, although influent concentrations values were between 82 and 308 mgO_2/ l. The dissolved oxygen concentration can be measured by an electrochemical sensor for continuous determination of oxygen [6]. For COD, were performed 19 simulations for the increasing values of flow starting from 110.00 m^3/h up to 257.00 m^3/h. Concentration values from the influent and effluent have been determined experimentally by potassium dichromate method according to SR ISO 6060/1996 [5].

Table 2. Experimental values for COD

Probes	Influent flow	Influent COD	Effluent COD	Probes	Influent flow	Influent COD	Effluent COD
	m³/h	mg/l	mg/l		m³/h	mg/l	mg/l
1	110.00	346.56	63.84	11	142.63	470.08	54.24
2	114.38	470.08	54.24	12	171.25	264.00	46.80
3	121.71	519.20	61.60	13	171.38	331.00	55.90
4	122.33	546.56	68.32	14	201.42	293.00	92.20
5	125.04	342.72	28.56	15	202.25	252.72	94.88
6	125.25	428.40	66.64	16	212.08	288.00	76.80
7	129.58	508.80	57.60	17	212.63	205.20	84.14
8	132.25	431.20	70.40	18	255.96	212.00	54.40
9	130.00	380.64	58.56	19	257.00	280.80	93.60
10	141.79	518.40	57.60				

The results obtained of the simulation are compared to the experimental ones as was shown in figure 2. If in the case of biochemical oxygen demand after 5 days the results can vary widely from one day to another day, from a flow or even at the same flow, in case of oxygen concentration determined by the COD also from the influent and effluent varies more than in the previous simulation.

This absence of linearity is present as well in simulation of this parameter, but the trend keeps disorganized pattern of actual data. However data from simulation is close to the real values and the mathematical model can be used to predict the effluent of the oxygen concentration normally determined experimentally with COD method.
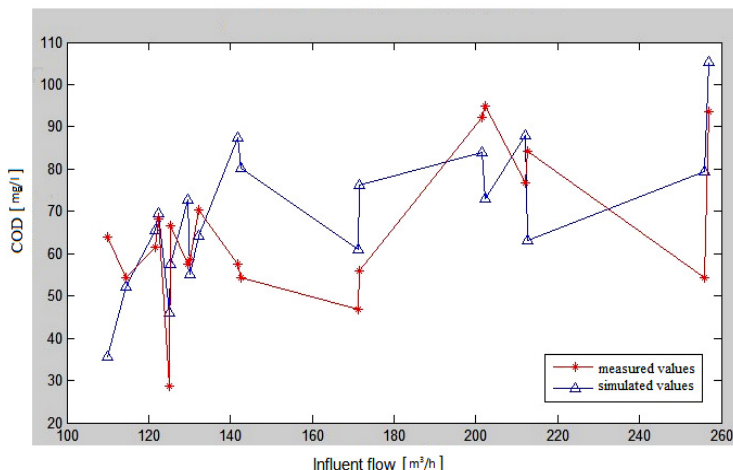

Figure 2. Simulated and measured values of COD from Gherla's WWTP

All simulation data are below to the maximum allowed by the standard NTPA-001/2005, below 125 mg / l. Block diagram of the model in Simulink can be seen in figure 3. In the left diagram can be seen the two input quantities of inflow in m³/h and biochemical oxygen demand after 5 days from the entry into the tank. The two enter in a multiplier which forwards them to the position S.

After completing the steps in the S output as is represented in figure 3, but also are sent to the workspace in the form of a matrix. Simulation time is set to 120 minutes.
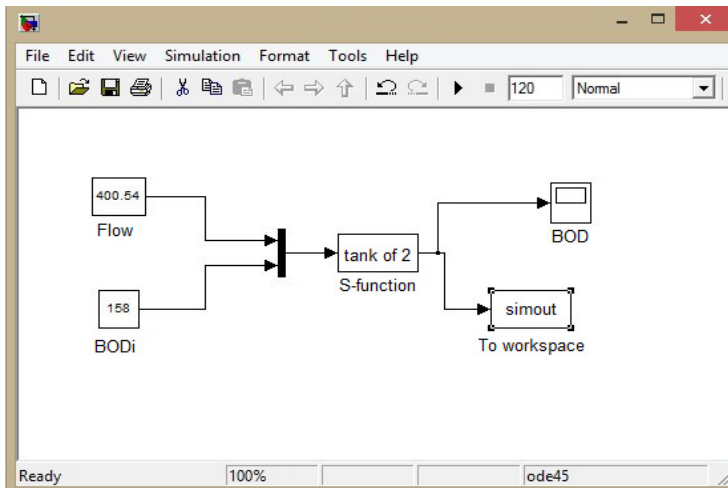

Figure 3. Block diagram of the model in Simulink

Data collected from the wastewater treatment plant keeps approximately a uniform trend, this was underlined by the results of simulations. In simulation we can't see a very good overlap of simulated results over determined experimentally, because the tank is circular and in case of rectangular tanks which is enough close to ideal form.

In some instances the tank geometry is very important for modelling, because in circular tanks the flow rate is smaller than in case of rectangular tanks, but it is not a rule.

CONCLUSIONS

In this paper, a procedure for getting a set of solutions for development of a mathematical model must incorporate the major events occurring within a system in a manner which is consistent with established knowledge about that system.

In the model should be included only those processes which are essential to a realistic solution and must select rate expressions for them that allow the use of simplified solution techniques without detracting from the applicability of the results.

The formal modelling of systems has been done with a mathematical model, which attempts to find analytical solutions enabling the prediction of the behavior of the system from a set of parameters and initial conditions. Modelling techniques include statistical methods, computer simulation, system identification, and sensitivity analysis; however, one of these is as important as the ability to understand the underlying dynamics of a complex system. Models applied for prediction aim at providing an accurate and fast image of a real systems behavior under different conditions [7].

Models may be linear with respect to variables or parameters; furthermore, a model can be nonlinear to parameters and linear to variable [8]. Linear models are used frequently, because the analytical solution can be found. For nonlinear models numerical solutions are predominant. Term mechanistic, physiological and white-box are used to describe that models structure is based on physical, chemical and biological laws.

Simulation is a reasonable way to extrapolate performance and scaling up process; additionally, it helps in understanding behavior and mechanisms of processes. Also the effects of system parameters and disturbances can be investigated using process simulation [9].

EXPERIMENTAL SECTION

We considered a tank which has: width 8.15 m and height of 5.7 m, with the volume of 4050 m³. It was considered as a static system with a piston-type flow with changing parameters as the water moves into the tank.

Were taken into account the following simplifying assumptions:

• All parameters are constant in radial section of the reactor (flow piston type).
• The flow rate is considered constant.
• Flow regime is considered ideal (flow regime shift (type D).
• Density and water temperature are considered constant and have not been taken into account.
• The influence of pH was not taken into account, which is assumed constant.
• Ammonification was considered constant.

- Biomass concentration in the tank was considered constant (specific death rates, the increase is much smaller than reaction rates).
- The vapour pressure of the water surface was not been considered.

To achieve simulation method was used Matlab/Simulink software. The mathematical model of the aeration tank consists of a system by a differential equation for each parameter to be determined. For numerical solutions of differential equations using the method of integration ODE45 (Dormánd-Prince) with variable step and relative tolerance of 10^{-3}. For calculation was used Matlab program version 7.14.0.739.

Knowing the size of the tank could calculate the cross section area as follows:

Wetted area is calculated first using the formula:

$$A_u = H \cdot l \tag{1}$$

where: A_u - wetted area [m^2]
H - height of the tank [m]
l - width of the tank [m]

Wetted perimeter is then calculated:

$$P_u = 2 \cdot (H + l) \tag{2}$$

Pu - wetted perimeter [m].

This is necessary to determine equivalent diameter, which has the following formula:

$$D_{ech} = 4 \cdot \frac{A_u}{P_u} \tag{3}$$

Dech - equivalent diameter [m]

Having calculated the equivalent diameter of the cross-sectional area can be calculated:

$$A = \frac{\pi \cdot (D_{ech})^2}{4} \tag{4}$$

A - cross-sectional area of the tank considered [m^2]

Input flow is known from experimental data and calculated using the above area can cause water flow rate:

$$w = \frac{F}{A} \tag{5}$$

W - water flow rate [m / h]; F - experimentally measured water flow [m^3/h]

All these equations are part of the mathematical model, namely the algebraic equations of the model.

Differential equations of the model are:

For BOD_5:

$$\frac{dBOD_5}{dt} = -Y_1 \cdot \frac{(BOD_5 - C_i)}{w} \tag{6}$$

For COD:

$$\frac{dCOD}{dt} = -Y_2 \cdot \frac{(COD - C_i)}{w} \tag{7}$$

where:

$\dfrac{dBOD_5}{dt}$ - represents the changes in biochemical oxygen demand after 5 days

Y_1 - theoretical stoichiometric ration

Y_2 - theoretical stoichiometric ration

C_i - standard oxygen concentration (1.5 mg / ml)

In the last decade, stringent quality standards are being applied to effluent plants, whether by regulatory authorities or environmentally concerned plant management. More often than not now, limits on nitrates, ammonia, phosphates, suspended solids, etc. are applied to outfalls [4].

To realise an optimum biological process, it is necessary to assure the best environment for the bacteria. A few important parameters are oxygen, pH and temperature, as well as suspended solids which indicate the bacteria concentration in the tank. Advanced monitoring of the bacteriological processes based on oxygen, ammonia and nitrate makes it possible to satisfy strict legal regulations and to optimize energy consumption at the same time.

Acknowledgments

REFERENCES

1. J. Hur, B.-M. Lee, T.-H. Lee, D.-H. Park, *Sensors*, **2010**, *10(4)*: 2460-2471.
2. K.Z. Abdalla, G. Hammam, *International Journal of Sciences: Basic and Applied Research*, **2014**, *13*, *1*, 42.
3. M. Henze, W. Gujer, T. Mino, M. van Loosdrecht, *Scientific and Technical Report*, **2000**, 6–8-16-26.
4. M.D. Roman, M.V. Muresan*, International Journal of Latest Research in Science and Technology*, **2014**, *3, 2*, 30.
5. NTPA-001/2005, *Normative act regarding the determination of limits of loading with pollutants of industrial and town wastewaters at evacuation in natural receptors*, **2005**.
6. E.M. Pică, *Development and study of an electrochemical sensor for continous determination of oxygen*, PhD Thesis, University Babes-Bolyai, Cluj-Napoca, **1990**.
7. H. Haimi, M. Mulas, K. Sahlstedt R. Vahala, *Helsinki University of Technology Water and Wastewater*, **2009**, *9*, 7.
8. S.A. Dellana, D. West, *Environmental Modelling & Software*, **2008**, *24*, *1*, 96.
9. S. Marsili-Libelli, *Advances in Biochemical Engineering/Biotechnology,* **1989**, *38*, 90-148.
10. http://www.water.me.vccs.edu/courses
11. http://www.eea.europa.eu
12. http://www.environmental-expert.com
13. http://www.iasj.net
14. https://fortress.wa.gov

KINETICS OF THE CORROSION PROCESS OF HOT DIP GALVANIZED STEEL REINFOCEMENT IN FRESH CONCRETE

VASILE RUS[a,c,*], ANDREEA HEGYI[b], HORAȚIU VERMEȘAN[c], ANCUȚA ELENA TIUC[c]

ABSTRACT. The quality of concrete structures is largely reflected by its durability. According to literature, the rebar corrosion initiation is delayed and the life duration of concrete structures reinforced with hot dip galvanized rebar is extended with up to 70 years compared to life duration of concrete structures reinforced with non-galvanized steel rebar. It is well known that the galvanized rebar surface activates in contact with the alkaline environment of fresh concrete, forming a crystalline compound namely calcium hydroxizincate. This crystalline compound is important for the kinetic and corrosion mechanism of rebar embedded in concrete. This work aims to evidence the galvanized rebar corrosion kinetics in fresh concrete, during the concrete hardening. Electrochemical methods were used during experiments. The test results show an activation of the zinc layer of galvanized rebar in contact with the alkaline environment of concrete, during the first days after rebar embedding in concrete. Zinc corrosion products formation lead to better corrosion resistance of galvanized steel rebar, compared to the resistance of non-galvanized steel rebar.

Keywords: hot dip galvanized steel reinforcement, concrete, corrosion, calcium hydroxizincate

INTRODUCTION

The quality of reinforced concrete structure is given by its durability, which is the period of time the structure maintains all the characteristics required for the proper use as established in the design. The technical performances of reinforced concrete structures decrease exponentially with time, due to the exponential increase of the degradation rate of both concrete and reinforcement. [1, 2, 8, 9, 15]

[a] *S.C. Betak S.A., 4 Industriei str., RO-420063, Bistrita, Romania*
[b] *INCD URBAN-INCERC, 117 Calea Floresti, RO-400524, Cluj-Napoca, Romania*
[c] *Technical University of Cluj-Napoca, Faculty of Materials and Environmental Engineering, 103-105 Muncii Blvd., RO-400641, Cluj-Napoca, Romania*
* *Corresponding author: rusvasile@betak.ro*

According to literature, the main factors that cause the reinforced concrete degradation are (starting from the most important to the least important): reinforcement corrosion, acid solutions aggression, sulfate attack, alternating wet and dry conditions, repeated freeze-thaw cycles, levigation, internal stress, external forces, salt crystallization, the aggregates reaction with concrete, and abrasion. [10, 11] Note that the reinforcement corrosion is the main cause for concrete degradation and for the reinforced concrete structures and components durability decrease.

Corrosion of reinforced concrete structures should be studied regarding concrete/steel rebar system interaction with the surrounding environment, and regarding the rebar interaction with concrete [12].

Many rebar corrosion protection methods are proposed worldwide, all having both advantages and disadvantages. Among these, hot dip galvanizing of steel reinforcement has been studied for the past 50-60 years and based on theoretical and electrochemical arguments, laboratory and in situ testing, is proved to be one of the most effective corrosion protection methods up to this day. [1-7, 13-16] Hot dip galvanizing is used for 2% of the total amount of steel reinforcement in the US and for 1% in Europe, but these values are increasing every year, especially for the structures designed to be used in extremely corrosive, marine or tropical climate environments. [1, 2, 7, 13-16]

Literature [3-6, 13-16] indicates that corrosion occurs 2-3 days after the hot dip galvanized steel rebar contact with fresh concrete. Corrosion products forms following the corrosion initiation, some of which some play a passivation role, such as calcium hydroxizincate, while other corrosion products, such as zinc oxides and hydroxides - that are insoluble in water, do not have a passivation role. In order to obtain calcium hydroxizincate, about 10 μm thick zinc coating is used. Because the corrosion products layer is adherent and compact at the surface of the galvanized steel reinforcement, it is more resistant to corrosion. On the other hand, zinc is less noble than steel, thus ensuring steel cathodic protection. As such, the steel is protected for as long as the zinc layer is not fully consumed.

Previous results obtained by the authors [17-21] support the fact that by using hot dip galvanized reinforcements the durability of concrete structures is increased and the work in this paper searches to clear the kinetics of the corrosion process of hot dip galvanized steel reinforcement in fresh concrete.

The aim of the experiments was to analyze the kinetics of hot dip galvanized steel rebar in fresh concrete, until concrete hardening. This study is important because most reactions in concrete take place in this phase; such as the cement hydration – hydrolysis, the concrete pH stabilization, and the activation of the hot dip galvanized steel rebar surface, followed by the calcium hydroxizincate formation [13-16].

RESULTS AND DISCUSSION

The experimental chronoamperometry curves were plotted, showing the current density variation for 24 hours, at constant potential. Experimental tests of samples with non-protected or with hot dip galvanized reinforcement embedded in various concrete age were made. Concrete age is given by the time passed since concrete pouring (samples preparations) till the tests. This time, the samples were all kept in identical conditions in laboratory. The results are shown in Figure 1 and Figure 2.
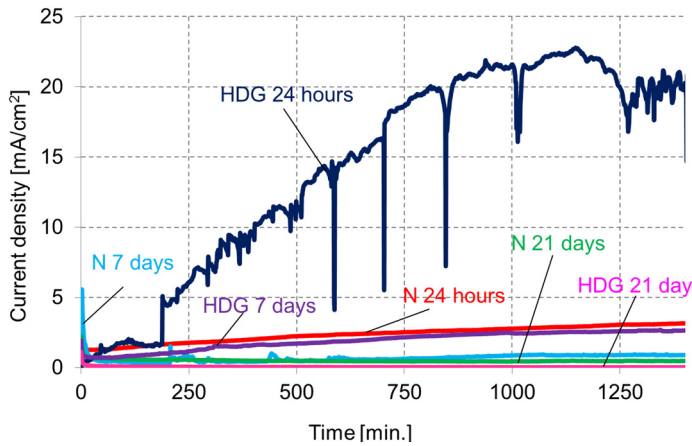
Figure 1. Current density evolution for the galvanized and non-galvanized steel rebar, during concrete hardening
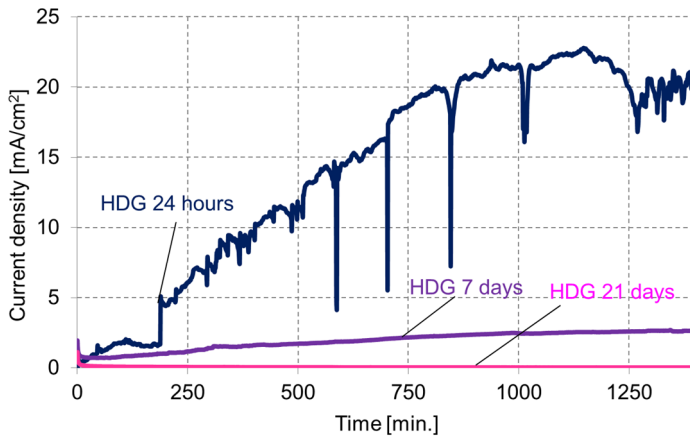
Figure 2. Current density evolution for the galvanized steel rebar in concrete, during concrete hardening

Twenty-four hours after concrete casting, the current density is high in the case of the hot dip galvanized rebar. This was considered an activation indicator due to the fact that the zinc-coating surface of galvanized rebar activates when introduced in alkaline concrete environment. Thus, a fraction of zinc is consumed, resulting specific corrosion products. The peaks of the "HDG 24 hours" plot indicate that the passive layer regenerates. This layer is subsequently attacked by alkaline concrete and destroyed.

According to the chronoamperometry tests of galvanized steel rebar, the corrosion current density strongly decreases after 7, respectively 21 days from the concrete casting (Figure 2). This is a qualitative sign for the zinc corrosion rate dropping due to the formation of a thicker or more compact corrosion products layer. Moreover, as it can be seen, the diagram of concrete/HDG rebars samples after 21 days since rebars embedment, does not show current densities peaks. This was interpreted as a passive layer formation on HDG rebars surface, enough resistant to prevent metal surface activation and corrosion.

By comparing the data obtained, it can be seen that 24 hours after concrete casting, the zinc coating on steel rebar exhibit a much stronger activation than the non-galvanized steel. The tests conducted 7 days after concrete casting, show that the difference between the current densities of galvanized and non-galvanized reinforcement is much lower compared to the values found 24 hours after rebar embedding in concrete. However, the values obtained for the galvanized steel samples are higher, showing a higher corrosion rate compared to that of the non-galvanized steel rebar.

Twenty-one days after rebar embedment in concrete, the current density drops significantly, both for the galvanized and non-galvanized rebar. This was considered a stabilization point for the two metals surfaces due to the formation of specific corrosion products layer. This time however, the current density of galvanized steel was very low; it almost linearly increased with time and was lower than the current density of non-galvanized steel.

Twenty-one hours after rebar embedment in concrete, the galvanized steel showed a lower corrosion rate compared to the non-galvanized steel, due to the protective corrosion products layer formation on zinc surface. Although this corrosion products passive layer also formed on the non-galvanized steel surface, the passivizing capacity of the corrosion products layer on zinc surface was stronger, as shown by the current density decrease with time.

The linear polarization plots recorded, in Tafel interpretation, are shown in Figure 3. The corrosion potential, corrosion current and corrosion rate are shown in Table 1.

From Figure 3 and Table 1 it can be seen that the galvanized rebar/fresh concrete system, noted with „initial HDG", show the more negative corrosion potential (-1424 mV). This indicates a powerful activation of the zinc surface immediately after rebar embedment in the alkaline environment of fresh

concrete. Also, the corrosion current of this system is the highest (115.62 µA/cm^2), indicating a high corrosion rate. On contrary, the non-galvanized steel rebar/ fresh concrete system, noted with „initial N", shows a potential shifts toward positive values, with 794 mV, but still remaining in the negative domain of metal surface activation. The corrosion current recorded for the non-galvanized rebar system is lower compared to the galvanized rebar system. Thus, the corrosion rate of the non-galvanized steel rebar system is lower immediately after rebar embedment in fresh concrete, when compared to the galvanized rebar system.
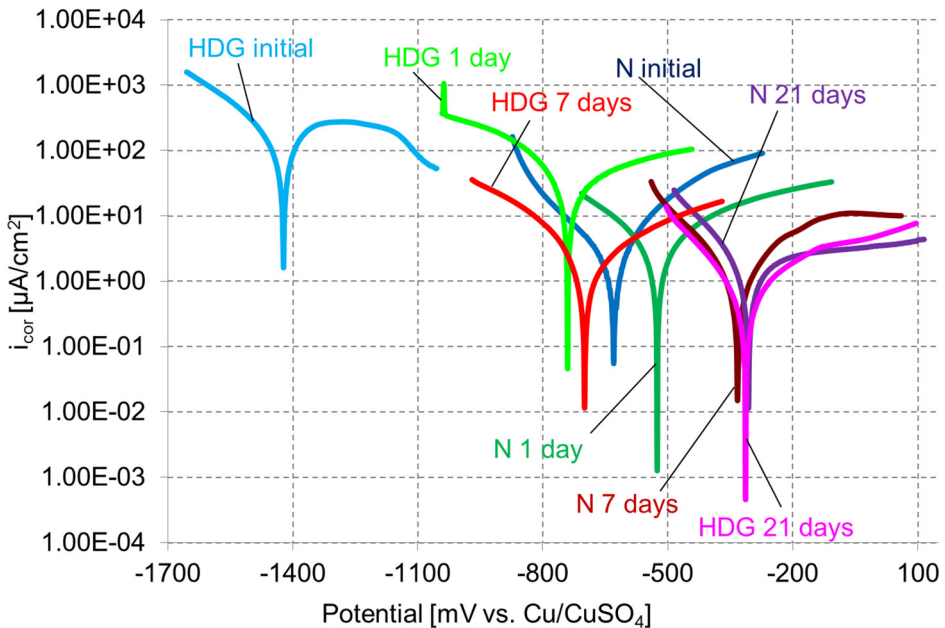

Figure 3. Tafel plots recorded for the samples with galvanized or non-galvanized steel rebar in concrete

Tests conducted 24 hours after rebar embedment in concrete show a corrosion potential fast shifting toward positive values and a corrosion current decrease, for all samples. Even so, the corrosion potential of galvanized steel remains more negative, with 215 mV, and the corrosion current values remains much higher compared to the non-galvanized steel. These results are also supported by literature. According to literature [3-6], zinc reacts with the alkaline environment when introduced in fresh concrete, forming a passive layer that is essential for subsequent corrosion protection.

The electrochemical systems kept in laboratory for 7 days were tested. The results showed passivation of both rebar types, as the corrosion potential shifted towards positive values. Also, the corrosion current decreased.

Between day 7 and day 21, the both rebar system starts to stabilize. The corrosion potential becomes more positive and the corrosion current values decrease. During this period of time, the differences between the two rebar systems corrosion potentials and corrosion currents are smaller compared to previous time intervals.

Table 1. Kinetic corrosion parameters determined from the polarization curves for the galvanized and non-galvanized steel samples, at various concrete ages

Electrochemical system	E [mV]	$i_{cor.}$ [µA/cm^2]	$v_{cor.}$ [µm/an]
N Initial	-630	19.59	227.19
N 1 day	-525.5	12.11	140.48
N 7 days	-333	1.18	13.69
N 21 days	-313.5	0.94	10.94
HDG initial	-1424	115.62	1734.37
HDG 1 day	-740.5	60.80	911.97
HDG 7 days	-701.5	1.62	24.36
HDG 21 days	-315	0.65	9.69

Tests conducted on the electrochemical systems 21 days after concrete casting indicate rebar passivation. The corrosion potential for the galvanized steel sample is -315 mV, and for the non-galvanized steel sample is -313.5 mV. Also, the corrosion current strongly decreases in both rebar types.

As seen in Figure 3, the corrosion current of galvanized rebar is lower 24 hours after concrete casting. During the first 7 days after rebar embedding in concrete, the potential shift toward positive values is stronger (with 722.5 mV). In the same time, the corrosion current decreases. According to this data, most of the passive layer forms during this period of time. Experimental results show that the passive layer does not form during the first 24 hours from the rebar embedding in concrete. During the time interval between day 7 and day 21, the corrosion current decrease was lower (0.98 µA/cm^2), even though the corrosion potential shifted significantly toward positive values (386.5 mV).

The changes that occur in the corrosion kinetics of the non-galvanized steel, as shown in Figure 3, are not as significant when compared to the galvanized steel system. The corrosion potential shifts toward positive values, indicating the steel passivation in hardened concrete. The corrosion current also decreases. Although the non-galvanized steel system corrosion current is initially lower compared to the galvanized steel, 21 days later after rebar embedment in concrete, it becomes higher. This shows a higher rate of non-galvanized steel corrosion, 21 days after concrete casting.

Regarding the effectiveness of corrosion protection, the galvanized rebar showed a higher corrosion rate in the first 7 days when compared to the non-galvanized rebar. During the time interval between day 7 and day 21 from rebar embedment in concrete, the corrosion rates of both rebar types reverses. The effectiveness of corrosion protection EP (Scheme 1) becomes positive: 11.45%. This is an indicator of a passive layer formation on the galvanized rebar surface.

If we consider the corrosion rate constant during the first 7 days after rebar embedment in concrete and equal with the initial corrosion rate, the zinc layer thickness would decrease with approximately 34 μm. If we consider the corrosion rate constant during the first 7 days after rebar embedment in concrete and equal to the corrosion rate in the 7th day after rebar embedment in concrete, a 0.5 μm zinc layer thickness would have been consumed. As the corrosion rate is not constant during this time interval, the simple arithmetic mean of these two values was calculated. Thus, the consumed zinc layer calculated thickness, of approximately 17 μm, is close to the values found in the literature (10-15 μm) when an efficient passive layer forms on the galvanized rebar surface.

According to data shown in Table 1, neither of the rebar systems reaches the passive state condition 21 days after concrete casting. According to Table 1, the corrosion potential of the HDG electrochemical system, 21 days after concrete casting (HDG 21), indicates a lower rebar corrosion, close to passivation state, while the corrosion potential of the N 21 system, indicates a higher rebar corrosion (50%).

CONCLUSIONS

The conclusions from experimental data are:
1. Zinc surface activates after galvanized steel rebar embedment in fresh concrete. This is evidenced by the corrosion current density recorded using chronoamperometric method and by the kinetic parameters recorded using the linear polarization method. All the experimental values found decreased with time (hours, days) after galvanized rebar embedding in fresh concrete.

2. The studied parameters decrease with time was due to a passive layer formation on the galvanized rebar surface, which inhibits corrosion process. Additional testing of passive layer was not conducted, considering it was as described/ in accordance with literature.

3. The galvanized steel rebar surface showed an initial higher activation compared to the non-galvanized steel rebar. However, it displayed a faster and stronger passivity. Thus, the corrosion potential shift toward positive values was more significant (1109 mV) for the galvanized sample, compared to the non-galvanized sample corrosion potential (316.5 mV). Also, the galvanized steel rebar corrosion rate decreased in time from higher values (911.9 μm/year) compared to the non-galvanized steel rebar corrosion rate (of 227.2 μm/year) to lower values (9.7 μm/year) compared to the non-galvanized rebar (10.9 μm/year).

Initially, the HDG steel surface strongly activates due to contact with alkaline concrete. Corrosion products form on the galvanized surface, with passivation role, as shown by the corrosion potential shifting toward positive values and by the corrosion current and corrosion rate values decrease. Twenty-one days after both reinforcement types embedment, the kinetic parameters show a much more reduced corrosion of HDG rebars corrosion compared to non-galvanized rebars.

EXPERIMENTAL SECTION

The electrochemical cell used, as shown in Figure 4, has the following components: the working electrode (the rebar), the reference electrode - Cu/CuSO$_4$, and the graphite counter electrode, all embedded in the fresh concrete matrix. All the experiments were conducted on the same concrete type; using PC 52 ø8 mm reinforcement, and using hot dip galvanized (HDG) or non-galvanized (N) rebar samples.

The reinforcement rods were galvanized by immersion in a hot galvanizing bath at a temperature of 450°C, thus obtaining a 140 μm thick zinc layer. The coating thickness obtained through hot dip galvanizing was determined by electromagnetic method, using a PHYNIX – Surfix device, and by testing the coating dissolution, according to SR ISO 1460 and SR EN ISO 2178.

The samples were built by introducing the three electrodes (working electrode, reference electrode and counter electrode) in fresh concrete (right after concrete preparation). The samples were kept in laboratory conditions until testing.
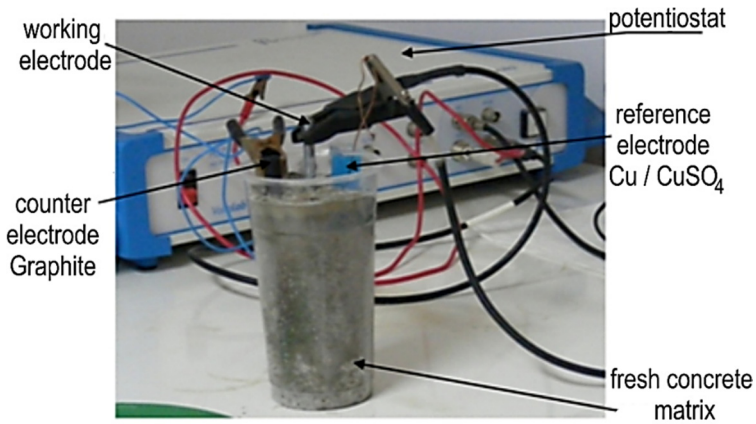
Figure 4. The electrochemical cell

The C 20/25 class concrete was prepared according to the mix design shown in Table 2, according to NE 012-2007 normative. The CEM I 42.5N cement used had the oxide composition as shown in Table 3.

The built electrochemical systems were coded as following:

(HDG x) – Hot dip galvanized steel rebar in concrete; tested x days after rebar embedment in concrete;

(N x) – Non-galvanized steel rebar in concrete, tested x days after rebar embedment in concrete.

Table 2. The concrete used for samples building, submitted to electrochemical testing

The basic components for 1 m^3 concrete		[Kg/ m^3 concrete]
Water		123
CEM I 42.5N cement		308,3
Total of aggregates		1869
Size of aggregates used [mm]	0-4 mm	1121,4
	4-8 mm	747,6

Table 3. The oxide composition of the cement used for the concrete preparation

No.	Cement type	Oxide composition [%]										
		P.C.	SiO_2	Al_2O_3	Fe_2O_3	CaO	MgO	K_2O	Na_2O	TiO_2	SO_3	Cl^-
1	CEM I 42.5 N	2.05	15.06	6.23	3.5	61.9	7.0	1.0	0.25	0.31	2.58	0.015

Information regarding the process kinetics is obtained by analyzing the chronoamperometry curves at the constant potential of 500 mV (vs. Cu/CuSO4). The current density was recorded every 60 seconds for 24 hours at various concrete maturation stages (1 day, 7 days, 21 days after rebar embedment in concrete).

Quantitative information was obtained using linear polarization. The potential scanned with a rate of 2 mV/sec, for ±300 mV compared to the open circuit potential, at room temperature. Based on the Tafel experimental plots, the main kinetic indicators were recorded (corrosion potential, corrosion current and corrosion rate). The experiments were conducted after various numbers of days since rebar embedment in concrete (immediately after, and 1, 7 and 21 days after rebar embedment in concrete).

The effectiveness of corrosion protection offered by hot dip galvanization method for each time period after the concrete preparation was calculated using equation (1)

$$\text{EP} = \frac{v_{cor.}^N - v_{cor.}^{ZT}}{v_{cor.}^N} * 100 [\%] \tag{1}$$

where:
$v_{cor.}^N$ = non-galvanized steel corrosion rate, [mm/year];
$v_{cor.}^{ZT}$ = galvanized steel corrosion rate, [mm/year].

ACKNOWLEDGMENTS

REFERENCES

1. M.C. Alonso, I. Martinez, J. Fullea, V. Ibarra, In-situ monitoring of galvanised reinforced concrete structures. The Spanish experience, INTERGALVA, Madrid **2009**.
2. C. Andrade, C. Alonso, *Constr Build Mater*, **1996**, *10*(5), 315.
3. C. Andrade, C. Alonzo, Electrochemical Aspects of Galvanized Steel, in Galvanized Steel Reinforcement in Concrete, Elsevier, Editor S.R. Yeomans, **2004**, 111.
4. T. Belleze, M. Malavolta, A. Quaranta, N. Ruffini, G Roventi, Corrosion behavior in concrete of three differently galvanized steel bars, Cement & Concrete Composites, **2006**, 28.
5. M. Carbucicchio, R. Ciprian, F. Ospitali, G. Palombarini, *Corrosion Science,* **2008**, *50* (9), 2605.

6. I. Cornet, B. Bresler, Galvanized reinforcement for concrete – II, International Lead Zinc Research Organization, New York, **1981**, 1.

7. J.A.A. Gonzàlez, *British Corrosion Journal,* **1982**, *17*(1), 21.

8. I. Lingvay, Coroziunea provocata de curenții de dispersie vagabonzi, Ed. Electra, București, **2005**, *25*, 113.

9. C. Mircea, Durabilitatea elementelor și structurilor de beton precomprimat- http://www.incerc cluj.ro, iunie **2005**, 7.

10. V. Nicolau, Betonul armat, Ed. Tehnică, București, **1962**, 7, 25, 93, 108, 163.

11. I. Nicula, T. Oneț, Beton armat, Ed. Didactica și Pedagogică, București, **1982**, *5*, 40.

12. T. Visan, Electrochimie si coroziune pentru doctoranzii ELCOR, Ed. PRINTECH, Bucuresti, **2002.**

13. S.R. Yeomans, Galvanized Steel in Reinforced Concrete, Elsevier B.V., Amsterdam, **2004**, 297.

14. S.R. Yeomans, Considerations of the characteristics and use of coated steel reinforced in concrete, NISTIR 5211, Univ. New South Wales, Canbera, **2004**.

15. C. Budan, D.N. Stoica, A.M. Cotescu, *Revista Romana de Materiale*, **2010**, *40*(2), 132-140.

16. S.R. Yeomans, *Corrosion*, **1994**, *50*, 72.

17. Andreea Hegyi, H. Vermeșan, G. Vermeșan, V. Rus, Internaționale Conference on Advanced Composites Engineering COMAT Brasov **2010**, 116.

18. Andreea Hegyi, H. Vermeșan, G. Vermeșan, V. Rus, E. Grunwald, Research on the corrosion protection of galvanized rebar in concrete, Jahrbuch Oberflachen technic, band 66, Eugen G. Leuze Verlag, Germania, **2010**, 229.

19. Andreea Hegyi, H. Vermeșan, V. Rus, *International Review of Applied Science & Engineering,* **2010**, *1*(1-2), 45.

20. Andreea Hegyi, V. Rus, C. Bumbuc, H. Vermeșan, *Metalurgia International,* **2011**, *16*, 6, 10.

21. Andreea Hegyi, H. Vermeșan, C. Bumbuc, *Metalurgia International,* **2010**, *15*, 11, 74.